Sources of Neogene erosion in the European Central Alps.

The cooling history of the Lepontine Dome revealed by low-temperature thermochronology and numerical 'sandbox' modelling

Dissertation
zur Erlangung des Doktorgrades der Naturwissenschaften
vorgelegt dem Fachbereich Geowissenschaften der Universität Bremen
von Simon Elfert

Bremen, 22.04.2014

Betreuende Erstgutachterin: Prof. Dr. Cornelia Spiegel
Zweitgutachterin: Prof. Dr. Katrin Huhn

Datum des Kolloquiums: 21. Mai 2014

Erklärung

Hiermit versichere ich, daß ich

(I) die Arbeit ohne unerlaubte fremde Hilfe angefertigt habe,

(II) keine anderen als die von mir angegebenen Quellen und Hilfsmittel benutzt habe, und

(III) die den benutzten Werken wörtlich oder inhaltlich entnommenen Stellen als solche kenntlich gemacht habe.

Darüber hinaus erkläre ich hiermit, dass ich mich weder zuvor einem Promotionsverfahren unterzogen habe, noch ein solches beantragt habe.

Bremen, den 22.04.2014

(Simon Elfert)

Acknowledgements

Many thanks to Prof. Dr. Cornelia Spiegel for giving me the opportunity and support to explore the world of geosciences as an ecologist. Thank you, Conny, for your constructive reviews and insightful discussions. Also many thanks to Prof. Dr. Katrin Huhn for critically discussing our joint project and being the second assessor of this PhD thesis.

Furthermore, I thank my 'PhD siblings' Linda and Wolfgang for the great assistance, motivation and friendship. Also great thanks to Anke, Vera and Angelika. You are the heroes of the lab! Moreover, thank you Barbara and Frank for the encouraging conversations.

Among all the great people, who helped me during these years, I, first and foremost have to give my dearest thank to my wonderful wife Romy. Thank you for the strength you are giving me and your patience! Finally, I have a great family, who I can rely on. Thank you.

Of course, there are many more people, friends, who thought of me, encouraged and supported me, what I really appreciate. Thanks to all of you.

1. Zusammenfassung

Gebirge entstehen durch das Zusammenspiel von verschiedenen Kräften. Um diese zu verstehen, müssen sowohl die Einflüsse von endogenen als auch von exogenen Prozessen bestimmt werden. Seit über hundert Jahren wird die geologische Geschichte der europäischen Zentralalpen von Wissenschaftlern untersucht und rekonstruiert. Dementsprechend sind heute viele der geotektonischen Strukturen und metamorphen Überprägungen (Druck/Temperatur bedingte Veränderungen) der alpinen Gesteinseinheiten erforscht. Über die Jahre sind Modellvorstellungen gereift, welche die Entwicklung der Alpen in weiten Zügen erklären können. Allerdings wirft die Exhumierungsgeschichte der Alpen während des Neogens noch immer einige Fragen auf. Über den Charakters der mio-pliozänen Exhumierung der Zentralalpen wird in der Literatur durchaus kontrovers diskutiert. In Folge dessen herrscht Uneinigkeit über die Bedeutung und das Zusammenspiel von Tektonik und Klima auf die alpine Gebirgsbildung (und Topographie).

Die vorliegende Doktorarbeit ist Teil des ESF EUROCORES Programms TOPO-EUROPE mit der Zielsetzung, die neogene Exhumierungsgeschichte der Zentralalpen anhand der Abkühlungsgeschichte des Lepontin Doms (Tessin, Schweiz) zu rekonstruieren.

Der Lepontin Dom liegt im Kern der Zentralalpen. Die hier anstehenden Gesteinsdecken wurden während der alpinen Gebirgsbildung tief versenkt und seit dem frühen Miozän wieder freigelegt. Die Exhumierung dieser Gesteine ging mit einer Abkühlung einher. Die Proben für diese Studie wurden entlang von zwei horizontalen Profilen im zentralen Lepontin (in etwa Nord-Süd orientiert, entlang der Flüsse Ticino und Maggia) genommen. Um die Exhumierungsgeschichte des Untersuchungsgebiets zu rekonstruieren wurden in dieser Doktorarbeit zwei Methoden aus der Niedrigtemperatur-Thermochronologie angewendet: die Spaltspur-Analyse und die (U-Th-Sm)/He Datierung an Apatiten. Gemeinsam decken diese beiden Methoden einen Temperaturbereich zwischen ~110 °C und 40 °C ab, was einer Tiefe von ~3,3 km bis ~1 km unter der Oberfläche entspricht, wenn man einen geothermischen Gradienten von 30 °C km^{-1} zugrunde legt. Durch inverse thermische Modellierung der Spaltspur- und (U-Th-Sm)/He-Daten lassen sich Rückschlüsse auf das Exhumierungsverhalten der Oberkruste ziehen.

Darüber hinaus wurde ein neuartiger Ansatz entwickelt um numerische „Sandkasten"-Modelle mit der Spaltspur-Thermochronologie zu verbinden. Zunächst wurden verschiedene Experimente mit einem etablierten numerischen „Sandkasten"-Modell durchgeführt. Auf der Grundlage der Diskreten Elemente Methode simulierte das Modell sowohl Bewegung als auch Deformation von granularen Stoffen bei Einwirkung einer bestimmbaren Deformationskraft. Der Aufbau der Experimente wurde an die Tiefenstruktur der West- und Zentralalpen (abgeleitet aus reflexionsseismischen Untersuchungen) angelehnt, so dass aus der Entwicklung der resul-

tierenden numerischen Partikelkeile Rückschlüsse auf Gebirgsbildungsprozesse und damit auf (tiefkrustale) Materialeigenschaften der Alpen gezogen werden konnten.

Allerdings simulieren diese numerischen „Sandkasten"-Experimente weder Temperatur noch Erosion (wobei letzteres für die Exhumierung eine entscheidende Rolle spielt). Am Ende eines Experiments steht die Berechnung einer Erosionsoberfläche, was gleichzeitig den ersten Teil des neu entwickelten Ansatzes darstellt. Anschließend wird aus der vertikalen Entfernung eines ausgewählten Partikels zur Erosionsoberfläche (also seiner Tiefe) die Temperatur berechnet. Da die Partikelpositionen während des Modelllaufs aufgezeichnet werden, können für einzelne Partikel Zeit-Temperaturpfade für die Dauer eines Experiments rechnerisch ermittelt und über eine thermische Vorwärtsmodellierung in synthetische Spaltspurdaten überführt werden.

Als letzter Schritt wurde die Entwicklung der Zentralalpen seit dem Oligozän entlang des seismischen NFP20-Ost-Profils (ein Teil der Europäischen Geotraverse) mit einem weiteren numerischen „Sandkasten"-Experiment rekonstruiert. Nach der Projektion des beprobten und analysierten Ticino-Profils auf das modellierte Profil, wurden Partikel aus dem numerischen „Sandkasten"-Experiment ausgewählt, die von ihrer Position her den Datenpunkten entlang des Ticino-Profils entsprachen, bzw. das Profil nach Norden und Süden erweiterten. Die Bewegungspfade dieser Partikel wurden in synthetische Spaltspurdaten übersetzt. Die Berechnung der dafür notwendigen Zeit-Temperaturpfade erfolgte auf der Grundlage von drei verschiedenen Szenarien, in denen jeweils der Beginn verstärkter Erosion (interpretiert als tief greifende Taleinschneidung) verändert wurde. Die synthetischen Spaltspurdaten und die zugrunde liegenden thermischen Geschichten der drei Szenarien wurden mit den gemessenen Spaltspurdaten entlang des Ticino-Profils und der daraus abgeleiteten Exhumierungsgeschichte verglichen.

Die synthetischen Spaltspurdaten zeigen im Bezug auf die gemessenen thermochronologischen Daten und ihrer thermischen Modellierung die gleichen Trends in den Abkühlpfaden und eine vergleichbare Größenordnung der Abkühlalter. Zusätzlich ist ihre räumliche Verteilung weitgehend identisch mit den jüngsten Abkühlaltern im Zentrum des Lepontin Doms bzw. in dem Bereich entlang des Lepontin äquivalenten numerischen „Sandkasten"-Profils. Aus den Ergebnissen der thermochronologischen Analysen des Lepontin Doms und dem zuletzt genannten numerischen „Sandbox"-Experiment kann mit Bezug auf die neogene Exhumierungsgeschichte des Lepontin Doms ein erstes Fazit gezogen werden: Während des Miozäns traten episodische, stetige, schnelle und langsame Abkühlung kleinräumig nebeneinander auf. Die Abkühlung in den südlichen Bereichen erfolgte verhältnismäßig früh und episodisch (Temperaturen von 110 °C wurden bereits im frühen Miozän erreicht). Die erhobenen thermochronologischen Daten zeigen darüber hinaus, dass der Südosten im Vergleich zum zentralen südlichen Bereich früher abkühlte. Erst im mittleren bis späteren Miozän erreichte auch der zentrale Teil des Lepontin Doms Temperaturen von unter 110 °C und kühlte in der Folgezeit schnell und gleichmäßig ab. Der nördliche Lepontin Dom kühlte wiederum früher (Temperaturen von 110 °C wurden bereits im frühen Miozän erreicht), allerdings gemächlicher ab. Die Ergebnisse des numerischen „Sandbox"-Experiments lassen vermuten, dass diese nördlichen Gesteinseinheiten starke Versätze während des Miozäns erfahren haben. Da die Einheiten dabei aber vor allem horizontal bewegt wurden, kühlten sie trotz schneller Bewegung nur langsam ab.

Die Strukturanalyse des numerischen „Sandkasten“-Experiments deutet darauf hin, dass basale Akkretion einen entscheidenden Einfluss auf die Entwicklung der Zentralalpen und des Lepontin Doms hatte. Überträgt man die strukturelle Entwicklung des Modells auf die Zentralalpen, dann wurden die Aar- und Gotthard Externmassive seit dem frühen Miozän gemeinsam mit der nördlichen Steilzone des Lepontins entlang zweier großer Störungszonen exhumiert.

Eine solchartige miozäne Abkühlungsgeschichte kann demzufolge mit einer Einengungs-Tektonik aufgrund anhaltender Konvergenz der europäischen und adriatischen Platten erklärt werden, die für die flache Überschiebung der Lepontischen Grunddecken verantwortlich ist. Die Nordwärtsbewegung der Grunddecken wurde jedoch durch den Aufstieg der Externmassive und der nördlichen Steilzone verlangsamt, was wiederum zu einer großskaligen Auffaltung der zentralen Lepontischen Decken führte, die bis ins späte Miozän anhielt. Einengungs-Tektonik stellte also während des Miozäns einen wichtigen Mechanismus der Exhumierungsgeschichte der Zentralalpen dar.

Im Gegensatz zur kleinräumigen miozänen Variabilität, verlief die Exhumierung des Lepontin Doms seit dem Pliozän vergleichsweise einheitlich und insgesamt schneller. Der Wechsel im Exhumierungsverhalten deckt sich mit den gleichzeitig ansteigenden Sedimentationsraten in den Alpinen Vorlandbecken, die in der Literatur berichtet werden.

Während die miozänen Exhumierungsmuster entlang tektonischer Störungszonen verfolgt werden konnten, ist diese Abhängigkeit für die pliozäne Exhumierung nicht mehr nachvollziehbar. Das numerische „Sandkasten“-Experiment, das nur durch Einengungs-Tektonik angetrieben wird, spiegelt keine strukturelle Veränderung in den entsprechenden Zeitschritten wider. Es deutet also alles darauf hin, dass die der Exhumierung zugrunde liegenden Kräfteverhältnisse sich zu Beginn des Pliozäns verändert haben. Folglich hat Einengungs-Tektonik fortan für die Zentralalpen, wenn überhaupt, nur eine untergeordnete Rolle gespielt. Die gemessenen thermochronologischen Daten und die daraus abgeleitete pliozäne Exhumierungsgeschichte stimmen am besten mit den Daten aus dem numerischen „Sandkasten“-Experiment überein, in dem eine um 5 Ma einsetzende Taleinschneidung simuliert wird. Die Änderung im Exhumierungsverhalten an der Mio-Pliozängrenze könnte also auf ein stärker erosives Klima zurückzuführen sein, wobei der unabhängige Nachweis dafür bisher fehlt.

Es kann festgehalten werden, dass ein Wechsel im Exhumierungsregime an der Mio-Pliozängrenze festgestellt werden kann, aber dass die Frage nach dem dominierenden pliozänen Gebirgsbildungsprozess weiterhin unbeantwortet bleibt.

Das zweite Fazit dieser Doktorarbeit betrifft die Bewertung des hier entwickelten interdisziplinären Ansatzes zur Kopplung numerischer „Sandkasten“-Modellierung mit der Apatit-Spaltspur-Thermochronologie:

Der neue Ansatz erwies sich für beide Disziplinen als gewinnbringend. Auf der einen Seite konnten die synthetischen Spaltspurdaten die strukturelle Analyse in den numerischen „Sandkasten“-Experimenten unterstützen, da Positionen und Größenordnungen der Keildeformation durch die Abkühlmuster deutlich angezeigt wurden. Auf der anderen Seite wurde der Einfluss tiefkrustaler Eigenschaften und Geometrien auf die Exhumierung der Oberkruste durch

numerische „Sandkasten“-Experimente untersucht und über die synthetischen Spaltspurdaten direkt in die Interpretation gemessenener thermochronologischer Daten integriert.

Spaltspur-Thermochronologie ist in der Lage den Zeitpunkt einer verstärkten Taleinschneidung aufzulösen, indem gemessene Abkühlalter mit synthetischen Altern aus Taleinschneidungsszenarien verglichen werden. Allerdings sollten Proben für solche Untersuchungen möglichst in schnell exhumierenden oder tektonisch aktiven Bereichen eines Gebirges genommen werden, weil Taleinschneidungsszenarien hier zu gut unterscheidbaren synthetischen Abkühlaltern führen. Weiterhin ist darauf zu achten, dass sich die Szenarien stark genug von einander unterscheiden: Um den Beginn einer verstärkten Taleinschneidung mittels Spaltspur-Thermochronologie aufzulösen, sollte der zeitliche Abstand dieses Zeitpunktes zwischen unterschiedlichen Szenarien mindestens 4 Ma betragen.

Des weiteren konnte die Bedeutung von horizontalen Bewegungspfaden auf die Exhumierung im Zusammenhang mit flachen Überschiebungen deutlich gemacht werden. Das Resultat lautet, dass die Geschwindigkeit geodynamischer Prozesse in derlei Umgebungen leicht unterschätzt werden kann, wenn einzig die Exhumierungsrate zur Rekonstruktion der geodynamischen Entwicklung herangezogen wird.

2. Summary

Untangling the relationship between different controlling factors of mountain-building has to consider and determine the possible impact of endogenous and exogenous processes. Generations of geoscientists accomplished to unveil much of the structure and metamorphic overprints of the European Central Alps and propose robust models to explain a good part of its evolution. The Neogene exhumation history, however, is still poorly understood. On the one hand, timing and mode of Mio-Pliocene exhumation in the Central Alps are controversially discussed. On the other hand, as a consequence, there is disagreement as to the significance and interplay of tectonic and climatic forces from early Miocene times.

This thesis is part of the ESF EUROCORES program TOPO-EUROPE and investigates the Neogene exhumation history of the Central Alps. In particular it focusses on the cooling history of the Lepontine Dome (Canton of Ticino, Switzerland).

The Lepontine Dome is a core region of the Central Alps, comprising the most deeply buried rocks of the Central Alps, being exposed first in the early Miocene. Sampling for this study along two roughly north-south oriented horizontal profiles followed the valley bottoms of the Ticino and Maggia rivers. To investigate the exhumation history, which is related to cooling, low-temperature thermochronology was applied: fission track analyses (AFT) and (U-Th-Sm)/He dating (AHe) on apatites. Combined, these methods are sensitive to temperatures between ~110 and 40 °C, corresponding to a depth of approximately 3.3 km to 1 km below the surface, assuming a geothermal gradient of 30 °C km^{-1}. Thus, the exhumation process through the upper crust can be deduced from inverse thermal history modelling of AFT and AHe data.

Additionally, a new approach combining numerical 'sandbox' experiments and AFT analysis was developed. The experiments were conducted by applying an established numerical 'sandbox' model, utilising a granular model approach based on the Discrete Element Method. Setup of the numerical 'sandbox' experiments is based on the deep structure of the Alps, derived from reflection seismic. Therefore, inferences on orogenic processes and mechanical properties can be drawn from the evolution of the resulting particle wedges and their structure. Neither temperature nor erosion are directly simulated in the numerical 'sandbox' experiments. The first step of the newly developed approach, therefore, is to calculate the evolution of an erosional surface after the experimental run. That allows to allocate temperature information to discrete particles by translating depth below surface into temperature and analyse the thermal history with respect to the particle pathways. Subsequently, forward thermal history modelling of the derived time-temperature histories yields synthetic AFT data.

Finally, the Central Alps were simulated along a north-south oriented profile, following the NFP20-east seismic profile (part of the European Geotraverse) by utilising another numerical

'sandbox' experiment. The Ticino horizontal profile was projected onto the model profile. Afterwards particles of the numerical 'sandbox' experiment were selected, which correspond to the sample locations along the Ticino profile or extended the profile to the north or south. The calculated thermal histories of these numerical 'sandbox' particles were used to derive synthetic AFT data.

Three scenarios were performed to test for the timing of onset of effective erosion related to valley incision. The calculated thermal histories of the selected particles and their resulting synthetic AFT data were compared to the results of inverse thermal history modelling, based on the data observed and the data observed itself.

Synthetic AFT data, derived from numerical 'sandbox' modelling coincides with the observed data in showing comparable cooling paths and ages in the same spatial distribution, in that youngest cooling ages are predicted in the central part which corresponds to the Lepontine Dome. As a first outcome, the Neogene exhumation history of the Lepontine Dome can be inferred from the combination of the data observed from the Lepontine Dome with the synthetic AFT data derived from the numerical 'sandbox' experiment:

Both show small-scale variability with respect to Miocene cooling of the Lepontine Dome (or the corresponding part of the model profile): early (i.e. from early Miocene within the the temperature sensitivity of the AFT system) and episodic cooling in the southern part (migrating from east to west as shown by the data observed), long-lasting steady cooling in the centre (temperatures below 110 °C are reached only in middle to late Miocene times) and early but slow (though probably also episodic) cooling in the north. The northern part cooled to temperatures below 110 °C in early Miocene.

Structural analysis of the numerical 'sandbox' experiment suggests that wedge growth in the Central Alps is mainly driven by basal accretion. Adapting the evolution of that part of the numerical 'sandbox', interpreted as being equivalent to external Aar-/Gotthard massifs, to the Alps, the external massifs and the northern steepbelt were exhumed along two deep fault zones from the early Miocene on.

Compressional tectonics associated with long-lasting convergence of the European and Adriatic plates, is suggested as underlying trigger of Miocene exhumation of the Lepontine Dome. As a result, the Lepontine basement nappes were thrust northwards. Rapid exhumation of the external massifs and the northern steep belt slowed down the northward movement and caused large-scale folding in the centre of the dome until latest Miocene.

In contrast to small-scale differential cooling across the Lepontine Dome during the Miocene, inverse thermal history modelling of the data observed points to a change in the exhumation regime of the Lepontine Dome at the Miocene-Pliocene boundary. Increasing exhumation rates during the Pliocene line up with concurrently increasing sedimentation rates in the Alpine foreland basins as reported in the literature.

In contrast to Pliocene cooling, Miocene differential cooling was obviously related to tectonic structures. The numerical 'sandbox' experiment is only driven by compressional tectonics and the resulting structural evolution lacks the change in the exhumation regime, revealed by the data observed. Thus, all in all, controlling mechanisms of exhumation changed in latest Miocene/

early Pliocene times with compressional tectonics playing a subordinate role afterwards, if at all.

The data observed and inverse thermal history modelling best line up with the calculated thermal histories and the synthetic AFT data from the numerical 'sandbox' experiment, derived for the scenario simulating the onset of effective valley incision at 5 Ma. Thus, changing exhumation patterns at the Mio-Pliocene boundary possibly indicates a change in the erosion regime, associated with more erosive climatic conditions. Independent proof of a climate change at ~5 Ma, however, is still lacking. In the end, the results of this thesis distinctly point to a change of the exhumation regime of Lepontine Dome at the Mio-Pliocene boundary, but are not able to reveal the underlying triggers of that change.

As a second outcome, combining numerical 'sandbox' modelling and AFT thermochronology proved most valuable for both disciplines: On the one hand, synthetic AFT data supports structural analyses of numerical 'sandbox' experiments as they distinctly show locations and magnitudes of deformation. On the other hand, numerical 'sandbox' experiments allow to consider lower crustal geometries and mechanic properties in the interpretation of thermochronologic studies, as their impact on the exhumation of the upper crust can be evaluated.

The onset of effective valley incision can be investigated by AFT thermochronology by comparing data observed with synthetic AFT data derived from different incision scenarios. Sampling for such studies should concentrate on rapidly cooling and / or tectonically active areas, because synthetic AFT ages between different incision scenarios differ most significantly there. Please note that the onset of valley incision should differ by at least 4 Ma between the scenarios to resolve the differences in the resulting synthetic AFT data by the data observed.

Furthermore, the significance of lateral displacement in low-angle thrusting settings is emphasized. Interpreting low-temperature thermochronologic data from such sites requires to consider the lateral movement vector in concert with the vertical vector for not underestimating the pace of geodynamic processes.

Contents

List of Figures

List of Tables

3. Introduction

3.1. Initial situation and motivation

Understanding the call-and-response of an orogeny needs reverse deduction: In the first place, the results of mountain-building (structures, patterns, mass distributions) have to be identified. From that, the underlying processes can be proposed, before, the associated control mechanisms can be inferred. The example of the late stage exhumation of the European Central Alps (Fig. 1) illustrates well that there is already disagreement as to the processes and, hence, the triggering drivers are still under discussion:

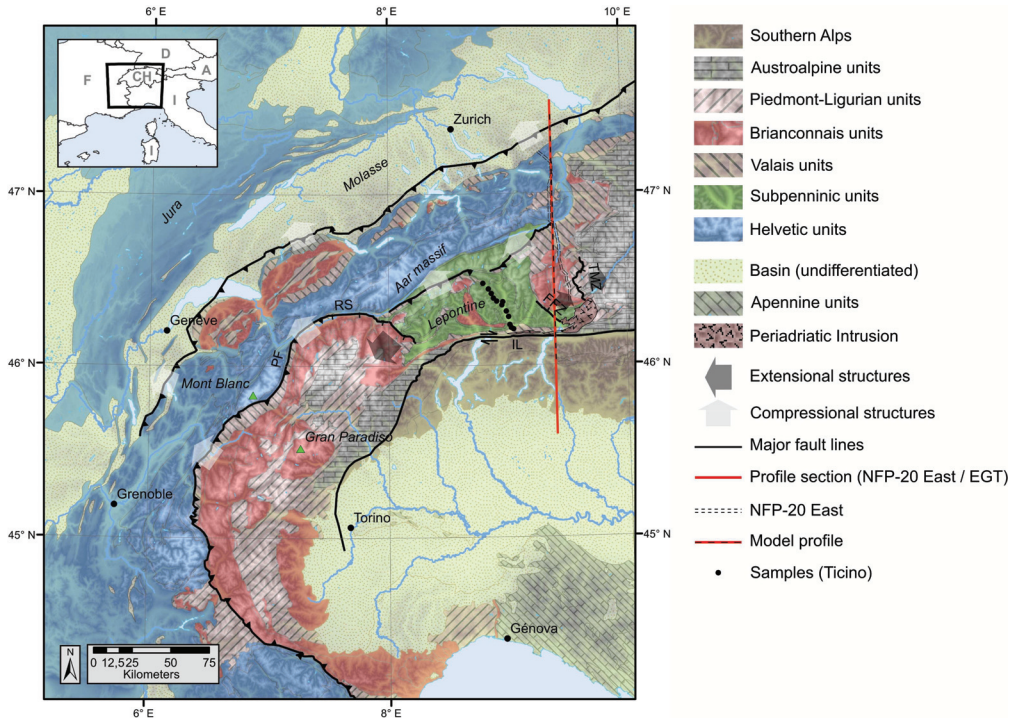

Fig. 1.: Overview map with major tectonic units of the European Western and Central Alps. Fault zones: FFZ: Forcola Fault Zone. IL: Insubric Line. PF: Penninic Front. RS: Rhône-Simplon Line. TMZ: Turba Mylonite Zone. Further fault lines: Main thrust fault of the Helvetic units onto the Molasse, thrust faults within the Subpenninic units separating the Gotthard to the north and the Lepontine Dome to the south. Map after Tectonic Map of the Swiss Federal Office of Topography and Schmid et al. (2004a). Fault zones after Schmid et al. (2004a) and Bousquet et al. (2012). Line of NFP20-East from Pfiffner et al. (1988). Samples along the Ticino valley from Elfert et al. (2013).

Based on the sedimentation record in the Alpine foreland basins, several studies suggest episodic Neogene exhumation of the hinterland (Kuhlemann et al., 2002; Carrapa, 2009; Cederbom et al., 2011). Strongly increasing sedimentation rates at ~5 Ma in the Alpine foreland basins (Kuhlemann et al., 2002) and worldwide (Hay et al., 1988; Molnar, 2004; Molnar and England, 1990) are in agreement with the assumed doubling in Pliocene exhumation rates for the Western and Central Alps based on a large dataset of cooling ages (Vernon et al., 2008). Hinterland studies found indications for temporal variability in Mio-Pliocene exhumation rates in the Lepontine Dome (Timar-Geng et al., 2004; Vernon et al., 2009). Both, tectonic and climatic changes are suggested for these changes (Kuhlemann et al., 2002; Willett et al., 2006).

Other studies (both detrital foreland and hinterland studies), however, did not find any indication for changing Alpine exhumation in the last 10 to 15 Ma (Bernet et al., 2001, 2009; Glotzbach et al., 2010). Consequently, exhumation is presumed to be constantly tectonically driven since Miocene time, lining up with isotope data from marine isotopes, lacking indications for a worldwide increase of Plio-Pleistocene sedimentation rates (Willenbring and von Blanckenburg, 2010).

In addition to exhumation style (episodic vs. continuous exhumation) and control (climate vs. tectonics), the evolution of the Alpine drainage system is not yet fully untangled. While several studies proposed large-scale and partly even reiterated north- and southward migration of the main drainage divide in Mio-Pliocene times (Schlunegger et al., 1998, 2007; Kühni and Pfiffner, 2001; Kuhlemann et al., 2001; Spiegel et al., 2001), Garzanti and Malusa (2008) suggested a persistent drainage system in the Lepontine area of the Central Alps since the Oligocene related to stable pathways of the Ticino and Toce rivers. However, Valla et al. (2011) found glacial erosion at middle Pleistocene times to be mostly responsible for final valley incision and relief development.

Summarising, the European Alps are probably one of the most intensively studied orogens worldwide. But despite more than hundred years of research, evolution, processes and triggers are still not fully understood and especially the Neogene exhumation history of the European Central Alps is highly controversially in respect to mode, trigger and timing.

The first motivation of this thesis is helping to unpack the history of this relatively young orogen by adding a piece of the puzzle: How did exhumation of the Central Alps look like during the Neogene? What triggered exhumation? Did exhumation change? If so, why did exhumation change?

Numerical modelling is increasingly used to reinforce perceptual reconstruction of natural processes. All the more, as a full understanding of processes and timescales are beyond human experience (large-scale plate tectonic activity over millions of years). Still, numerical modelling is often limited to special applications (and scales as well), since it is based on the equations the modeller implements or allows to be used in the model run. Models may work fine in the respective environment, but the future of modelling will be the coupling of different discipline- and scale-specific approaches to achieve a scale comprehensive view of nature with respect to both, time and space. Therefore, the second motivation is to combine two well established methods of the geosciences (apatite fission track analyses and numerical ‘sandbox’ modelling),

providing scientific progress with respect to the applied methods and a fuller understanding of orogenic processes.

The Lepontine Dome (Figs. 1, 2) is a key area of the European Central Alps and an excellent laboratory to investigate the Neogene Alpine orogeny, due to its tectonic and metamorphic history. It is intensively studied by seismic, structural and metamorphic surveys and, hence, well suited to test for new methodological approaches like relating large-scale deep-seated processes to small-scale upper crustal responses.

3.2. Approaches and own contribution

The project 'Thermo-Europe', as part of the ESF EUROCORES program TOPO-EUROPE, aimed to reveal the coupling of climate and tectonics through thermochronometry. This thesis forms part of the 'Thermo-Europe' individual project IP2 'Sources and Sinks of Pliocene erosion: Investigating the latest-stage exhumation history of the Alps' and investigates the Neogene evolution of the Lepontine Dome, from two different views:

The first pillar of this thesis is the generation and introduction of a new thermochronologic data set comprising fission track analyses and (U-Th-Sm)/He dating on apatites (AFT and AHe, respectively) from the Lepontine Dome. Both methods yield thermal fingerprints of the analysed samples corresponding to cooling through the temperature ranges of ~110 to ~60 °C (AFT) and ~85 to ~40 °C (AHe). Cooling is associated with exhumation and, therefore, thermal history modelling of the AFT and AHe data yields information about denudation and upper crustal processes. The new data and its interpretation were published in Tectonophysics (Elfert et al., 2013; Paper Contribution 1, Tab. 1).

Tab. 1.: Paper Contribution 1: Status and individual contributions

Title:	Long-lasting tectonic activities of the Lepontine Dome. New evidence from low-temperature thermochronology
Authors:	**Simon Elfert**, Wolfgang Reiter, and Cornelia Spiegel
Status:	published (Tectonophysics, Vol. 608 (p. 222-236), http://dx.doi.org/10.1016/j.tecto.2013.09.033)
Originally submitted:	25.07.2013
First revision submitted:	23.09.2013
First revision accepted:	27.09.2013
Concept (Idee)	30 %
Data collection (Datenerhebung)	100 %
Realisation (Umsetzung)	80 %

As second pillar, an interdisciplinary approach was developed to derive synthetic AFT data from numerical 'sandbox' experiments (Discrete Element Method). Therefore, the effect of deep-crustal geometries and mechanic properties on the evolution of an orogenic wedge as simulated by the numerical 'sandbox' experiments are related to upper crustal processes as being described by the synthetic AFT data. In particular, the thermal histories of selected particles

were extracted by a set of self-written scripts (Python programming language), considering a computed erosional surface as reference for depth and the related temperature at any given point in time and space (particletracker v. 3.1 and other scripts in Appendix C). The basic approach was developed in close collaboration with Linda Wenk (during her PhD thesis. MARUM, University of Bremen) with equal share for both projects. Scripting, debugging and application of the Python code, however, is done by the author of this thesis. The extracted time-temperature histories were used for thermal history modelling, yielding synthetic AFT data. Based on a series of numerical 'sandbox' experiments, the conceptual influence of deep-seated mechanic and kinematic properties on the evolution of AFT cooling ages are investigated and prepared for publication in Journal of Geophysical Research (Paper Contribution 2, Tab. 2).

Tab. 2.: Paper Contribution 2: Status and individual contributions

Title:	Describing orogenic wedges by a combination of numerical 'sandbox' models and low-temperature thermochronology I: Linking lower crustal geometries and mechanic properties with upper crustal processes
Authors:	Linda Wenk, **Simon Elfert**, Cornelia Spiegel and Katrin Huhn
Status:	In preparation for submission to Journal of Geophysical Research
Intended submission:	May/June, 2014
Concept (Idee)	30 %
Data collection (Datenerhebung)	50 %
Realisation (Umsetzung)	50 %

Finally, the coupled approach was utilized bidirectionally: On the one hand, synthetic AFT ages were used to improve the structural analyses of wedge deformation in numerical 'sandbox' experiments. On the other hand, numerical 'sandbox' experiments and the derived synthetic AFT data are used to interpret the data observed from the Lepontine Dome (first pillar) with respect to the deep structure and the influence of the erosion regime. Additionally, the relation between exhumation and geodynamic activity was probed depending on the structural position across an orogenic wedge. The results are prepared as companion to the second paper contribution (Paper Contribution 3, Tab. 3).

Tab. 3.: Paper Contribution 3: Status and individual contributions

Title:	Describing orogenic wedges by a combination of numerical 'sandbox' models and low-temperature thermochronology II: Applications to upper crustal processes of the European Central Alps
Authors:	**Simon Elfert**, Linda Wenk, Katrin Huhn and Cornelia Spiegel
Status:	In preparation for submission to Journal of Geophysical Research
Intended submission:	May/June, 2014
Concept (Idee)	30 %
Data collection (Datenerhebung)	70 %
Realisation (Umsetzung)	70 %

In conclusion, this thesis presents both, a classical low-temperature thermochronology study and a new methodological approach. On the one hand, the Neogene evolution of the Lepontine Dome is investigated with respect to the style, trigger(s) and timing of exhumation. On the other hand, interpretation of low-temperature thermochronologic data is improved by coupling of numerical 'sandbox' modelling with AFT analyses.

4. Geological background

4.1. Geological setting

The European Central Alps border the Western Alps and the Eastern Alps and basically comprise geotectonic nappes derived from the European margin (Helvetic and Subpenninic units) and from the former Penninic realm (Fig. 1, Schmid et al., 2004a). The Penninic realm of the Central Alps contained oceanic basins (Valais and Piedmont-Ligurian) and a small ribbon continent (Briançonnais) between the European plate to the north and the Adriatic plate to the south. The Southern Alps, located south of the Central Alps contain basement and sedimentary cover units derived from the Adriatic plate. The Adriatic plate is the detached northern part of the Apulian plate, which in turn was part of the African plate (Stampfli et al., 2002). Also the Austroalpine units of the Central and Eastern Alps are of Apulian origin, but these ones were mostly detached from their crustal root during the Alpine orogeny (Schmid et al., 2004a).

The Lepontine Dome (Fig. 2), being subject of this study, is situated in the Central Alps and bounded by major tectonic structures to the west (Rhône-Simplon fault zone), to the east (Forcola fault zone/Turba-Mylonite zone), to the north (Aar-/Gotthard external massif) and to the south (Insubric Line being part of the Periadriatic Line). It consists of the Ticino and Toce subdomes, forming one culmination near Biasca and a second culmination near Baceno, respectively (Fig. 2). The central Maggia steep zone represents the transition zone between the subdomes. Additional steep belts evolved at the southern and northern boundaries of the Lepontine Dome. The southern anticlinal steep belt exhibits southdipping foliations, whereas the northern steep belt is formed by synclines with northdipping foliations.

4.2. Geodynamic evolution of the Central Alps

The Alpine orogeny involves a complex succession of opening and subduction of several oceanic basins, followed by the collision of the European continental plate and the Adriatic plate:

The opening of the Alpine Tethys (the western extension of the central Atlantic ocean) already took place in the Early to Middle Jurassic and is associated with the Pangaea breakup (e.g., Frisch, 1979; Stampfli and Hochard, 2009). Several micro-plates, derived from and repeatedly attached to the African plate were also divided by smaller oceanic basins in early Cretaceous times.

During the Eo-Alpine orogeny (i.e. the Cretaceous Alpine orogeny), eastward directed shortening caused subduction and high-pressure metamorphism associated thereof (Froitzheim et al., 1996; Von Blanckenburg and Davies, 1995; Engi et al., 2004, and references therein). Addition-

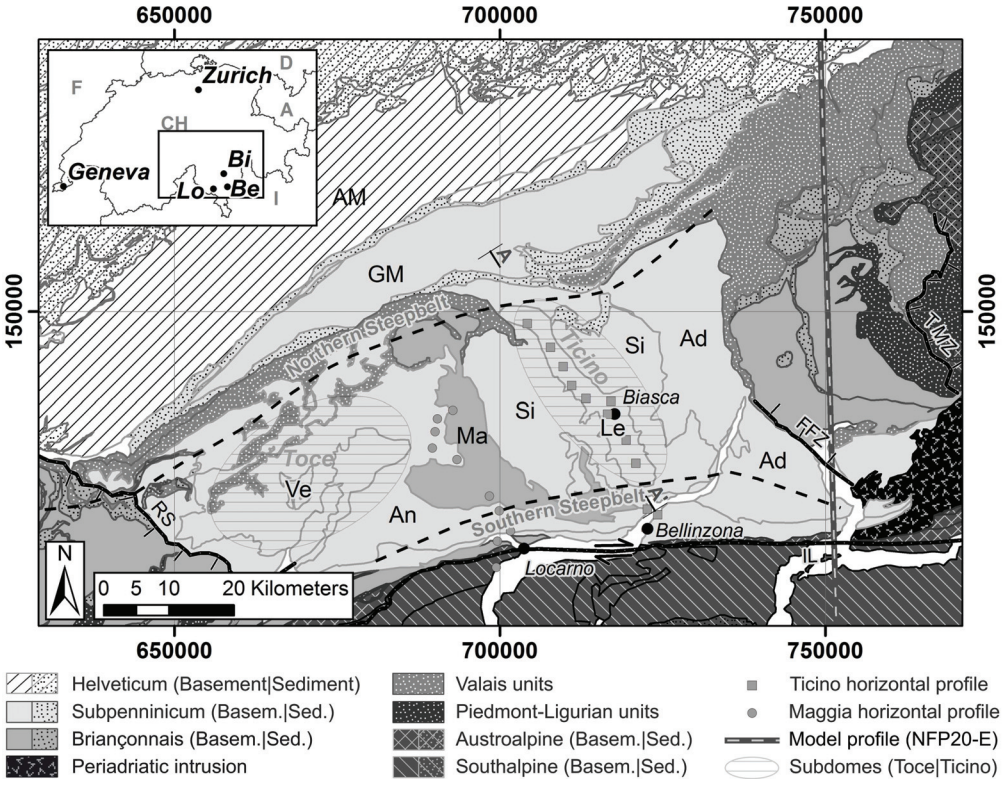

Fig. 2.: Simplified geological map of the Lepontine Dome and sample locations (after Elfert et al. (2013)). Dark grey squares and dots: own samples along Ticino and Maggia valley (Elfert et al., 2013); light grey dots: previously published AFT data by Hurford, 1986; Rahn, 2005; Glotzbach et al., 2009; Janots et al., 2009). Grey lines: Major nappe boundaries. AM: Aar massif, GM: Gotthard massif; Lepontine nappes: Ad: Adula, An: Antigorio, Ma: Maggia, Le: Leventina, Si: Simano (outcropping east and west from the Leventina), Ve: Verampio; Structures: FFZ: Forcola Fault Zone, IL: Insubric Line, RS: Rhône-Simplon Line, TMZ: Turba Mylonite Zone. A-A': terminations of cross section in Fig. 12. Grid units referring to Swiss Grid (CH03). Map after Tectonic Map of the Swiss Federal Office of Topography, Milnes (1974) and Schmid et al. (2004b).

ally, the eastern part of the south Penninic ocean (also called Piedmont-Ligurian ocean or Alpine Tethys) was affected by this first Alpine orogeny (Frisch, 1979).

From mid-Cretaceous times on until early Paleogene times, the south Penninic oceanic lithosphere, the Briançonnais terrane (middle Penninic) and the north Penninic oceanic lithosphere (Valais ocean) were successively subducted in response to north-south directed convergence (Frisch, 1979). The subsequent subduction of the distal European margin (after ~50 Ma) defines the onset of continent-continent collision (Schmid et al., 2004b).

Within the down-dipping accretion channel, the formerly adjacent geotectonic units were rearranged to a nappe pile. Associated with this nappe stacking, the involved units underwent high-temperature metamorphism, which resulted in classical Barrow-type metamorphic mineral zones (Niggli, 1960; Frey and Ferreiro Mählmann, 1999; Engi et al., 2004).

Slab-break-off resulted in isostatic buoyancy, expelling and backthrusting of the formerly subducted European upper crust and the overlying nappe stack of Penninic units (Von Blanckenburg

and Davies, 1995; Wiederkehr et al., 2008, 2009). The Adriatic plate indented between the European upper and lower crust and triggered further uplift and deformation in the Central Alps (Müller, 1989; Von Blanckenburg and Davies, 1995; Schmid et al., 2004b).

The ongoing compression and associated crustal thickening initiated extensional processes parallel to the orogen trend (at least in the case of the Central and Eastern Alps; Ratschbacher et al., 1989; Steck and Hunziker, 1994; Frisch et al., 2000; Selverstone, 2005. The Lepontine Dome is tectonically unroofed as footwall to both the westwards dipping Rhône-Simplon normal fault and the eastwards dipping Forcola and Turba-Mylonite normal fault zones since Eocene time. Major extension took place between 25 Ma and 13 Ma (Mancktelow, 1985, 1992; Schlunegger and Willett, 1999; Frisch et al., 2000; Campani et al., 2010). As a result, most deeply buried nappes (e.g., Verampio, Leventina, Antigorio) were exposed adjacent to structurally higher nappes (e.g., Simano, Adula; Fig. 2).

Furthermore, continued convergence of the European and Adriatic plates prolonged deformation in the Central Alps, associated with Miocene to late Miocene backfolding and backthrusting of the Alpine orogenic wedge, clearly postdating nappe stacking (Milnes, 1974; Merle et al., 1989; Wiederkehr et al., 2009).

5. Methodology

5.1. Apatite fission track analysis

5.1.1. Basic concept of spontaneous fission in apatites

Among others, apatites incorporate Thorium and Uranium. Spontaneous fission of ^{232}Th, ^{234}U, ^{235}U and ^{238}U in apatites results in two positively charged fission fragments, a few Neutrons and kinetic energy, which initiates rapid migration of the two fragments through the grain's lattice in opposite direction (Fleischer et al., 1965; Tagami and O'Sullivan, 2005). The widely accepted 'ion explosion spike' model (Fleischer et al., 1965, 1975) explains track formation in that the two daughter isotopes (the fission fragments) cause ionisation and lasting repulsion along their trajectory through the crystal lattice. In this way, a fission track remains which can be identified by transmission electron microscopy. To visualise fission tracks by optical microscopy, samples have to be etched (sec. 5.1.3).

With respect to both, relative abundance and spontaneous fission half-life, in general, all fission tracks in natural apatites can be ascribed to the spontaneous fission of ^{238}U (Wagner and Van den haute, 1992; Tagami and O'Sullivan, 2005). Only in apatites with exceptionally high amounts of Th, this source has to be appropriately considered.

Crucially, fission tracks are not stable and fade again ('anneal') with time (Fig. 3) depending on (a) temperature, (b) cooling rate, (c) the kinetic properties of the host mineral and (d) the crystallographic orientation of the track (Fleischer et al., 1965, 1975; Wagner and Reimer, 1972; Carlson et al., 1999; Barbarand et al., 2003).

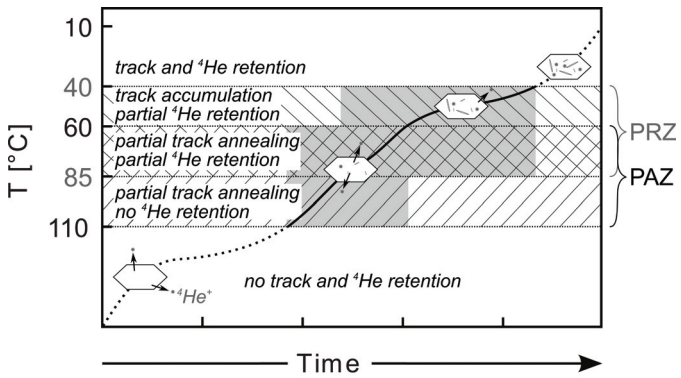

Fig. 3.: Apatite fission track and (U-Th-Sm)/He analyses are based on the accumulation of fission tracks and 4He particles through time. Retention and associated accumulation of tracks and ^{4}He particles starts with cooling below 110 °C and 85 °C, depending on the cooling rate within the partial annealing zone (PAZ) and the partial retention zone (PRZ), respectively.

(a, b) Early studies proposed a closure temperature according to the concept of blocking temperatures (Dodson, 1973; Schaer et al., 1975) below which fission tracks were retained. However, Wagner and Reimer (1972) already discovered that relevant fission track shortening is going on within a temperature range and that this range in turn depends on the cooling rate of the host rock. Between ~110 °C and ~60 °C, the track density decreases (Gleadow and Duddy, 1981; Gallagher et al., 1998), due to fading of tracks, which does not lead to total annealing (depending on the time spend within). This temperature range is called partial stability zone (Wagner, 1979) or – presently more common – partial annealing zone (PAZ; Fitzgerald and Gleadow, 1990; Wagner and Van den haute, 1992; Lisker et al., 2009). Track annealing below 60 °C is less than 10 % and is covered by modern annealing algorithms (cf., Spiegel et al., 2007).

(c) Track annealing in apatites depends on kinetic properties which, in turn, are related to the chemical composition of the apatite grain and the resulting cell parameters (Carlson et al., 1999; Barbarand et al., 2003). Apatites form a group of phosphate minerals. The regular chemical formula for apatites is $Ca_{10}PO_4[F, Cl, OH]_2$. The anion (F, Cl or OH) acts as name giver (i.e. flourine-apatite, chlorine-apatite or hydroxyl-apatite, respectively). Apart from the regular chemical composition, Ca can be substituted by Fe^{2+}, Mn^{2+}, Na^{+}, REE^{3+} (rare earth elements), Sr^{2+} or U^{4+}, and possible substitutions in the P-site include Si, S and C. The anion site is mostly substituted by F, Cl or OH (see Barbarand et al., 2003; Donelick et al., 2005). Especially on the anion site, substitution strongly affects the parameters of the unit-cell and with that the annealing properties of an apatite grain (Carlson et al., 1999; Barbarand et al., 2003). Generally, pure flourine-apatites seem to anneal more easily compared to apatites with higher Cl content (> 0.4 wt.%; Green et al., 1989; Barbarand et al., 2003. Thus, tracks of chlorine-apatites are stable at higher temperatures, although end-member flourine-apatites may in some cases also show high resistance to annealing (e.g., Ketcham et al., 1999), but hitherto no correlation between substitution and annealing behaviour has been found to explain all the variability of annealing (Carlson et al., 1999; Barbarand et al., 2003). Donelick (1993) and Burtner et al. (1994) introduced the diameter of the etch pit (Dpar; i.e. the etch figure of a fission track visible at the surface of an polished grain) as a proxy for the solubility of a grain, which in turn is related to the bulk composition. Dpar values correlate positively with the cell parameter a and mean track lengths, which both are directly associated with the annealing kinetics (Barbarand et al., 2003). Small Dpar values ($\leq$ 1.75 μm) indicate low resistance to annealing, while larger Dpar values usually point to high resistance, although fast annealing apatites may in some cases also show large Dpars (Carlson et al., 1999; Ketcham et al., 1999; Donelick et al., 2005).

(d) Furthermore, annealing of fission tracks in apatites is anisotropic. Fission tracks parallel to the crystallographic c-axis anneal significantly slower compared to those oblique or perpendicular to the grain's c-axis (Green and Durrani, 1977; Green et al., 1986; Donelick, 1991; Barbarand et al., 2003).

Summarizing, fission tracks shorten during the time spent in the PAZ, associated with decreasing track density. The density of apatite fission tracks and the distribution of the fission track lengths, therefore, reflect the cooling history since the host rock entered the PAZ (Wagner and Van den haute, 1992).

5.1.2. Carrying out of apatite fission track analyses

From the beginning of fission track analyses in the early 1960s (Price and Walker, 1962a,b; Fleischer et al., 1975), several procedures were developed (e.g., Gleadow, 1981, 2002; Hurford, 1990). According to Tagami and O'Sullivan (2005), the external-detector method (Naeser, 1976; Hurford and Green, 1982; Hurford, 1990) is the most widely accepted procedure in fission track dating. In the following, the analytical procedure of the external-detector method is introduced by exemplarily outlining its application for the samples in this thesis:

Coarse separation included crushing, sieving and density separation on a vibrating table. During the subsequent fine separation, paramagnetic components (magnetic separator), lighter minerals (density separation with LST fastfloat – density: 2.85 g ml^{-1}) and heavier minerals (density separation with methylene iodide – density: 3.3 g ml^{-1}) were excluded, resulting in apatite concentrates.

Apatites were mounted on glass slides in epoxy resin, ground and polished with gamma alumina polishing suspension (polishing grain size down to 0.05 μm) to reveal internal surfaces. Mounts were etched in 5 M HNO_3 for 20 s in 20 °C to reveal spontaneous fission tracks, intersecting the internal surface.

Low-U micas, used as external detectors, were tightly attached to both the mounts and CN5 dosimeter glasses. Subsequently, samples and monitor glasses were irradiated with slow, thermal neutrons (with a flux density of $1.3 \cdot 10^{16}\ ncm^{-2}$ - $1.5 \cdot 10^{16}\ ncm^{-2}$) at the Garching FRM II reactor (Munich, Germany). Afterwards, micas were untied and etched in 40 % HF for 30 minutes at 20 °C to reveal the induced fission tracks registered on the micas' surfaces.

Spontaneous and induced tracks on appropriate grains (e.g., mounted parallel to crystallographic c-axis, no dislocations, adequate size, well polished) were counted under 1000x magnification using an optical microscope (Zeiss Axioplan). FT-Stage 3.12b (©Trevor Dumitru, 1992-1995) was used to identify corresponding areas on mount and mica.

Furthermore, up to 100 lengths of horizontal confined tracks were measured in grains, mounted parallel to the crystallographic c-axis. To increase the number of confined tracks, for nearly all samples, up to three additional mounts had to be prepared, which were irradiated with ^{252}Cf-derived fission-fragments at Melbourne University (Australia). These mounts were exposed in 1 cm distance to the Cf source for 2.5 h and etched afterwards following the same routine as for the first mounts.

As a proxy for the kinetic properties, up to five Dpars were measured on each analysed grain (dating and/or track length measurement).

5.1.3. Apatite fission track age determination

The basic age equation can be written as:

$$t = \frac{1}{\lambda_d} ln \left(1 + \left(\frac{\lambda_d}{\lambda_f}\right) \left(\frac{N_s}{N_i}\right) I \, \sigma_f \, \Phi\right) \tag{5.1}$$

Therein t is time; λ_f and λ_d are the decay constants for spontaneous fission and total decay (including α-decay), respectively; N_s and N_i are the numbers of spontaneous and induced fission tracks, respectively per unit volume; I is the constant isotopic ratio between ^{235}U and ^{238}U ($7.527 \cdot 10^{-3}$). σ_f is the cross section for induced nuclear fission of ^{235}U by thermal neutrons ($580.2 \cdot 10^{-24}\ cm^2$) and Φ is the thermal neutron fluence.

Since fission track analyses cannot encompass the grain as a volume and only fission tracks which intersect the revealed surface of a grain can be measured under optical microscope, volume terms in the age equation have to be substituted with surface densities:

$$t = \frac{1}{\lambda_d} ln \left(1 + \left(\frac{\lambda_d}{\lambda_f}\right) \left(\frac{\rho_s}{\rho_i}\right) Q \, G \, I \, \sigma_f \, \Phi\right) \tag{5.2}$$

Therein ρ_s is the density of spontaneous fission tracks on a grain (i.e. $\frac{N_s}{\Omega}$, where N_s: number of spontaneous fission tracks counted over area Ω); ρ_i is the density of induced fission tracks on the corresponding mica (i.e. $\frac{N_i}{\Omega}$, where N_i: number of induced fission tracks counted over area Ω); Q is an integrated factor of registration and observation efficiency of fission tracks; G is an integrated geometry factor of the etched surface.

Although, solving eq. 5.2 is generally possible given that all variables are known, uncertainties remain in the specification of the decay constant for spontaneous fission (λ_f. Bigazzi, 1981; Wagner and Van den haute, 1992. Both the neutron flux (Φ) and the registration (or procedure) factor (Q) may also be measured directly (Van den haute et al., 1998). The authors determine Φ, using two standard metal monitors (Co and Au). However, the calculation of Q, incorporating the registration efficiency, revelation of fission tracks and observer bias requires an accurate value for λ_f which is yet to be widely accepted (Van den haute et al., 1998).

Thus, the recommended and common approach is to apply a ζ-calibration factor (Fleischer et al., 1975; Hurford and Green, 1983; Hurford, 1990).

The ζ-calibration factor is given by:

$$\zeta = B \, \frac{I \, \sigma_F}{\lambda_F} \tag{5.3}$$

with B: a calibration constant, which has to be empirically determined by the relationship between the neutron flux (Φ) and the density of (induced) fission tracks (ρ_d) on the mica of the dosimeter (i.e. the monitor glasses):

$$\Phi = B \, \rho_d \tag{5.4}$$

with $\rho_d = \frac{N_i}{\Omega}$, where N_i: number of induced fission tracks counted over area Ω.

Finally, ζ is substituted for the corresponding terms in the age equation:

$$t = \frac{1}{\lambda_d} ln \left(1 + \lambda_d \, \zeta \, g \, \rho_d \, \frac{\rho_s}{\rho_i} \right) \tag{5.5}$$

with: t: fission-track age; g: geometry factor for spontaneous fission track registration (at same routine and experiment conditions Q is negligible; Tagami and O'Sullivan, 2005). For a more detailed derivation of the equations please see Wagner and Van den haute (1992), Gleadow (2002), Donelick et al. (2005) and Tagami and O'Sullivan (2005).

Solving eq. 5.5 for ζ yields (Hurford and Green, 1983; Hurford, 1990):

$$\zeta = \left(\frac{e^{\lambda_d t_{std}}}{\lambda_d \left(\frac{\rho_s}{\rho_i} \right)_{std} \rho_d} \right) \tag{5.6}$$

The ζ-value is derived as the weighted mean from repeated determination of track densities on age standards of known age (t_{std}) and the corresponding external detectors of both the age standard and the dosimeter.

The ζ-calibration factor, first and foremost, depends on the used dosimeter and the personal fission track registration of the observer. Furthermore, the neutron flux (Φ) and therewith the factor B may differ between irradiation facilities. All fission track ages in this thesis are determined by Simon Elfert with a ζ-value of 332 and a standard deviation of 8 using CN5 dosimeter glasses (Tab. 4). Age standards were also irradiated at Garching FRM II reactor (Munich, Germany). Altogether six age standards (four Durango apatite and two Fish Canyon apatite standards) were included in the calculation.

Fission track cooling ages of this thesis are calculated by utilising TRACKKEY for windows (version 4.2.g; Dunkl, 2002). The reported central AFT ages and relative standard errors are internally derived by TRACKKEY according to Galbraith and Laslett (1993).

Tab. 4.: Single ζ-values derived from Durango and Fish Canyon age standards (each standard was repeatedly analysed. Only the most recent analysis is presented here). N_g: number of grains, N_s: number of spontaneous tracks, N_i: number of induced tracks.

No.	Date	Location	Internal label	Irradiation	N_g	N_s	N_i	Density ratio	Zeta	Standard deviation
1	09/12/09	Durango	DU-HB6	HB57	11	331	3932	84	340.66	20.32
2	04/02/10	Durango	06-AD1	HB57	30	588	6926	85	329.31	15.19
3	10/02/10	Fish Canyon	FC5	HB57	4	49	678	72	388.6	57.86
4	10/03/10	Fish Canyon	FC III	HB54	25	199	1621	123	293.32	22.81
5	28/10/10	Durango	DU-HB9	HB57	30	880	10290	86	325.48	12.68
6	01/11/10	Durango	DU-HB8	HB57	9	213	2918	73	389.33	28.4

5.2. Apatite (U-Th-Sm)/He dating

5.2.1. Basic concept of (U-Th-Sm)/He dating on apatites

In contrast to apatite fission track analyses, which is based on the spontaneous decay of ^{238}U, (U-Th-Sm)/He (AHe) dating is based on α-decay and the associated production and retention

of ^{4}He (α-particles) within a grain (Rutherford, 1905; Strutt, 1905; Lippolt et al., 1994; Wolf et al., 1996; Farley, 2000, 2002; Ehlers and Farley, 2003). Mother isotopes for ^{4}He are ^{235}U, ^{238}U, ^{232}Th and ^{147}Sm as well as several daughter isotopes in the decay chain of ^{235}U, ^{238}U and ^{232}Th (Lisker et al., 2009). The different half-lifes of the potential mother isotopes (already considering the entire decay chain) result in the following ^{4}He production Farley (2002):

$$\begin{aligned} {}^4He = 8 \cdot {}^{238}U \cdot \left(e^{\lambda 238 \cdot t} - 1\right) + 7 \cdot {}^{235}U \cdot \left(e^{\lambda 235 \cdot t} - 1\right) + \\ 6 \cdot {}^{232}Th \cdot \left(e^{\lambda 232 \cdot t} - 1\right) + 1 \cdot {}^{147}Sm \cdot \left(e^{\lambda 147 \cdot t} - 1\right) \end{aligned} \tag{5.7}$$

with λ_i: α-decay constant of mother isotope (e.g., reported in Donelick et al., 2005; Dickin, 2009) and i: mass number.

^{4}He may get lost from apatites through α-ejection. As a result of the α-decay, kinetic energy (4-8 MeV) moves the ^{4}He particle away from the decay site (Farley, 2002; Ehlers and Farley, 2003). Ketcham et al. (2011) refined the mean stopping distances of ^{4}He emitted from ^{238}U, ^{235}U, ^{232}Th and ^{147}Sm in apatites (18.81 μm, 21.8 μm, 22.25 μm and 5.93 μm, respectively). ^{4}He, emitted from U, Th or Sm isotopes, which were located close to the grain's rim (less then the corresponding stopping distance), therefore, may be conveyed out of the grain immediately after its production. Consequently, AHe dating is sensitive to zonation of the dated grains in that ^{4}He production can be underestimated in case of a (U-Th-Sm)-rich rim, due to α-ejection.

Furthermore, ^{4}He can get lost from the grain by diffusion (Zeitler et al., 1987). Diffusion kinetics highly depends on temperature (Fig. 3): At high temperatures (above ~85 °C) all ^{4}He is lost, while below 40 °C loss of ^{4}He is negligible for most cooling histories (Wolf et al., 1996, 1998; Green and Duddy, 2006). Between ~85 °C and 40 °C ^{4}He is partly retained (Partial Retention Zone, PRZ; Wolf et al., 1998).

Chemical composition does not seem to affect ^{4}He diffusion within apatites (House et al., 2002; Shuster et al., 2006). Even if fission track annealing proofed to be anisotropic in apatites, anisotropy only plays a minor and therefore negligible role for ^{4}He diffusion (Farley, 2000).

However, lattice defects and voids derived from α-recoil (and to a much lower frequency also from spontaneous fission) can act as traps for ^{4}He particles and therewith retard diffusion (Shuster et al., 2006; Flowers et al., 2009; Gautheron et al., 2009, 2013). The basic idea is that diffusion requires a certain amount of energy. Since it takes less energy for ^{4}He to move within a void space than it takes to move from a void space into the solid matrix, it will stay 'trapped' and behave comparable to a gas inside a bubble within a solid (Shuster et al., 2006). On the other hand, radiation damage can in particular cases also increase diffusivity if the amount of α-decay produces overlapping recoil damage zones. Although this is unlikely for apatites due to comparatively low U concentrations, zircons do have higher Uranium concentrations. In concert with long residence times below the PRZ, this may cause concatenation of recoil damage zones and therewith create fast pathways for ^{4}He atoms, resulting in enhanced ^{4}He loss out of the grain. For apatites, however, radiation damage is rather associated with enhanced ^{4}He retention (Shuster et al., 2006).

AHe dating basically determines the time since ^{4}He is retained in the grain, which is derived after measuring the contents of ^{4}He, ^{238}U, ^{235}U, ^{232}Th and ^{147}Sm (eq. 5.7). To solve eq. 5.7, a Taylor iteration can be used until the differences between the calculated and measured ^{4}He were minimised (i.e. the 'raw' age). However, for a reliable cooling age determination, the possible underestimation, related to α-ejection, has to be considered. Therefore, the 'raw' age is divided by the total fraction (FT) of retained ^{4}He particles to correct for α-ejection (eq. 5.8, from Farley et al., 1996; Farley, 2002). ^{4}He-loss associated with α-ejection is mostly controlled by the grain geometry (in particular the surface to volume ratio, represented in the parameter R) and the different stopping distances of the parent isotopes (Farley, 2002).

$$F_T = \frac{\int_0^{R+S} (4\pi r^2)\, F(r)\, U(r)\, dr}{\int_0^{R+S} (4\pi r^2)\, U(r)\, dr} \tag{5.8}$$

Therein R is the sphere radius of a sphere, which equals the surface to volume ratio of the analysed grain. S is the stopping distance of the parent isotope (i.e. thought of as radius of a sphere, the centre of which is the location of the decaying parent isotope). r is the distance between the parent isotope and the centre of the sphere. $F(r)$ is the fraction of ^{4}He particles derived from mother isotopes at the distance r from R, not being ejected and thus retaining in the grain (note that F_T is related to the entire sphere, while $F(r)$ is only related to one part in the course of integration). $U(r)$ is a weighting factor and depicts the distribution of parent isotopes, assumed to be radially symmetric (Fig. 4).

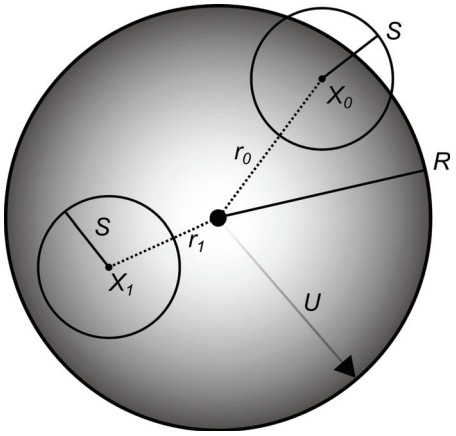

Fig. 4.: Calculation of the F_T factor is based on a sphere with the same surface to volume ratio as an analysed grain. R: radius of the sphere. X: position of a decaying isotope. r: distance between the decaying isotope and the centre of the sphere. S: stopping distance. U: weighting factor, depicting the distribution of parent isotopes within the crystal.

After all, α-correction and eq. 5.7 assume that all ^{4}He particles retained in the dated grain are derived from parent isotopes within the same grain (Farley et al., 1996). Spiegel et al. (2009) showed that ^{4}He can also be implanted from neighbouring grains, such that 'raw' ages, already may be overestimated. To correct for possible ^{4}He implantation in cases of (U-Th-Sm)-rich neighbouring minerals and / or an observed correlation between AHe ages and effective Uranium concentration (i.e. the summarised concentrations of parent isotopes normalised by the

ratio of their natural abundance compared to ^{238}U), Spiegel et al. (2009) recommend to mechanically abrade the outer part of the grain before the analysis, rather than perform α-correction afterwards.

In case that implantation is unlikely, eq. 5.8 can be simplified in that r is integrated from 0 to R only.

5.2.2. Carrying out (U-Th-Sm)/He dating on apatites

AHe dating for this thesis was performed on selected apatite grains (for coarse and fine separation see sec. 5.1.2). Grains were hand-picked under stereomicroscope (Olympus SZX16, maximum resolution: 230x) and selected according to sufficient size (smallest diameter $\geq$ 60 μm; Farley et al., 1996, morphology (preferably euhedral crystals) and purity (free of inclusions and cracks). For detecting tiny inclusions, grains were viewed in ethanol under transmitted and cross-polarised light.

Suitable grains were digitally photographed and measured (parallel and perpendicular to the crystallographic c-axis, Fig. 5). Up to three similar grains with respect to shape, dimensions and F_T-factor were encapsulated into Pt-tubes (i.e. multi-grain aliquots). Degassing and measuring of ^{4}He, ^{238}U, ^{235}U and ^{147}Sm was externally performed at the University of Melbourne (Australia): Degassing of aliquots was performed by laser heating with a solid-state diode laser with a wavelength of 820 nm and fibre-optic coupling (for 10 min. at 920 °C).

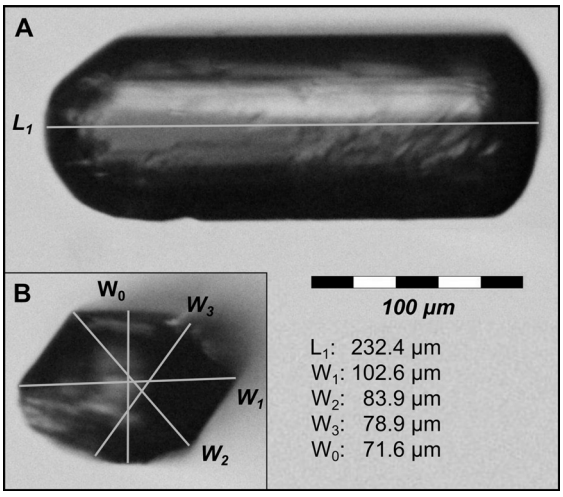

Fig. 5.: Photos of an exemplary grain (from sample Maggia-H15). Lengths and widths are taken from pictures parallel (A) and perpendicular (B) to the crystallographic c-axis. W_0 is measured as smallest diameter. A grain is excluded if W_0 is < 60 μm. This specific grain is analysed as MH15#5 in the first multigrain aliquot of Maggia-H15, yielding an AHe age of 6.11$\pm$0.72 Ma (Elfert et al., 2013).

In a first step, the concentration of a known gas mixture (^{3}He/^{4}He) is determined by a Balzers quadrupole mass spectrometer. Afterwards, the same amount of ^{3}He (as in the known gas mixture) is added to the extracted ^{4}He from the aliquot and analogously measured as concentration.

The ^{4}He gas level from the aliquot was then derived from the difference in the concentrations of the two gas mixtures.

In a second step, U, Th and Sm contents were measured by a second-generation Varian quadrupole ICP-MS after dissolving of the aliquots in 5 % HNO_3. For one sample of this study, two multi-grain aliquots (altogether six grains) were combined before dissolution, due to very low ^{4}He gas levels (measured in the first step) to enhance the amount of U, Th and Sm (measured in the second step).

All AHe ages are α-corrected as abrasion was not possible on the relatively small sized grains. F_T values are derived for each parent isotope and weighted with the single-grain mass (as most AHe ages are derived from multi-grain aliquots), natural abundance of parent isotopes and their corresponding α-decay constants. Grains with individual F_T values less than 0.6 are discarded in this thesis, in order to avoid over-interpretation.

The total analytical error (derived from replicated analyses of Durango age standards at Melbourne University) and the individual F_T errors are assumed with 6.2 % and 10 %, respectively. Central ages (after Vermeesch, 2008) are calculated if more than one AHe analysis of a sample succeeded.

5.3. Thermal history modelling

5.3.1. Basic concept of thermal history modelling

For AFT analyses densities of spontaneous and induced fission tracks are measured, as well as the distribution of confined track lengths, and proxies for the annealing properties of each single grain such as Dpar.

The AFT age determination is based on the track densities. However, solely 'cooling ages' are insufficient to infer the thermal history of a sample, as demonstrated in Figure 6. Although, track density is related to track shortening, such that in the first place track length reduction leads to density reduction, this relation is decoupled at temperatures below 60 °C (Fig. 7A): Density is only reduced rapidly at high temperatures. At temperatures below 60 °C track density reduction is negligible. Fission tracks, however, are perceptibly shortened even at surface temperatures (Gleadow and Duddy, 1981; Spiegel et al., 2007). Thus, while high temperatures (110 °C to 60 °C) influence both, track length distribution and cooling age, low temperatures (below the PAZ) only impact the track length distribution. This is due to an incomplete track registration (i.e. density measurements are only carried out by counting fission tracks, registered on one internal surface, while confined track lengths are measured in the volume of the mounted grain).

The basis of thermal history modelling are laboratory annealing experiments, where track shortening is measured for specific times and temperatures (e.g., Wagner, 1968; Wagner and Reimer, 1972; Green et al., 1986; Carlson et al., 1999; Barbarand et al., 2003).

Traditionally, the resulting relationships between track length shortening, time and temperature are depicted and extrapolated to geological times in Arrhenius plots (e.g., Wagner and Reimer, 1972; Wagner, 1979; Green et al., 1985, Fig. 7B). Arrhenius plots were then utilized to

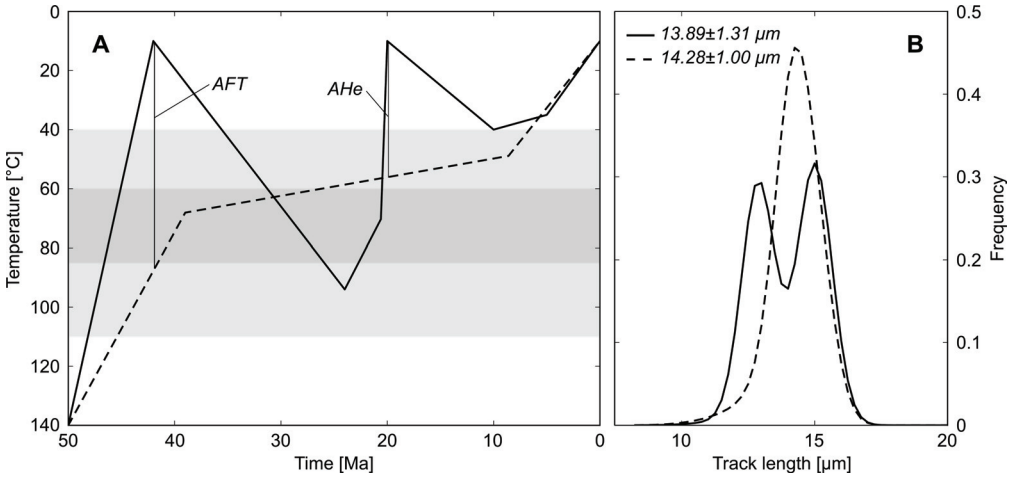

Fig. 6.: Artificially constructed time-temperature histories (A) and the resulting track length distributions (B). Both thermal histories yield the same cooling ages (AFT: 41.9 Ma, AHe: 19.9 Ma). Reheating (solid line) can be identified in analysing the track length distribution (bimodal distribution). Steady cooling histories (dashed line) yield unimodal track length distributions. Mean track length and standard deviations are given in B.

forwardly infer track length distributions for proposed thermal histories: Based on a given initial track length and a proposed cooling history, the distribution of track lengths can be derivated.

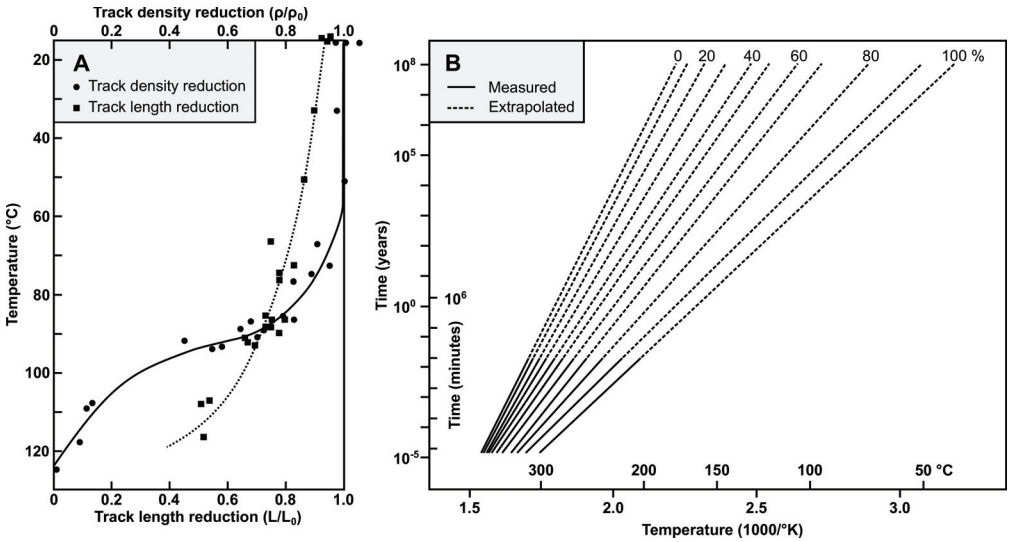

Fig. 7.: Track density reduction (i.e. the basis of fission track age determination) shows a different sensitivity to temperature as track length distribution (A, after Gleadow and Duddy, 1981). Track lengths still (slowly) anneal at low temperatures, whereas the track density remains nearly constant from cooling below 60 °C. ρ: track density at a given temperature. ρ_0: final track density after cooling to the surface. L: mean track length at a given temperature. L_0: length of a fresh induced fission track. The Arrhenius plot (B, after Wagner and Reimer, 1972) shows the percentage of track shortening depending on time and temperature. The same amount of track shortening as resulting from a specific temperature for a specific time results from exposing the sample at a higher temperature (note: i.e. negative x-direction) for a shorter period.

A thermal history model describes the Arrhenius relationships of track annealing mathematically (called annealing algorithm). Based on the annealing algorithm, AFT ages and track length distributions can be predicted for proposed thermal histories (i.e. forward modelling). The big advantage of computer based thermal history modelling compared to manually utilising Arrhenius plots is that vast numbers of time-temperature histories can be simulated and statistically evaluated against a given track length distribution (i.e. inverse modelling).

Early work of Laslett et al. (1987), which only considered the kinetic properties of Durango apatites, is nowadays mostly replaced by the multi-kinetic annealing model of Ketcham et al. (2007a). To account for the variability in apatite annealing kinetics, Ketcham et al. (1999) developed a first multi-kinetic inversion model, which was later improved in terms of one-step parameter fitting, c-axis projection (to correct for anisotropic annealing) and adopting a larger dataset (Ketcham et al., 2007a).

The basic assumptions is formulated as (Ketcham et al., 2007a):

$$g(l; l_0,\ \alpha,\ \beta) = f(t,\ T;\ C_i) \tag{5.9}$$

Therein g is a function of the measured mean track length l (incorporating the initial track length l_0 and two fitted parameters α and β). f is a fanning function of time t and temperature T (incorporating a further set of fitted parameters C_i) according to Crowley et al. (1991), where contours of constant annealing are defined (Ketcham et al., 1999). The needed parameters for the Arrhenius relationship are extracted from large datasets with most divers kinetic properties, and allow, in turn, to apply the model onto a large range of differently composed apatites.

The choice of the annealing algorithm depends on the chemical composition of the apatites of a study and the cooling ages (i.e. is the algorithm able to extrapolate towards the geological time of interest?). Some alternative models are the fanning linear model which is derived form the pure Durango approach (Laslett et al., 1987; Crowley et al., 1991), the former model of Ketcham et al. (1999) without the dataset of Barbarand et al. (2003) and an annealing model optimized for flourine-apatites (Crowley et al., 1991).

5.3.2. Performance of thermal history modelling

In this thesis, the HeFTy program (v. 1.75; Ketcham, 2005) is applied to predict time-temperature histories. The AFT system is parametrised by the number of spontaneous and induced fission tracks and track length distribution. Track annealing is computed according to the multi-kinetic annealing model Ketcham et al. (2007a) taking c-axis projection (Ketcham et al., 2007b) into account. Dpar values of the analysed grains serve as a proxy for the bulk annealing properties.

For the simulation of the AHe system, the contents of U, Th and Sm as well as the uncorrected mean age and the mean sphere radius (the radius of a sphere equivalent, i.e. with the same surface to volume ratio) were considered. ^{4}He diffusion is derived using the radiation damage accumulation and annealing model of Flowers et al. (2009). Stopping distances of the relevant α emitter (eq. 5.7) are taken from Ketcham et al. (2011).

AFT and AHe data were used for forward and inverse thermal history modelling to identify possible cooling histories and evaluate their statistical agreement with the observed datasets. Constraints for inverse thermal history modelling were set loosely to allow the widest possible interpretation of the data. In this respect, for most samples only the present day surface temperature (assumed as 10 °C) and a pre-PAZ assumption were fixed (>120 °C at 20 Ma or zircon fission track ages (sensitive to temperatures of 240±20 °C; cf. Brandon et al., 1998), where available).

For inverse thermal history modelling, 10,000 time-temperature paths (within the limits of the manually set constraints) are randomly chosen according to a Monte-Carlo algorithm. Goodness-of-fit (GOF) tests are performed after Ketcham (2005) testing for the statistical agreement between the computed and the observed cooling ages (AFT and AHe), and after Kuiper (1960) evaluating the computed track length distribution against the observed. Statistical agreement is interpreted as 'good' if the mean GOF value is greater or equal to 0.5 and the minimum GOF value supersedes a threshold t (eq. 5.10):

$$t = \frac{1}{N+1} \tag{5.10}$$

with N: number of performed GOF tests (i.e. $N = 3$ for a thermal model with AFT age, AFT track length distribution and AHe age).

Time-temperature paths, failing the conditions for 'good' statistical agreement, but with all GOF values exceeding 0.05 are called 'acceptable' according to the The HeFTy user manual (2009, Fig. 8): 'a good result implies the time-temperature path is supported by the data, while an acceptable time-temperature path is not ruled out by the data' (HeFTy user manual, 2009, chapter 4, page 3). Accordingly, the best-fitting model neither necessarily needs to be reasonable from a geological point of view, nor represents the 'true and only' thermal history of a sample. It rather stresses that the corresponding time-temperature path is in good statistical agreement with the data.

5.4. Numerical 'sandbox' modelling

5.4.1. Basic concept of the Discrete Element Method

The Discrete Element Method (DEM) deals with single particles (discrete elements) which interact on the basis of shear and normal forces (Cundall and Strack, 1978). Based on the granular model approach, particle assemblages comprising rigid balls or plates (according to the 3D or 2D approach, respectively) are synthesised. After the deposited particles have reached an equilibrium of forces, an external impulse is applied to start the simulation. This can be the movement of a boundary wall against the particle group for example. Depending on the physical properties of the adjacent particles (e.g., the coefficient of friction, shear and normal stiffness, and density), an overlap with the wall is caused. Depending on the magnitude of overlap and the physical properties of the particles, forces are computed which in turn are used to derive movements according to simple force-displacement laws (eq. 5.11; see also Mindlin and Dere-

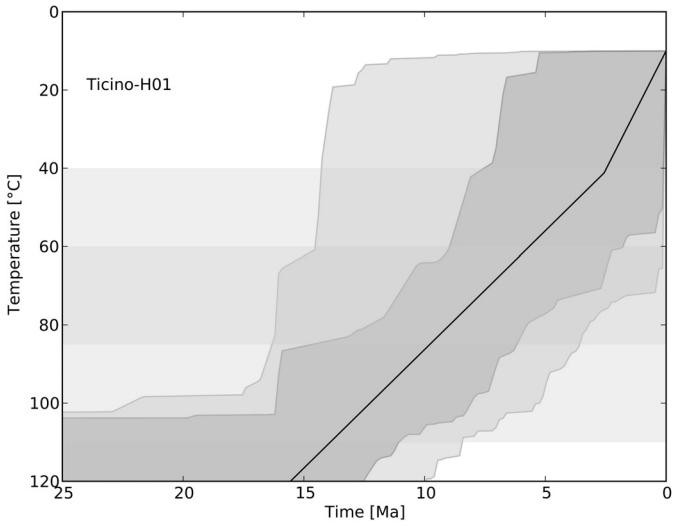

Fig. 8.: Exemplary time-temperature history derived from inverse thermal history modelling (sample Ticino-H1 from Elfert et al., 2013) showing the envelopes for thermal histories which are statistically in 'good' (dark grey) or 'acceptable' (light grey) agreement with the data. Solid line: Weighted mean path of 'good' paths.

siewicz, 1953; Cundall and Strack, 1979. The resulting particle movements may cause overlap with neighbouring particles, leading to a progressing stress impulse through and an associated deformation (i.e. motion) of the particle assemblage (Cundall and Strack, 1978).

Motion of particles is driven by contact forces (eq. 5.11) depending on the physical properties of the modelled particles. Given force, velocities and displacements are derived and new force-displacement relationships for all particle contacts are computed. According to these force-displacement relationships, forces are redistributed, which in turn are used to derive new velocities and displacements, and so on (Fig. 9).

$$\sum F = m \cdot a \tag{5.11}$$

Therein F is force, m is mass and a is acceleration (i.e. motion) of a particle.

Forces are derived by rheological models. In case of an elasto-plastic material behaviour, such as is used in the performed experiments, normal forces related to reversible elastic deformation can be described, based on the behaviour of a spring (Hooke's law, eq. 5.12):

$$\sigma = E \cdot \varepsilon \tag{5.12}$$

With σ: stress tensor, E: modulus of elasticity and ε: strain tensor

Shear stress, on the other hand, related to plastic deformation, can be described by expanding the strain term by a sliding element (or St.-Venant element) (eq. 5.13):

$$\varepsilon = \varepsilon_{Hooke} + \varepsilon_{St.-Venant} \tag{5.13}$$

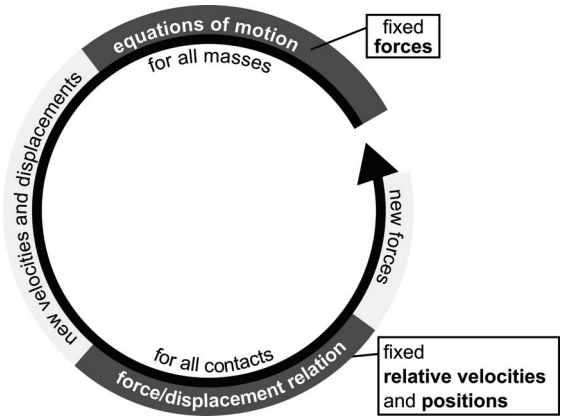

Fig. 9.: Sketch for the computational steps in PFC2D during a model run (after ITASCA, 2014). Forces are derived according to force-displacement laws. The forces are translated into motion, which in turn changes the stress field. New forces are derived based on the new conditions.

Until a certain stress threshold σ_F (incipient failure) is reached, the basic formulation of Hooke's law (eq. 5.12) is used, resulting in reversible, pure elastic deformation and particle overlap. Once σ_F is reached, irreversible plastic deformation sets in. However, once failure occurs, further increasing angular stress leads to softening of shear strength of brittle material until stable sliding conditions are established (Lohrmann et al., 2003). Further on, sliding only depends on material roughness (e.g. shape, friction).

5.4.2. Performance of Numerical 'sandbox' Modelling

For the numerical 'sandbox' experiments (Paper Contributions 2 and 3), the Particle Flow Code 2D (PFC2D; Cundall and Strack, 1978; ITASCA, 2004) was applied.

To simulate elasto-plastic behaviour of brittle material, forces are portioned by PFC2D into normal forces and shear stresses. Additionally, gravity was active during the model run. The Mohr-Coulomb criterion, depending on the particle friction was used to mark the onset of plastic deformation and shearing. The modulus of elasticity (Young's modulus) was calculated from normal and shear particle stiffness. Miyakawa et al. (2010) proofed this approach suitable to simulate orogenic processes like brittle, upper crustal deformation. Associated with numerical realisations of plates, balls and rotation, the overall friction is not equal to the particle friction. Therefore, the particle friction had to be calibrated. Calibration results and further parametrisation are outlined in the corresponding paper contributions (Paper Contributions 2 and 3).

Particle positions, forces and information about the internal structure of the particle assembly can be tracked at each time step. More detailed descriptions of PFC2D are provided by Cundall and Strack (1978, 1979, 1983), Cundall (1987) and the PFC2D ITASCA handbook (2004).

The experimental settings of three conceptional experiments were based on present day 2D seismic profiles from the European Alps (Paper Contribution 2). Based on these three experiments, the effect of lower crustal conditions on upper crustal processes (in particular exhumation and erosion patterns) was investigated by calculating synthetic AFT ages from numerical particle pathways (sec. 5.4.3). Within the model, a down-going décollement in a subduction / collision

scene is simulated by an inclined wall, moving in positive x-direction. In doing so, it underthrust a fixed backstop, simulating the thrust plate. In two scenarios, an additional fixed block is implemented right in front of the backstop simulating a lower-crustal fragment. Altogether, three scenarios were applied: (i) high frictional décollement and lower-crustal fragment, (ii) weak décollement and lower-crustal fragment, and (iii) high frictional décollement without lower-crustal fragment.

The fundamental insights of this study were applied to a real world case study in the European Central Alps. Therefore, the model setup had to be calibrated, until the final stage of the experiment reproduced the present day crustal configuration as derived from the seismic profile NFP-20 East (e.g., Schmid et al., 1996, Paper Contribution 3). Besides the down-going décollement, also the backstop was lowered to simulate the sinking of the thrusted plate in response to overthrusting of the subducted plate associated with a slab break-off and suture oversteepening.

5.4.3. Coupling numerical 'sandbox' modelling and AFT analyses

Heat flow and temperature distribution is integrated by various studies in different DEM applications (e.g., Hunt, 1997; Peters, 2002; Vargas and McCarthy, 2002; Kwapinska et al., 2006; Rickelt, 2011; Rickelt et al., 2013). Temperature is derived from conductive, convective and / or radiative heat flow in these studies. Rock temperature decreases during exhumation, i.e., when a rock approaches the surface. Exhumation is mainly triggered by erosion, therefore erosion becomes a major factor impacting the temperature distribution. Erosion, however, is not considered in previous DEM studies.

The first step of our approach, therefore, is to calculate erosion for the numerical 'sandbox' experiment. This allows to track the distance of a selected particle to the erosional surface (note that 'erosional surface' means the surface of the evolving particle wedge which is exposed by erosion, rather than a plain erosion surface s.str.). Assuming a geothermal gradient allows to derive a time-temperature history for that particle, which in turn is taken for forward thermal history modelling, yielding synthetic AFT data (age, mean track length, track length distribution).

The approach of coupling numerical 'sandbox' models and AFT analysis is briefly outlined in the following. A more detailed description is given in the paper contributions 2 and 3.

First of all, model time had to be translated into geological time. In the conceptional studies (Paper Contribution 2), time was linked to the movement along the model detachment, which in turn is related to assumed crustal shortening. In a case study concerning the Lepontine Dome of the European Alps (Paper Contribution 3), the model was run until the resulting topography approximately matched the present day cross section.

Erosion and subsequently thermal histories for selected particles were derived after running the numerical 'sandbox' experiments. For each time step, an erosional surface (in addition to the modelled one) was calculated from the current particle arrangement, the assumed initial (real world) maximum elevation and the present day (real world) maximum elevation. The basic assumption therein is that the ratio between the simulated elevation at any point along

a modelled profile length and the simulated maximum elevation of that profile length equals the ratio between the elevation of the erosional surface at the same point and the maximum elevation of the erosional surface (Fig. 10). Subsequently, temperature at any point in time and space (within the particle assemblage) can be derived by determining its distance to the surface and assuming a geothermal gradient (eq. 5.14).

$$T_{x,y,s} = ((eE_{x,s} - mH_{x,s} + (eE_{x,n} - mH_{x,n})) \cdot g_t) + T_{surf} \tag{5.14}$$

Therein T is the temperature at point x/y at time step s, eE is the erosional surface elevation (notice $eE_{x,s}$ refers to timestep s, whereas $eE_{x,n}$ refers to the end of the simulation - same for mH), mH is the height of the particle above the model bottom ($eE_x - mH_x$ can be read as depth below the erosional surface), g_t is the geothermal gradient and T_{surf} is the surface temperature.

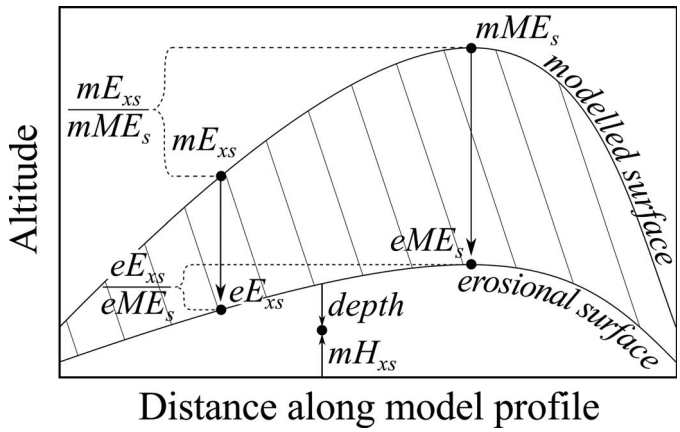

Fig. 10.: Derivation of depth below the surface of a given point (mH_x) at a given time (s), assuming the ratio between the modelled maximum elevation (mME_s) and the modelled local elevation (mE_{xs}) equals the ratio of the erosional maximum elevation (eME_s) and the erosional local elevation (eE_{xs}).

Eventually, the time-temperature history of any particle at any time during the model run can be extracted and used for forward thermal history modelling (sec. 5.3). In doing so, synthetic AFT data can be derived from numerical 'sandbox' modelling not only for the final stage of the experiment (corresponding to the present day situation), but also for any intermediate model step.

For the conceptual study, numerical particles were selected for AFT analyses, which intersected the erosional surface at the time of 'sampling'. This procedure can be interpreted as sampling along long-wavelength mountain ridges.

For the case study, however, observed and synthetically derived AFT data were compared. Because AFT data depends on elevation, only data points of the same elevation are directly comparable. Thus, the numerical particles selected for AFT analyses had to be on the same elevation as the corresponding samples.

Consequently, to assure the complete exhumation of a particle until the end of the simulation, an extra term VI is introduced that successively reduces the local erosional surface, which can be interpreted as valley incision (eq. 5.15). Hence, selection particles can be interpreted as

sampling along the bottom of an incised valley. VI has to be substituted for eE in eq. 5.14. To receive further indications to the geodynamic interpretation of the study area, the onset of effective valley incision can be controlled.

$$VI_{x,s} = eE_{x,s} - \left(\frac{s}{n}\right)(eE_{x,n} - mH_{x,n}) \tag{5.15}$$

With VI: valley incision at point x at time step s and n: number of time steps.

5.5. Sampling design (AFT and AHe)

Since AFT and AHe dates depend on elevation, a sampling design with either horizontal or elevation (i.e. nearly vertical) profiles is preferred for interpreting low-temperature thermochronological dates. Differences in elevation along a horizontal profile may cause age scatter as ages on top of the ridges are generally expected to be older than at the valley bottom. For this thesis, samples are taken along two horizontal profiles across the central Lepontine Dome, along the valley bottoms of the Ticino river (515±215 m a.s.l.) and the adjacent Maggia river (434±188 m a.s.l.; Fig. 2). Both profiles are roughly north-south oriented, with an east-west spacing between the profiles of about 20 km.

The Ticino horizontal section contains 12 samples along 37 km profile length and solely comprises samples of the central Lepontine Dome, intersecting the Ticino subdome. The Maggia horizontal profile, however, also involves the Ivrea zone, south of the Insubric Line, reaching into the centre of the Lepontine Dome. Thus the Maggia profile covers both, the Adriatic margin (Southern Alps) and the Penninic units of the Central Alps.

Furthermore, samples were taken along six elevation profiles, located at the northern and southern terminations as well as in the centres of the horizontal profiles. Both, the results from the horizontal profiles and the progress of the analyses of the elevation profiles (18 AFT ages, track length measurements on 10 samples and 12 successful AHe analyses) are documented in the appendix (B, C).

6. Interpretation and discussion of the results

Firstly, new AFT and AHe data from the Lepontine Dome were generated and interpreted by thermal history modelling (sec. 6.1; Paper Contribution 1, i.e. Elfert et al., 2013). Secondly, an approach to combine numerical 'sandbox' modelling and AFT analyses was developed (sec. 6.2; Paper Contribution 2) and applied to the same area of the Central Alps that was investigated using AFT and AHe thermochronology (sec. 6.3; Paper Contribution 3).

6.1. Neogene cooling of the Lepontine Dome

Cooling ages of structurally low Subpenninic nappes (Leventina, Antigorio; Fig. 2) decrease distinctly towards the centre of the Lepontine Dome (AFT: 5 Ma, AHe: 4 Ma) and increase to the south and to the north (AFT: 19 Ma, 11 Ma; Fig. 11). Thermal history modelling revealed small-scale differential cooling across the dome during the Miocene (Elfert et al., 2013):

The southern part of the Lepontine Dome (along and north of the Insubric Line) cooled episodically from early to late Miocene times. Age jumps across east to west oriented nappe boundaries (Figs. 2, 11) suggest that cooling in the south of the Lepontine can be associated with southward oriented backthrusting during the Miocene. The southern termination of the Ticino profile cooled earlier to temperatures below 110 °C than the southern termination of the Maggia profile. Either backthrusting lasted longer in the central parts (Maggia) or migrated from east to west, following the proposed movement of the Adriatic indenter (Steck and Hunziker, 1994).

The northern part of the Lepontine Dome (south of the northern steep belt) also cooled to temperatures below 110 °C from early Miocene times on, but rather slowly and steadily. The centre of the Lepontine Dome cooled steadily until latest Miocene/early Pliocene times. However, cooling below 110 °C was more rapidly and distinctly later than along both, the southern and the northern terminations.

Younger cooling ages (compared to the northernmost ages of the Ticino profile, Elfert et al., 2013) and steady exhumation since the early Miocene are reported from the northern steep belt and the adjacent Aar-/Gotthard massif (Glotzbach et al., 2009; Janots et al., 2009). Thus, the northern steep belt and the Aar-/Gotthard massif seem to have acted as a backstop for the bordering Lepontine nappes which were thrust northwards associated with ongoing convergence of the European and Adriatic plates until latest Miocene times (Fig. 12). Probably, thrusting was slowed down by this northern backstop, resulting in updoming associated with large-scale folding of the Lepontine Dome in north-south direction.

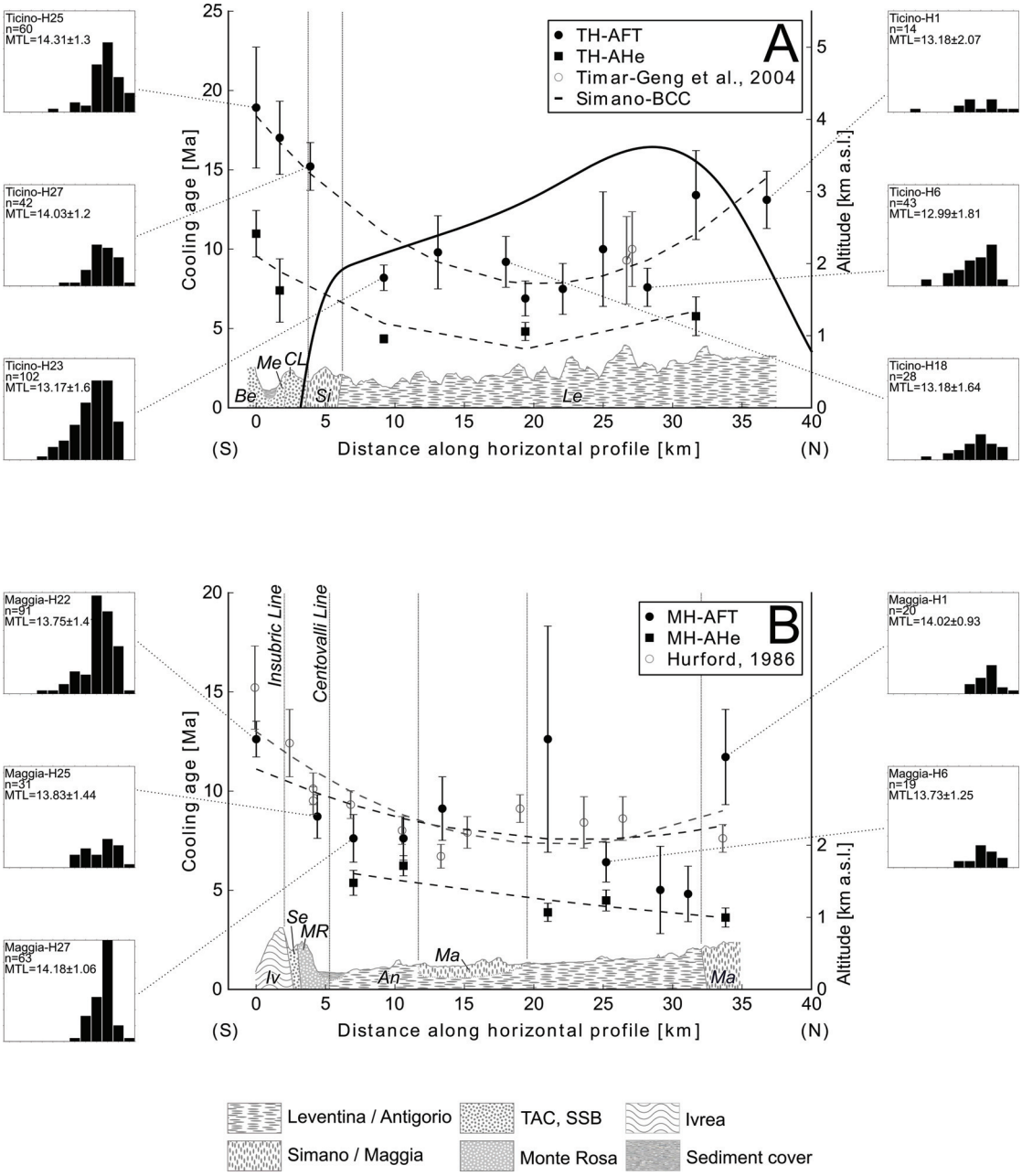

Fig. 11.: Cooling ages and 1 σ-error along Ticino (A) and Maggia (B) horizontal profiles (500±200 m; from Elfert et al., 2013). Track length distributions are shown for samples with sufficient number of track lengths for thermal history modelling. Dashed lines represent a 2^{nd} order trendline to the data. BCC: Basement-Cover-Contact (Pfiffner et al., 1990). Additionally, cross sections along the profiles (i.e. not along the adjacent ridges, because in some cases this would result in the wrong nappe allocation) are drawn. Dipping angles after Pfiffner et al. (1990); Berger et al. (2005) and Maxelon and Mancktelow (2005). An: Antigorio, Be: Bellinzona, CL: Cima Lunga, Iv: Ivrea, Le: Leventina, Ma: Maggia, Me: Mergoscia, MR: Monte Rosa, Se: Sesia, Si: Simano, SSB: Southern Steep Belt, TAC: Tectonic Accretion Channel.

Furthermore, cooling patterns along the Maggia valley indicate notable vertical movements along the Antigorio-Maggia boundary between 12 Ma and 2.5 Ma, probably related with normal-faulting along the Rhône-Simplon fault (Elfert et al., 2013).

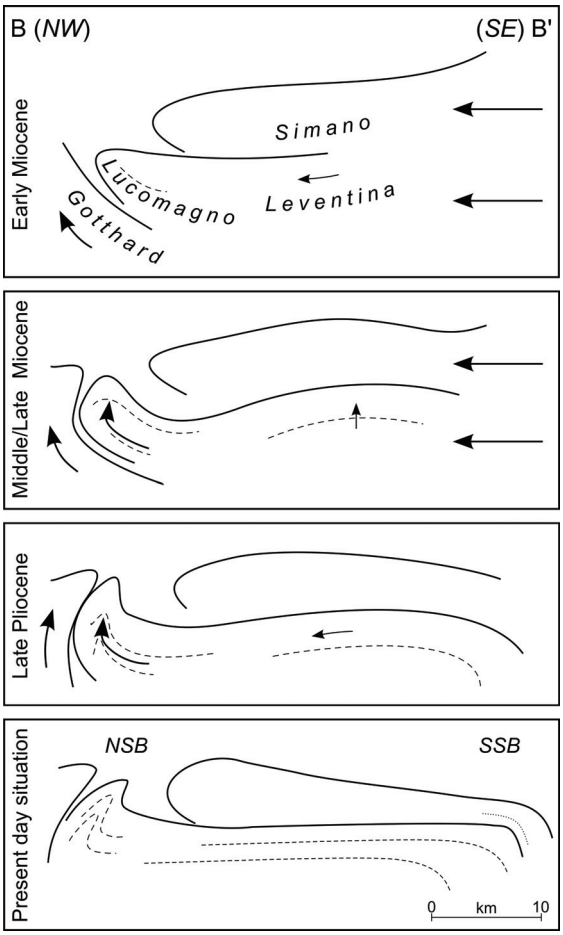

Fig. 12.: Proposed model of the structural evolution across the Ticino culmination (cross section AA' in Fig. 2) since Miocene times (from Elfert et al., 2013). Early Miocene: convergence leads to successive northward thrusting of the Penninic nappe stack (after Schmid et al., 1996). Middle/Late Miocene: northward movement of the Subpenninic nappes is decelerated by the barrier of the exhuming Gotthard massif resulting in large-scale nappe folding. Late Pliocene: decreasing compression leads to cessation of folding of the central nappes, while the northern steep belt (NSB) still exhumes. Present day situation: steep belts north and south of a rather flat lying central nappe stack (after Rütti et al., 2008). SSB: southern steep belt.

In contrast to small-scale variability during Miocene exhumation (regarding both styles and rates), thermal history modelling suggests uniform and accelerated Plio-Pleistocene cooling across the Lepontine Dome. Miocene cooling was directly associated with tectonic structures. Plio-Pleistocene cooling, however, seems to have been independent thereof, indicating en-block exhumation of the central Lepontine area. Enhanced Pliocene exhumation coincides with increased sedimentation rates in Alpine foreland basins (Kuhlemann et al., 2002). On the one hand, uniform exhumation supports the assumption of climate controlled erosion (Willett et al., 2006). On the other hand, tectonic control cannot be completely ruled out and an independent proof for changed climatic conditions in the Alps at the Miocene-Pliocene boundary is still lacking.

Thus, controlling factors of exhumation seem to have changed at ~6-4 Ma, but the reason for this change cannot be resolved by the applied methods.

6.2. Numerical 'sandbox' experiments – Conceptual parameter sensitivity

The first series of numerical 'sandbox' experiments proved sensitive for different internal parameters (exemplarily shown for the basal friction) and general model setup (deep seated geometries). In all numerical 'sandbox' experiments double-vergent wedges evolved (Fig. 13), but shape (e.g. slopes of the flanks, location of the crest) and internal structure (e.g., fault location, fault dipping angles) differed:

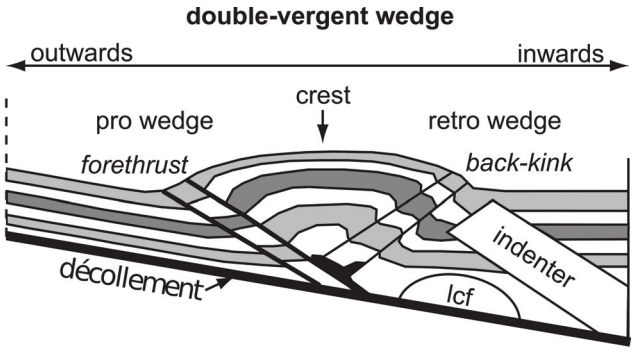

Fig. 13.: Simplified scheme of a double-vergent orogenic wedge (modified after Persson and Sokoutis, 2002). The lower crustal fragment (lcf) is only implemented in Sc1 and Sc2.

High basal friction values resulted in underthrusting of incoming material (eq. 5.14). Thus, basal accretion along the pro-wedge flank became the dominant process for the development of the resulting wedge. The crest migrated from the far side of the fixed backstop inwards (in the direction towards the fixed backstop). In contrast, deformation over a weak décollement was mostly associated with frontal accretion and material addition at the back-side, hence resulting in a flatter, bidirectionally evolving wedge with flatly dipping flanks. Like in the case of high basal friction, the crest migrated inwards, though distinctly slower.

Thus, the strength of the décollement, simulating the lower crust of a down-going plate in a subduction scene, crucially influences the uplift style.

A third scenario lacked an additional fixed block above the décollement (simulating a lower-crustal fragment in the first two scenarios) resulting a wider wedge. In contrast to the first two scenarios with implemented lower-crustal fragment, the wedge rose at first near the fixed backstop. As a result, the crest migrated outwards in the course of the simulation.

Therefore, lower-crustal geometry strongly impacts both, width and migration direction of the resulting wedge (Fig. 14).

Depending on the aforementioned parametrisation and the geometry, different cooling patterns evolved along the profile, which were depicted by the synthetic AFT cooling age distribu-

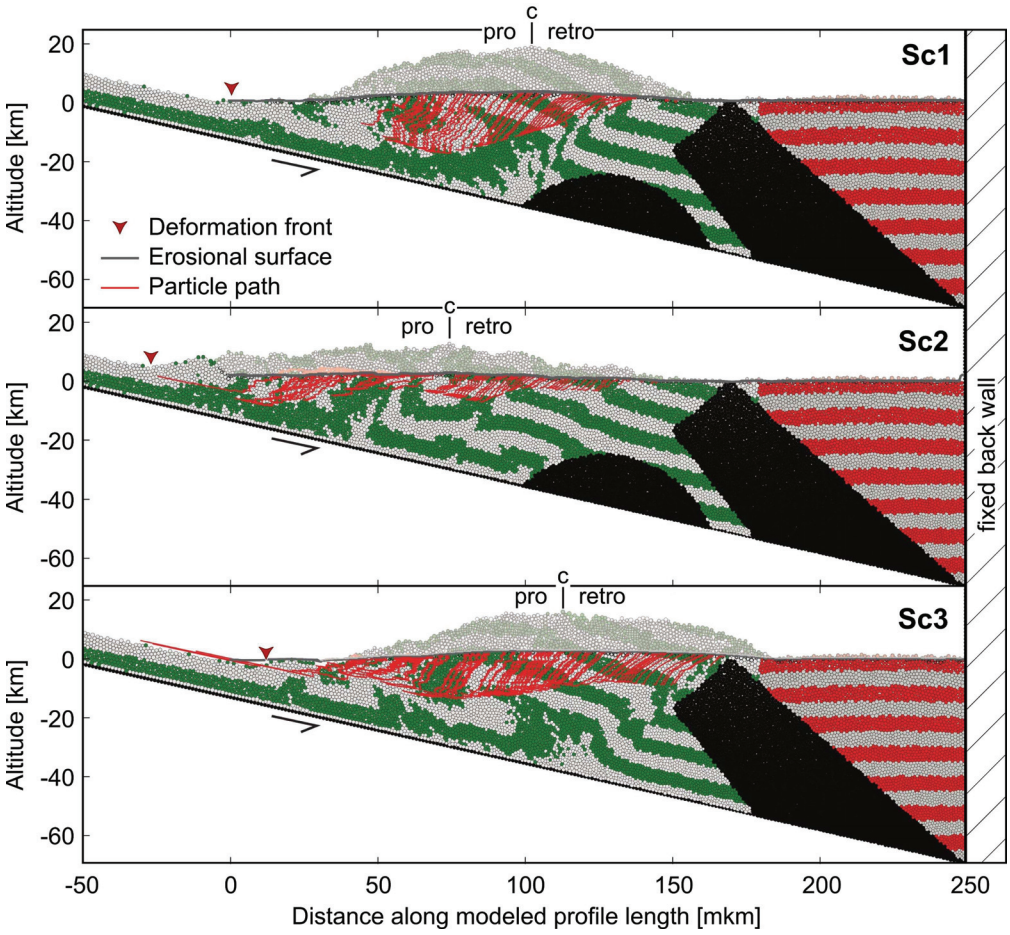

Fig. 14.: Particle setting of the conceptual experiments after 119 km shortening (corresponding to 32 Myr of orogeny). Particle pathways (red lines) reaching the erosional surface (grey line) and the outcrop position of the deformation fronts (red triangle) are shown. Grey, green and red coloured particles are used as marker horizons of the upper crustal material. Black particles represent the fixed lower crustal material. Sc1: high frictional detachment and lower crustal fragment. Sc2: weak frictional detachment and lower crustal fragment. Sc3: high friction detachment without lower crustal fragment.

tion: In case of a high décollement strength, youngest AFT ages are derived in the centre of the wedge, while they gradually increase towards both wedge flanks (Fig. 15). AFT ages increase faster if a lower-crustal fragment is implemented and show smoother age slopes if it is missing. Above a weak décollement, frontal accretion leads to a continuous series of backthrusts. AFT ages in the footwalls exceed the recently exhumed counterparts of the hanging walls, resulting in an alternating series of younger and older cooling ages (Fig. 15).

Summarising, synthetic AFT ages are expected to show a U-shaped distribution over a high frictional décollement in a collision scenario. Low basal friction rather leads to sinusoidally formed AFT ages along the modelled profile length.

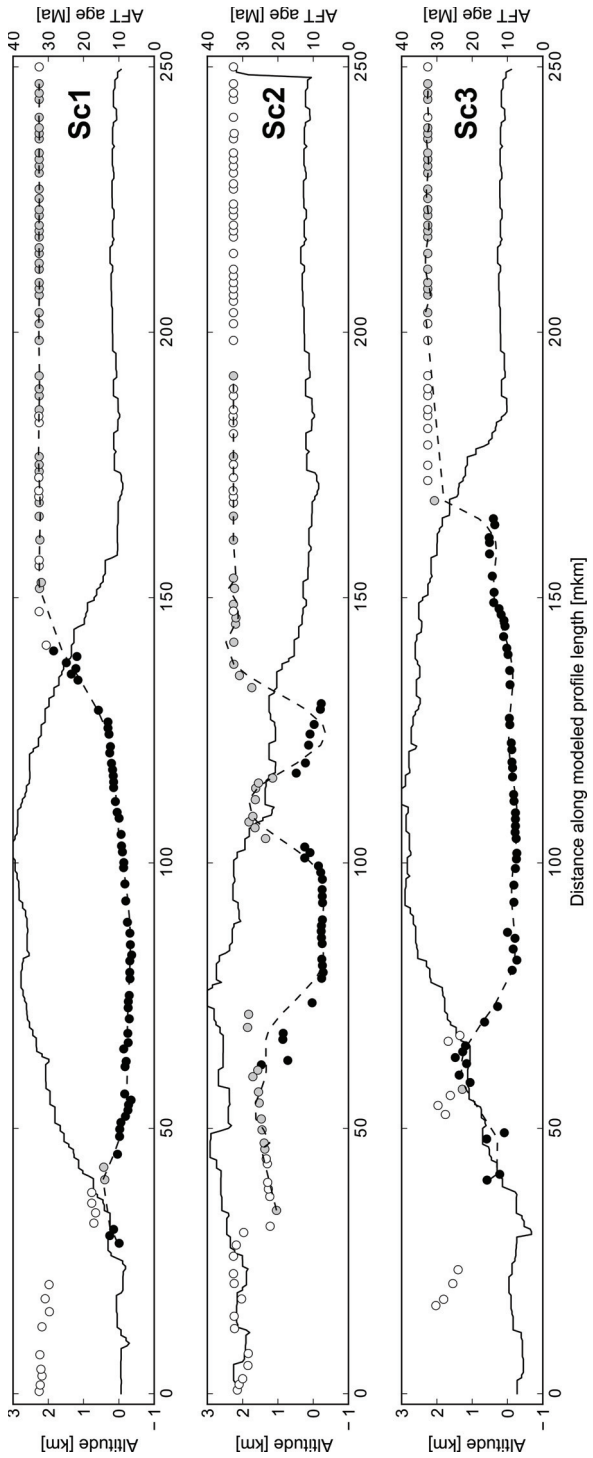

Fig. 15.: Synthetic AFT cooling ages, derived from the conceptual experiments after 119 km shortening (corresponding to 32 Myr of orogeny). Ages are plotted against the erosional topography (black line). Beforehand, time-temperature histories were evaluated with respect to their significance. Since erosion and temperature were derived after the model run, the resulting thermal histories are occasionally unrealistic. Only time-temperature histories with a complete reset of the AFT system (> 110 °C) are fully trusted (for details, please see Paper Contribution 2, sec. 3.3.2). Black, grey and white drawn ages are derived from meaningful, partly meaningful and invalid thermal histories, respectively. Sc1: high frictional detachment and lower crustal fragment. Sc2: weak frictional detachment and lower crustal fragment. Sc3: high friction detachment without lower crustal fragment.

6.3. Numerical ‘sandbox’ experiment – Application: the Lepontine Dome

A fourth numerical ‘sandbox’ experiment was based on the NFP20-East profile across the eastern part of the Central Alps. Beginning with the presumed deep structure along the profile in Oligocene times (based on the kinematic evolution model from Schmid et al., 1996), ongoing subduction and sinking of the Adriatic indenter was simulated. The major resulting structures of the numerical ‘sandbox’ experiment correspond well with the observed structures along the NFP20-East profile with respect to the long-wavelength topography, as well as the location and deep structure of the Insubric Line, the Lepontine Dome (i.e. culmination I in the numerical ‘sandbox’), the northern steep belt and the external massifs (i.e. culmination II in the numerical ‘sandbox’; Figs. 16, 17).

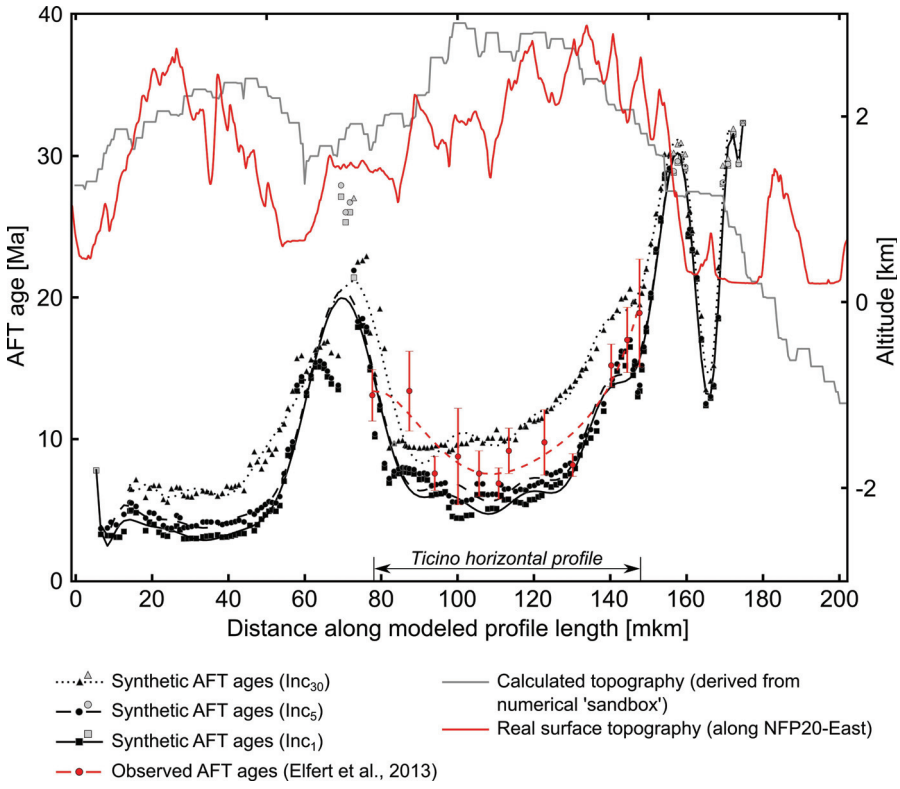

Fig. 16.: Calculated and observed topographies as well as synthetic and observed AFT ages along the profile. Three scenarios were tested with onset of valley incision at 30 Ma (Inc_{30}), 5 Ma (Inc_5) and 1 Ma (Inc_1). Grey markers: Low-quality time-temperature histories (see also Fig. 15). Lines through the AFT data represent trend polynomials of the corresponding AFT ages.

After successfully reproducing the present day cross section of the European Central Alps, synthetic AFT ages for particles at the same altitudinal level as the Ticino horizontal profile were derived. Analogously to the conceptual studies (sec. 6.2), the predicted AFT ages along the profile were distributed in U-shapes with youngest cooling ages in the centres of the culminations (Fig. 16). Synthetic AFT ages below culmination I (interpreted as being equivalent

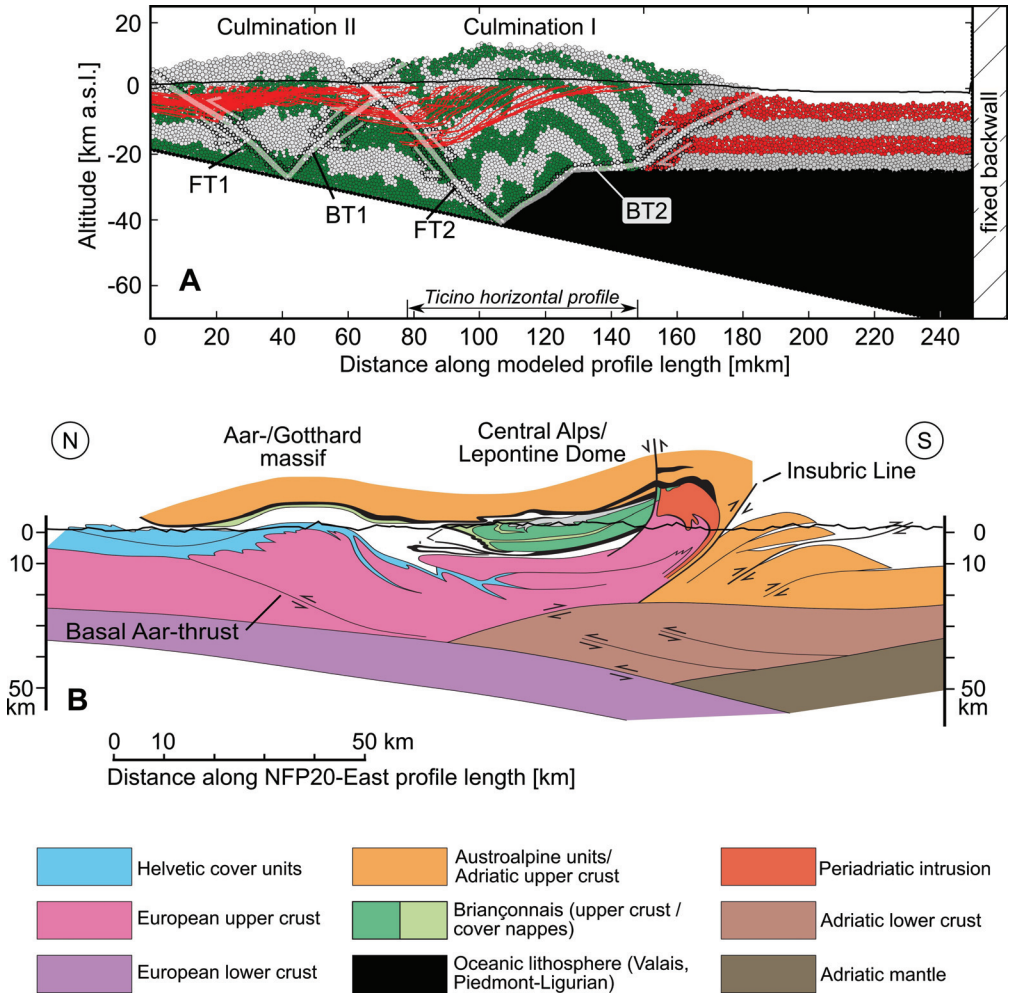

Fig. 17.: Particle setting at the end of the numerical 'sandbox' experiment (A). Green and light grey particles: European upper crust. Red and dark grey particles: Adriatic upper crust. Black body: Adriatic indenter (sunken Adriatic lower crust/mantle). Red lines: Pathways of particles located at 510 m a.s.l. at the end of the simulation. Narrow black line: Calculated erosional topography. B: Seismic profile along the NFP20-East profile (after Schmid et al., 2004b). Please note stretching in horizontal direction for reasons of clarity. Periadriatic intrusions are not simulated in the numerical 'sandbox' experiment and, hence, are not expected to appear as further culmination in subplot A.

to the Lepontine Dome) were slightly older than those of culmination II (interpreted as being equivalent to the Aar-/Gotthard massif).

To ensure the complete exhumation of a selected particle, the erosional surface was successively locally incised. The onset of valley incision had obvious impact on the height of the AFT ages, without changing the general U-shaped age pattern: The earlier valley incision started, the older were the corresponding AFT ages. Below the culmination I AFT ages of 4.5 Ma, 5.6 Ma and 9.2 Ma were predicted for an onset of valley incision at 1 Ma, 5 Ma and 30 Ma, respectively (Fig. 16).

Finally, projection of the Ticino profile from the Lepontine Dome onto the modelled profile length allowed for comparison of the data observed (AFT data and results from thermal history

modelling along the Ticino river; Paper Contribution 1) with the calculated thermal histories from the numerical 'sandbox' experiment and the synthetic AFT data.

The simulated time-temperature histories derived from the pathways of the numerical 'sandbox' particles agree well with the results from inverse thermal history modelling of the corresponding observed data. For reasons of clarity, cooling, geological time and cardinal directions are artificially adapted for the numerical 'sandbox' experiment, also being aware of actually relating to calculated temperature, model time and a Cartesian coordinate system, respectively.

Following this terminology, both numerical particles and observed samples show moderate cooling since middle Miocene times in the north, rapid, late Miocene cooling in the centre, and episodic cooling since early Miocene time in the south. Consequently, the distributions of synthetic and observed AFT ages show a remarkable resemblance with respect to the pattern shape and its location. Youngest ages are predicted for the centre of the profile below culmination I, corresponding to the Lepontine Dome. Exactly in the corresponding part of the Lepontine profile, youngest AFT ages were actually observed. Both, synthetic and observed AFT ages increase from the centre towards the terminations of the profiles.

Structural analyses of the numerical 'sandbox' experiment demonstrate that backthrusting in the part of the particle wedge that correspond to the northern steep belt is mainly responsible for the uplift of culmination I. Thus, wedge evolution of the numerical 'sandbox' experiment is in agreement the kinematic evolution model, as proposed in sec. 6.1 (Paper Contribution 1).

Finally, best match with observed AFT data is obtained for synthetic AFT data resulting from the scenario simulating Pliocene valley incision. Due to the simplifying assumptions of the numerical 'sandbox' experiment (see Paper Contribution 2), findings of this study must be very carefully adapted to the Central Alps on the one hand. On the other hand, the good agreement between synthetic and observed data points to an onset of valley incision at ~5 Ma (or slightly earlier) in the Lepontine Dome.

In general, combining AFT thermochronolgy and numerical 'sandbox' experiments can be used to investigate the onset of valley incision if (i) regions of most rapid exhumation and / or tectonic activity are preferentially sampled and (ii) the onset of valley incision differs at least by more than 4 Myr between the scenarios of valley incision. Otherwise, differences between synthetic AFT data of different scenarios may be too small to be resolved by AFT thermochronology on real samples.

Furthermore, the newly developed approach of coupling numerical 'sandbox' modelling and AFT thermochronology, helps to quantitatively integrate the influence of lateral displacement on exhumation in the interpretation of thermochronology data. Commonly, cooling is translated into exhumation by assuming a vertical uplift vector. Accordingly, slow cooling is transferred into slow exhumation, which in turn is often interpreted as tectonic stagnation. In low-angle thrusting settings, however, horizontal displacement may be of equal importance as vertical movement. In this case, rapid (lateral) movement must not necessarily result in fast exhumation and related cooling. Vice versa, slow cooling, revealed from thermal history modelling of observed data, may be associated with rapid low-angle thrusting without substantial exhumation.

In fact, this case is suggested by the numerical 'sandbox' experiment for the region, interpreted as being equivalent to the northern part of the Lepontine Dome (south of the northern steep belt).

The influence of lateral displacement on exhumation depends on the structural position of a sample in the orogenic wedge and the associated exhumation style: Particles along the wedge flanks are strongly laterally transported, while the particles at the crest of the wedge exhibit mostly vertical pathways. Consequently, cooling ages in the centre are youngest, increasing towards the wedge margins. Small-step episodic exhumation and highly variable displacement directions are found along the pro-wedge flank (representing the hanging wall of a major fault thrust in our case), resulting in old cooling ages and long mean fission track lengths. Such small step, episodic uplift is characteristic for basally accreted rock columns, which, hence, has to be considered as possible driving mechanism if slow and apparently steady cooling histories are predicted by inverse thermal history modelling (as is the case for the northern part of the Ticino profile in the Lepontine Dome). The example from the Central Alps showed that the geodynamic interpretation of thermochronology data can be significantly refined by using numerical 'sandbox' experiments in concert with the analysis of particle pathways and synthetic cooling paths.

7. Conclusion and outlook

A new set of low-temperature thermochronology data from the Lepontine Dome revealed that exhumation style and timing in the Central Alps varied on small-scale during the Neogene. Furthermore, a new approach was developed to combine numerical 'sandbox' modelling with AFT thermochronology. This approach was applied to the Central Alps, providing (i) general improvements for the interpretation of thermochronologic data, (ii) recommendations for sampling designs of thermochronologic studies aiming at the investigation of valley incision history and (iii) a refinement of the interpretation of Neogene cooling of the Lepontine Dome:

The southern part of the Lepontine Dome exhumed episodically from early Miocene on (migrating from east to west). The centre of the dome cooled rapidly and steadily until late Miocene times, postdating cooling in both the southern and northern part of the Lepontine Dome (south of the northern steep belt). The results suggest that Miocene exhumation south of the northern steep belt occurred in small episodic steps presumably associated with low-angle thrusting and basal accretion. The latter is assumed to be related to the evolution of large fault zones, exhuming the external Aar-/Gotthard massifs and causing backthrusting of the northern steep belt.

During the Alpine collision, the Aar-/Gotthard massifs and the northern steep belt acted as backstop for the northwards thrust central Lepontine nappes since the early Miocene. As a result, the central Lepontine nappes experienced large-scale folding until late Miocene, triggered by long-lasting compressional forces.

Because Miocene differential cooling was bound to tectonic structures, we interpret the Miocene exhumation of the Lepontine Dome as being triggered by tectonic forces. Extension is long known to have unroofed the Lepontine Dome and can also be monitored in the cooling history of the Maggia valley. However, the results of this thesis suggest that compression, related to long-lasting convergence of the European and Adriatic plates is another major contributor for Miocene exhumation of the Lepontine Dome.

In contrast to the variable exhumation patterns during the Miocene, the Lepontine Dome exhumed uniformly from Pliocene times on. A climate-controlled erosion regime would explain the observed shift towards uniform exhumation, though paleoclimate studies so far do not indicate a climate change at ~5 Ma (Cederbom et al., 2011, and references therein). Changing conditions in the Lepontine Dome go along with increasing exhumation rates. Therefore, the results of this thesis line up with hinterland and detrital studies proposing changing conditions in the Alpine exhumation and increasing sedimentation rates in the Alpine foreland basins at ~5 Ma (e.g., Kuhlemann et al., 2002; Vernon et al., 2008; Cederbom et al., 2011), without being able to resolve the underlying controls of this change.

The newly developed approach to couple numerical 'sandbox' modelling and AFT analysis demonstrates the influence of deep crustal mechanic properties and geometries on upper crustal exhumation processes. Particularly, basal and frontal accretion processes can be monitored and distinguished by the resulting AFT patterns. Analysing the relationship between particle paths and exhumation, furthermore, emphasizes the significance of horizontal displacement in low-angle thrusting settings. This should be taken into account, when interpreting low-temperature thermochronologic data in low-angle thrusting scenes. In this regard, lateral displacements are expected along the flanks of an orogenic wedge rather than in the centre. Lateral displacement in concert with high variability of exhumation and movement direction is found along the pro-wedge flank of an orogenic wedge. Here, the exhumation rate only poorly reflect the geodynamic activity.

This thesis improves the understanding of the Mio-Pliocene exhumation history of the Lepontine Dome with respect to exhumation style, triggers and timing by applying low-temperature thermochronolgic analyses (AFT and AHe) and different modelling approaches (thermal history modelling and numerical 'sandbox' modelling). Furthermore, the combination of AFT thermochronology and numerical 'sandbox' modelling helps understanding the interplay between lower and upper crustal processes.

One of the most pressing questions in the recent literature concerning the latest stage evolution of the Central Alps is the trigger of Pliocene exhumation. On the one hand, enhanced (global) erosion rates at ~6 Ma are associated with global cooling (e.g., Herman et al., 2013). On the other hand, Pliocene erosion in the Western Alps is interpreted to be tectonically dominated (e.g., Baran et al., 2014). Full three-dimensional modelling approaches may increase our understanding of the interplay between compressional and extensional tectonics as well as the influence of climatic conditions. Finally, the coupled approach of numerical 'sandbox' modelling and AFT analysis may be adapted to other geodynamic environments (e.g., the Himalayas or the Southern Alps, New Zealand) to proof its validity and trigger further improvement in interdisciplinary research.

Paper Contribution 1:
Long-lasting tectonic activities of the Lepontine Dome. New evidence from low-temperature thermochronology

Authors: Simon Elfert, Wolfgang Reiter, and Cornelia Spiegel
Published in Tectonophysics, Vol. 608 (p. 222-236),
http://dx.doi.org/10.1016/j.tecto.2013.09.033

Abstract

To investigate the Neogene exhumation history of the central European Alps, we apply low-temperature thermochronology in combination with thermal history modelling. Fission track and (U–Th–Sm)/He ages on apatites from the central Lepontine Dome (Ticino, Switzerland) indicate higher exhumation rates in the centre of the dome and rather moderate exhumation at the northern and southern boundaries since Neogene times. We present a model for explaining the latest stage exhumation of the central Lepontine Dome and show that (I) both episodic and continuous exhumations are found on small-scale throughout the Neogene, (II) compressional tectonics control the exhumation until the Late Neogene, (III) the exhumation regime changes between 6 and 4 Ma and (IV) increasing hinterland exhumation rates at the Mio-Pliocene boundary cannot be related to tectonic structures of the dome and they are thus explained by climatic changes.

Keywords: Lepontine Dome; European Alps; Neogene exhumation; fission track; (U-Th-Sm)/He

1. Introduction

During the last decade, the latest stage exhumation history of the European Central Alps has been controversially discussed, especially with respect to style and dominant triggers of exhumation (e.g. Selverstone, 2005; Willett, 2010, and references therein).

While several studies suggest episodic exhumation of the Alps since the Neogene (Carrapa, 2009; Cederbom et al., 2011), others find evidence for rather continuous evolution, indicating that the Central Alps have reached an exhumational equilibrium (Bernet et al., 2001, 2009; Glotzbach et al., 2010, 2011). In contrast to this assumed steady exhumation, Kuhlemann et al. (2002) reported a strong increase in sedimentation rates at ~5 Ma in circum-Alpine basins, indicating enhanced hinterland erosion. Likewise, Vernon et al. (2008) compiled a large dataset of cooling ages and suggested a doubling of exhumation rates of the Western Alps around 5 Ma. Indications for varying exhumation rates during Mio-Plio-Pleistocene times are found especially in parts of the Lepontine area of the Central Alps (Timar-Geng et al., 2004; Vernon et al., 2009). On the other hand, thermochronologic data from the external massifs of the Central Alps did not yield evidence of enhanced exhumation since Pliocene times (Glotzbach et al., 2009, 2010). However, the increase of Plio-Pleistocene sedimentation rates, which is not only proposed for the European Alps, but worldwide (Molnar and England, 1990; Molnar, 2004, and references therein), was challenged by Willenbring and von Blanckenburg (2010), on the basis of isotope data from marine sediments.

Furthermore, the trigger mechanisms of Neogene and Quaternary exhumation of the Alps are also disputed. On the one hand, climate change towards wetter conditions following the Messinian salinity crisis may have caused enhanced erosion and subsequent transportation of detritus (Willett et al., 2006). On the other hand, thermochronologic studies suggest that the exhumation of the external massifs of the Central Alps is mostly controlled by tectonic activity (Reinecker et al., 2008; Glotzbach et al., 2010).

To address questions of mode (episodic vs. continuous exhumation) and trigger (climate vs. tectonics), we investigated the exhumation history of the central Lepontine Dome (Fig. 18). The Lepontine Dome is situated in the core of the Central Alps, comprises deeply buried rocks and was subject to erosion since the middle Miocene. We present new apatite fission track (AFT) and (U–Th–Sm)/He (AHe) data from two transects along the Maggia and Ticino rivers, crossing the central Lepontine Dome.

Due to the overlapping temperature sensitivities of the AFT and AHe systems, continuous cooling histories can be deduced from the combination of both methods and thermal history modelling. All AFT and AHe cooling ages of the study area are Neogene in age, thus providing insights into the late stage exhumation of the Lepontine Dome.

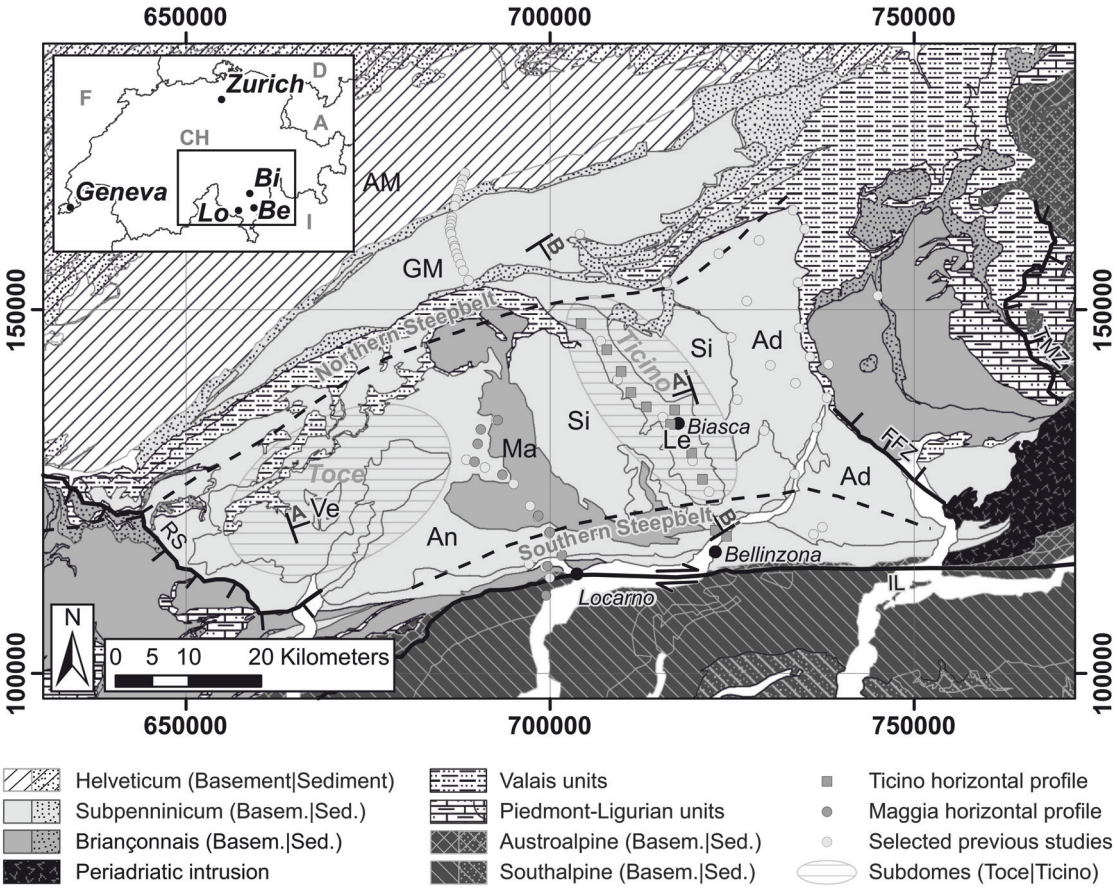

Fig. 18.: Simplified geological map of the Lepontine Dome and sample locations (dark grey squares and dots: own samples along Ticino and Maggia valley; light grey dots: previously published AFT data by Hurford (1986); Rahn (2005); Glotzbach et al. (2009); Janots et al. (2009)). Grey lines: Major nappe boundaries. AM: Aar massif, GM: Gotthard massif; Lepontine nappes: Ad: Adula, An: Antigorio, Ma: Maggia, Le: Leventina, Si: Simano (outcropping east and west from the Leventina), Ve: Verampio; Structures: FFZ: Forcola Fault Zone, IL: Insubric Line, RS: Rhône–Simplon Line, TMZ: Turba Mylonite Zone. A–A' and B–B' terminations of cross sections in Figs. 19 and 24. Grid units referring to Swiss Grid (CH03). Map after Tectonic Map of the Swiss Federal Office of Topography, Milnes (1974) and Schmid et al. (2004a).

The overall questions are: Is the exhumation regime of the Lepontine Dome changing significantly in Mio-Plio-Pleistocene times? If so, does climate change trigger the exhumation in Pliocene times? Or can exhumation patterns rather be correlated with tectonic structures and their activity?

2. Geological setting

The Lepontine Dome is situated in the core of the Central European Alps (Fig. 18). To the north the dome is bordered by the Aar-/Gotthard massif, which is part of the Helvetic realm and therefore represents the European margin (Schmid et al., 2004a). To the south, the Insubric Line separates the Lepontine area from the Southern Alps, which were derived from the Adriatic plate (Frey and Ferreiro Mählmann, 1999; Schmid et al., 1989). Extensional fault zones border the Lepontine Dome to the east (Forcola Fault Zone, Turba Mylonite Zone) and west (Rhône–Simplon Fault Zone). The Oligocene Bergell intrusion is located adjacent to the Lepontine Dome to he south–east. Sandwiched between the Helvetic units and the Southern Alps, the formerly deeply subducted Penninic nappes are situated. These consist of former oceanic basins (Lower and Upper Penninicum), the Briançonnais terrane (Middle Penninicum) and distal European margin (Subpennicum; e.g. Milnes, 1974; Schmid et al., 2004a).

2.1. Geodynamic evolution of the Central Alps since Miocene times

In Miocene times, collision of the European and Adriatic plates was long on the way and ongoing convergence of the two continents caused a steady shift of the Alpine pro- and retro-wedge to the north and to the south, respectively. The Adriatic plate had already detached the upper from the lower European crust and split in between as an indenter (Müller, 1989; Von Blanckenburg and Davies, 1995; Schmid et al., 2004b). At ~20 Ma, the basal thrust beneath the Aar massif was activated (Schmid et al., 2004b).

As a result of crustal overthickening, the Alps experienced west–east extension coeval with collision-related ongoing north–south convergence (Mancktelow, 1992; Schlunegger and Willett, 1999; Frisch et al., 2000). While major extension took place between 25 and 13 Ma (Mancktelow, 1992; Schlunegger and Willett, 1999; Frisch et al., 2000), first extensional faulting in the eastern parts of the Central Alps can be tracked back into the Eocene (Turba Mylonite Zone: Eocene to early Oligocene, Nievergelt et al., 1996; Schmid et al., 1996; Forcola fault-/Misox Zone: late Oligocene to middle Miocene, Meyre et al., 1998; Fig. 18). From 20 Ma on, the Simplon Fault Zone to the west of the Central Alps (Fig. 18) is mostly responsible for the exhumation of the Lepontine Alps, exposing the most deeply buried rocks of the Central Alps (Steck and Hunziker, 1994; Berger et al., 2005; Maxelon and Mancktelow, 2005; Campani et al., 2010).

2.2. Doming of the Lepontine area

The term 'Lepontine Dome' actually addresses different doming features, which formed during the evolution of the Lepontine Alps. Firstly, nappe stacking, associated with continent–continent collision, led to regional metamorphism. This barrow-type metamorphism resulted in the prominent mineral zones of the Lepontine Alps, outlining a metamorphic dome which is crosscut by the Insubric Line to the south (Engi et al., 2004; Maxelon and Mancktelow, 2005 and references therein; Berger et al., 2011). Secondly, unroofing, related to west–east extension since Oligocene to middle Miocene times, led to structural doming (Nievergelt et al., 1996; Meyre et al., 1998; Frisch et al., 2000). Thus the Lepontine Dome is both a metamorphic and a structural dome (Wiederkehr et al., 2009). In this paper, we will introduce another structural doming feature, associated with continent–continent collision which is so far undetected.

2.2.1. Metamorphic doming of the Lepontine Dome

At least two types of metamorphism are recorded in the rocks of the Lepontine Alps resulting from different phases of orogeny: In Eocene times, the subducted Penninic nappes underwent high pressure metamorphism up to eclogite facies (Von Blanckenburg and Davies, 1995; Engi et al., 2004, and references therein). Subsequently, regional metamorphism associated with nappe stacking and crustal thickening, overprinted most of these high pressure metamorphites and led to the prominent metamorphic mineral zones of the Lepontine Dome (Niggli, 1960; Frey and Ferreiro Mählmann, 1999; Engi et al., 2004). Classic Barrow zones from greenschist to amphibolite facies can be found, with temperatures rising locally even up to 800 °C (Bousquet et al., 2008; Frey et al., 1980). In the south, peak temperatures were already reached during the mid-Oligocene, while the northern Lepontine Dome experienced peak temperatures not before early Miocene (Engi et al., 2004; Janots et al., 2009; Wiederkehr et al., 2009).

Metamorphic isograde crosscut the nappe boundaries, but are cut off by the Insubric Line and the Simplon Fault Zone (Engi et al., 1995, 2004; Todd and Engi, 1997). This implies that heating outlasted nappe stacking in the Lepontine Dome and predates later tectonic processes (Trommsdorf, 1966; Frey and Ferreiro Mählmann, 1999, and references therein). However, the interpretation of metamorphic isograde and the chronology of nappe emplacement, backfolding and regional metamorphism are questioned by several studies (Milnes, 1975; Steck and Hunziker, 1994), such that mineral zone boundaries are not interpreted as metamorphic isograde in the strict sense (Engi et al., 2004).

2.2.2. Structural doming of the Lepontine Dome

In response to the anticlockwise rotation of the Adriatic indenter, extensional faulting and doming migrated from east to west (Merle et al., 1989; Steck and Hunziker, 1994 and references therein; Schlunegger and Willett, 1999). Extension along normal faults – especially the Simplon fault – led to tectonic unroofing of the formerly subducted nappe stack of the Penninic units. Updoming commenced contemporaneously with the Bergell intrusion at ~32–30 Ma (Steck and

Hunziker, 1994) resulting in a first culmination north of Biasca (Ticino subdome, ~25–20 Ma) and a second further to the west in the area south–east of Baceno (Toce or Simplon subdome, ~20–10 Ma. Merle et al., 1989; Steck and Hunziker, 1994; Fig. 18). Thus, tectonic unroofing formed two anticlines in east–west orientation, separated by the Maggia steepzone in the centre (e.g. Preiswerk, 1918; Merle et al., 1989). The formerly deeply buried Verampio and Leventina nappes form the cores of the Toce subdome in the east and the Ticino subdome in the west (Figs. 18, 19A).

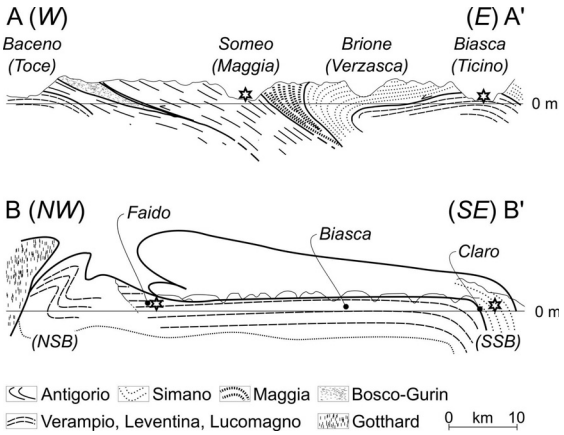

Fig. 19.: Cross sections of the central Lepontine Dome from west to east (AA') and northwest to southeast (BB') (after Merle et al., 1989; Rütti et al., 2008). Section lines in Fig. 18. Stars indicate the location of the Maggia and Ticino profiles (AA') and the terminations of the Ticino profile (BB').

The southern and northern boundary of the dome is formed by two steep belts (Milnes, 1974; Schmid et al., 1989; Berger et al., 2011; Fig. 18). Backfolding of the nappe stack from Oligocene to early Miocene times led to steeply southdipping foliations and the formation of the southern steep belt (Milnes, 1974; Hurford, 1986; Berger et al., 2011). The northern steep belt is also the result of backfolding. However, backfolding in the north occurred later (after 18 Ma) and formed synclinal folds with northdipping foliations (Maxelon and Mancktelow, 2005; Wiederkehr et al., 2008). Maxelon and Mancktelow (2005) suggested that a late deformation phase in the northern steep belt is related to the exhumation of the Aar-/Gotthard massif and can thus be dated by AFT ages from these massifs (see Schaer et al., 1975; Soom, 1990; Michalski and Soom, 1990; Hunziker et al., 1997; Rahn and Seward, 2000a; Glotzbach et al., 2009, 2010). If this assumption is true, then deformation of the northern steep belt continued until latest Miocene times.

In between these two steep belts, the nappes of the central Lepontine Dome are situated, forming comparably flat lying anticlines (Maxelon and Mancktelow, 2005; Rütti et al., 2005, 2008; Figs. 18, 19B). However, the outline of the Ticino subdome, defined by the basement-cover contact of the Simano nappe, shows a concentric dome with its highest point north of Biasca (Pfiffner et al., 1990).

3. Methodology

3.1. Analytical methods

For investigating the latest stage cooling history of the Lepontine Dome, we applied fission track and (U–Th–Sm)/He analyses on apatites.

AFT analysis is based on the accumulation of lattice defects within the apatite crystal caused by the spontaneous fission of ^{238}U. At high temperatures (> 110 °C) the crystal lattice anneals completely, whereas fission tracks are almost completely retained below 60 °C (Gleadow and Duddy, 1981; Gallagher et al., 1998). Between ~110 and 60 °C, tracks anneal partially. Fission track shortening depends on the residence time in the partial annealing zone (PAZ). Thus, the track length distribution reflects the thermal history of a sample.

AHe analysis is based on the production of ^{4}He particles, associated with the decay of ^{238}U, ^{235}U, ^{232}Th (Zeitler et al., 1987; Lippolt et al., 1994; Wolf et al., 1996) and ^{147}Sm (Grist and Zentilli, 2005). At temperatures above ~85 °C, ^{4}He is lost from the grain by diffusion. Between 85 °C and 40 °C, ^{4}He is partly retained in the crystal, while below 40 °C, ^{4}He loss by diffusion is mostly negligible (Wolf et al., 1998). Raw AHe ages have to be corrected to account for ^{4}He loss by α-ejection, associated with parent isotopes located close to the grain's rim (Farley et al., 1996; Farley, 2002). Analytical details (AFT and AHe analyses) are described in the Appendix I.

3.2. Thermal history modelling

Inverse thermal history modelling with the HeFTy programme v. 1.7.5 (Ketcham, 2005) was carried out for finding thermal histories that are in accordance with the observed thermochronologic data. The number of spontaneous and induced tracks for each counted grain, the track length (TL) distribution of a sample and the corresponding Dpar values were used as input parameters for the AFT system. The annealing model of Ketcham et al. (2007a) and c-axis projection (Ketcham et al., 2007b) were chosen.

AHe ages were integrated into thermal history modelling, using the uncorrected mean AHe age and the mean sphere radius of the grains (in most cases multigrain aliquots were used, see analytical details in the Appendix A). He diffusion was computed with the radiation damage accumulation and annealing model of Flowers et al. (2009).

In addition, zircon fission track (ZFT) data from Hurford (1986) were used as time–temperature constraints for the Maggia horizontal profile, assuming a ZFT closure temperature of 240±20 °C (Hurford, 1986; Brandon et al., 1998).

To evaluate the simulated time–temperature paths statistically, a goodness of fit (GOF) test is carried out by HeFTy, validating the consistency between the simulation results and both the measured age (after Ketcham, 2005) and the observed TL distribution (after Kuiper, 1960). Time–temperature paths with a GOF value less than 0.05 are discarded. GOF values between 0.05 and 0.5 are interpreted as "acceptable", while time–temperature paths with a GOF value > 0.5 are classified as "good paths".

3.3. Sampling design

To avoid the influence of sample elevation on the cooling ages, samples were taken along two horizontal profiles (500 m ± 200 m a.s.l) on the valley bottoms of the Ticino river and the Maggia river (Fig. 18, Tab. 5). The Ticino horizontal profile exactly crosscuts the culmination of the Ticino subdome from north to south and comprises twelve samples distributed over 37 km length. Ten samples at ~3.5 km intervals were taken from outcrops along the Maggia river, following the transition zone between the Ticino and the Toce subdomes for 34 km. The Maggia profile starts in the Ivrea zone, south of the Insubric Line, i.e. it crosses the boundary between the Southern Alps (Adriatic margin) and the Central Alps (Penninic units). The east–west distance between both profiles is about 20 km.

Tab. 5.: Sample locations (coordinates refer to the Swiss Grid CH1903).

Sample	Geotectonic unit	x [m]	y [m]	Elevation [m]
Ticino-H1	Leventina	704,220	148,157	710
Ticino-H4	Leventina	707,811	144,514	730
Ticino-H6	Leventina	709,757	141,561	490
Ticino-H9	Leventina	711,072	138,663	377
Ticino-H11	Leventina	713,242	136,698	370
Ticino-H18	Leventina	717,082	136,257	318
Ticino-H13	Leventina	716,576	134,288	402
Ticino-H22	Leventina	719,424	130,319	311
Ticino-H23	Leventina	720,932	126,737	326
Ticino-H27	Simano	721,777	121,573	300
Ticino-H28	Mergoscia	722,695	119,680	377
Ticino-H25	Bellinzona	724,259	118,848	475
Maggia-H-1	Maggia	692,794	134,861	622
Maggia-H-3	Antigorio	690,436	133,569	470
Maggia-H-5	Antigorio	690,068	131,584	481
Maggia-H-6	Antigorio	689,637	129,095	433
Maggia-H-10	Antigorio	693,410	127,319	390
Maggia-H-14	Maggia	698,390	121,690	307
Maggia-H-15	Antigorio	699,920	119,454	551
Maggia-H-27	Antigorio	701,651	116,311	288
Maggia-H-25	Monte Rosa	699,651	114,766	250
Maggia-H-22	Ivrea	699,460	110,737	246

4. Results and interpretation

4.1. Apatite fission track analyses

The 22 samples from the horizontal profiles show AFT ages from 5 to 19 Ma (Tab. 6). AFT ages of the Ticino profile range from 7 to 19 Ma with youngest cooling ages in the centre of the dome and oldest ages towards the terminations of the profile (Fig. 20A). Along the Maggia profile, AFT ages range from 5 to 13 Ma (Tab. 6, Fig. 20B) and show a complex exhumation pattern, probably related to the nappe boundaries. Comparing AFT ages of adjacent nappes along both profiles generally reveals a trend towards younger ages in the structurally lower nappe. Nappe boundaries in the southern steep belt (SSB; for location see Fig. 18) are broadly east–west oriented, and cooling ages decrease from the south towards the central dome. Following the Maggia river the Maggia profile cuts the boundary between the structurally lower Antigorio nappe and the higher Maggia nappe three times, which results in a patchy AFT pattern along the profile. Note that the boundary between the Maggia nappe and the Antigorio nappe is broadly north–south oriented. Thus, age jumps across this nappe boundary have to be interpreted differently from age jumps across nappe boundaries in the SSB, due to their perpendicular orientation.

Tab. 6.: Results of AFT analysis[a].

Sample	No. of grains	ρ_s	N_s	ρ_i	N_i	ρ_d	N_d	P(x^2) [%]	Central age [Ma]	$\pm 1\sigma$	Dpar [μm]	N_{TL}	MTL [μm]	St.dev	MpTL [μm]	St.dev	U [ppm]
Ticino-H1	21	0.80	58	16.72	1217	16.53	26077	60.4	13.1	1.8	2.26	14	13.18	2.15	14.30	1.33	11.31
Ticino-H4	8	1.07	25	22.36	521	16.81	25196	63.0	13.4	2.8	2.22	4	12.93	2.76	14.11	1.81	15.40
Ticino-H6	20	0.54	40	19.78	1466	16.78	25196	77.8	7.6	1.2	2.14	43	12.99	1.83	14.10	1.26	14.20
Ticino-H9	10	0.23	8	6.70	233	17.53	26314	53.7	10.0	3.6	2.15	3	13.02	2.34	14.11	1.66	4.29
Ticino-H11	9	1.14	23	62.77	1263	24.82	37324	23.3	7.5	1.6	2.38	16	13.22	1.30	14.23	0.92	30.82
Ticino-H18	20	0.67	44	29.88	1971	24.95	37324	26.1	9.2	1.6	2.27	28	13.18	1.67	14.12	1.23	14.95
Ticino-H13	20	0.62	44	36.99	2636	24.87	37324	90.7	6.9	1.1	2.35	1	11.10	-	12.53	-	17.88
Ticino-H22	9	1.28	19	54.57	809	25.00	37324	93.3	9.8	2.3	2.30	18	13.29	1.55	14.26	1.09	22.98
Ticino-H23	20	2.02	133	102.66	6756	25.08	37324	47.7	8.2	0.8	2.26	102	13.17	1.61	14.19	1.17	49.05
Ticino-H27	27	1.54	108	41.65	2924	24.80	36872	86.1	15.2	1.5	2.15	42	14.03	1.22	14.83	0.88	21.60
Ticino-H28	24	0.81	58	19.79	1410	24.88	36872	60.4	17.0	2.3	2.24	40	14.00	1.42	14.80	0.97	9.58
Ticino-H25	20	0.54	26	11.87	571	25.04	37324	99.5	18.9	3.8	2.45	60	14.31	1.31	15.06	0.93	5.93
Maggia-H-1	13	0.65	41	23.81	1509	24.01	36507	2.9	11.7	2.4	2.19	20	14.02	0.95	14.77	0.70	13.75
Maggia-H-3	11	0.46	14	27.45	839	16.86	26077	29.6	4.8	1.4	2.09	-	-	-	-	-	24.10
Maggia-H-5	3	0.43	6	24.79	345	16.80	26077	19.0	5.0	2.2	2.23	1	16.14	-	16.42	-	27.97
Maggia-H-6	11	1.67	67	70.61	2831	16.73	26077	30.5	6.4	1.0	2.15	19	13.73	1.28	14.56	0.94	51.05
Maggia-H-10	5	0.94	5	29.84	158	23.95	36507	27.3	12.6	5.7	2.27	5	13.14	1.08	14.08	0.77	14.89
Maggia-H-14	16	0.66	35	20.13	1066	16.66	26077	72.6	9.1	1.6	2.08	-	-	-	-	-	13.53
Maggia-H-15	21	0.58	54	30.02	2793	23.70	36507	90.1	7.6	1.1	2.24	7	12.68	0.92	13.79	0.73	18.85
Maggia-H-27	19	0.88	40	45.74	2083	23.82	36507	61.5	7.6	1.2	2.47	63	14.18	1.07	14.90	0.78	21.43
Maggia-H-25	26	1.09	70	34.60	2214	16.59	26077	91.8	8.7	1.1	2.11	31	13.83	1.46	14.74	1.00	22.45
Maggia-H-22	24	1.58	258	49.29	8068	23.76	36507	79.6	12.6	0.9	2.79	91	13.75	1.42	14.57	1.04	23.64

[a]No. of grains - number of counted grains. $\rho_s/\rho_i/\rho_n$ - track densities [10^5 tracks cm^{-2}] (spontaneous/induced/on dosimeter). $N_s/N_i/N_d$ - number of counted tracks (spontaneous/induced/on dosimeter). P(x^2) - probability of obtaining the chi-square value (x^2) for n degree of freedom (with n = {No. of grains} - 1). σ - standard error of AFT central age (Galbraith and Laslett, 1993). Dpar - averaged diameter of etch figures from analysed grains. N_{TL} - number of track length measurements. MTL - mean track length. St.dev - standard deviation. MpTL - mean projected track length. U - uranium concentration.

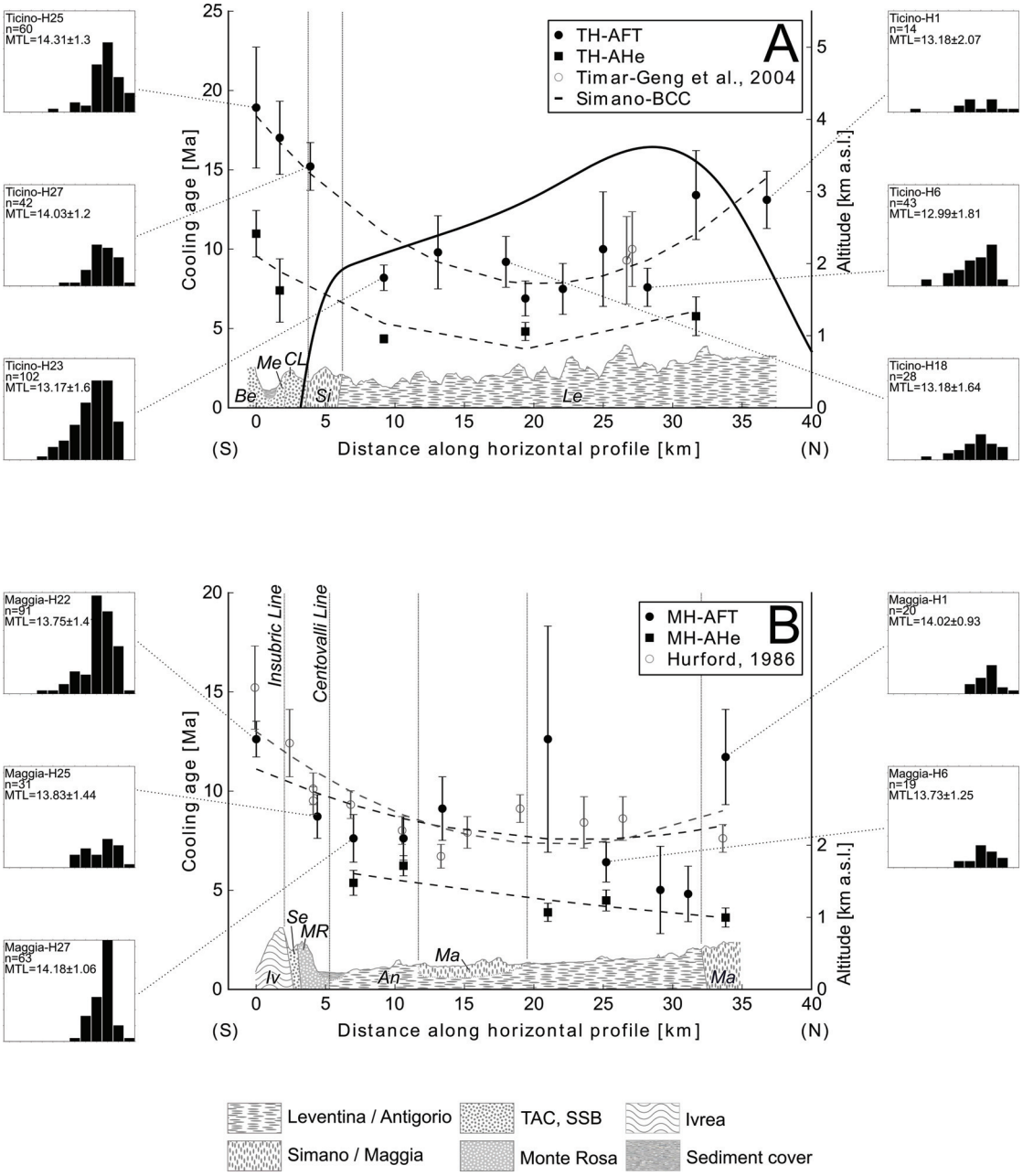

Fig. 20.: Cooling ages and 1 σ-error along Ticino (A) and Maggia (B) horizontal profiles (500 m $\pm$ 200 m). Track length distributions are shown for samples with sufficient number of track lengths for thermal history modelling (Fig. 21). Dashed lines represent a 2^{nd} order trendline to the data. BCC: Basement-Cover-Contact (Pfiffner et al., 1990). Additionally, cross sections along the profiles (i.e. not along the adjacent ridges, because in some cases this would result in the wrong nappe allocation) are drawn. Dipping angles after Pfiffner et al., 1990, Berger et al., 2005 and Maxelon and Mancktelow, 2005. An: Antigorio, Be: Bellinzona, CL: Cima Lunga, Iv: Ivrea, Le: Leventina, Ma: Maggia, Me: Mergoscia, MR: Monte Rosa, Se: Sesia, Si: Simano, SSB: Southern Steep Belt, TAC: Tectonic Accretion Channel.

Early AFT studies using the population method did not detect a north to south oriented U-shaped pattern with youngest ages in the centre of the dome (Wagner et al., 1977; Hurford, 1986). However, the new data, based on the external detector method, is supposed to be more accurate

and is, furthermore, in good agreement with recently published AFT data of the Leventina nappe (Timar-Geng et al., 2004, Fig. 20A).

Dpar values vary between 2.08 and 2.79 μm, showing an indistinct correlation with the AFT ages of the Maggia profile (R^2 = 0.22). Uranium contents vary between 4 and 51 ppm and correlate indistinctly negative with the AFT ages (R^2 = 0.22 for the Ticino profile and R^2 = 0.24 for the Maggia profile). Both, relatively low Uranium contents (most of the samples contain 10 to 30 ppm Uranium) and young cooling ages, made it difficult to measure sufficient numbers of horizontal confined tracks for statistically sound thermal history modelling. For eight samples 40 or more TL could be measured. Mean TL of samples from the Maggia valley range from 13.75 μm to 14.18 μm (considering only mean TL with N_{TL} > 20 and referring to non-projected length data). Samples from the Ticino profile show slightly shorter mean TL than those from the Maggia profile, ranging from 12.99 μm to 14.31 μm (again considering only samples with more than 20 TL measurements).

4.2. Apatite (U–Th–Sm)/He analyses

AHe analyses were successfully applied to 23 aliquots from ten samples along the horizontal profiles (Tab. 7). To enhance the amount of ^{4}He, for all but one sample multigrain aliquots had to be prepared (see also Appendix A). Still, in several cases, even multigrain aliquots yielded no ^{4}He gas levels above background. These aliquots were excluded from further analysis (not listed in Tab. 7). Furthermore, we did not take AHe ages into account if they were older than the corresponding AFT age within error limits (italic in Tab. 7). We trust the AFT ages more because we made use of multigrain aliquots and most of the excluded AHe ages were unrealistically old (occasionally Cretaceous in age and older). Successful AHe analyses yielded ages between 4 and 11 Ma (Tab. 7, Fig. 20), showing the following trends across the central Lepontine Dome: AHe ages along both horizontal profiles decrease from the southern terminations towards the central dome (from 4 to 11 Ma along the Ticino profile and from 4 to 6 Ma along the Maggia profile). The northernmost sample of the Ticino profile again yields an older age compared to the central samples, thus resembling the AFT age pattern also in the northern part of the dome. Uranium, Thorium and Samarium contents scatter largely (Tab. 7). AHe ages correlate neither with grain size nor with effective Uranium content (effective Uranium (eU) computed as $eU = [U] + 0.235 \cdot [Th] + 0.0053 \cdot [Sm]$).

Tab. 7.: Results of AHe analysis[b]. Aliquots, which yielded AHe ages older than the respective AFT age are in italic and were excluded from further interpretation. Bold digits refer to the sample age and the associated error (i.e. the central age and standard deviation in case of more than one successful analysis).

Sample	N_g	Raw age	Error	F_T	Cor. age	Error	C. age	1σ	ø r	Mass	U	Th	Sm	He
		$[Ma]$	$[Ma]$		$[Ma]$	$[Ma]$	$[Ma]$	$[Ma]$	$[\mu m]$	$[\mu g]$	$[ppm]$	$[ppm]$	$[ppm]$	$[ncc]$
Ticino-H1	*3*	*12.96*	*0.80*	*0.76*	*17.13*	*2.02*			*59.55*	*13.85*	*6.43*	*2.46*	*22.40*	*0.16*
	3	2.90	0.18	0.73	3.97	0.47			54.51	10.23	6.41	1.88	14.94	0.03
Ticino-H4	3	6.17	0.38	0.76	8.08	0.95	**5.78**	**1.22**	58.80	13.09	7.01	4.15	25.39	0.08
	3	4.29	0.27	0.76	5.65	0.66			57.78	9.09	7.80	3.93	22.74	0.04
Ticino-H13	3	3.66	0.23	0.76	**4.82**	**0.57**			57.55	11.40	11.43	1.41	17.65	0.06
Ticino-H22	*3*	*17.08*	*1.06*	*0.65*	*26.49*	*3.12*			*40.19*	*4.51*	*1.28*	*1.34*	*1.18*	*0.02*
	3	2.62	0.16	0.66	3.98	0.47			40.29	47.42	25.08	2.11	25.08	0.06
Ticino-H23	3	3.26	0.20	0.73	4.44	0.52	**4.36**	**0.26**	49.97	39.98	20.38	0.84	20.38	0.13
	1	3.41	0.21	0.74	4.60	0.54			51.05	2.16	45.38	2.09	43.27	0.04
	3	*6.76*	*0.42*	*0.73*	*9.26*	*1.09*			*49.60*	*46.27*	*44.77*	*3.93*	*44.77*	*0.33*
	1	*146.14*	*9.06*	*0.67*	*216.50*	*25.48*			*46.40*	*2.14*	*0.20*	*1.38*	*0.12*	*0.02*
	1	*127.07*	*7.88*	*0.66*	*191.20*	*22.50*			*42.30*	*1.80*	*54.34*	*2.50*	*51.82*	*0.02*
	1	*19.47*	*1.21*	*0.73*	*26.53*	*3.12*			*61.45*	*0.95*	*59.52*	*7.60*	*73.13*	*0.14*
	1	*132.16*	*8.19*	*0.74*	*178.25*	*20.97*			*60.70*	*5.16*	*0.03*	*1.04*	*0.03*	*0.02*
Ticino-H28	3	4.18	0.26	0.75	5.59	0.66	**7.4**	**1.99**	55.62	13.38	7.13	1.77	17.81	0.05
	3	7.17	0.44	0.76	9.50	1.12			56.50	0.02	6.46	1.39	13.84	0.10
	3	9.42	0.58	0.67	14.00	1.65			40.03	4.58	3.81	2.46	2.65	0.02
Ticino-H25	3	6.39	0.40	0.66	9.64	1.13	**10.97**	**1.46**	41.13	3.61	12.69	5.24	6.21	0.04
	3	6.91	0.43	0.72	9.57	1.13			53.77	7.30	17.15	5.08	4.96	0.11
	3	*12.87*	*0.80*	*0.69*	*19.84*	*2.33*			*38.47*	*4.53*	*4.88*	*5.03*	*3.76*	*0.04*
	2	*23.69*	*1.47*	*0.71*	*33.54*	*3.95*			*46.40*	*4.13*	*5.39*	*3.52*	*3.30*	*0.07*
	3	*20.73*	*1.28*	*0.71*	*29.04*	*3.42*			*48.54*	*8.97*	*0.96*	*0.62*	*0.76*	*0.03*
	1	*218.98*	*13.58*	*0.77*	*285.63*	*33.61*			*65.40*	*5.72*	*0.12*	*0.88*	*0.04*	*0.05*
	3	2.29	0.14	0.76	2.99	0.35			54.89	15.84	10.57	1.64	3.93	0.05
Maggia-H1	3	3.60	0.22	0.79	4.57	0.54	**3.61**	**0.48**	59.52	16.81	11.77	3.36	4.64	0.09
	2	2.60	0.16	0.82	3.16	0.37			74.22	19.26	6.17	1.08	2.21	0.04
	3	*82.96*	*5.14*	*0.78*	*106.90*	*12.57*			*48.41*	*14.45*	*0.21*	*0.31*	*0.09*	*0.04*
Maggia-H5	*1*	*118.95*	*7.37*	*0.66*	*179.80*	*21.16*			*41.47*	*2.29*	*0.43*	*4.65*	*1.21*	*0.05*
Maggia-H6	4	3.38	0.21	0.76	**4.47**	**0.53**			45.06	14.82	5.85	3.92	0.72	0.04
Maggia-H10	3	3.00	0.19	0.78	**3.87**	**0.46**			52.20	15.17	18.81	9.81	9.81	1.73
	3	4.84	0.30	0.79	6.11	0.72			60.85	21.01	7.48	4.12	1.18	0.10
	6	3.83	0.24	0.71	5.41	0.64			46.35	14.51	3.29	1.79	0.57	0.03
Maggia-H15	3	4.50	0.28	0.68	6.59	0.78	**6.22**	**0.51**	43.46	7.39	11.53	5.93	1.32	0.05
	3	4.04	0.25	0.77	5.22	0.61			60.13	19.27	3.05	1.01	0.71	0.03
	3	5.91	0.37	0.74	7.99	0.94			51.65	7.98	4.13	3.26	1.25	0.03
Maggia-H27	3	3.83	0.24	0.71	**5.36**	**0.63**			52.22	8.23	13.54	2.28	15.53	0.05
	2	*10.58*	*0.66*	*0.76*	*13.86*	*1.63*			*58.68*	*7.96*	*4.75*	*1.05*	*2.24*	*0.05*
	3	*14.90*	*0.92*	*0.73*	*20.36*	*2.40*			*49.55*	*9.80*	*5.76*	*0.71*	*9.93*	*0.11*
	3	*21.91*	*1.36*	*0.78*	*28.00*	*3.29*			*66.32*	*19.57*	*3.10*	*0.41*	*3.15*	*0.17*

[b] N_g - number of grains per aliquot. Error - total analytical error. F_T - weighted factor for α-ejection correction. Cor. age - corrected age. C. age - Central age after (Vermeesch, 2008). 1σ - error of central age. ør - average radius . U/Th/Sm - concentrations of U ($^{235}U + {}^{238}U$)/^{232}Th/^{147}Sm. He - volume [nano-cm^3] of ^4He.

4.3. Thermal history modelling

Five samples from the Maggia profile (MH-1, MH-6, MH-22, MH-25 and MH-27) and seven from the Ticino profile (TH-1, TH-6, TH-18, TH-23, TH-25, TH-27 and TH-28) were used as a basis for thermal history modelling. AHe ages were included into the models for three samples from both, the Maggia and the Ticino profiles (MH-1, MH-6, MH-27 and TH-23, TH-25, TH-28). Most of these samples contained less than the 100 TL, which is the number of measurements usually recommended for TL analysis. However, since the TL are narrowly distributed and indicate a simple cooling history, we still consider the modelling results as meaningful (cf. Rahn and Seward, 2000b). Nevertheless, the statistical limitations, particularly for samples TH-1, MH-1 and MH-6 should be kept in mind.

4.3.1. Ticino profile

Thermal history modelling yielded differing time–temperature patterns along the Ticino profile for Miocene cooling (Fig. 21A). The three southernmost samples (TH-25, TH-28, TH-27; from south to north, belonging to the Bellinzona, Mergoscia and Simano nappe, respectively) show episodic cooling with fast cooling during the early and middle Miocene, and slow cooling throughout the late Miocene. Cooling was earlier in the southernmost Bellinzona and Mergoscia nappes (TH-25 and TH-28 entering the PAZ at 21–13 Ma and 19–14 Ma, respectively) and propagates northwards little later (TH-27 entering the PAZ at 17–13 Ma). Age jumps across the nappe boundaries at the southern termination of the Ticino profile (Fig. 20), therefore, suggest early to middle Miocene vertical movements along these tectonic structures.

In contrast, steady cooling during the middle and late Miocene is derived from the samples of the central dome (TH-23, TH-18, TH-6; from south to north, all belonging to the Leventina nappe). Entering the PAZ later than the adjacent southern samples (9–8 Ma, 12–7 Ma, 9–6 Ma, respectively), these samples cool moderately fast through the PAZ and further on.

Finally, for the northernmost samples (TH-1 and TH-4, both belonging to the Leventina nappe), and thus, for the northern Lepontine Dome, a third modus of cooling was obtained. Entering the PAZ between ~20 Ma and 11 Ma or even earlier (Fig. 20A, 22A — for TH-4 only forward modelling was applied), the samples slowly cool until Pliocene times. From Plio-Pleistocene times on, cooling rates increase again.

The Leventina nappe is one of the structurally lowest nappes of the Lepontine Alps (Kündig, 1936; Berger et al., 2005, and references therein). All but the three southernmost samples belong to this tectonic unit. Therefore, the differential cooling histories along the central and northern part of the Ticino profile cannot be explained by movements along nappe boundaries.

From the Miocene–Pliocene boundary on, all good fit models along the Ticino profile reveal a uniform cooling history, although the range of time–temperature paths in agreement with the observed data is relatively broad. For reasons of clarity, weighted mean paths are shown instead of inversions (Fig. 22A). Though small deviations from these paths are still in agreement with the observed data, these paths depict the general cooling style derived from the inversions such as early episodic cooling in the south, monotonous cooling in the centre and early, but slow

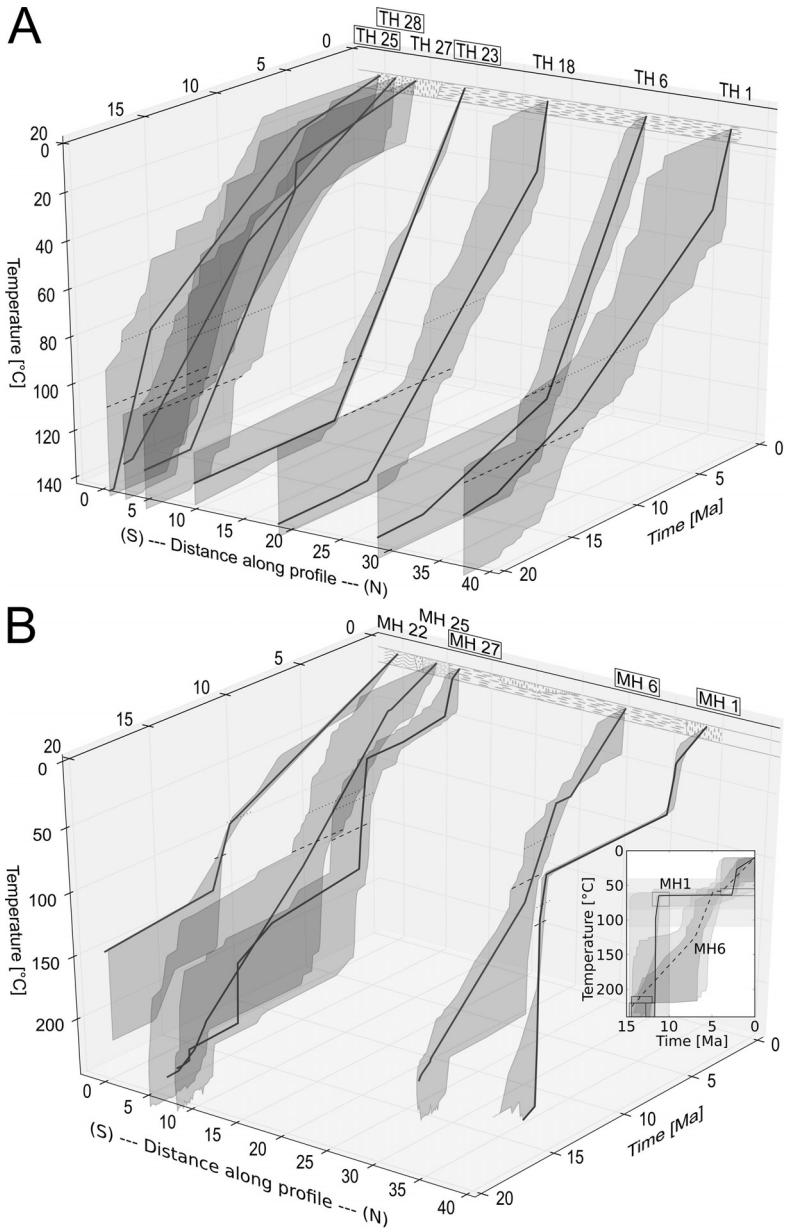

Fig. 21.: Cooling histories from inverse thermal modelling for the Ticino (A) and Maggia (B) horizontal profiles. Shown are best-fit models (lines) and ranges of statistically "good"-fitting models (envelopes). Models which include AHe ages are framed. Dashed lines point to crossing of the 110 °C isotherm, and dotted lines to crossing of the 85 °C isotherm for the best-fitting model path. Simplified cross sections are drawn at top rear parts of both plots (legend cf. Fig. 20). Inset in (B): Time–temperature paths of samples MH-1 and MH-6 (solid and dashed lines for best-fit models; envelopes comprise statistically "good" and "acceptable" paths), showing the movements along the nappe boundary of the Maggia and Antigorio nappes (see Appendix A for all time–temperature models).

cooling in the north. Furthermore, the relative similarity in cooling patterns between the central and northern samples is also implied by forward modelling of samples, which do not contain a sufficient number of TL for inversions (dashed inner lines in Fig. 22A).

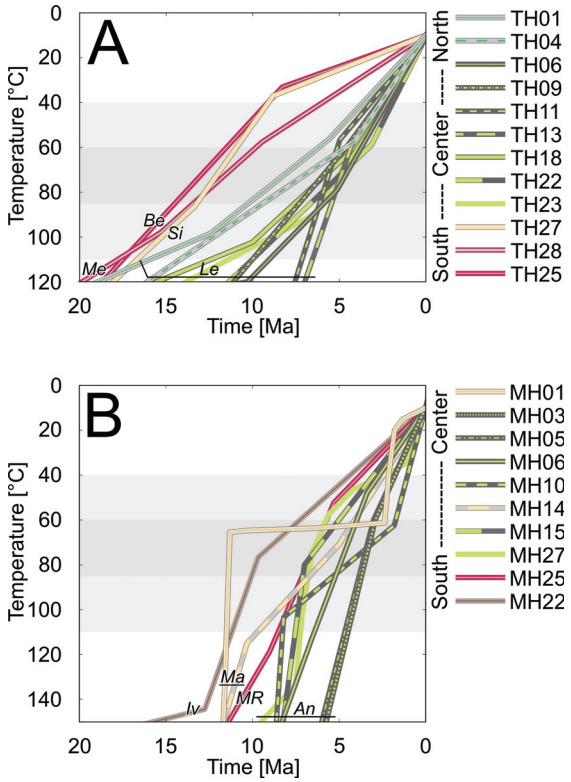

Fig. 22.: Cooling histories for the Ticino (A) and Maggia (B) horizontal profiles. Weighted mean paths from inverse thermal history modelling (straight lines) and forward models (dashed lines) are shown. Forward models are used for samples without a sufficient number of track lengths for statistically sound inverse thermal history modelling. Red lines: TAC, SSB; fawn lines: Simano/Maggia; green lines: Leventina/Antigorio; brown line: Ivrea; Abbreviations cf. Fig. 20.

4.3.2. Maggia profile

Analogous to the Ticino profile, inverse thermal history modelling suggests episodic cooling for the southernmost Maggia profile (samples MH-22 and MH-27; the southernmost and third sample from the south, belonging to the Ivrea unit and the Antigorio nappe, respectively; Fig. 21B). The best fit model of MH-25 (second sample from the south, belonging to the Monte Rosa nappe), however, shows steady cooling since early Miocene times. The best fit models of these three samples, thus, give indications that the southern part of the Maggia profile experienced small-scale differential cooling. Nevertheless, all three samples cool rapidly through the PAZ from 12.5–12 Ma, 10–6.5 Ma and 9–6.5 Ma on, respectively, slowing down after leaving the PAZ.

By contrast, the sample MH-6 from the central part of the Lepontine Dome cools rather continuously throughout the Miocene. The PAZ is entered at 8–6 Ma during a period of rapid cooling, which lasts until the Pliocene, when cooling rates slightly slow down. MH-6 belongs to the Antigorio nappe and therefore represents the lowest structural level outcropping along the Maggia profile. Maxelon and Mancktelow (2005) suggested to assign the Antigorio units not only to the same structural level, but also to the same nappe as the Leventina units.

Note that, due to high elevations in the northern Maggia valley, the Maggia horizontal profile only reaches to the centre of the dome, while the Ticino profile extends to the northern part of the dome. Therefore, the Maggia profile can only be compared to the southern portion of the Ticino profile. With this in mind, and only taking into account the samples from the SSB and the (directly comparable) Antigorio–Leventina nappe, both profiles show a similar cooling age pattern, with youngest ages in the centre of the Lepontine Dome. This implies that the underlying exhumation history leading to the cooling age distribution was not locally restricted but affected larger areas of the Lepontine Dome.

The modelled time–temperature history of the Maggia nappe sample MH-1, though located right next to the sample MH-6 (but belonging to the Maggia nappe), differs significantly from the rest. It reveals a pronounced episodic cooling even more distinct than the southern samples of the Maggia profile. The AFT age of 12 Ma, along with only slightly shortened TL and an AHe age of 4 Ma allows only for a narrow range of time–temperature histories in agreement with the observed data. For this sample, very rapid cooling to ~65 °C between 11.5 and 11 Ma is followed by very slow cooling until 3 Ma.

The differences between the AFT cooling ages of the Antigorio nappe and the Maggia nappe, indicate significant vertical movements along the Antigorio–Maggia boundary prior to 5 Ma. The inferred exhumation history from inverse thermal history modelling suggests rapid overthrusting associated with rapid cooling of the Maggia nappe before 11 Ma (inset in Fig. 21B). Subsequently, the Maggia nappe is displaced again by normal faulting along the Antigorio nappe, as suggested by higher cooling rates of the Antigorio nappe compared to the Maggia nappe. Both samples have cooled down to 65 °C at 5 Ma and have thus reached a similar crustal level. From this time on, both nappes are juxtaposed and show a similar cooling behaviour, so that no further movements along the nappe boundaries are inferred, at least within the sensitivity limits of the applied thermochronometers.

Furthermore, inverse thermal history modelling indicates uniform cooling from Plio-Pleistocene times on also along the rest of the Maggia profile. Prior to this phase, three samples that do not belong to the Antigorio nappe (MH-1, MH-22, MH-27; Fig. 22B), experienced an additional cooling impulse.

4.3.3. First résumé

Miocene cooling varies within and between the two horizontal profiles across the central Lepontine Dome, despite short distance to each other. Three different cooling patterns in the Ticino profile, and thus across the Ticino subdome, are identified (very fast and episodic, fast and steady, slow and steady). The present day rocks of the SSB along the Ticino profile were already cooled down to the low-temperature part of the PAZ in mid-Miocene times, while the structurally lower Antigorio–Leventina nappe was still buried more deeply.

Cooling along the Maggia profile occurs later than along the Ticino profile. Furthermore, the time–temperature history of the Maggia profile is dominated by an episodic cooling style.

Except for the samples of the Maggia nappe, cooling impulses successively attenuate towards the central Lepontine Dome, until reaching nearly steady conditions.

Differences between cooling ages of adjacent nappes can at least partly be related to movements along the nappe boundaries. The observed and modelled data indicate a complex interrelationship for the Antigorio and Maggia nappes.

The Plio-Pleistocene time–temperature history is characterised by moderately fast cooling of all samples (~11 °C Ma^{-1} on average). While cooling rates along the weighted mean and forward modelled time–temperature paths vary significantly before the Plio-Pleistocene boundary, they are more uniform afterwards and range between 3 °C Ma^{-1} to 17 °C Ma^{-1} (Fig. 22). Thus, differences in timing and rates along and between the two profiles are minor compared to the complex Miocene cooling pattern.

Despite numerous attempts, no common Miocene evolution for both profiles and for the different parts of the profiles could be extracted from the thermochronological data by inverse thermal history modelling, thus reinforcing the spatial and temporal variability in Miocene cooling across the central Lepontine Dome. Furthermore, distinct successions of cooling patterns can be inferred: Cooling (I) successively affects the south, the north and the centre of the Lepontine Dome and (II) migrates from east to west.

5. Discussion

Samples from the horizontal profiles cover the SSB, the central Lepontine Dome and border the northern steep belt (NSB; Figs. 18, 19B). One sample is taken from south of the Insubric Line. The evolution of these structural elements seems to be the key for understanding the differences of the cooling patterns across the Lepontine Dome.

5.1. Neogene exhumation of the southern steep belt

All but one of the samples from the southern terminations of the profiles located within or south of the SSB show episodic cooling behaviour. The change from the cooling patterns of the SSB (red and fawn paths in Fig. 22A) to the central Ticino profile (greenish paths in Fig. 22A) suggests a direct link between cooling history and tectonic structures. This is also indicated by the jumps of AFT cooling ages across the nappe boundaries (Fig. 20). The SSB resulted from backthrusting and back-folding processes along the Insubric Line (Milnes, 1974; Hurford, 1986; Steck and Hunziker, 1994). The Bellinzona and Mergoscia nappes experienced rapid cooling at least since ~17.5 Ma lasting until ~8–9 Ma (Fig. 22A), which we interpret as indicating active backthrusting for these nappes. The Simano nappe, situated further to the north, also experienced rapid cooling until ~9 Ma. But as the Simano nappe was still at ~60 °C at that time, the two samples further south already cooled down to 40 °C. The subsequent cooling of the Simano nappe (slower than before, but still faster than the samples of the southernmost nappes) suggests a northward migration of backthrusting. Further to the west, along the Maggia profile, backthrusting along the SSB started later, between ~13 Ma to 10 Ma (Fig. 22B). This is in line with the overall east–west exhumation trend across the Lepontine Dome. Afterwards, rapid cooling migrated to the north, affecting the southernmost Antigorio nappe until ~7 Ma.

Backthrusting along the Insubric Line started in late Eocene to Oligocene times (Schmid et al., 1996; Maxelon and Mancktelow, 2005) resulting in the formation of the SSB. Maxelon and Mancktelow (2005) proposed this phase to be completed at ~25 Ma, while Schmid et al. (1996) assumed continued activity until 19 Ma. Hurford (1986) suggested major backthrusting of Central Lepontine units over the Southern Alps between 23 Ma and 16 Ma. Rapid cooling until 19 Ma in the SSB reported by (Hurford, 1986) was associated with thermal relaxation after a heating pulse resulted by the emplacement of the hot and formerly deeply subducted Adula and Cima Lunga units (Engi et al., 1995).

The assumptions of Hurford (1986) and Engi et al. (1995) are roughly in agreement with our new data, although our data allow a more precise temporal bracketing of backthrusting activity and a higher spatial resolution. Age jumps across nappe boundaries (this study), suggest

active backthrusting across nappe boundaries and indicate that backthrusting lasted longer than previously assumed.

In conclusion, Miocene rapid cooling of the Lepontine area migrates both from south to north and from east to west. This is in agreement with the suggested movement of the Adriatic indenter (Steck and Hunziker, 1994) and reinforces the association of the Miocene cooling pattern with tectonic processes.

The time–temperature history of the SSB is characterised by early to middle Miocene episodic cooling and steadily decreasing cooling rates throughout the middle and late Miocene. Cooling paths in good statistical agreement with the thermochronologic data suggest subsequently increased cooling rates between Pliocene times and the present, underlining the episodic cooling character of the SSB.

5.2. Miocene exhumation south of the northern steep belt

Processes of the NSB cannot be directly resolved from our data. The higher elevations of the NSB did not allow sampling along the same altitude level as for the rest of the profiles. Furthermore, apatite bearing lithologies are rare in the NSB, so that only few AFT dates were published from the NSB (Janots et al., 2009). Here, we compare our data with these dates, and also with dates from the Aar-/Gotthard massif bordering the NSB to the north (Glotzbach et al., 2009). Samples from the NSB and Aar/Gotthard massif were taken from higher elevations and therefore AFT ages older than the northernmost samples of our study would be expected. The northernmost samples of the Ticino profile yielded AFT ages of 13.1 Ma and 13.4 Ma. Cooling rates are low throughout the middle and late Miocene (dark green lines in Fig. 22A) compared to the rest of the profiles.

Instead of the expected older ages, samples from the Gotthard tunnel (~1100 m) cluster at ~6 Ma and surface samples (1220 m to 2580 m) yielded AFT ages between 7 Ma and 9.6 Ma (Glotzbach et al., 2009). Janots et al. (2009) reported similar AFT ages of 6.7 (1150 m) and 7.5 Ma (1915 m) for the NSB.

Summarizing, all AFT ages from the NSB and the adjacent Aar-/Gotthard massif are (I) younger than the northernmost ages determined for the horizontal profiles in this study and (II) do not show an offset across the Lepontine–Gotthard boundary. Thus, exhumation of the external massifs and of the NSB is younger than the exhumation of the northern part of the central Lepontine Dome and the border between the regions of different exhumation histories is situated along the southern border of the NSB.

Referring to Wiederkehr et al. (2008), the NSB was formed by backfolding after 18 Ma, and thus, after the onset of detachment along the basal thrust of the Aar massif at ~20 Ma (Schmid et al., 2004b). The associated exhumation of the external massifs may be responsible for the formation of the NSB in the first place. Jointly, both the external massifs and the NSB exhume steadily at least since ~14 Ma (Glotzbach et al., 2010) or even since ~19 Ma (Janots et al., 2009).

AFT ages indicate that exhumation of the NSB continued until at least the late Miocene (Janots et al., 2009), most likely related to ongoing backthrusting activity (Maxelon and Mancktelow,

2005). We explain this by long-lasting northward thrusting related to ongoing convergence of the European and the African plates, and, based on the thermal histories derived from our thermochronological data, we propose that thrusting affected the whole nappe stack of the Lepontine Dome including the Subpenninic basement nappes until late Miocene (see also Section 5.3 for more details).

As outlined in the last paragraph, both the external massifs and the NSB were rapidly exhumed from early Miocene times. By contrast, the adjacent northern Ticino profile yielded far older AFT ages associated with comparatively low cooling rates at least since middle Miocene times (Fig. 22A).

This contrast may be explained by structural and lithological differences between both regions. Foliations are steeply inclined in the north (NSB and external massifs) and distinctly flatter south of the NSB. Furthermore, the external massifs comprise a strong crystalline body, representing a massive backstop. Thus, the external massifs and the NSB may have acted as a barrier against the northward propagating internal Subpenninic nappes (i.e. Leventina and the structural higher nappes directly south of the NSB) and decelerated both their exhumation and their northward movement (see also Section 5.3).

5.3. Late Miocene doming

Assuming a geothermal gradient of 30 °C km^{-1} (after Hurford, 1986), paleo-temperatures derived from thermal history modelling can be translated into depths below surface. Fig. 23 depicts the inferred amount of overburden, which is eroded from the two profiles since 10 Ma. Only minor erosion is suggested for the southernmost samples between 10 Ma and 2 Ma. The eroded section since 10 Ma increases towards the centre of the profiles before decreasing again towards the northern terminations. Thus, Fig. 23 illustrates that (I) the SSB shows a fundamentally different cooling/erosion pattern then the rest of the Lepontine Dome (chapter 5.1), (II) between 10 Ma and 6 Ma, the centre experienced much more erosion than the margins of the dome, and (III) that from 6 to 4 Ma on, erosion was homogeneously distributed across the Lepontine Dome.

Thus, in contrast to the AFT ages of the dome margins, young AFT ages in the central parts of the dome correspond to fast cooling during the late Miocene (Figs. 21, 23). This pattern, with high exhumation rates in the centre of the Lepontine Dome and low rates at its southern and northern margins, suggests that north–south directed doming is still going on until the late Miocene (~5 Ma), much longer than previously assumed.

Probably, the Miocene slowdown of northward motion caused by the exhumation of the NSB and the external massifs during ongoing convergence (Section 5.2) caused large-scale folding of the Lepontine nappes (Fig. 24). This would explain the U-shaped AFT age distribution in the Ticino profile and the associated cooling patterns. With exception of the Maggia nappe (see Section 5.4), the cooling age pattern of the Maggia profile mimics the cooling age distribution along the Ticino profile, suggesting that north–south oriented folding affected the complete central Lepontine Dome until the Miocene–Pliocene boundary.

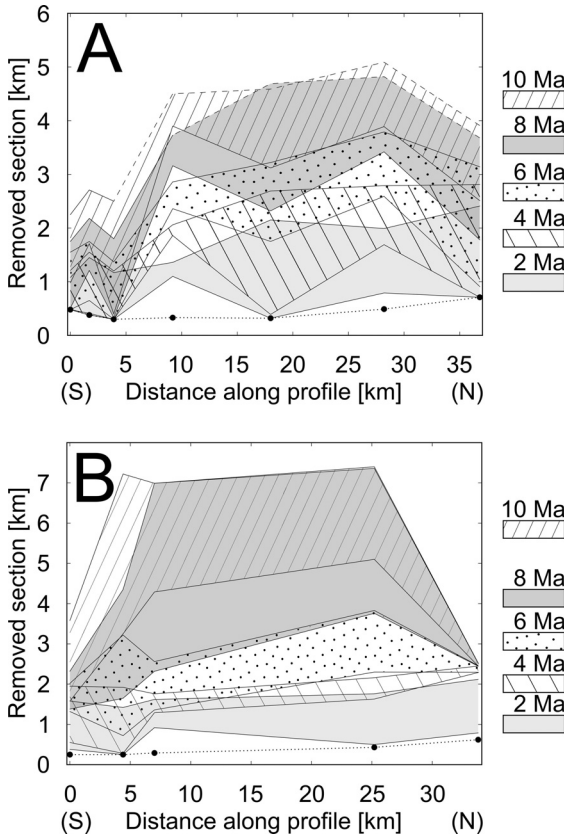

Fig. 23.: Removed overburden along the Ticino (A) and Maggia (B) profiles, separated for different time slices. Data inferred from inverse thermal history modelling (envelopes comprising statistically good solutions) with an assumed geothermal gradient of 30 °C km−1. Dashed lines taken from paths > 120 °C (Ticino profile), i.e. above the thermal sensitivity of the AFT method and thus associated with high uncertainties.

Timar-Geng et al. (2004) already argued for small scale differential cooling in the central Lepontine Dome within the last 10 Ma, and farther east, AFT ages also show a U-shaped distribution in north–south direction across the Adula nappe (Rahn, 2005). Rahn (2005) associated the observed AFT age pattern with the metamorphic grade, in that youngest AFT ages are related to most deeply buried rocks. Therefore, the results imply an influence of Mesoalpine tectonometamorphic processes on the latest-stage exhumation. Such a relation was not confirmed by our data for the central Lepontine, showing no correlation with metamorphic zonation. Instead, we suggest active updoming by folding for the central Lepontine Dome until latest Miocene/early Pliocene. This is in agreement with the preserved antiformal structures of the Leventina nappe (Rütti et al., 2005) and the basement-cover contact of the overlying Simano nappe (Pfiffner et al., 1990, Fig. 20A).

If our interpretation is right, large-scale folding presumably would also bulge the isotherms of the AFT and the AHe systems, resulting in changes of the geothermal gradient. Therefore the amount of the eroded section in Fig. 23 is associated with uncertainties. In fact, the U-shaped AFT age pattern may also be the result of isotherm warping and relaxation, and thus simply a

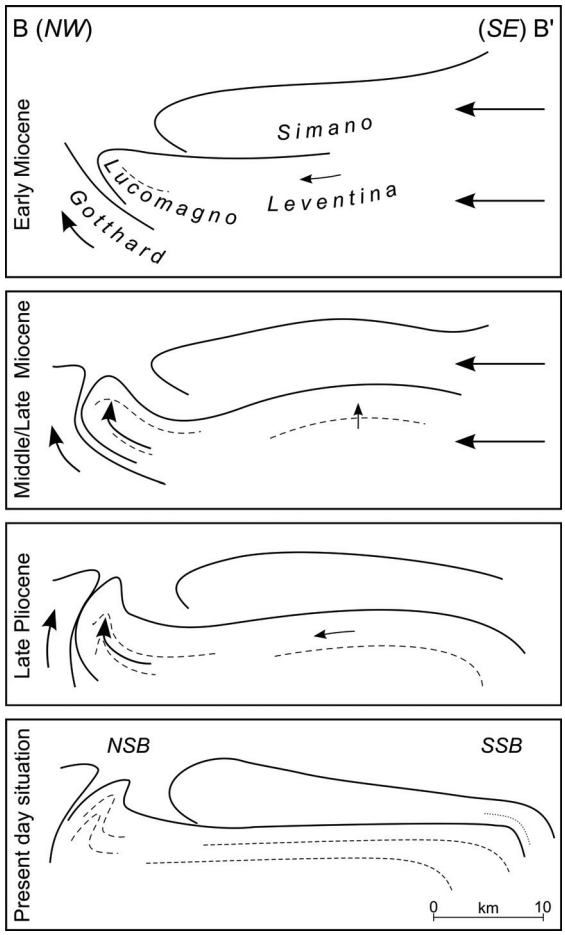

Fig. 24.: Proposed model of the structural evolution across the Ticino culmination (cross section BB' in Fig. 18) since Miocene times. Early Miocene: convergence leads to successive northward thrusting of the Penninic nappe stack (after Schmid et al., 1996). Middle/Late Miocene: northward movement of the Subpenninic nappes is decelerated by the barrier of the exhuming Gotthard massif resulting in large-scale nappe folding. Late Pliocene: decreasing compression leads to cessation of folding of the central nappes, while the NSB still exhumes. Present day situation: steep belts north and south of a rather flat lying central nappe stack (after Rütti et al., 2008).

consequence of earlier doming. Although rapid cooling argues against this explanation, it should be further explored by numerical modelling that takes heat conduction into account.

5.4. Miocene exhumation of the Maggia transition zone

While the Ticino profile crosscuts the culmination of the Ticino subdome from south to north, the Maggia profile is located along the transition zone between the Ticino subdome and the Toce subdome. The profile reaches from south of the Insubric Line to the central Lepontine. Note that the northernmost sample of the Maggia profile (MH-1) marks almost the central point between the Ticino and Toce culminations (Fig. 18) and is thus situated much further to the south than the northernmost sample of the Ticino profile.

Structural analyses relate the Maggia steepzone to Oligocene to early Miocene deformation (Merle et al., 1989; Maxelon and Mancktelow, 2005), suggesting that Miocene cooling along the Maggia horizontal profile is closely linked to the early structural evolution of the Lepontine Dome. For the Miocene, our data indicate three subsequent tectonically driven processes affecting the Maggia transition zone.

(I) Samples from the central Maggia nappe and the southernmost SSB enter the apatite PAZ at about the same time (between ~12.5 Ma and 11 Ma), indicating that both areas were situated at approximately the same crustal level during the middle Miocene. The narrowly constrained time–temperature history in the central Maggia nappe (MH-1; Fig. 21) indicates very rapid cooling between 11.5 Ma and 11 Ma. This cooling phase postdates both the formation of the Maggia steepzone (32–25 Ma; Maxelon and Mancktelow, 2005) and the transition of rapid cooling from the eastern to the western part of the dome (until 20 Ma; Steck and Hunziker, 1994). Late rapid cooling in the central Maggia nappe therefore suggests a reactivation of the Maggia steepzone, possibly related to the activity along the Rhône–Simplon fault and associated rapid cooling of its footwall at ~12–10 Ma (Steck and Hunziker, 1994).

(II) Considering only samples from the SSB and the Antigorio nappe, the cooling age distribution along the Maggia profile nearly mimics the cooling age pattern of the Ticino profile from south to the central Lepontine, though ages are generally younger (Fig. 20). Thus, updoming associated with large-scale folding affected the whole central Lepontine Dome, though compressional tectonics seem to either have lasted longer farther west or migrated from east to west, following the movement of the Adriatic indenter.

(III) Differences between the AFT ages of adjacent nappes can be related to faulting along the nappe boundaries (Fig. 20). While the southern nappe boundaries of the profile are roughly east–west oriented, offsets of the cooling ages across these southern boundaries indicate north–south oriented movements. However, the cooling patterns across the Antigorio–Maggia contact (central Lepontine Dome) can be explained by different processes. In this area, the nappe boundary is roughly north–south oriented and age jumps across the Antigorio–Maggia boundary, therefore, have to be related to east–west oriented processes. Thus, vertical movements along the Antigorio–Maggia boundary between 12 Ma and 2.5 Ma are most likely related to east–west extension, related to normal faulting along the Rhône–Simplon fault. Our data indicate vertical movements along major nappe boundaries across the central Lepontine Dome until late Neogene times. This is in apparent contradiction to earlier studies showing that Oligocene to early Miocene metamorphic isograde crosscut the nappe boundaries without offset (Niggli and Niggli, 1965; Trommsdorf, 1966; Frey and Ferreiro Mählmann, 1999). However, since metamorphic isograde were largely extrapolated across the area of our two profiles, potential offsets may not be obvious from field observations.

Estimating the amount of eroded section since late Miocene times also shows the variation of exhumation in time and space for the Maggia horizontal profile (Fig. 23B). While the southernmost samples of the profile and the samples from the Maggia nappe were already relatively close to the surface at 10 Ma (~2 to 3.5 km depth), the central Antigorio samples were exhumed rapidly from 8 Ma on and reach the same crustal level only at ~6 to 4 Ma.

After 4 Ma, however, the eroded section is nearly uniformly distributed along the entire profile.

The southernmost sample of the Maggia profile is derived from the Ivrea zone south of the Insubric Line. Similar cooling patterns compared to the adjacent samples of the Maggia profile, however, suggest that activity along the Insubric Line did not affect the exhumation in the Central Alps from middle Miocene times on.

To summarize the data of both profiles, we can conclude that the southern portions of the profiles were earlier exhumed to shallow crustal levels than the central parts, and that exhumation successively affects the south, the north and the centre of the dome and also migrates from east towards the west.

5.5. Pliocene change in exhumation regime

While Miocene cooling varies significantly across the Lepontine Dome in terms of rates and styles, thermal history modelling indicates fast and rather uniform cooling from 6–4 Ma onward, independent from tectonic structures such as the northern and southern steep belts, subdomes, and nappe boundaries (Fig. 22). Thus, from the Miocene–Pliocene boundary onwards, the investigated part of the Lepontine Dome experienced accelerated and en-block exhumation. Though tectonic controlling factors for Pliocene exhumation cannot be ruled out completely, exhumation is no longer obviously related to tectonic structures (as it were in the Miocene). This seems to point to a change in the controlling factors for Pliocene exhumation in the Lepontine Dome. These results (i) are in agreement with increasing Pliocene sedimentation rates in the circum-Alpine basins, as suggested by Kuhlemann et al. (2002), and (ii) would fit to a climatic control on Pliocene erosion of the Alps, as proposed by Willett et al. (2006). However, independent proof for changed climatic conditions which may have caused homogeneously distributed accelerated exhumation of the Alps, is still lacking. So in conclusion, our data support the assumption of a changed Alpine erosion regime as early as the Miocene–Pliocene boundary (Kuhlemann et al., 2002), but the reason for this change still remains unclear.

By contrast, the Pleistocene was definitely a time of changing climate, leading to wide-spread glaciation of the Alps (Muttoni et al., 2003; Preusser et al., 2011). Contemporaneously, the erosion regime of the Central Alps and their forelands changed (Vernon et al., 2009; Cederbom et al., 2011; Schlunegger and Mosar, 2011; Valla et al., 2012). This is in agreement with the exhumation history of the Lepontine Dome derived from our data, with ongoing rapid and homogeneous exhumation during the Pleistocene to the present. From our data, no change of exhumation patterns at the Pliocene–Pleistocene boundary (i.e., during the onset of Alpine glacia-

tion) can be inferred. This may, however, be beyond the resolution of the thermochronological dating methods applied.

6. Conclusions

New thermochronologic data from the Lepontine Dome revealed a formerly unknown U-shaped cooling pattern related to a complex exhumation history. The following main conclusions can be drawn from these data:

(I) Miocene cooling in the centre postdates cooling of the southern and also of the northern Lepontine Dome.

(II) Different exhumation styles (i.e. episodic and continuous exhumation) occurred contemporaneously and juxtaposed on a small spatial scale of less than 40 km: While the southern steep belt was rapidly exhumed in the middle and late Miocene, continuous cooling patterns – though with different onsets and rates – were found further north in the Ticino valley. Cooling along the transition zone between the Toce and Ticino subdomes again differs in style and timing.

(III) Miocene cooling patterns of the Lepontine Dome can be related to the formation of the southern and northern steep belts, doming of the central Ticino culmination, and the formation of the Maggia steep zone. Thus, tectonics, namely extensional fault zones and long-lasting compression resulting from continent–continent convergence, controlled the Miocene exhumation of the dome. We suggest that contemporaneous to east–west extension, the NSB along with the external massifs acted as a backstop to the north, causing deceleration of the northward motion of the central nappes and resulting in large-scale folding in north–south direction. Hence the Lepontine Dome is a threefold dome, comprising collision related metamorphic zonations, east–west extension related unroofing, and a third domal structure, related to long-lasting north–south compression.

(IV) Exhumation patterns of the Lepontine Dome changed between 6 Ma and 4 Ma from differential to uniform. Contemporaneously increasing exhumation rates may be explained by climatic changes towards more erosive conditions, but independent proof for such a climate change is still missing.

(V) Ongoing increased hinterland exhumation during the Pleistocene until the present is most probably related to Alpine glaciation, underlining a climatic control on the latest period of Central Alpine exhumation.

Acknowledgements

We thank Massimiliano Zattin for reviewing this manuscript and helping improving it with his insightful comments. This study is part of the EUROCORES TOPO-EUROPE project from the European Science Foundation and was funded by the German Science Foundation (DfG project SP673/5-1). Special thanks to Meinert Rahn, Adrian Pfiffner and Stefan Schmid for critically discussing the implications of this study and providing further resources. Also we thank Barry Kohn (University of Melbourne) for support and advice regarding the AHe analyses. Furthermore, we thank Anke Toltz, Vera Kolb and Angelika Freesemann (all at University of Bremen) for sample processing.

Appendix I

Performance of AFT analyses

AFT analyses were performed using the external detector method (Hurford and Green, 1982; Hurford, 1990) and the zeta-calibration method (Hurford and Green, 1983) with a zeta value of 332 and a standard deviation of 8 using CN5 dosimeter glasses (Simon Elfert). Apatite concentrates were mounted on glass slides, polished and etched in 5 M HNO_3 for 20 s at 20 °C. Low-U micas were tightly attached to the sample mounts as external detectors for the induced fission tracks. Samples were irradiated at Garching FRM II reactor (Munich, Germany). Afterwards micas were etched in 40 % HF for 30 min at 20 °C.

In addition, lengths of horizontal confined tracks parallel to c-axis were measured. Where possible, up to 100 confined track lengths (TL) measurements were taken. Due to the relatively low U contents and young cooling ages of the samples, up to three mounts were irradiated with ^{252}Cf-derived fission-fragments at Melbourne University to increase the amount of TL measurements. Fission track etch figures are used as a measure for the kinetic properties of apatite. Therefore, we measured the diameters of up to five etch figures on the surface of each analysed apatite crystal (Dpars, see Burtner et al., 1994; review of Donelick et al., 2005).

Performance of AHe analyses

Suitable, inclusion-free grains were selected under polarised light microscope and encapsulated into Pt-tubes. Degassing, measurement of ^{4}He, subsequent dissolving of the aliquots and measurement of ^{238}U, ^{232}Th and ^{147}Sm was carried out at Melbourne University. Due to the low U-contents and young AHe ages, for all but one sample multigrain aliquots had to be prepared. In most cases three grains per aliquot yielded sufficient gas for a successful analysis. In rare cases up to six grains were combined.

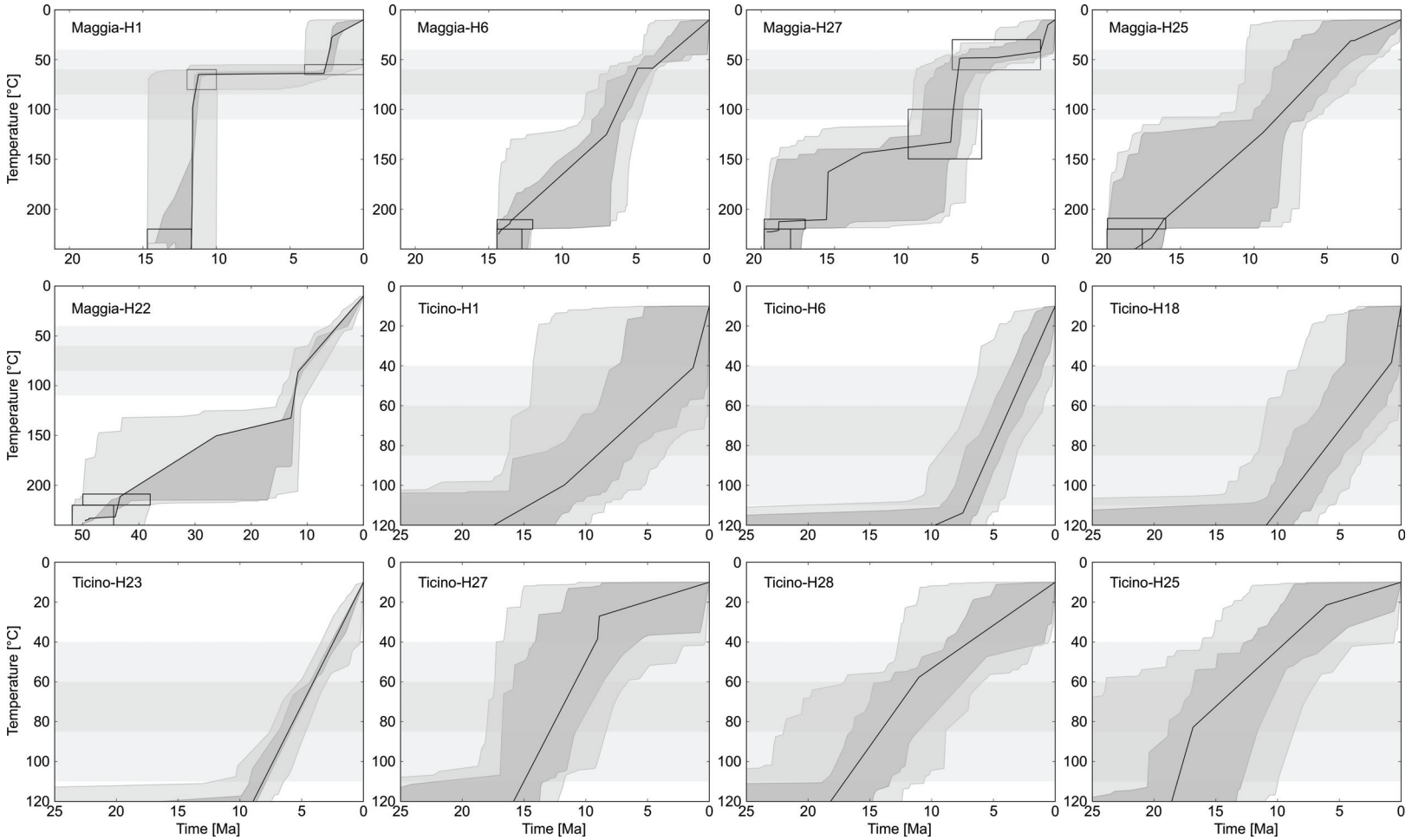

Fig. 25.: Time–temperature paths from inverse thermal history modelling. Black line: Best-fit model, dark grey envelope: statistically "good-fitting" models, light grey envelope: statistically "acceptably-fitting" models, grey horizontal bars: overlap of the ^{4}He partial retention zone (40-85 °C, Wolf et al., 1998 and partial annealing zone of fission tracks (60-110 °C, Gallagher et al., 1998, black rectangles: modelling constraints. Beside the constraints for zircon fission track ages (see chapter 3.2), further constraints were set after forward modelling, where necessary.

Paper Contribution 2:
Describing orogenic wedges by a combination of numerical 'sandbox' models and low-temperature thermochronology I: Linking lower crustal geometries and mechanic properties with upper crustal processes

Authors: Linda Wenk, Simon Elfert, Cornelia Spiegel and Katrin Huhn
In preparation for submission to Journal of Geophysical Research.
Intended submission: May/June, 2014

Abstract

To examine the influence of deep crustal mechanic properties on the structural evolution of an orogenic wedge, we develop three 2D numerical 'sandbox' experiments, based on the granular model approach, with varying décollement friction and with or without a deep seated undeformable fragment above the décollement. To increase the understanding for effects of these deep crustal properties on the upper crust, we combine these models with apatite fission track analysis by deriving synthetic apatite fission track ages from the time-temperature histories of discrete particles. Apatite fission track (AFT) analysis is sensitive to a temperature range from ~110 °C to ~60 °C. This way, we relate the structural evolution of an orogenic wedge, associated with lower crustal settings, with the thermal history of the upper crust, associated with the exhumation processes.

We verify that orogenic wedges over a high frictional décollement grow by basal accretion, whereas a low frictional décollement results in frontal accretion. Orogenic wedges grow more compact, when compressed by an undeformable fragment at the décollement as compared with settings without such deep seated fragments. Additionally, we found that high décollement strength yields a single U-shaped distribution of AFT age pattern related to maximum uplift in the central part of the double-vergent wedge. In contrast, low décollement strength results in a more W-shape distribution of the AFT ages with alternating young and old cooling ages along the simulated wedge. Furthermore, a non-deformable lower crustal fragment leads to a stronger pronounced U-shaped AFT age pattern above it. In contrast, the AFT age pattern evolves flatter if the lower crustal fragment is missing, indicating more uniform cooling as compared to strongly inhomogeneous cooling above a lower crustal fragment.

Summarizing, synthetic cooling patterns mirror the structural evolution of orogenic wedges and improve the interpretation of numerical ‘sandbox’ experiments.

Keywords: Double-vergent wedge; numerical process simulations; thermal modeling; apatite fission track (AFT) thermochronology

1. Introduction

Fold-and-thrust belts such as the Alps or the Apennines are formed during continent-continent collisions or subduction along active continental margins as a result of the continuous deformation and compression of incoming material (e.g., Schmid et al., 1996; Jolivet et al., 1998; Von Eynatten et al., 1999; Kühni and Pfiffner, 2001). In some cases, the incoming material is pressed against a stiff undeformable plate fragment which is called an indenter. If the indenter has a similar vertical height as the incoming material, the material is uplifted during the accretion process and can be distribute above the indenter resulting in a double-vergent wedge, which migrates bi-directionally along a pro- and a retro-flank of the wedge (Fig. 26; e.g., Byrne et al., 1993; Persson and Sokoutis, 2002).

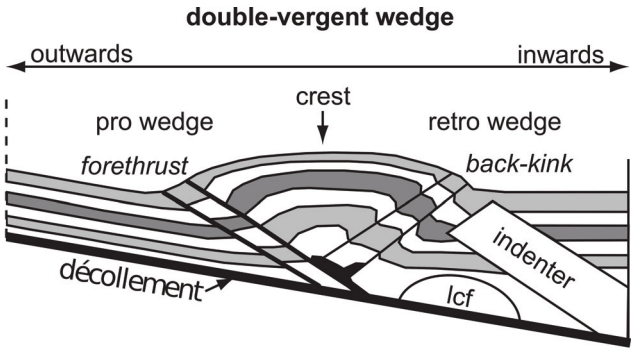

Fig. 26.: Simplified schema of a double-vergent orogenic wedge (modified after Persson and Sokoutis, 2002. (lcf) lower crustal fragment

Mechanics and kinematics of double-vergent wedges are investigated by various analog modeling studies (e.g., Beaumont et al., 1992; Storti et al., 2000). Additionally, numerical modeling successfully approached the dynamics of double-vergent wedges (e.g., Willett et al., 1993; Persson and Sokoutis, 2002). They found that the evolution and shape of such orogens are influenced by various factors such as the push from the rear (e.g., Chapple, 1978), the basal pull (e.g., Willett et al., 1993), the strength of the basal décollements (e.g., Hardy et al., 1998) or the backstop geometry (e.g., Koons, 1990). Thus, if these crustal conditions have an important influence on the evolution and mechanics of double-vergent wedges, they should also affect upper crustal processes such as uplift, erosion and sedimentation, which in turn trigger feedback mechanisms on the regional exhumation patterns (e.g., Cloos and Shreve, 1988). Regional exhumation can vary on small scale and in short intervals due to the temporal variability and the interplay of different exogenous and endogenous triggers (e.g., Carrapa, 2009; Cederbom et al., 2011; Glotzbach et al., 2011). Until now, the effects of lower crustal conditions such as décollement strength

or undeformable fragments on upper crustal mechanics and kinematics are not fully understood, due to their different temporal and spatial scales. Additionally, the previous conceptional models dealing with fold-and-thrust belt kinematics (e.g., Willett et al., 1993) exclude detailed information about mass transport patters and particle paths.

Natural exhumation and denudation processes are usually addressed by applying methods such as low-temperature thermochronology combined with thermal history modeling. Such approaches allow for deducing time-temperature histories of rocks, which give inferences about denudation and about spatial distribution, timing and rate of exhumation (e.g., Gallagher et al., 1998).

To investigate the effect of deep seated processes and geometries (e.g., lower crustal fragments) on near surface processes and mass transports patterns of orogenic wedges, a combination of numerical Discrete Element 'sandbox' experiments and apatite fission track (AFT) analysis is used in this study. In a first step, three numerical 'sandbox' experiments utilizing a granular model approach based on the Discrete Element Method (DEM; Cundall and Strack, 1978) are developed. This technique was successfully used to simulate large scaled deformations and complex tectonic processes (Burbidge and Braun, 2002; Naylor et al., 2005; Miyakawa et al., 2010). We use the European Western Alps for our case study, since they are intensively investigated by seismic reflection surveys, providing a sound basis for the numerical 'sandbox' experiments. Based on the deep structure along the seismic NFP20-West profile (Schmid et al., 2004b) the effect of different boundary conditions on wedge evolution and resulting exhumation patterns are tested (Sc1, Sc2, and Sc3; Fig. 27):

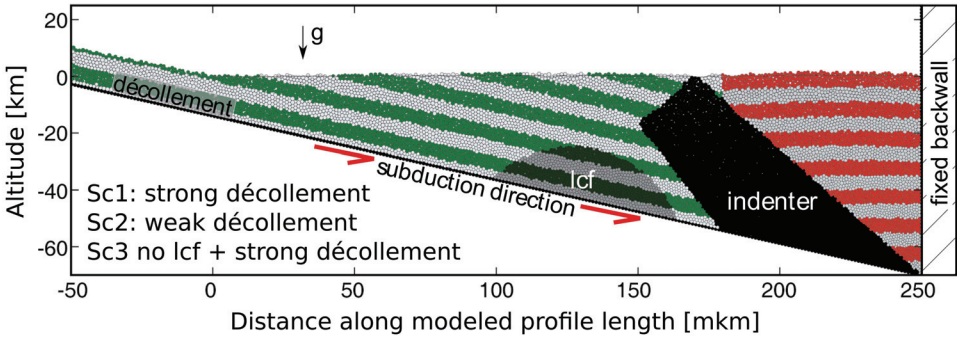

Fig. 27.: Model setup. The lower crustal fragment (lcf) is only implemented in two of three experiments (Sc1 and Sc2). Grey, green and red colored particles are used as marker horizons of the upper crustal material. Black particles: fixed lower crustal material and fixed side wall and bottom wall (i.e. the décollement). g: gravity. mkm: model km, i.e. distance along modeled profile length.

The first experiment (Sc1) acts as a reference model with a high frictional décollement and a lower crustal fragment as evident from the seismic profile. To test the influence of the décollement strength on upper crustal processes and exhumation paths, the friction coefficient of the décollement is reduced in a second experiment (Sc2). Omitting the lower crustal fragment in

a third experiment (Sc3), allows for evaluating the effect of deep seated fragments and, hence, the shape of the lower crust (lcf) on the evolution of an orogen. Summarizing, the difference between Sc1 and Sc2 is the friction along the décollement and the difference between Sc1 and Sc3 the missing lower crustal fragment in Sc3.

In a second step, synthetic AFT ages were derived. As prerequisite, erosion was calculated after the model run, as it was not implemented in the numerical 'sandbox' experiments itself. Particle positions throughout the model run were used to extract time-temperature histories (where temperature was derived from the distance to the erosional surface). Finally, forward modeling of time-temperature histories of discrete particles yielded synthetic AFT ages. The differences in the evolution and spatial distribution of the synthetic AFT ages between the experiments can be associated with the underlying deep seated conditions and, therefore, can be used to estimate their effect on near-surface processes.

In addition to this conceptual study, we show in a second paper (Elfert et al., in prep.) that this approach can also be used to better understand observed cooling patterns of natural samples from the Central Alps and reconsider the importance of lateral displacement when interpreting exhumation rates derived from thermochronology.

1.1. Evolution of double-vergent wedges

Double-vergent wedges grow while material is frontally or basally accreted at the pro-wedge, and simultaneously added by thrusts at the retro-wedge (Fig. 26; Willett et al., 1993). Wedge evolution is associated by the development of forethrusts and back-kinks. The latter ones are local, small-scale, fault-like structures (Fig. 26). During the evolution of double-vergent wedges, at least two different deformation stages were identified (Mandl, 1988; Willett et al., 1993; Storti et al., 2000). The first stage is characterized by high-velocity thrusting in the retro-wedge in concert with low displacement folding and thrusting in the pro-wedge (Fig. 26). During the subsequent second stage, the main deformation is located in the pro-wedge where low-frequency, high-displacement thrusting occurs, while low-velocity thrusting is active in the retro-wedge. The switch from stage 1 to stage 2 is triggered by the wedge uplift as soon as the flanks of the wedge reaches a critical angle, and the inward wedge domain behaves similar to a backstop (Mandl, 1988; Willett et al., 1993). Willett et al. (1993) describe a third stage in which the retro-wedge develops a break in slope. In this moment, the slope angles along the retro-wedge flank decrease due to the evolution of a new backthrust.

Based on these three different stages, double-vergent wedges evolve asymmetrically with different shapes and internal geometries in the pro-wedge versus the retro-wedge. However, the structural evolution and the principle stresses within the double-vergent wedges are defined by the relation of the internal friction of the incoming material and the internal friction of the décollement on which the wedge grows (Koons, 1990; Smit et al., 2003). Above a low frictional detachment, a low tapered, frontally accreted pro-wedge evolves (e.g., Davis and Engelder, 1985). There, material is slightly uplifted and accreted along steep dipping forethrusts with lower offsets (Chapple, 1978; Davis and Engelder, 1985; Bonini, 2007). In the case of a

high frictional detachment, the material is far underthrust away from the deformation front (DF) of the pro-wedge towards the center of the wedge. This basal accretion is followed by strong vertical material uplift (e.g., Davis et al., 1983). In this study, we discuss the wedge evolution of the numerical 'sandbox' experiments with respect to the three stages described by Willett et al. (1993).

2. Method

2.1. Discrete Element Method

The Discrete Element Method (DEM) is a numerical modeling technique based on a granular model approach. It allows for the investigation of the deformation behavior of crustal materials through the implementation of particle assemblages (e.g., Burbidge and Braun, 2002; Naylor et al., 2005; Miyakawa et al., 2010). For our study, we use the commercial code PFC2D (Cundall and Strack, 1978; ITASCA, 2004). This software uses discretized rigid elements with a spherical shape that can be displaced in any direction. In response to applied boundary conditions, the particles interact and overlap with their neighboring elements (Cundall and Strack, 1978). These interactions cause contact forces, which are calculated through the magnitude of the overlap in combination with the physical particle properties (e.g. the coefficient of friction (μ), shear and normal stiffness (k_s, k_n), and density (ρ)) via simple physical force-displacement laws (Mindlin and Deresiewicz, 1953; Cundall and Strack, 1979). The code allows to obtain detailed information about particle position and forces, as well as information about the internal structure of the particle assembly at each time step. For a more detailed description of the code, please see e.g., Cundall and Strack (1978, 1979, 1983), Cundall (1987) or the PFC2D ITASCA handbook (2004).

The natural rocks simulated here show an elasto-plastic material behavior. This is implemented in the numerical approach using the Hooke's law for the elastic deformation. For the plastic material behavior, the Mohr Coulomb (MC) criterion takes effect. Both describe the elasto-plastic material behavior and, therewith, the brittle deformation behavior of the upper crust enabling the simulation of the deformation processes of accretionary wedges (Miyakawa et al., 2010; Wenk and Huhn, 2013).

2.2. Apatite fission track analysis

Thermochronology derives the time-temperature history of rocks by taking advantage of the temperature sensitivity of different radiometric dating methods. Cooling can be associated with the exhumation of rocks, where temperatures decrease from high values at depth to surface values. In this study, we apply apatite fission track (AFT) analysis (Wagner and Reimer, 1972; Hurford and Green, 1981, 1982) and create a synthetic dataset of AFT cooling ages for simulated DEM particles based on their pathways. The procedure to yield synthetic AFT ages from model particles is described in sec. 3.3.2 on in more detail.

Generally, AFT thermochronology is based on the spontaneous fission of ^{238}U, which causes defects ('fission tracks') of the crystal lattice. Until cooling below ~110 °C, fission tracks anneal completely. Within the partial annealing zone between 110 °C and 60 °C, fission tracks are shortened, but are not completely annealed (e.g., Wagner and Reimer, 1972; Gleadow and Duddy, 1981; Gallagher et al., 1998). Below 60 °C, fission track are largely stable with less than 10 % shortening (Spiegel et al., 2007), and further accumulate with time. An AFT age is derived from the density of fission tracks in a crystal and, therefore, refers to the elapsed time since the rock's temperature was between 110 °C and 60 °C (Fig. 28).

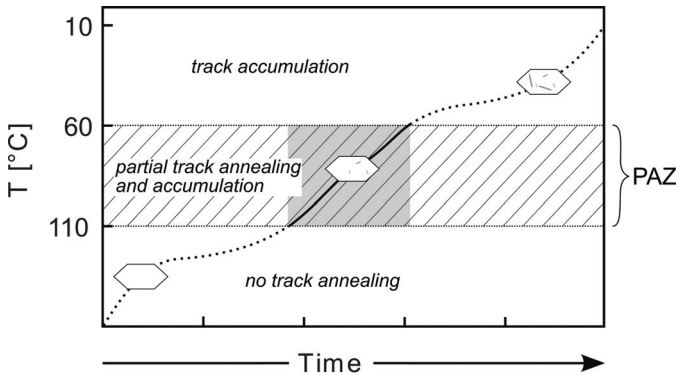

Fig. 28.: Schematic cooling path of a rock through time. At temperatures between 110 °C and 60 °C fission tracks in apatite are preserved and only partially annealed. Below 60 °C fission tracks in apatite retain almost without shortening ($<$ 10 %).

The thermal history between ~110 °C and 60 °C can be inferred from the distribution of fission track lengths, which in turn is related to the cooling rate of a rock within the zone of partial annealing (e.g., Gleadow and Duddy, 1981; Gleadow and Fitzgerald, 1987).

AFT thermochronology depicts the cooling of the upper crust (~1.8 to 3.3 km depth at a geothermal gradient of 30 °C km^{-1}, which is impacted by endogenic and exogenic dynamics.

3. Model approach

3.1. Model setup

For the general model setup, the present day seismic profile of the western Alps (NFP20-WEST, Schmid et al., 1996, 2004b) has been used as a reference and starting point for forward modeling. This seismic profile is simplified to focus on the general influence of the deeper crust on the upper crust by using three different boundary conditions (Fig. 27). This simplified approach allows for development of conceptual models for AFT patterns, which occur in dependence on deep crustal conditions.

The numerical 2D 'sandbox' consists of a fixed box bottom with a length of 350 km that dips in a fixed angle of β = 12° inwards (direction of subduction, Fig. 27). The bottom is bordered by a fixed vertical 120 km high side walls (Fig. 27). Box bottom and side wall are composed of particles with a homogeneous radius of 600 m, and act together as stiff, undeformable boundaries. During all experimental runs the box bottom moves with a constant velocity in positive x-direction to simulate a down-going plate of a subduction zone. The top of the box-bottom particles acts as the décollement. The entire box is filled with 12,000 randomly distributed particles with three particle sizes with diameters of 500, 600, 700 m to prevent symmetrical particle packing (Saltzer and Pollard, 1992). These particles are deposited under the force of gravity, on the box bottom ($g = 9.81\ ms^{-2}$) to create a triangular undeformed 'sediment' body. To allow for continuous addition of particles into the numerical sandbox the detachment is extended beyond the outward edge (i.e. into the direction of negative x-values). On top of the extended detachment a 10 km thick layer is deposited simulating the undeformed 'sediments' (i.e. the incoming sequence) in front of the pro-wedge. This region is partly included in the figures, as some wedges extend outwards (i.e. towards the extended detachment).

After particles are deposited and stress equilibrium is achieved, three different initial states (Sc1, Sc2, Sc3) are designed based on the deep structure of the NFP20-West profile (Fig. 27; Schmid et al., 1996, 2004b). A stiff, non-deformable indenter is created by fixing a group of particles in all experiments. This fixed part has a thickness of ~26 km at the top and ~35 km at the bottom to simulate the upstanding Ivrea body (Adriatic lower crust) in the cross section of the NFP20-West profile (Fig. 27; black particles). It dips with an angle of 45° inwards simulating an overthrusting, lower crust in a subduction setting (Schmid et al., 2004b).

To investigate the influence of different geological deep-seated structures on the mass transport pattern and on the cooling paths of the particles in two experiments (Sc1, Sc2) a second particle group in a semi-circular shape (radius 30 km) is additionally fixed implemented directly on top of the detachment (between 100 and 160 mkm; i.e. model kilometer which is the distance

along the modeled profile length). It simulates a lower crustal fragment (lcf) of the deeper crust with rough or convex surface such as it occurs in the Alps (Schmid et al., 1996; semi-transparent particles in Fig. 27).

All physical parameters are adopted from previous studies on numerical experiments simulating the evolution of orogenic wedges (Naylor et al., 2005; Wenk and Huhn, 2013). The material properties (e.g., μ_p, ρ, k_n, k_s) to simulate the brittle materials are held constant through all experiments (Tab. 8). For experiments Sc1 and Sc3, the coefficient of friction of the particles building up the basal box bottom which partly acts as detachment is higher as in experiment Sc2. The boundary particles of the fixed sidewalls are given properties similar to the brittle material layer (Tab. 8).

Tab. 8.: Material properties of the numerical 'sandbox' experiments (conceptual study)

Particles	Coefficient of friction (μ_p)	Density (ρ) $[kg\ m^{-3}]$	Normal stiffness (k_n) $[Nm^{-1}]$	Shear stiffness (k_s) $[Nm^{-1}]$
Model particles	0.6	2700	$1 \cdot 10^{13}$	$1 \cdot 10^{13}$
Side-wall particles	0.6	2700	$1 \cdot 10^{13}$	$1 \cdot 10^{13}$
Box bottom	0.1 / 0.2	2700	$1 \cdot 10^{13}$	$1 \cdot 10^{13}$

3.2. Model limitations

This study aims a conception of large-scale coherences of crustal evolution in compressed orogens. Consequently, we did not consider a fine stratification with property variations between the orgen strata. For reasons of simplicity, we also disregarded the influence of fluids and implemented neither erosion nor isostasy in the numerical 'sandbox' experiments. Such variations on material properties or model constraints would lead to differential strength patterns across the particle assembly resulting in varying stress fields. Furthermore, we use a numerical 2D model, being well aware of the three dimensional complexity in natural settings. We, therefore, can only draw inferences on orogen perpendicular processes (i.e. compression) and not on orogen parallel processes (e.g., extension). Due to all these simplification, the resulting fault angles and particle paths can be compared relatively to each other, but not to natural structures (Morgan and Boettcher, 1999). However, this allow to compare the results with previous 2D-studies on double-vergent wedges such as Willett et al. (1993).

Real world AFT ages and erosion patterns can be affected by long-wavelength topography or small- scale tectonic structures. Nevertheless, to perform model runs in a reasonable time frame higher implemented particle size and homogeneous incoming material properties are used. Thus, only large scale trends can be investigated which, however, is sufficient for a conceptual study.

3.3. Analysis and interpretation techniques

During the experimental-run, particle positions are saved every 0.05 % shortening (i.e. storage step of 200 m 'subduction'. Parameter s in the following equations) for each experiment. Thereby, a detailed picture of particle positions and relative displacements are recorded enabling the monitoring of internal deformation, e.g., fault zones. Horizontal layers in the particle configuration images are colored in accordance with analog sandbox experiments to visualize the internal structures by offsets or folding of the layers (Fig. 27).

The relative displacements of each particle in the x- and y-directions are extracted for each storage step and are used to calculate a normalized displacement field for the model cross section. This reveals zones where particles exhibit large relative offsets. If two groups of particles move into opposing direction, it can be interpreted as a fault zone (Morgan and Boettcher, 1999; Huhn et al., 2006). Based on our model configuration, whereupon the origin of our coordinate system is located on the lower left side (Fig. 27), these faults are interpreted as forethrusts or backthrusts. However, only thrusts that are active during the extracted periods can be observed. Thus, the tracking of older inactive faults is not possible with these relative displacement plots. Therefore a combination of particle configuration images and relative displacement plots is essential (cf. chapter 4).

In addition, the granular model approach enables to track single particles during the entire experiment to gain a deeper insight into the mass transport pathways and the resulting cooling paths. In this study, selected particles are tracked and saved for a detailed analysis of particle transport pathways, and displacement rates in space and time. This approach provides an opportunity to get a first impression of the wedge kinematics and deformational domains on deep and shallow crustal level.

Furthermore, pathways are used to derive time-temperature histories for particles (see sec. 3.3.1 and sec. 3.3.2), which in turn are used for forward thermal history modeling, yielding synthetic AFT data (age, mean track length, track length distribution) that would theoretically result from the simulated particle pathway.

3.3.1. Computing the erosional surface

The temperature of a particle at a particular time is derived by assuming a geothermal gradient and multiplying it by the depth [km below the surface] of the particle. However, since the numerical 'sandbox' experiment does not contain erosion, which would result in exhumation and, therewith, cooling, the uppermost particles cannot serve for estimating the actual surface. Instead, the erosional surface level at a given point along the modeled profile length must be calculated for each storage step and only particles, intersecting this erosional surface are selected for AFT analyses. Note that we refer to 'erosional surface' in the sense of the exposed surface after erosion is calculated and not in terms of a plain erosion surface (s.str.). We derive the erosional surface of each storage step from the model itself (see below for details, eq. 3.1 to eq. 3.5 and Fig. 29). Thereby, we account for the modeled evolution of the particle wedge.

The presented approach can be applied on multiple geological settings even if estimates for the surface evolution are lacking.

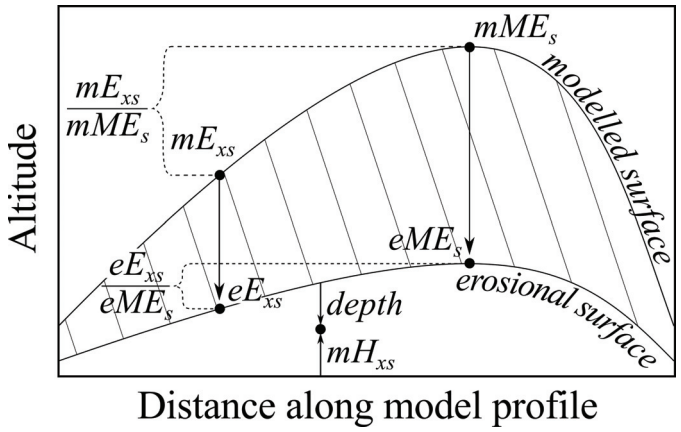

Fig. 29.: Derivation of depth below the surface of a given point (mH_x) at a given time (s), assuming the ratio between the modeled maximum elevation (mME_s) and the modeled local elevation (mE_{xs}) equals the ratio of the erosional maximum elevation (eME_s) and the erosional local elevation (eE_{xs}; eq. 3.3).

To achieve realistic dimensions, we correlate the horizontal movement at the model detachment with the estimated convergence of the European and Adriatic plates (Schmid et al., 1996). Schmid et al. (1996) assumed a flat topography in terms of elevation above sea level for the Central Alps 32 Myr ago and 119 km shortening since then. Accordingly, we model 119 km of shortening and interpret the overall model time as being equivalent to 32 Myr of orogeny. Analogously, we define the initial and final maximum elevations (eME_i – 'erosional Maximum Elevation initial', eME_n – 'erosional Maximum Elevation after n storage steps') as eME_i = 500 m and eME_n = 3000 m (see Tab. 9 for all abbreviations in the equations). Note that we model forwardly from a setting based on the present day deep structure of the Western Alps. Boundary conditions (from the past evolution of the Central Alps) are adapted for realistic dimensions only. The results of this study, therefore, hold conceptual insights. In the companion paper to this study (Elfert et al., in prep.), we adapt the results of our approach to the Central Alps by forward modeling based on the (unknown) setting of the Central Alps at 32 Ma, simulating the orogeny until the present day situation is reached.

Before the erosional surface is calculated for any storage step, the maximum modeled surface elevation (i.e. altitude of the highest lying particle) for each step is determined. An index q is allocated to each storage step s, which indicates the relation between the modeled maximum elevation of the current storage step (mME_s) and the modeled maximum elevation of the last storage step (mME_n, eq. 3.1).

$$q_s = \frac{(mME_s - mME_i)}{(mME_n - mME_i)} \tag{3.1}$$

Afterwards, the mME of each storage step (i.e. still without erosion) is substituted by the erosional maximum elevation (eME, eq. 3.2) with respect to the q of each storage.

$$eME_s = eME_i + (q_s \cdot (eME_n - eME_i)) \tag{3.2}$$

Maximum exhumation is assumed at the point of maximum uplift. The relation of the erosional elevation (i.e. surface altitude) at any point x along the profile at storage step s ($eE_{x,s}$) and the corresponding maximum elevation of the erosional surface (eME_s) should, therefore, equal the relation of the modeled elevation (at that point and time: $mE_{x,s}$) and the corresponding mME_s. Given that assumption, the actual surface (i.e. with erosion) is determined for all points and times (eq. 3.3, Fig. 29). By this means, varying speed of uplift (variation of q_s over time) is translated into varying speed of exhumation. The boundary conditions for the calculation of eE are valid for the modeled profile length, but not for the outwards extended detachment (negative x-values) and its layer of additional particles (see sec. 3.1). Consequently, the erosional surface is only calculated between 0 mkm and 250 mkm.

$$eE_{x,s} = eME_s \cdot \left(\frac{mE_{x,s}}{mME_s} \right) \tag{3.3}$$

3.3.2. Computing temperatures and AFT cooling ages

At specific time intervals within each model run (each 20 km shortening), particles located at the calculated erosional surface at that time are extracted ('sampled'). From these extracted particles the AFT cooling ages at that time are calculated to determine the evolution of AFT pattern through time. Note that the particles of the numerical sandbox do not inherit time-temperature information prior to the simulated cycle of orogeny (in contrast to real samples, which were not reset during the current cycle of orogeny). Thus, the synthetic AFT ages may only slightly exceed the simulated model runtime (until 'sampling') at the most.

Assuming a geothermal gradient (g_t) of 30 °C km^{-1} and a surface temperature (T_{surf}) of 10 °C, the temperature at a given point (x, y) and at a particular storage step s ($T_{x,y,s}$) is derived based on the distance of the modeled height of a particle $mH_{x,s}$ to $eE_{x,s}$ (eq. 3.4). Therein, $mH_{x,s}$ is y-value in the coordinate system of the numerical 'sandbox' and the term ($eE_{x,s}$ - $mH_{x,s}$) can be interpreted as depth below surface.

$$T_{x,y,s} = ((eE_{x,s} - mH_{x,s}) \cdot g_t) + T_{surf} \tag{3.4}$$

The interpretation of a synthetic AFT age only makes sense if the corresponding particle is positioned at the surface at the end of the simulation. Thus, we only consider particles, which intersect the erosional surface with their upper half (i.e. their central point is below the erosional surface) at the time of 'sampling'. The distance between the center of the particle and the erosional surface at the time of 'sampling' is added to the $mH_{x,n}$ of each of the previous storage steps (eq. 3.5). By this means, it is ensured that the particle's depth at the time of 'sampling' is zero. In other words, the time-temperature history of that part of the particles, which actually intersects the surface at the time of 'sampling', is calculated and saved.

$$T_{x,y,s} = ((eE_{x,s} - (mH_{x,s} + (eE_{x,n} - mH_{x,n}))) \cdot g_t) + T_{surf} \tag{3.5}$$

The HeFTy program (version 1.7.5; Ketcham, 2005) is used to predict synthetic AFT ages from the time-temperature paths of the selected particles (i.e. particles, which intersect the erosional surface). These were imported in HeFTy and forward modeled, using the annealing model of Ketcham et al. (2007a).

Finally, all time-temperature histories were evaluated with respect to their significance (Fig. 30). In several cases, particles, which intersected the erosional surface at the end of the simulation, were above the erosional surface (i.e. already 'completely eroded') during previous steps. Only those particles, which experienced a complete reset of the AFT system during the model run were fully trusted.

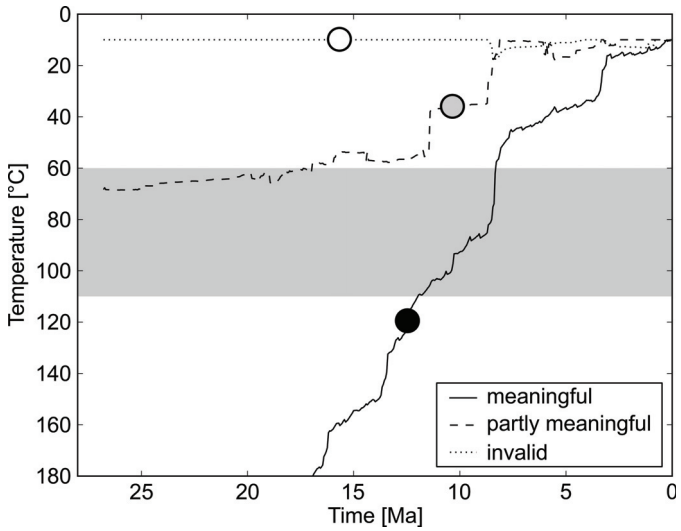

Fig. 30.: The derived time-temperature paths are used for thermal history modeling and evaluated with respect to their information on the exhumation history. (Black balls/black line) meaningful tT-history, particle completely reset with respect to the AFT system. (Grey balls/dashed line) partly meaningful tT-history, no complete reset, but sufficient tT-information. (White balls/dotted line) invalid tT-history, mainly at or above the computed erosional surface.

Tab. 9.: Abbreviations and setting of coupling parameters (to calculate the erosional surface and temperature)

Parameter	Indices	Meaning and units	Setting
Q		Topography index []	-
	s	*storage step*	
mME		modeled Maxium Elevation [km]	-
	s,i,n	*storage step, initial (0), no. of storage steps*	
eME		erosional Maximum Elevation [km]	eME_i = 0.5
	s,i,n	*storage step, initial, no. of storage steps*	eME_n = 3
mE		modeled Elevation [km]	-
	x,s	*distance along modeled profile length, storage step*	
eE		erosional Elevation [km]	-
	x,s	*distance along modeled profile length, storage step*	
T		Temperature [°C]	T_{surf} = 10
	x,y,s,surf	distance along modeled profile length, height, storage step, surface	
mH		modeled height of a particle (i.e. y value) [km]	-
	x,s	distance along modeld profile length, storage step	
g	t	Geothermal gradient [°C km-1]	g_t = 30

4. Results

To investigate the temporal progress of wedge accretion, we present six development stages until 119 km shortening. Referring to Schmid et al. (1996), the Alpine Belt experienced 119 km shortening in the last 32 Ma. Accordingly, the investigated development stages can be interpreted as snapshots after 5.4 Myr (20 km shortening), 10.8 Myr (40 km shortening), 16.1 Myr (60 km shortening), 21.5 Myr (80 km shortening), 26.9 Myr (100 km shortening) and 32 Myr (119 km shortening) of orogeny.

4.1. Experiment Sc1 (high frictional detachment, indenter, lower crustal fragment)

4.1.1. Mechanical and kinematic evolution

A double-vergent wedge evolves in the reference experiment Sc1 due to the movement of the basal box bottom (Fig. 31). After 20 km of shortening, the pro-wedge flank rises with a steep slope angle (α_1~21°), associated with active forethrusts cropping out at the DF with a dipping angle of ~14° (Fig. 32). Underthrusting of the material along these flat thrusts result in basal accretion (Fig. 32). Accordingly, the pro-wedge is continuously uplifted against the lower crustal fragment and the indenter. The retro-wedge flank evolves flatter with a narrow slope angle of α_2~5°. The crest and the steepest particle paths are located at ~55 mkm. With ongoing shortening, new forethrusts are established at the deformation front, which successively migrate into the wedge, where they get reactivated as out-of-sequence thrusts with rising angles between 19° and 27° (Fig. 32). Simultaneously, due to material stacking, backthrusts (dipping angle ~57°) occur with distinct offsets and the crest with the highest particle uplift starts to migrate inwards to the position of 60-70 mkm. The resulting slope angles of the pro- and the retro-wedge flank remain similar with α_1~22° and α_2~9°. After ~52 km shortening, the slope angle remains relatively constant at an angle of α_1~16° at the frontal wedge and an angel of α_2~17° at the retro slope (Fig. 33). A new steeper forethrust of ~22° dipping angle occurs after 60 km shortening and gives rise to a small uplift structure in front of the main wedge structure, which is subsequently underthrust again, according to the general uplift style of Sc1. The crest is located at ~80 mkm.

After 100 km shortening, the uplifted structure is completely underthrust, resulting in a temporarily steeper frontal flank (α_1~20°). In the last time slice, after 119 km shortening, again a new steep forethrust (of ~23°) rises from the detachment and leads to an outward movement of the pro-wedge flank (Figs. 31, 32). The corresponding backthrusts rise steeper with 47°. Ad-

ditionally, reactivated out-of-sequence thrusts evolve steeper with increasing distance to the DF (Fig. 32) and rearrange the underthrust material. This results in a further uplift and steepening of the wedge crest (α_1~16°)and corresponds with the particle paths which start rising shortly inwards of the DF with a gradient that increases proportionally with increasing distance to the DF (Fig. 32).

At the retro-wedge flank of this imbricated wedge, one main active backthrust is observed (Fig. 32), which is regularly activated through the model run. This backthrust cuts through the surface with ~51° and runs in a slight curve upward but does not touch the implemented indenter nor the lower crustal fragment. The offset along the backthrust is relatively small, hence, it evolves as a back-kink. The retro-wedge flank develops slightly steeper with a slope angle α_2~17°.

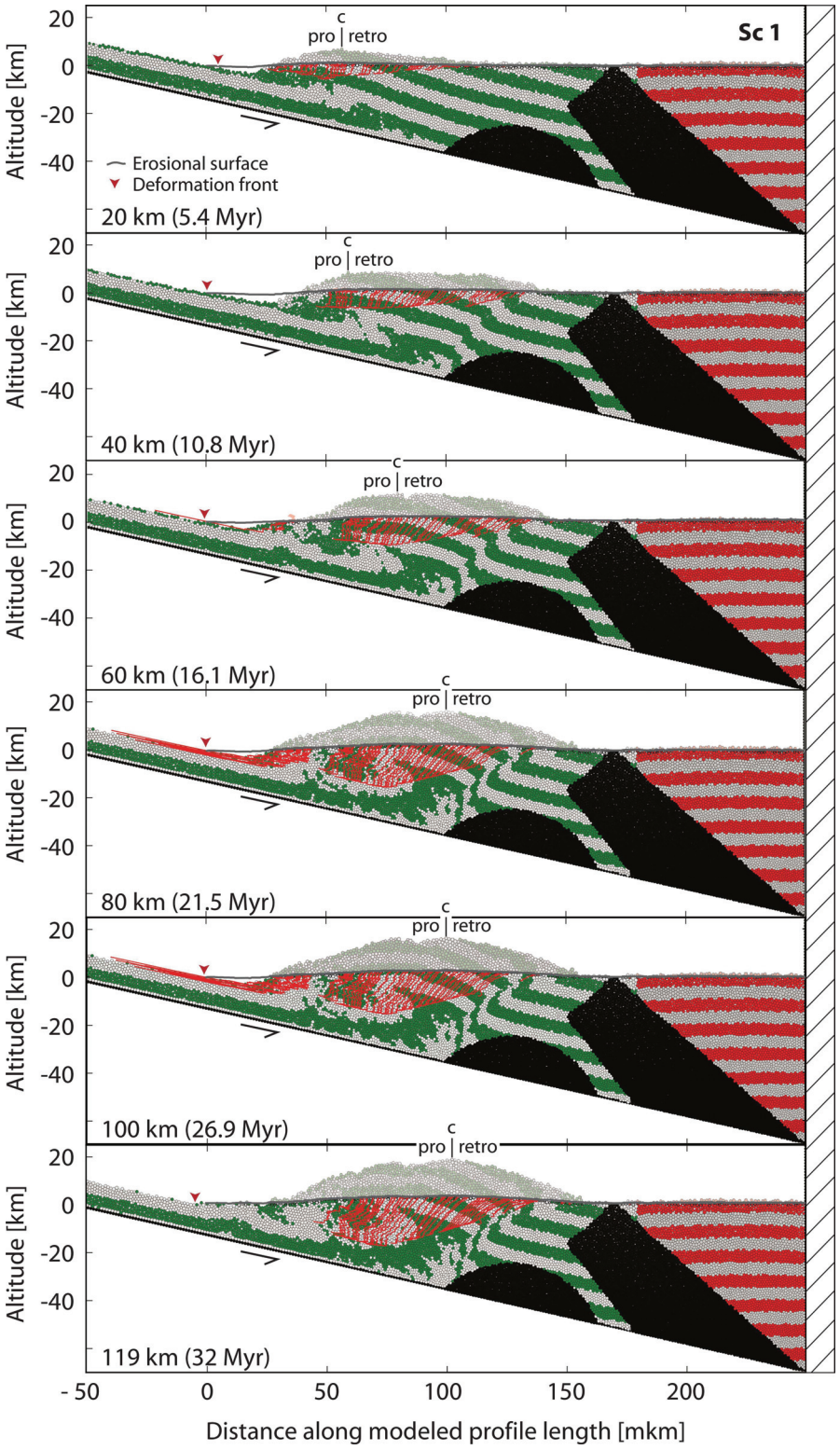

Fig. 31.: Particle setting of experiment Sc1 after 20 km, 40 km, 60 km, 80 km, 100 km and 119 km shortening. For reasons of clarity, the eroded section (calculated after simulation) is grayed out. Only those particles are selected, which crop out at the erosional surface at the time of sampling. (Red lines) particle paths for selected particles reaching erosional surface (gray line; see sec. 3.3.1). (mkm) model km, i.e. distance along modeled profile length. (c) crest. (pro) pro-wedge. (retro) retro wedge.

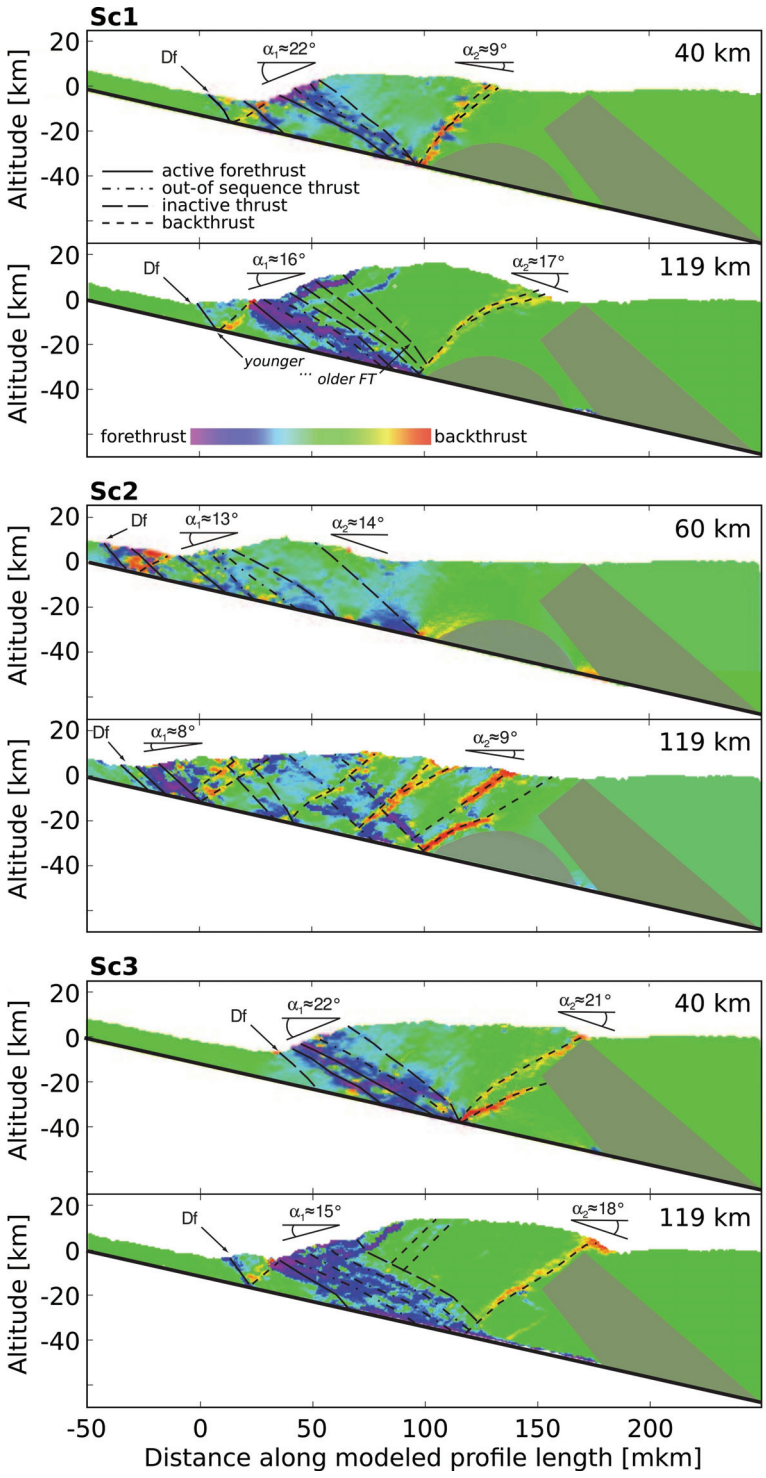

Fig. 32.: Gradient of displacement plot showing an early characteristic active thrust pattern (after 40 km or 60 km shortening, corresponding to 10.8 Myr or 16.1 Myr of orogeny) and the final state after 119 km shortening corresponding to 32 Myr of orogeny. In contrast to the particle configuration images (e.g., Fig. 31), the complete particle assemblage (including the eroded section) is interpreted as erosion is calculated after the model run and thus does not impact the stress field of the numerical 'sandbox' experiments. From top to bottom: Sc1 (high frictional detachment, indenter and lower crustal fragment), Sc2 (low frictional detachment, indenter and lower crustal fragment) and Sc3 (high frictional detachment, indenter). (Df) deformation front. (FT) forethrust. (α) slope angle at the pro-wedge flank (1) and retro-wedge flank (2). (mkm) model km, i.e. distance along modeled profile length.

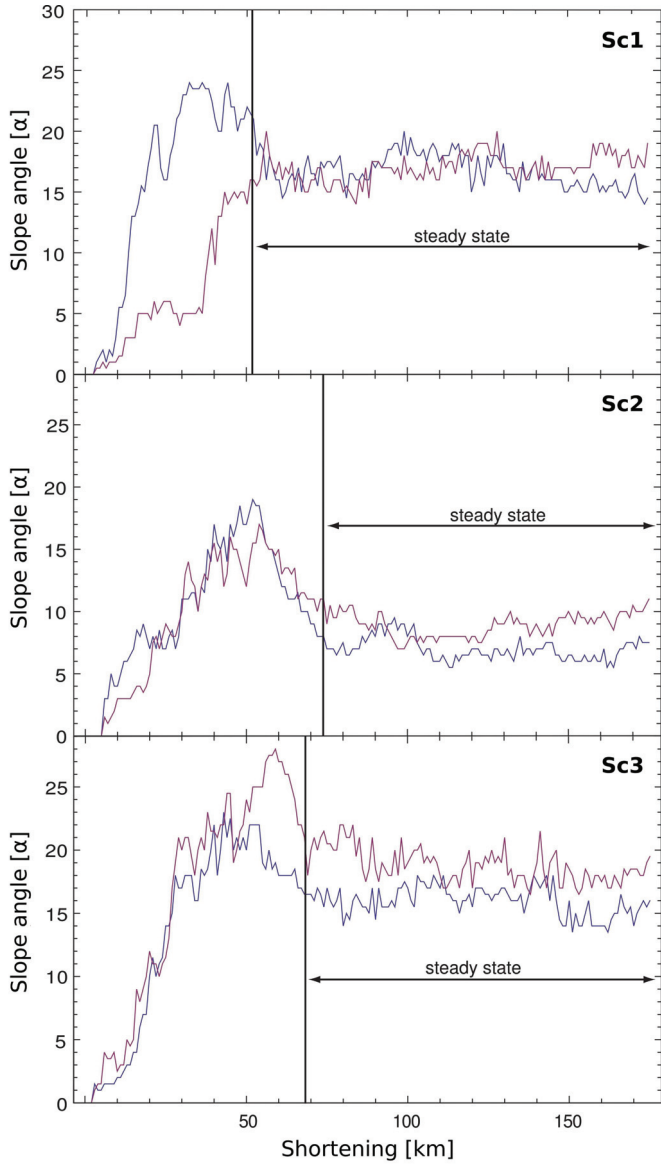

Fig. 33.: Evolution of slope angles along the pro (blue lines) and retro-wedge flanks (red lines). From top to bottom: Sc1 (high frictional detachment, indenter and lower crustal fragment), Sc2 (low frictional detachment, indenter and lower crustal fragment) and Sc3 (high frictional detachment, indenter).

4.1.2. Thermal history

After 20 km shortening, synthetic AFT ages from experiment Sc1 vary from 2.4 Ma to 5.5 Ma and show a distinct U-shaped distribution between 40 mkm and 80 mkm (Fig. 34). Beyond that, AFT ages are homogeneously distributed. Youngest ages are predicted in the center of the growing wedge (at 50-60 mkm) and older ages towards the pro- and retro-wedge flanks (Fig. 34). Thus, the central parts seem to be rapidly exhumed, associated with enhanced deformation, during the first stage of orogeny, while the outer parts cooled more slowly, without significant deformation. Note that the particles do not hold temperature information before the model run. Thus, AFT ages in the range of the model run time (in this case, 20 km shortening correspond to 5.4 Myr of orogeny) indicate that the particle intersected the erosional surface for the entire model run and accordingly was not exhumed since the model started. After 40 km shortening, the section of young AFT ages shifts to 80-125 mkm (Fig. 34). AFT ages range from 3.4 Ma to 11 Ma, with youngest ages between 110 mkm and 120 mkm.

The cooling age distribution evolves more complex after 60 km shortening, with young AFT ages, pointing to enhanced deformation, both in the center of the U-shaped distribution (5-6 Ma at 80-100 mkm) and along the pro-wedge flank (6-9 Ma at ~30 mkm). In between these regions and along the retro-wedge flank, AFT ages increase gradually up to 16 Ma (Fig. 34). This pattern gets even clearer after 80 km and 100 km shortening. Thus, along the pro-wedge flank a second, smaller U-shaped pattern evolves, corresponding to the contemporaneous forward jump of that pro-wedge flank. Youngest cooling ages of the major pattern migrate from ~85 mkm (5.2 Ma) to ~80 mkm (5.5 Ma), while the section of young cooling ages along the pro-wedge flank broadens towards ~40 mkm (6.5 Ma) and ~45 mkm (6 Ma) (Fig. 34). AFT ages along the pro-wedge flank at ~30 mkm increase to 22 Ma at the same time.

At the last time slice (119 km shortening), both former sections of young cooling ages merge and a broad, shallow U-shaped distribution of AFT ages establishes between 40 mkm and 140 mkm. Meanwhile, cooling ages at the very beginning of the pro-wedge flank (~30 mkm) decrease again (10-12.5 Ma), indicating a new section of rapid cooling, which is in line with the anew observed forward jump of the pro-wedge flank.

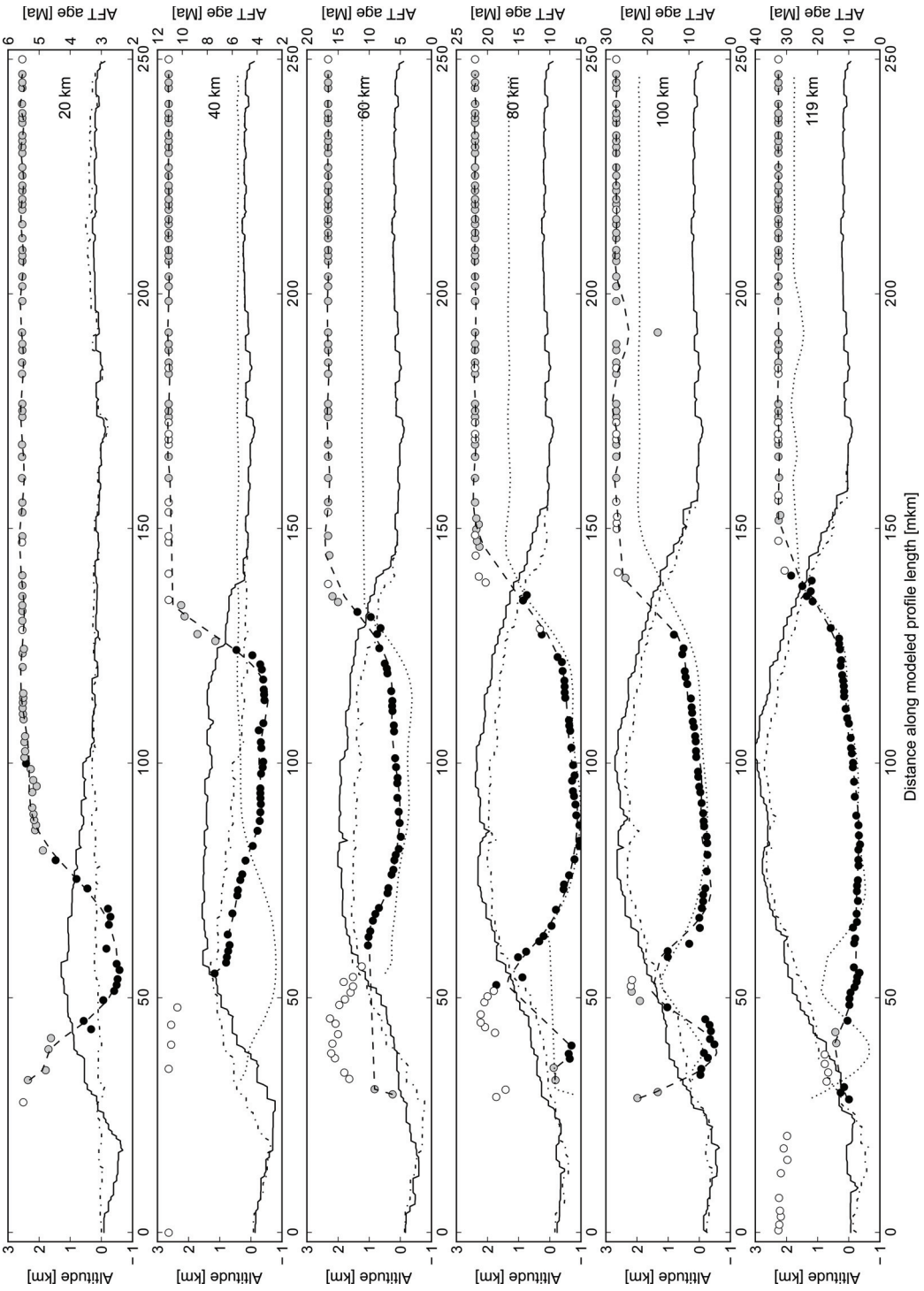

Fig. 34.: Evolution of the computed erosional surface and the synthetic AFT cooling ages of Sc1 through time. From top to bottom: situation after 20 km, 40 km, 60 km, 80 km, 100 km and 119 km shortening, corresponding to 5.4 Ma, 11 Ma, 16 Ma, 22 Ma, 27 Ma and 32 Ma orogeny, respectively. Black line: erosional surface of current time slice. Dash-dotted line: erosional surface of the last time slice. Balls: AFT ages (signature see Fig. 30). Dashed line: Trendline of valid AFT ages of the current time slice. Dotted line: Trendline of valid AFT ages of the last time slice. (mkm) model km, i.e. distance along modeled profile length.

4.2. Experiment Sc2 (low frictional detachment, indenter, lower crustal fragment)

4.2.1. Mechanical and kinematical evolution

Analogously to Sc1, a double-vergent wedge evolves in Sc2. But in contrast to Sc1, here, active forethrusts rise at the DF in steep angles (~37°), after 20 km shortening and, simultaneously, corresponding backthrusts of ~57° occur next to the retro-wedge flank. Consequently, within this setup the wedge grows by frontal accretion along steep forethrusts between the imbricated units. The highest uplift at this time slice is observed at ~25 mkm (Fig. 35). The pro-wedge flank and the retro-wedge flank evolve similarly with α_1~7.5° and α_2~5° (Fig. 32). With ongoing shortening, the double-vergent wedge extends by slowly propagating bidirectionally: The pro-wedge migrates outward due to the evolution of new steep forethrusts, and new backthrusts are activated further inwards cropping out at the retro-wedge flank (Fig. 32). Nevertheless, main deformation takes place at the retro-wedge flank. The slope angles increase, simultaneously, to maximum values of α_1~19° and α_2~17° after 50-55 km of shortening. Afterwards, slope angles decrease again until the wedge becomes stable after ~73 km shortening (Fig. 33).

After 80 km shortening, the crest position is located at ~30 mkm, with the thrust evolution and extension being more distinct at the pro-wedge than at the retro-wedge. However, between 80 km and 100 km of shortening, both the pro-wedge flank and the retro-wedge flank move far inwards due to the development of two backthrusts with distinct offsets. For the first time, the whole material between ~50 mkm and ~150 mkm is uplifted, which is shown by the whole range of steep particles paths (Fig. 35). Consequently, the crest has moved far inwards. After 119 km of shortening, highest uplift is observed at ~73 mkm (Fig. 35).

In contrast to experiment Sc1, this wedge evolves widely extended. Both, the pro-wedge flank and the retro-wedge flank of the wedge evolve similarly flat with angles of α_1~7° and α_2~8° (Fig. 33). A group of backthrusts cut out at the retro-wedge flank which are frequently reactivated and evolve with small offsets as back-kinks. The most inward positioned backthrust migrates along the lower crustal fragment. At the highest point of this fragment, the latter backthrust is cut by a flat forethrust and runs further inwards, now parallel to the indenter, but in a distinct distance (Fig. 32).

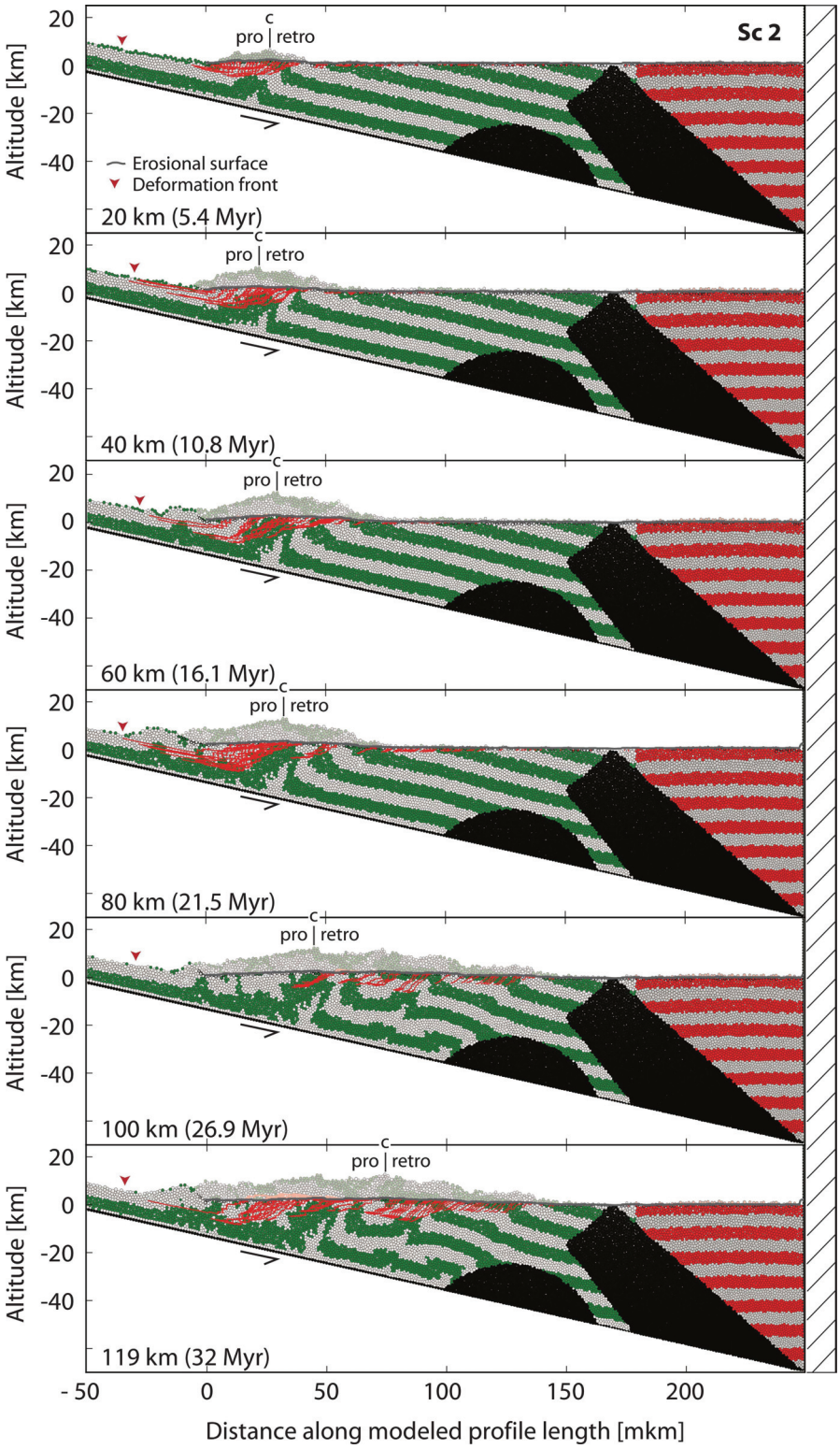

Fig. 35.: Particle setting of experiment Sc2 after 20 km, 40 km, 60 km, 80 km, 100 km and 119 km shortening. For reasons of clarity, the eroded section (calculated after simulation) is grayed out. Only those particles are selected, which crop out at the erosional surface at the time of sampling. (Red lines) particle paths for selected particles reaching erosional surface (gray line; see sec. 3.3.1). (mkm) model km, i.e. distance along modeled profile length. (c) crest. (pro) pro-wedge. (retro) retro wedge.

4.2.2. Thermal history

After 20 km shortening, a U-shaped distribution of cooling ages is established, similarly to the evolution of experiment Sc1 (Fig. 36). Nonetheless, youngest cooling ages are found more outwards (15-30 mkm) as compared to experiment Sc1, related to the observed back- and forethrusts in that region. Within the section of young cooling ages, two subregions can be distinguished with AFT ages clustering around 3 Ma (15-20 mkm) and 3.5 Ma (25-30 mkm). The youngest AFT age (2.4 Ma), however, is predicted at 33 mkm. The time-temperature history of the corresponding particle shows its affiliation to the grouping of particles further inwards with slow cooling for 3 Myr of orogeny, followed fast cooling. However, slow cooling of this particle occurs at temperatures between ~120 °C and 110 °C (i.e. above the temperatures of the partial annealing zone of the AFT system), while the adjacent particles are already positioned at ~60 °C at the beginning of the simulation (thus track annealing has only subordinate impact). Therefore, we interpret this youngest AFT age as model artifact. Apart from the profile section with young AFT ages (15-30 mkm), AFT ages are distributed homogeneously (~5.5 Ma). Exhumation starts at the very start of the profile. Further on, the distributions of AFT ages of experiment Sc2 (Fig. 36) are more complex in comparison to Sc1: Both subregions in the section with young cooling ages are still roughly preserved after 40 km shortening (Fig. 36). However, while AFT ages in the center of this section (23-30 mkm) cluster around 6 Ma and thus grow older with respect to the previous time-slice, youngest ages shift outwards (3.1 Ma at 13 mkm) and indicate constant and fast cooling (i.e. strong deformation) along the pro-wedge flank. Contemporaneously, the U-shaped distribution is also extended inwards until 42 mkm. Within this section (30-42 mkm), youngest cooling ages are calculated at 40 mkm, indicating deformation along the retro-wedge flank.

Shortening of 60 km and 80 km establishes this bimodal distribution of AFT ages with the frontal region of younger AFT ages shifting back and forth to 22 mkm (5.9 Ma) and 18 mkm (9 Ma), while the outwards region of younger AFT ages slowly migrates inwards to 48 mkm (4.6 Ma) and 50 mkm (8.3 Ma), (Fig. 36). The last two time-slices (100 km and 119 km shortening) depict the same AFT patterns as before, with a bimodal cooling age distribution at the start of the profile, although it is shifted by some 15 mkm in inward direction and synthetic AFT data are of poor quality until 60 mkm (cf. evaluation of time-temperature histories in sec. 3.3.2). Additionally, two more regions of very young AFT ages develop from 75 mkm to 130 mkm (Fig. 36). Cooling ages of this outward positioned section mainly cluster around 3-4 Ma and 7-8 Ma after 100 km and 119 km shortening, respectively. Still they are not homogeneously distributed, but rather in a further bimodal curving, culminating in the center at ~110 mkm. Thus, after 119 km shortening, the synthetic AFT ages indicate an uneven cooling style along the profile, alternating between regions of fast and slow cooling.

Exemplarily, Fig. 37 depicts such alternating AFT ages with three adjacent groupings of particles: Section A comprises particles, yielding young AFT ages after 100 km shortening, section B follows inwards to section A and comprises particles with old AFT ages. Finally, section C is adjacent to section B and comprises particles, which yield successively younger AFT ages with

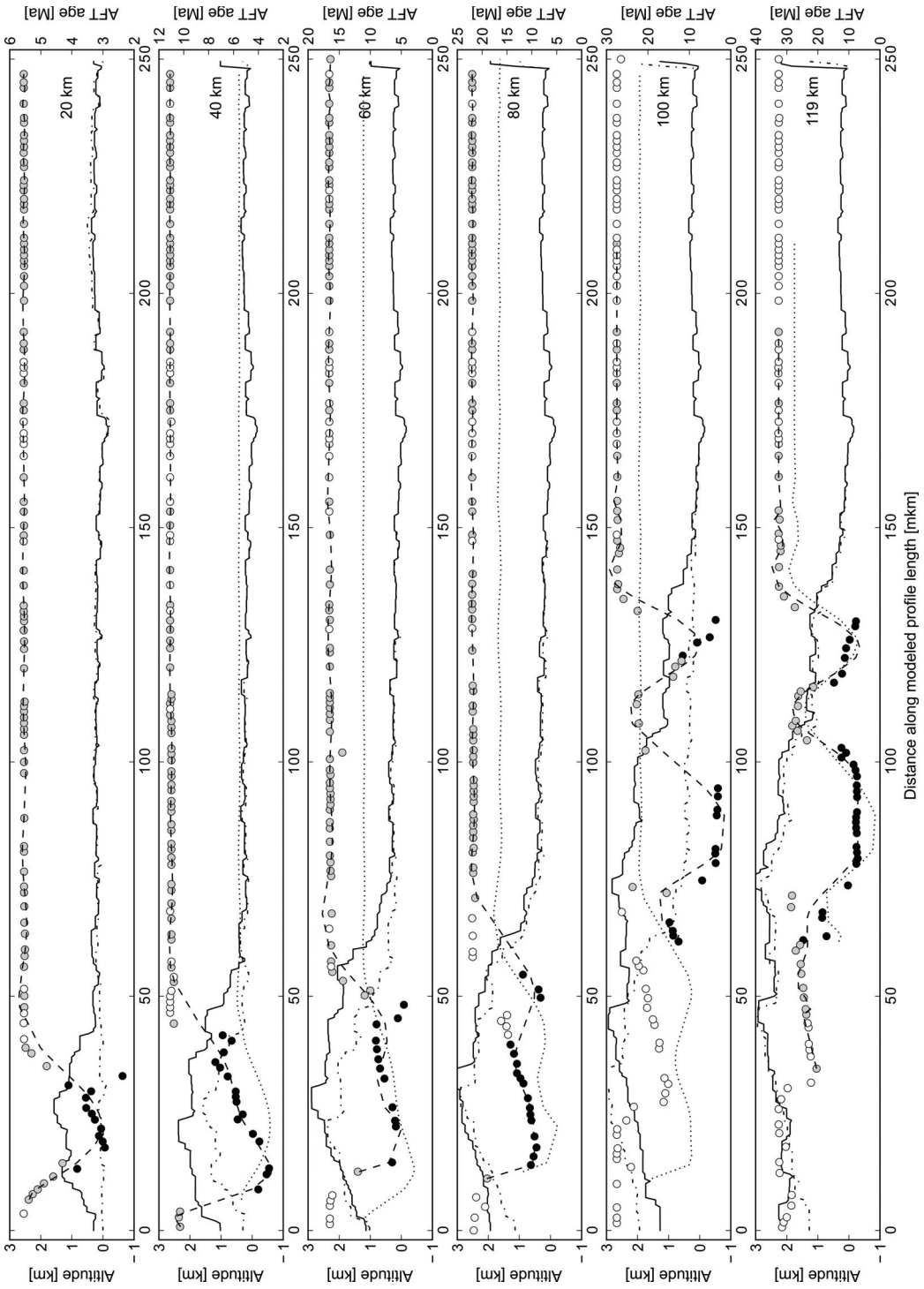

Fig. 36.: Evolution of the computed erosional surface and the synthetic AFT cooling ages of Sc2 through time. (Signatures see Fig. 34)

increasing distance to section B. Comparing the gradients of displacement within the wedge after 80 km and 100 km shortening, the W-shaped cooling age pattern between 80 mkm and 130 mkm (Fig. 36 and second frame from top in Fig. 37) can be associated with the development of backthrusts along the retro-wedge flank (Fig. 37 bottommost frame).

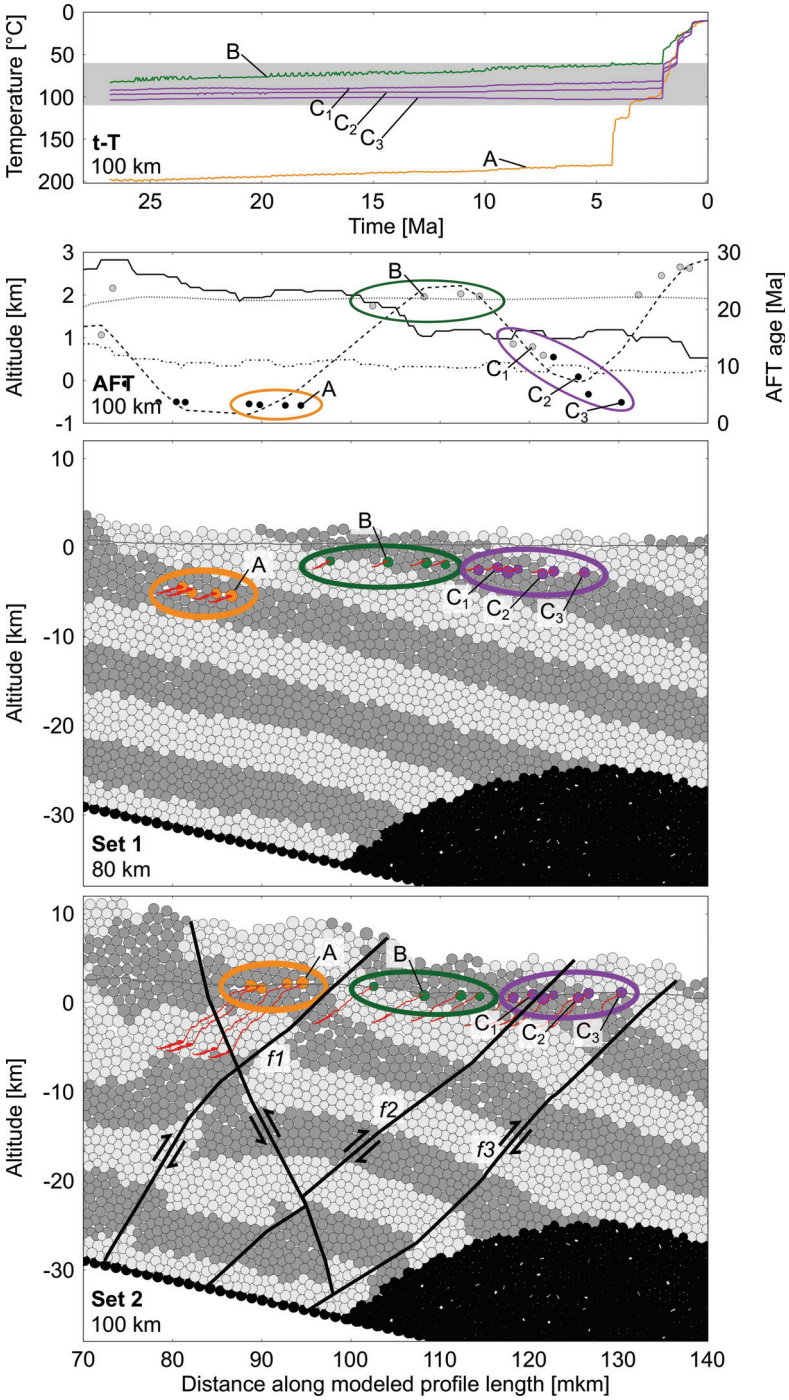

Fig. 37.: Synthetic AFT cooling ages reveal mode and rate of modeled fault systems. From top to bottom: t-T: Time-temperature paths of different particle groupings after 100 km shortening; AFT: clipping from Fig. 36 (signatures see Fig. 34) with adjacent AFT ages simultaneously indicating three different modes of exhumation; Set1: particle setting after 80 km shortening, observed particle groupings are marked; Set2: particle setting after 100 km shortening, observed particle groupings are marked, faults are observed from structural analyses.

Section A comprises particles, which are rapidly exhumed along a major backthrust (f1 in Fig. 37) between 80 km and 100 km shortening. In contrast, particles of section B, being located

in the footwall of the first mentioned fault, are hardly exhumed, at all. The third grouping of particles (section C) shows decreasing cooling ages with increasing proximity to the most inward located major fault in the clipping (f3 in Fig. 37), indicating their hanging wall position. However, the intermediate fault in the clipping of Fig. 37 (f2), located in the middle of the two major faults, intersects section C, but does not affect the cooling ages of the grouping. The amount of vertical offset (negligible at the central fault), therefore, crucially impacts the rate of exhumation and thus, the synthetic AFT age.

4.3. Experiment Sc3 (high frictional detachment and indenter)

4.3.1. Mechanical and kinematic evolution

In order to investigate the effect of deep seated solid bodies in the model setup, the lower crustal fragment is not integrated into experiment Sc3 (Figs. 27, 38). Apart from this, parametrization of Sc3 equals Sc1. Accordingly, the thrust system evolves similarly to that in Sc1 due to the high frictional basal detachment. In this case, after 20 km shortening the double-vergent wedge evolves between a dominant back-kink (~55° dipping angle) and a flat forethrusts (~19° dipping angle) with a second corresponding smaller back-kink (~59° dipping angle). The dominant back-kink runs parallel to the indenter, uplifting the retro-wedge (Fig 7-Sc3). Consequently, the retro flank evolves slightly steeper (α_2~12°) than the frontal flank (α_1~10°), where underthrusting along the flat forethrusts occurs (i.e. basal accretion). This imbalance in uplift is reflected by the particle paths showing steeper curves next to the indenter. The crest of the wedge is located at ~140 mkm (Fig. 38). Between 20 km and 40 km shortening, uplift along the pro-wedge becomes more pronounced, associated with a distinct offset along the forethrust. This goes along with a slope angle increase to α_1~22° and to α_2~21.5° and an outward shift of the crest to ~90 mkm. Corresponding, the particle paths become steeper along the pro-wedge flank.

With ongoing shortening, uplift is controlled by the combination of basal accretion along the forethrusts cropping out along the pro-wedge flank and backthrusting along the major back-kink. Migrating inwards, the steep forethrusts along the pro-wedge flank are rotated to flatter rising forethrusts (~15°) and frequently reactivated as out-of-sequence thrusts (Fig. 32). Underthrusting along the new forethrusts at the DF goes along with an alternation of de- and increasing slope angles. However, after 60 km shortening, the slope angles reach values of α_1~16.5° at the pro-wedge and α_2~18.5° at the retro-wedge flank. Afterwards, slope angle variations are smaller, but no adjustment occurs in contrast to the previous experiments.

Comparing the results with those of experiment Sc1, the wedge has much more space to evolve which results in a wider extended wedge structure. Due to the missing crustal fragment and the associated space on hand, the slope angle of the pro-wedge evolves slightly flatter (α_1~15°) than in the reference experiment Sc1. Similar to Sc1, one main backthrust is observed which crops out at the retro-wedge flank. This frequently reactivated thrust runs parallel and in a small distance to the indenter and shows a larger offset than the corresponding thrusts in Sc1. Thus, the retro-wedge flank develops steeper (α_2~18°. Fig. 32).

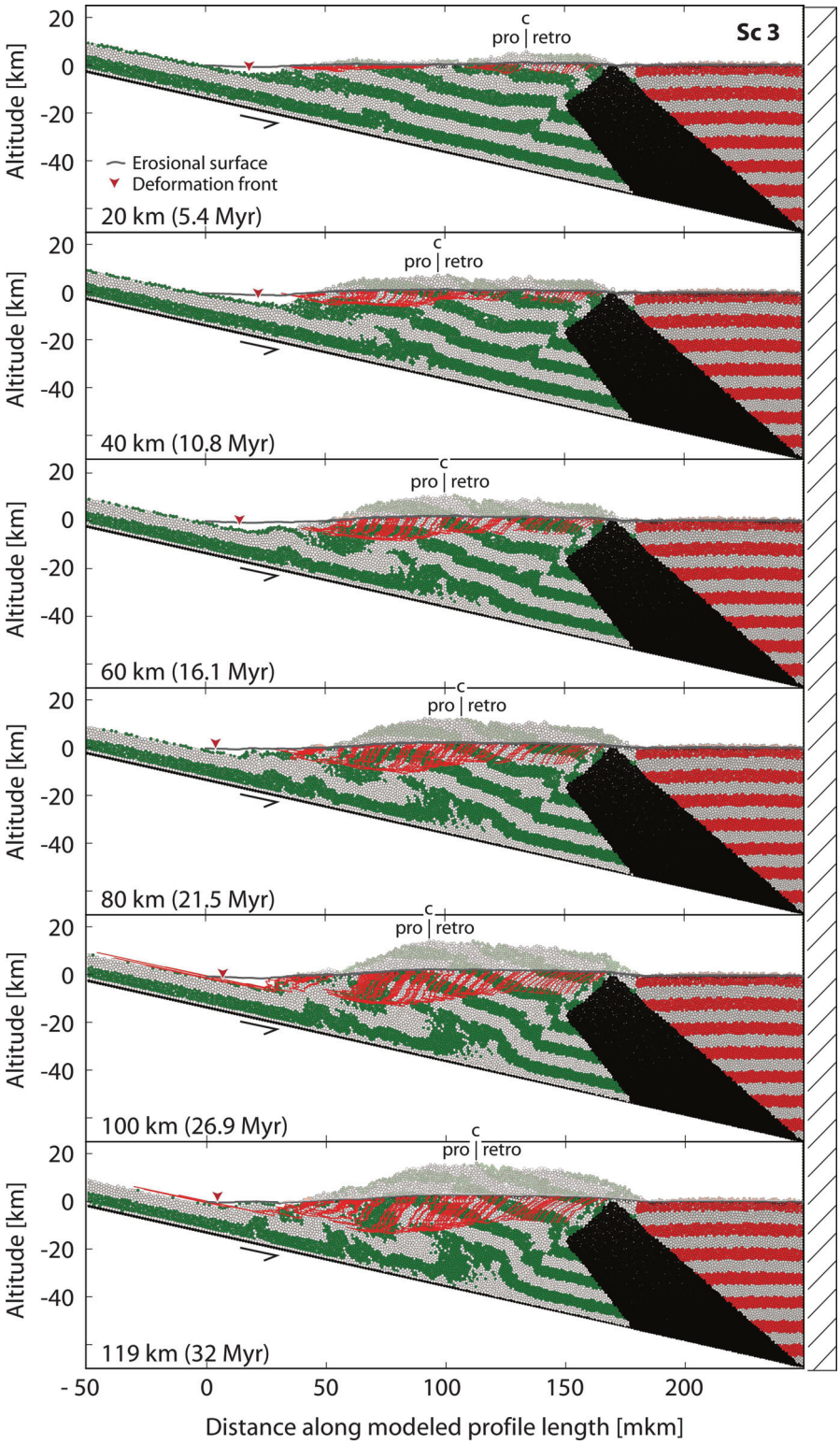

Fig. 38.: Particle setting of experiment Sc3 after 20 km, 40 km, 60 km, 80 km, 100 km and 119 km shortening. For reasons of clarity, the eroded section (calculated after simulation) is grayed out. Only those particles are selected, which crop out at the erosional surface at the time of sampling. (Red lines) particle paths for selected particles reaching erosional surface (gray line; see sec. 3.3.1). (mkm) model km, i.e. distance along modeled profile length. (c) crest. (pro) pro-wedge. (retro) retro wedge.

4.3.2. Thermal history

Youngest AFT ages range between 2 Ma and 3 Ma in experiment Sc3 after 20 km shortening (Fig. 39). In contrast to the previous experiments Sc1 and Sc2, the section with young cooling ages is far more inwards (127-157 mkm) and cooling ages are W-shapely distributed between 127-130 mkm and 146-157 mkm, pointing to enhanced deformation near the indenter. In between and towards both flanks of the particle wedge, cooling ages increase up to 4.7 Ma and 5.5 Ma, respectively.

This first major pattern is mostly preserved after 40 km shortening with young AFT ages (~8.4 Ma) at 125 mkm and a well-defined U-shaped distribution of AFT ages between 140 mkm and 161 mkm with AFT ages down to 6.8 Ma. An even more pronounced region with AFT ages as young as 4.1 Ma evolves between 57 mkm and 100 mkm as a second major region (Fig. 39). On the basis of the structural analysis (last section), young AFT ages in this second region (i.e. along the pro-wedge flank) can be related to pro-wedge deformation associated with underthrusting along flat forethrusts.

After 60 km shortening, both major regions begin to merge into a large and rather flat two-step distribution of AFT ages with young cooling ages (10-12 Ma) between 130 mkm and 164 mkm and even younger ages (6-7 Ma) between 68 mkm and 121 mkm (Fig. 39). A minimum age of 6.2 Ma is predicted at 85 mkm.

From 80 km on to 119 km shortening, one major pattern dominates the AFT age distribution: Between 65 mkm and 164 mkm, cooling ages form a U-shape with youngest ages in the center and older ages towards the pro-wedge flank and the retro-wedge flank (Fig. 39). After 80 km, 100 km and 119 km shortening, youngest cooling ages are predicted at 102 mkm (7 Ma), 103 mkm (6 Ma) and both at 82 mkm and 102 mkm (7.4 Ma), respectively. Besides, young AFT ages (~6 Ma, 6-10 Ma and 11-16 Ma) are also calculated at the very start of the pro-wedge flank (35-50 mkm) for these time slices, partially being even younger than in the center of the profile, reflecting deformation at the pro-wedge flank related to newly established forethrusts.

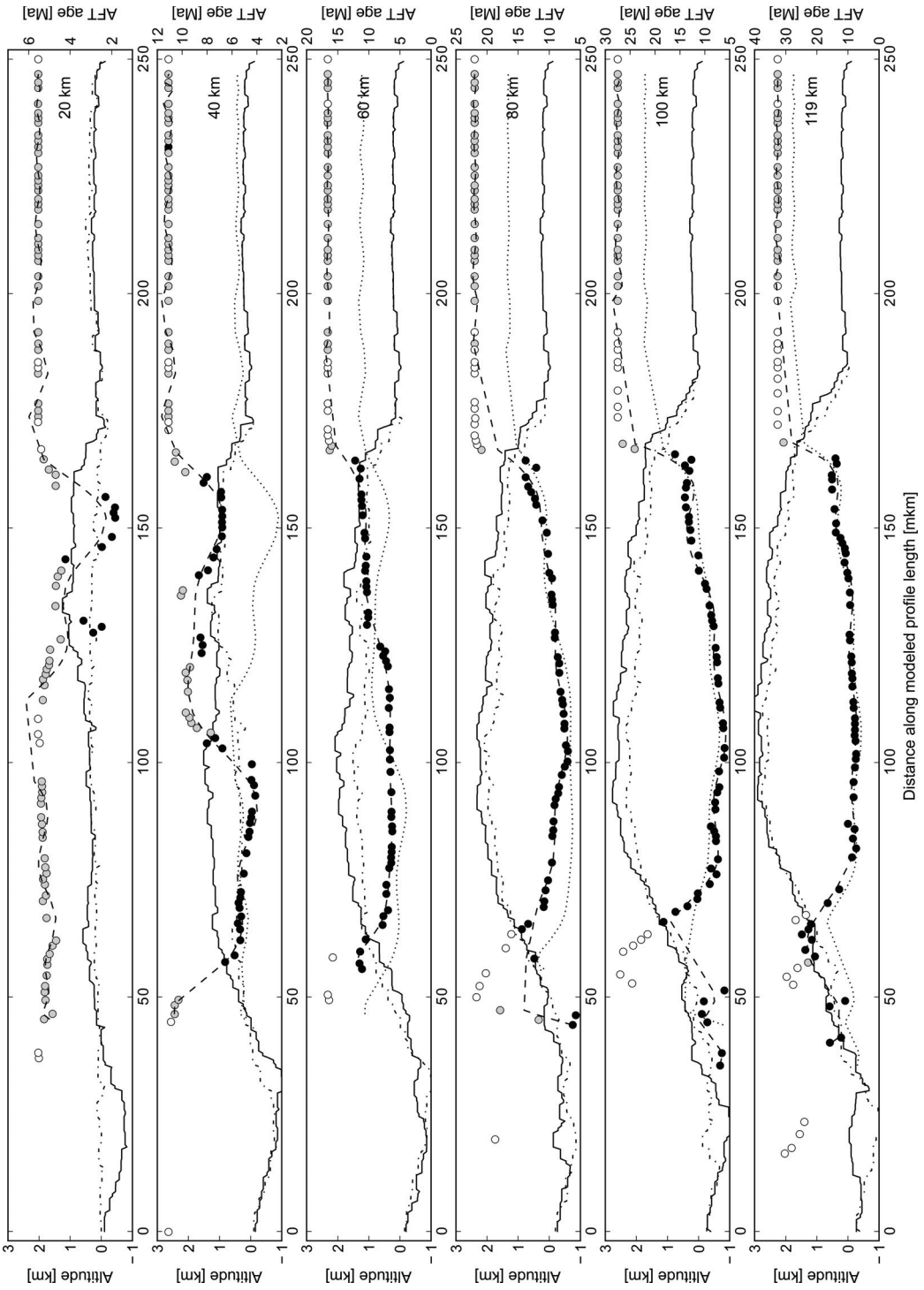

Fig. 39.: Evolution of the computed erosional surface and the synthetic AFT cooling ages of Sc3 through time. (Signatures see Fig. 34)

5. Discussion

In all three experiments Sc1, Sc2 and Sc3 double-vergent wedges evolve with a pro- and a retro-wedge flank due to the movement of the basal detachment. Structural evolution, wedge topography, and mass moving patterns of these wedges are affected by the simulated indenter, the lower crustal fragment and the basal friction value. This will be discussed in detail also in comparison with previous wedge studies (e.g., Willett et al., 1993; Storti et al., 2000) in the following sections. Therein, we allocate the evolution of the simulated particle wedges, reinforced by the synthetic AFT cooling age patterns to orogenic development stages 1, 2 and 3 according to Mandl (1988), Willett et al. (1993) and Storti et al. (2000). In general, AFT ages are notably younger after 20 km shortening, compared to the later storages, what is expected as the particles to not inherit temperature information before the model run begins. Synthetic cooling ages cannot exceed the range of the modeled time, while corresponding real samples, probably would have yielded older cooling ages. Instead of interpreting the range of ages, we concentrate on the shape of their distribution. Since all AFT cooling ages are computed from particles on the erosional surface, the relative difference between the ages are interpreted as differences in exhumation rates of the samples cropping out adjacent to each other. Consequently, the youngest ages within one time slice suggest highest erosion or denudation rates and, therefore, locate the main deformation at that amount of shortening.

5.1. Influence of detachment strength (coefficient of friction of lower crust)

Corresponding with the basal friction value of the detachment, the double-vergent wedge in Sc1 grows by underthrusting due to the high frictional décollement. In contrast, the wedge in Sc2 evolves as a result of the weak décollement by frontal accretion of imbricated units. This result is in agreement with a various amount of analog and numerical experiments dealing with the importance of the basal friction at the décollement (e.g., Davis et al., 1983; Mulugeta, 1988; Moore, 1989; Hardy et al., 1998; Burbidge and Braun, 2002; Lohrmann et al., 2003; Ellis et al., 2004; Gutscher et al., 1998).

Above a high frictional detachment (Sc1), main deformation takes place at the pro-wedge flank at the start of the experiment, without backthrusting along the retro-wedge. If we follow the description of Storti et al. (2000) in this experiment begins with stage 2 is recorded. The consequent uplift of the central wedge results in youngest cooling ages along that region. Therefore, the AFT data correctly reflect the structural evolution of the DEM model (Fig. 34).

The kinetic regime does not change for the whole model run, with main deformation along the pro-wedge flank, indicating that Sc1 simulates only stage 2 (Willett et al., 1993). In this case of high basal friction, the material is stronger compressed and pressed against both the lower crustal fragment and the indenter as compared to Sc2. The décollement strength of Sc1, therefore, prevents the evolution of stage 1 and stage 3, where deformation occurs at the retro-wedge. This also corresponds to AFT age patterns, which indicate a simple pattern with highest exhumation rates in the center of the wedge which are probably triggered by the continuous underthrusting.

Furthermore, forward jumps of the pro-wedge flanks go along with local exhumation impulses (cf. erosional surface evolution in Fig. 34), which are reported in the AFT age patterns with youngest cooling ages in the region of the latest uplift structure additional to young cooling ages along the center of the wedge (Fig. 34). Subsequent underthrusting can be monitored by the successive merging of these regions with young cooling ages between 80 km and 119 km shortening. At the beginning of experiment Sc2, the main activity takes place at the retro-wedge flank due to the development of relatively steep fore- and backthrusts. These structures evolve symmetrically, indicating reduced stress caused by the lower basal friction (Davis et al., 1983). Resulting, the wedge rather grows in horizontal direction as compared to Sc1 and the initial deformation occurs long way to the collisional zone. This phase can be allocated with stage 1 where dominant block uplift takes place. Similarly as in experiment Sc1, the structural interpretation can also be monitored by the AFT age patterns which indicate deformation and high exhumation rates along both flanks of the wedge in accordance with the most uplifted regions. After 40 km shortening the wedge reaches stage 2 with active thrusting at the DF and at the retro-flank. Consequently, the wedge evolves bidirectionally. The AFT ages also depict this outward trend with rapid exhumation along the pro-wedge flank (Fig. 36).

Generally, inverse thermal history modeling of a given track density and track length distribution yields information about the variation of the cooling / exhumation rate through time (e.g., Gallagher et al., 1998). This is also true for the succession of synthetic AFT ages derived for different time slices of the numerical ‘sandbox’ experiments. The younger the cooling age of a time slice the faster is the corresponding exhumation rate, as can be exemplarily seen in the results of Sc2 after 60 km shortening (Fig. 34): Though both flanks are simultaneously deformed, the amount of uplift and the associated exhumation along the retro-wedge flank distinctly exceeds uplift along the pro-wedge flank (note the dash-dotted line, depicting the erosional surface of the last time slice). Consequently, AFT ages along the center and pro-wedge flank are older than those along the retro-wedge flank, but younger than the majority of cooling ages, reflecting the ongoing (but compared to the retro-wedge weaker) deformation along the pro-wedge flank and uplift of the central part of the wedge.

Further on, continuous frontal accretion triggers uplift and rearrangement of material within the wedge along steep forethrusts. Additionally, also the retro-wedge flank is uplifted due to the slight compression induced by the box bottom. In this stage the central part of the wedge is no longer uplifted. Deformation and uplift is limited to the wedge flanks. This attitude of the structural wedge system indicates that the stage 3 is reached, including the development of

a new kink at the retro-wedge flank. Hence, the reduced basal friction in Sc2 allows that the wedge develops all three stages (Willett et al., 1993; Storti et al., 2000).

Synthetic AFT analyses give a detailed picture about the locations of uplifted regions and the amount of uplift rates depending on the décollement strength. Consequently, patterns of synthetic AFT ages can support the analysis of a wedge growing within a DEM model.

5.1.1. Influence of deep seated geometries

The wedges in experiment Sc1 and Sc3 grow under identical conditions, regarding the parameterization. The crucial difference between the experiments is the absence of the lower crustal fragment in Sc3 in the model setup. The wedge in Sc3 grows in an inward direction after 20 km of shortening, what can be interpreted as stage 1 (Storti et al., 2000), similarly to Sc2. Youngest AFT ages after 20 km shortening are computed at the collisional zone near the implemented indenter, and thus, monitor the main deformation along the retro-wedge flank. After 40 km shortening stage 2 is reached in Sc3 with underthrusting of incoming material along flat forethrusts at the pro-wedge flank – similar to the observations in Sc1 (Fig. 32). Accordingly, the synthetic cooling age pattern reflects the evolution with youngest AFT ages further outwards. Nevertheless, also the first deformed region near the indenter preserves the early cooling history with local minimum ages at 125 mkm and 151 mkm after 40 km shortening. The wedge extends through to the indenter, and consequently, has no further space to spread inwards. As result, a double-vergent wedge evolves with highest uplift in the center. That is also conveyed by the synthetic cooling ages. From 60 km shortening on, AFT ages are distributed in a unimodal U-shaped pattern along the simulated wedge indicating highest exhumation rates in the center.

Due to the missing crustal fragment, stage 1 is established in Sc3, before stage 2 begins with basal accretion along the pro-wedge flank. Comparable to the evolution in Sc1, the fixed indenter restricts the space for the wedge to grow and, hence, prevents that the wedge reaches the last stage. Synthetic AFT age patterns change depending on the geometry of the initial numerical model. In this case the missing of the lower crustal fragment lead to a flatter evolution of the AFT pattern in Sc3 as compared to Sc1. Furthermore, a stepwise uplift can be inferred in Sc3. Hence, uplift slowly decreases with increasing proximity to the indenter. Also in Sc1, uplift decreases towards the indenter. The lower crustal fragment, however, implemented in Sc1 leads to much steeper flanks of the strongly uplifted central region in Sc1 as compared to Sc3, where uplift impacts a much wider region as a result of the missing lower crustal fragment. Resulting, the geometrical changes of the deep crustal conditions in the numerical experiment have important influence on the AFT age pattern. The more compression occurs from the back side (in case of Sc1 from a composition of the indenter and the lower crustal fragment), the steeper the AFT age patterns evolve, whereas an oblique back-side (as in Sc3) allows a further spreading of the wedge with a more balanced uplift and resulting smoother AFT age patterns. This also has an influence on the evolutionary stages as more compression can prevent the evolution of the third stage, where deformation of the retro-flank occurs. Consequently, the AFT age patterns can help to assess the geometrical initial conditions of the backstops within the deep crust. Nevertheless,

additional information and more numerical tests are necessary to get an overall picture on which deep crustal effects and parameters have which effect on the particle paths and exhumation patterns.

6. Conclusion

We couple numerical 'sandbox' modeling and AFT thermochronology to investigate large-scale structures within a growing orogenic wedge, and focus on their effect regarding the exhumation processes.

The granular model approach allows getting information about particle position and movements. This enables a comprehensive qualitative structural analysis. Moreover, we calculated erosion and append temperature as a parameter to the particles of the numerical 'sandbox', thereby creating an interface between the granular model approach and apatite fission track thermochronology. After deriving synthetic AFT cooling ages from the time-temperature histories of numerical particles, the spatial distribution of these ages allows for a quantitative description and evaluation of the influence of deep seated (i.e. lower crustal) structures on near-surface (i.e. upper crustal) processes in addition to the qualitative insights into the structural evolution of the modeled wedge, revealed by the granular model approach.

Three numerical simulations with different deep crustal initial conditions were undertaken, in which either the décollement strength or the geometry (in form of a fixed lower crustal fragment) is varied. We could verify that the particle wedges grew by frontal accretion over a low frictional décollement and by basal accretion over a higher frictional décollement. High basal friction results in far underthrusting of the material and leads to a well-marked U-shaped AFT pattern with most rapid cooling in the central region of the wedge. Outwards jumps of the pro-wedge, are reflected by young AFT ages in that region. In contrast, under low frictional conditions, lower uplift occurs and the AFT ages are either W-shaped distributed or as a series of U-shaped patterns over the whole accretion phases.

In coherence with the presence or absence of the crustal fragment, the double-vergent wedges have reduced or extended space to grow, respectively, as expected with regard to previous studies. Accordingly, synthetic AFT ages show steeper or flatter U-shaped distributions with or without the compression induced by the lower crustal fragment, respectively.

Thus, synthetic cooling ages reflect exactly the structural evolution, as they allow for gaining a detailed picture where and when uplift occurs within the models. The synthetic AFT ages are sensitive to the current deformation stage, the exhumation rate and reflect the initial state of the deep seated conditions. Furthermore, former structural evolution is preserved in the AFT patterns, thus, both, the current stage and the evolution hitherto is depicted from the synthetic thermochronologic data.

Summing up: From a computed erosional surface, temperature values can be derived for any particle at any position at any time in the model run. The time-temperature history of selected

and tracked particles can be reconstructed, which in turn can be used for forward thermal history modeling, resulting in synthetic cooling ages.

(I) Synthetic AFT-patterns support the structural analysis and interpretation of a structural DEM model.

(II) We are able to detect and quantify the effects of deep seated structural geometries and rheologies on upper crustal structures during the evolution of a double-vergent orogenic wedge. Therein, we found that high compression or pressure results in steep AFT patterns, whereas low compression results in a moderate trend. Additionally, the AFT patterns hold information on uplifted regions and, therewith, on the accretion mechanism, from with characteristic properties of the décollement can be derived.

Acknowledgements

This study is part of the EUROCORES TOPO-EUROPE project from the European Science Foundation and was funded by the German Science Foundation (DfG-Research Center / Cluster of Excellence ‘The Ocean in the Earth System’ and DfG project SP673/5-1). We would like to thank Lisa-Carmen Eckhart, Sebastian Trüttner and Leonard Rossmann (University of Bremen) for support during data processing.

Paper Contribution 3:
Describing orogenic wedges by a combination of numerical 'sandbox' models and low-temperature thermochronology. II: Applications to upper crustal processes of the European Central Alps

Authors: Simon Elfert, Linda Wenk, Katrin Huhn and Cornelia Spiegel
In preparation for submission to Journal of Geophysical Research.
Intended submission: May/June, 2014

Abstract

Apatite fission track (AFT) thermochronology is a standard method for describing the tectonic evolution of the upper crust. It allows reconstructing cooling histories of rocks, which are transferred into exhumation histories and interpreted in terms of the geodynamic evolution. Here we present an approach for refining these interpretations by combining AFT thermochronology with numerical sandbox experiments. Unlike AFT thermochronology, numerical sandbox modeling allows tracking pathways of single particles as they move through an orogenic wedge. We test this combined approach for the example of the Lepontine Dome of the Central Alps. In a first step, we used numerical sandbox modeling for reproducing the main structural elements of the Central Alps, as observed from the field and from seismic reflection profiles. AFT data calculated from the particle pathways of the sandbox matched those actually observed from the Lepontine Dome regarding age range and pattern. Next we tested different scenarios of valley incision and in how far AFT thermochronology is able to resolve these. The best match between AFT data calculated from the sandbox and those observed from the Central Alps was achieved for valley incision starting at 5 Ma. Finally, we analysed particle pathways associated with different structural positions along the modeled profile in terms of their movement rates and directions. In the center of the modeled culmination (interpreted as being equivalent to the Lepontine Dome) pathways are characterized by continuous and mostly vertical movements. The overall displacement rate is thus mirrored by the exhumation rate derived from AFT thermochronology. Along the flanks of the culmination, by contrast, movement was equally fast or even faster than in the center, but more episodic in style and with a strong lateral component. Exhumation rates derived from such a setting would be slow and may erroneously be interpreted

as reflecting tectonic quiescence, while in fact they are associated with a highly active orogenic environment.

Keywords: Numerical ‘sandbox’; apatite fission track (AFT) thermochronology, Neogene exhumation, European Central Alps

1. Introduction

In a first paper, we combined numerical 'sandbox' modeling with low-temperature thermochronology and showed that, generally, geometries and mechanic properties of the lower crust directly influence cooling and exhumation patterns of the upper crust (Wenk et al., in prep.). Apart from quantifying this influence, other advantages of this methodological combination are that it is sensitive for testing different models of erosion and incision, and that it allows to visualize particle pathways, at least along two-dimensional profiles. Traditionally, interpretations of low-temperature thermochronological ages are based on transferring cooling rates into exhumation rates assuming a geothermal gradient. This concept inevitably only considers vertical particle paths, since lateral movements may not be associated with temperature changes. Numerical 'sandbox' models on the other hand, also take lateral movements (i.e. 2D) into account and may thus provide a more refined picture of the dynamics of orogenic wedges.

In this paper we apply the concept of combining numerical 'sandbox' modeling with low-temperature thermochronology to the European Central Alps, particularly to the area of the Lepontine Dome. The Lepontine Dome is situated in the core region of the Central Alps and was intensively studied in the past regarding its deep structures, its kinematic and metamorphic evolution, as well as its erosion and exhumation history (e.g., Niggli, 1960; Milnes, 1974; Frey and Ferreiro Mählmann, 1999; Maxelon and Mancktelow, 2005; Vernon et al., 2008). In a first step, we use a numerical 'sandbox' experiment for reproducing the structural evolution of the Central Alps along the deep seismic profile NFP20-East (Pfiffner et al., 1988, 1990, 1997; Schmid et al., 1996, 2004b; Diehl et al., 2009), as described by the kinematic model of Schmid et al. (1996). We derive synthetic apatite fission track (AFT) dates from the numerical 'sandbox' model and compare them to data observed from the same region (Elfert et al., 2013). In a second step, we use the numerical 'sandbox' experiment for testing different hypotheses for timing of valley incision to infer the development of the drainage system, as described in the literature (e.g., Kühni and Pfiffner, 2001; Kuhlemann et al., 2001; Spiegel et al., 2001; Schlunegger et al., 2007; Garzanti and Malusa, 2008). Specifically, we test three scenarios involving onset of valley incision in Oligocene, Pliocene, and Pleistocene times. Thirdly, we extract particle pathways from the numerical 'sandbox' model, relate the movement rates of the particles to their exhumation rates and compare the findings with the observed AFT data. This allows adding the lateral component of rock movement to the geodynamic evolution interpreted from low-temperature thermochronology data.

2. Geological setting

2.1. The European Central Alps

Basically, the Central Alps comprise Helvetic and Penninc units and are separated from the Southern Alps by the Insubric Line (e.g., Schmid et al., 1989, 2004a, Fig. 40). The Helvetic realm to the north represents the European margin, while the Southern Alps are of Adriatic origin. The Penninic realm (in between the Helvetic units and the Southern Alps) is derived from oceanic lithosphere of former oceanic basins (Valais ocean, Piedmont-Ligurian ocean) and a continental micro-plate (the Briançonnais terrain, formerly situated in between the aforementioned oceanic basins). The Penninic units and parts of the European distal margin (called Subpenninic units, cf. Schmid et al., 2004a) were subducted southwards below the Adriatic plate between the Cretaceous and the Eocene, arranged as nappe stack in the early Oligocene and expelled after slab breakoff and the associated isostatic imbalance (Von Blanckenburg and Davies, 1995; Schmid et al., 2004a,b). In the core of the Central Alps, the (Sub-)Penninic nappes stack is horizontally aligned with the Gotthard nappe right at the bottom (Berger et al., 2005). Later in this paper, we will refer to the (structurally lower) Leventina nappe and the adjacent (structurally higher) Adula nappe, which are both situated in the eastern Lepontine Dome (e.g., Berger et al., 2005).

Related to backthrusting along the Insubric Line, the Adriatic lower crust was depressed, and delaminated the upper from the lower European crust, acting as indenter from Oligocene times on (Müller, 1989; Von Blanckenburg and Davies, 1995; Schmid et al., 2004b).

Due to ongoing convergence, the European Alps evolved as a double-vergent orogenic wedge (Kühni and Pfiffner, 2001; Schmid et al., 2004b). The north-vergent pro-wedge, comprising the formerly subducted Penninic and Subpenninic nappes, overthrust the Helvetic realm of stable Europe (Fig. 40, Schmid et al., 1996, 2004b). To the north the Aar external massif (Helvetic realm) and the Gotthard nappe form the Aar-Gotthard massif (note that the Gotthard is not a 'massif' s.str., but is interpreted as backfolded nappe; cf. Schmid et al., 2004a). The Lepontine Dome is situated south of the Aar-Gotthard massif. Structural studies found evidence for complex large-scale folding and thrusting within the Lepontine Alps after nappe emplacement until late Miocene times (e.g., Milnes, 1974; Merle et al., 1989; Maxelon and Mancktelow, 2005). Among others, a belt of steep synclines with north dipping foliations (also called the northern steepbelt) evolved by backfolding and backthrusting south of the Aar-Gotthard massif during this Miocene deformation phase (Maxelon and Mancktelow, 2005; Wiederkehr et al., 2008).

With the Aar-Gotthard massif to the north and the Lepontine Dome to the south, the Central Alps form two mountain ranges in terms of long-wavelength topography. Extensional faults

border the Lepontine Dome to the west (Rhone-Simplon fault) and to the east (Forcola fault zone and Turba Mylonite zone; Fig. 40). Between 25 Ma and 13 Ma the Alps were affected by large scale orogen parallel extension, resulting in tectonic unroofing of the Lepontine Alps (Mancktelow, 1992; Schlunegger and Willett, 1999; Frisch et al., 2000). At ~15-14 Ma, the Subpenninic basement units of the Lepontine Dome were exposed (Spiegel et al., 2000, 2001).

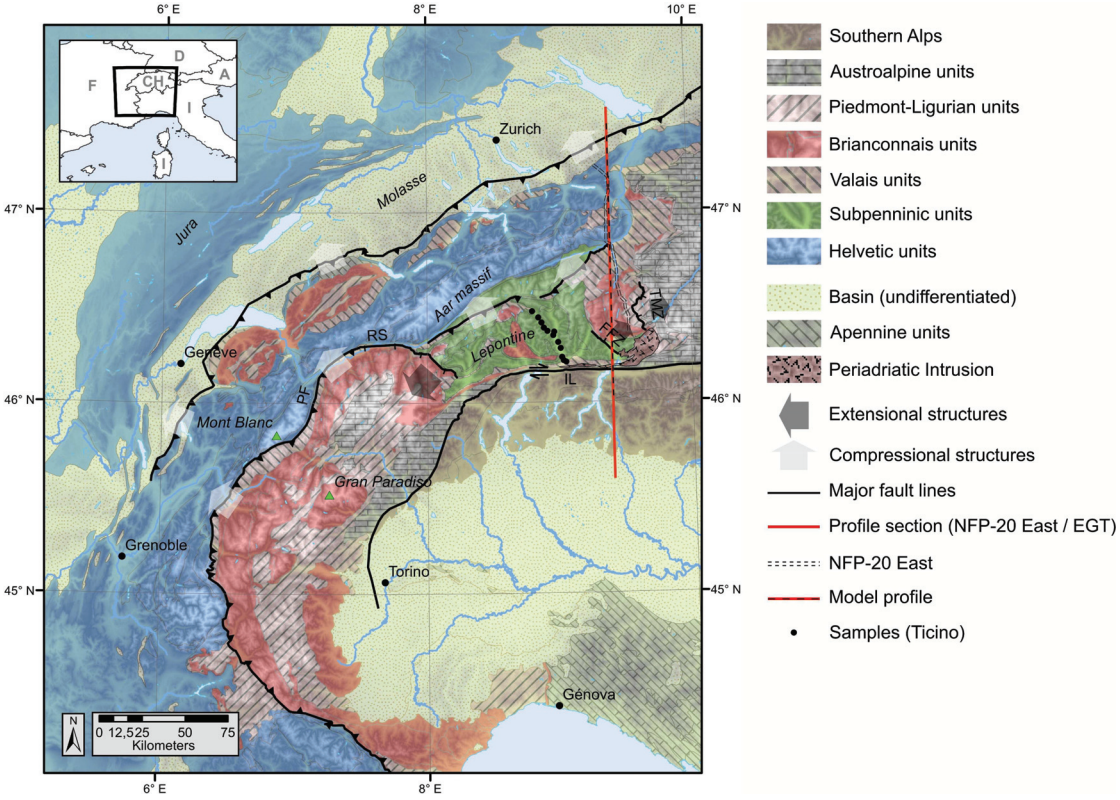

Fig. 40.: Overview map with major tectonic units of the European Western and Central Alps. Fault zones: FFZ: Forcola Fault Zone. IL: Insubric Line. PF: Penninic Front. RS: Rhône-Simplon Line. TMZ: Turba Mylonite Zone. Further fault lines: Main thrust fault of the Helvetic units onto the Molasse, thrust faults within the Subpenninic units separating the Gotthard to the north and the Lepontine Dome to the south. Map after Tectonic Map of the Swiss Federal Office of Topography and Schmid et al. (2004a). Fault zones after Schmid et al. (2004a) and Bousquet et al. (2012). Line of NFP20-East from Pfiffner et al. (1988). Samples along the Ticino valley from Elfert et al. (2013).

The numerical 'sandbox' experiment of this study is based on the deep structure of the Central Alps as revealed from the seismic reflection profile NFP20-East (Pfiffner et al., 1988, 1990, 1997; Schmid et al., 1996, 2004b; Diehl et al., 2009) and a published thermochronologic dataset from the Lepontine Dome (Elfert et al., 2013). The seismic NFP20-East profile is situated in close vicinity to the profile of Elfert et al. (2013) at the eastern border of the Lepontine Dome. It reveals the following deep structures (e.g., according to the interpretation of Pfiffner et al., 1988, 1990; Schmid et al., 1996): A lower crustal wedge of Adriatic origin acts as an indenter, delaminating the European lower and upper crust. The Adriatic Moho dips to the north, as a result of backthrusting of European upper crust. The nappe stack of the central Lepontine region

on top of the Adriatic indenter is nearly horizontally arranged and the Aar massif is underlain by a major thrust, the so-called Aar base thrust. Finally the Insubric fault delimits the European and the Adriatic crust.

2.2. Late-stage cooling of the Lepontine Alps

Fission track and (U-Th-Sm)/He ages on apatites from the central and eastern Lepontine Dome indicate small-scale differential cooling during the Miocene (e.g., Hurford, 1986; Timar-Geng et al., 2004; Rahn, 2005; Elfert et al., 2013). Cooling ages across the eastern Lepontine Dome (Mid-Miocene to Pliocene in age) are U-shapely distributed with youngest ages in center, suggesting exhumation related to late-stage updoming in the central Adula nappe (Rahn, 2005). The same cooling age pattern is found farther west across the Leventina and adjacent nappes: Youngest fission track ages are found in the center of the dome (7 Ma), increasing towards both, the northern and the southern margin of the Lepontine Dome (13 Ma and 19 Ma, respectively; Elfert et al., 2013). Thermal history modeling suggested episodic cooling north of the Insubric Line in the middle and late Miocene and continuous cooling farther north. However, cooling in the center postdated and outpaced cooling south of the northern steep belt. In contrast to previous studies, stressing the importance of extension related unroofing for the late Miocene exhumation of the Lepontine Dome (e.g., Steck and Hunziker, 1994), the observed cooling patterns may be explained by long-lasting tectonic compression playing a major role in the Miocene exhumation of the Lepontine Dome (Elfert et al., 2013).

2.3. Drainage evolution in the Lepontine Alps

The present day Rhine, Rhône and Po rivers are sourced in the Aar-Gotthard massif. Two triple junctions (one in the Aar massif separating the headwaters of Aare/Reuss [finally flowing into the Rhine], Rhine and Rhône and one in the Gotthard 'massif' separating the headwaters of Rhine, Rhône and Ticino [finally flowing into the Po]) define the route of the main drainage divide of the Alps (e.g., Schlunegger et al., 1998). Regarding the position and the evolution of the drainage divide since Oligocene times, three models are discussed: (I) The comparison of petrographical and thermochronological signatures from the hinterland with those of detrital samples from the southern Alpine foreland basins point to a largely constant position of the main Alpine drainage divide similar to the present day situation since Oligocene times (Garzanti and Malusa, 2008). (II) Similar studies with focus on the northern Alpine foreland basins, including the analysis of the evolution of catchment sizes, however, suggested that the main drainage divide was situated inside the Lepontine Dome (20-40 km north of the Insubric Line) in Oligocene times (Schlunegger et al., 1998, 2007). According to these authors, the main drainage divide migrated northwards towards the present situation during the Mio-Pliocene, associated with the exhumation of the Aar massif (see also Kühni and Pfiffner, 2001). Probably, the exhumation of the Aar basement is also responsible for the rerouting of the drainage system (i.e. the Rhône and Rhine headwaters running orogen-parallel). (III) Finally, sediment composition of the eastern

Alpine Molasse indicates an early southward shift of the drainage divide between 30 and 20 Ma (Brügel et al., 2000; Spiegel et al., 2001), which was subsequently followed by a northward shift at around 17 Ma (Schlunegger et al., 1998; Kuhlemann et al., 2001; Spiegel et al., 2001). Kuhlemann et al. (2001) interpreted the crosscurrently evolving sediment budgets of the north-western and the south-eastern foreland basins at ~11 Ma as another southward shift of the main drainage divide. This shift was then followed by another northward migration of the drainage divide, related to the final reorganization of the drainage system, resulting in the present day situation, which was largely established at ~3 Ma.

Strongly linked to the discussion of topographic and drainage evolution is the timing of valley incision. Garzanti and Malusa (2008) assumed major thalwegs of the Lepontine area to be established since Oligocene times. On the other hand, Kuhlemann (2007) related increasing sedimentation rates at ~5 Ma and ~2.7 Ma in the north Alpine foreland basin with the onset of effective valley incision. For the Mont Blanc region, Glotzbach et al. (2008) also proposed enhanced valley incision at ~3 Ma. According to Valla et al. (2011, 2012), the Rhône valley in the area of Martigny (Switzerland, canton Valais) was carved and shaped only from mid-Pleistocene glaciations at ~1 Ma.

3. Methodology

3.1. Discrete Element Method

For the numerical simulation of the evolution of the eastern Lepontine Dome we used the Discrete Element Method (DEM), which is based on a granular model approach. This technique allows for the investigation of large-scale deformation processes of rocks by using a particle assemblage. For our study, we utilize the commercial code PFC2D (Cundall and Strack, 1978; ITASCA, 2004). PFC2D is able to displace discretized rigid elements such as disks and balls in any direction in accordance with the applied boundary conditions (Cundall and Strack, 1978). The interactions between the particles cause simultaneous contact forces, which are calculated through the magnitude of the overlap in combination with the physical parameters of the interacting particles (e.g., the coefficient of friction (μ_p), shear and normal stiffness (k_s, k_n), and density (ρ) via simple physical force-displacement laws (Mindlin and Deresiewicz, 1953; Cundall and Strack, 1979; Morgan and Boettcher, 1999). For this study, a simple elasto-plastic material behavior is simulated similar to previous studies regarding orogenic wedge evolution (Morgan and Boettcher, 1999; Miyakawa et al., 2010).

3.1.1. Reverse numerical modeling

The first prerequisite to compare the results from the numerical 'sandbox' experiment to real world geological settings is to successfully reconstruct the present day structure of the study area. Thus, starting from an (unknown) initial construction, the final stage of the simulation has to match the present situation. The numerical 'sandbox' experiments of Wenk et al. (in prep.) were based on the deep crustal seismic reflection NFP20-West profile, simulating forwards. For this study, we have developed a numerical 'sandbox' experiment based on the kinematic evolution model for the NFP20-East profile from Schmid et al. (1996), with an upwardly oriented rigid backstop, simulating the Adriatic lower crust and mantle in early Oligocene times (~32 Ma) and a flat topography (in terms of elevation above sea level; Fig. 41). Starting with this initial (Oligocene) situation, the backstop was successively depressed, simulating the sinking Adriatic plate until it delaminated the European lower and upper crust (the Adriatic indenter). With the delamination, the present crustal configuration is reached. Thus, in accordance with the reconstruction of Schmid et al. (1996), the simulation time of our model is defined as covering 32 Myr of orogeny. For reasons of clarity, we adapt geological time for model runtime, assuming that total model runtime reaches from 32 Ma to the present. In the following, a certain model time is simple called by the corresponding geological time, although being aware that we actually relate to model time.

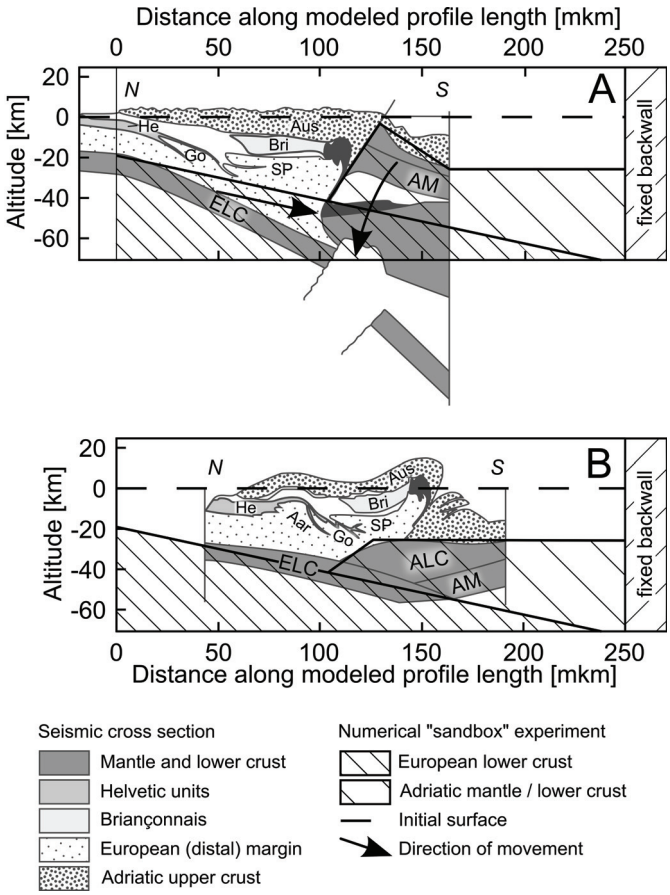

Fig. 41.: Model setup (A) of the numerical 'sandbox' experiment (thick lines and hatching) at the beginning of the simulation on the basis of the kinematic model (underlying gray and spotted cross section) of Schmid et al. (1996) and predefined movement of the numerical 'sandbox' (black arrows), simulating the sinking Adriatic plate (Adriatic indenter) and the subduction of the European lower crust. The lower sketch (B) shows the model constraints at the end of the simulation (thick lines and hatching: Numerical 'sandbox'. Gray and spotted underlying cross section: NFP20-East after Schmid et al., 1996). Aar: Aar external massif. ALC: Adriatic lower crust. AM: Adriatic mantle. Aus: Austroalpine nappes. Bri: nappes derived from the Briançonnais terrane. ELC: European lower crust. He: Helvetic nappes. Go: Gotthard nappe. SP: Subpenninic nappes. mkm: model km (i.e. distance along modeled profile length)

The numerical 'sandbox' consists of one vertical wall with a simulated height of 110 km as right hand border and one long fixed bottom wall with a simulated length of 530 km. The bottom wall dips with an angle of $\beta = 12°$ into the direction of the vertical wall and simulates the down-dipping European lower crust (Fig. 41). Side and bottom walls act as undeformable boundaries and consist of fixed particles with a radius of 600 m. Within the box 12,000 randomly distributed particles were generated (radii of 500, 600, 700 m). The different particle sizes prevent symmetrical particle packing (Saltzer and Pollard, 1992). These particles settle down under gravity on the bottom wall ($g = 9.81\ m\ s^{-2}$). Gravity is active during the entire experiment. Afterwards, a plain surface is produced by deleting excess particles. After particles are deposited and equilibrium is achieved, a group of particles in the shape of a triangle sticking out of a horizontal

top are implemented in a fixed position. This fixed part is located on top of the bottom wall and nearly reaches up to the surface at the beginning of the simulation (wide downward hatches in Fig. 41). It simulates an overthrusting lower crust in a collisional setting. To simulate sinking of this upstanding section until it delaminates the upper and lower crust of the overthrust plate, the corresponding particles shrink steadily during the experimental run. To allow for continuous addition of particles to the numerical 'sandbox', the detachment is extended beyond the outward (i.e. the opposite to the subduction direction) edge. On top of the extended detachment, a 10 km thick layer is deposited. This region is not included in the results figures, because it exists only to assure steady supplies of particles but has no direct impact on the wedge evolution.

During the experimental run, the bottom wall moves with a constant velocity in positive x-direction to simulate the subduction of a down-going plate. The basic material properties (e.g., μ_p, ρ, k_n, k_s) for the indenter were adjusted to simulate backthrusting along the edge of the indenter. All other particles (including the side wall particles) were parameterized as described in the companion study (Wenk et al., in prep., Tab. 10).

Tab. 10.: Material properties of the numerical 'sandbox' experiment

Particles	Coefficient of friction	Density	Normal stiffness	Shear stiffness
	μ_p	$\rho\ [kg\ m^{-3}]$	$k_n\ [N\ m^{-1}]$	$k_n\ [N\ m^{-1}]$
Model particles	0.6	2700	$1 \cdot 10^{13}$	$1 \cdot 10^{13}$
Side wall	0.6	2700	$1 \cdot 10^{13}$	$1 \cdot 10^{13}$
Bottom wall	0.1	2700	$1 \cdot 10^{13}$	$1 \cdot 10^{13}$
Indenter	0.05	2700	$1 \cdot 10^{13}$	$1 \cdot 10^{13}$

Please note that fault angles of the numerical 'sandbox' experiment can only be compared relatively to field data (see also Morgan and Boettcher, 1999). Furthermore, flank angles are measured on the originally modeled surface. Since erosion is calculated afterwards, they will always exceed those from the eroded surface.

We are aware that the numerical 'sandbox' experiment involves strong simplifications: To reconstruct the deep structure of the Central Alps, only simple geometries (shape and dipping angle of the downgoing plate, shape and evolution of the indenter) are implemented. We do not consider possible northwards movement of the Adriatic plate (subduction movement is the only active movement in the experiment) and disregard the complex processes of expelling of formerly subducted nappes along the tectonic accretion channel. Thus, the direction of particle paths (towards the subduction zone) is possibly reverse to the direction of rock displacement in the Central Alps. Furthermore, overthrusting is simulated continuously and steadily, corresponding to a steady convergence between the European and Adriatic plates. Lithological differences in upper crustal material are not considered. Additionally, we simulate brittle material behavior. Moreover, the particle sizes only allow for deriving large-scale structures extending several thousand meters. Finally, our approach does not contain erosion during the model run, but is calculated afterwards. Hence, particle loads are overestimated which cause slightly distorted stress fields.

3.2. Apatite fission track thermochronology and thermal history modeling

Apatite fission track (AFT) analysis is a well-established thermochronologic method to reconstruct the cooling history of rocks. It is based on the accumulation and length distribution of lattice defects within apatite crystals, derived from spontaneous fission of ^{238}U (Wagner and Reimer, 1972; Hurford and Green, 1981, 1982). Fission tracks in apatites are erased at temperatures above 110 °C due to lattice annealing. Between 110 °C and 60 °C, annealing becomes less efficient, resulting in shortening of fission tracks. Below 60 °C, fission tracks are mostly preserved and only little shortening (<10 %) takes place. AFT ages refer to the time elapsed since fission tracks started to accumulate as the crystal exhumed through the partial annealing zone (PAZ; 110 °C- 60 °C; Gallagher et al., 1998; Gleadow and Duddy, 1981. The distribution of fission track lengths depends on the residence time within the PAZ and thus, the time-temperature history of a sample can be deduced thereof (Fig. 42), reflecting the exhumation through the uppermost crust.

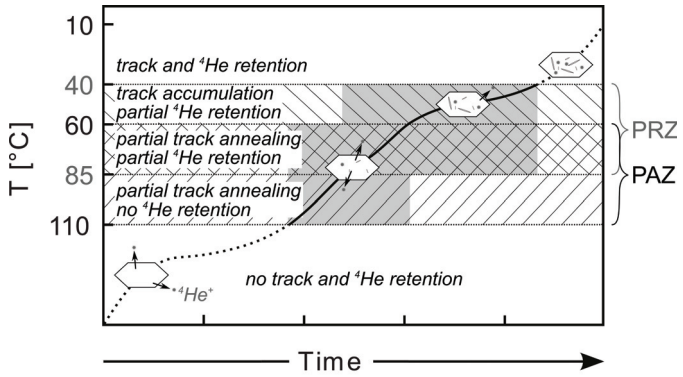

Fig. 42.: AFT and (U-Th-Sm)/He analyses are based on the accumulation of fission tracks and ^{4}He particles through time. Retention and associated accumulation of tracks and ^{4}He particles depend on the temperature and the cooling rate within the partial annealing zone (PAZ) and the partial retention zone (PRZ), respectively. In this study we concentrate on AFT data. Nonetheless, inverse thermal history modeling of the data observed was carried out on the basis of both, AFT and apatite (U-Th-Sm)/He dating (Fig. 45) and thus the thermal history within both, the partial annealing zone and the partial retention zone is considered.

Based on laboratory experiments (e.g., Carlson et al., 1999; Barbarand et al., 2003), track annealing can be described by algorithms, which in turn are used for extrapolating fission track annealing behavior to geological time scales (Laslett et al., 1987; Ketcham et al., 1999, 2007a). These algorithms allow calculating time-temperature paths that are in agreement with the fission track data observed (thermal history inversion), or to predict fission track data that would result from a given thermal history (forward modeling). For this study, we used the HeFTy software (Ketcham, 2005) and the annealing algorithm of Ketcham et al. (2007a) for deriving synthetic AFT ages from forward modeling of the time-temperature paths extracted from the numerical 'sandbox' experiment (section 3.3).

3.3. Coupling numerical 'sandbox' modeling and thermochronology

The numerical DEM approach allows obtaining detailed information about particle position, movement, granular texture, and forces (such as shear and normal forces). This reveals a detailed snapshot about the internal structures (i.e. stresses, deformation, fault systems) within the particle assembly at any time step. Furthermore, positions of single particles can be tracked throughout the model run. For this study we (1) choose a particle from the numerical 'sandbox' experiment, (2) track its path towards the surface, (3) assume a geothermal gradient valid for the time of particle movement and (4) derive a time-temperature history for that particular particle. This time-temperature path from the numerical 'sandbox' is then taken for forward thermal history modeling, calculating synthetic AFT data (age, mean track length, track length distribution) that would in theory result from the simulated particle path. These synthetic data are subsequently compared to data actually observed close to the location of seismic profile NFP20-East (Elfert et al., 2013).

Crucial, however, for obtaining temperature from particle position (Eq. 3.1) is to firstly calculate an erosional surface (eE), since erosion is not implemented in the numerical 'sandbox' experiment itself. We use the term erosional surface to label the exposed surface after erosion is calculated, rather than in the sense of a plain erosion surface (s.str.). To determine eE, we set the initial maximum elevation of the erosional surface ($s = 0$) to 500 m a.s.l., and the final maximum elevation ($s = n$) to 3000 m a.s.l.. For further details we refer to the companion paper (Wenk et al., in prep.).

$$T_{x,y,s} = ((eE_{x,s} - (mH_{x,s} + (eE_{x,n} - mH_{x,n}))) \cdot g_t) + T_{surf} \tag{3.1}$$

Where $T_{x,y,s}$ is the temperature of a particle at point x/y at time step s, therein is x the distance along the modeled profile length, and y ($= mH_{x,s}$) the vertical distance to the bottom of the numerical 'sandbox'; other variables: n: last time step, g_t: geothermal gradient = 30 °C km^{-1}, T_{surf}: surface temperature = 10 °C; cf. Eq. 5 in Wenk et al. (in prep.).

We associate geological time with the evolution of model topography. In particular, we have run the experiment until the modeled topography resembled the present day, real topography along the NFP20-East profile (approximately 1.7 times the runtime of Wenk et al. (in prep.)).

In the conceptual study of Wenk et al. (in prep.), particles were selected for thermal history modeling if they were located at the erosional surface at the end of the simulation. The erosional surface can best be interpreted as the long-wavelength mountain ridge. To allow for the comparison between the synthetic AFT data of this study and the data observed from the Lepontine Dome (Elfert et al., 2013), the approach of Wenk et al. (in prep.) is modified, because the Lepontine samples are taken along the valley bottom of the Ticino river (510 ±200 m a.s.l.) and not along the mountain ridges. Because of that, we introduce a further term VI ('valley incision') in the temperature equation to assure that the 'sampled' 'sandbox' particle (positioned at 510 m a.s.l.) is exhumed to the surface at the end of the simulation (Eq. 3.2).

$$VI_{x,s} = eE_{x,s} - \left(\frac{s}{n}\right)(eE_{x,n} - mH_{x,n}) \tag{3.2}$$

Finally, the elevation of the erosional surface (eE) in Eq. 3.1 has to be substituted by VI, in order to relate the particle temperature to the depth below the bottom of the 'incised' valley (Eq. 3.3) and not to the ridge (Eq. 3.1).

$$T_{x,y,s} = ((VI_{x,s} - (mH_{x,s} + (VI_{x,n} - mH_{x,n}))) \cdot g_t) + T_{surf} \tag{3.3}$$

To test for the impact of the onset of 'valley incision' on the AFT ages and the AFT age distribution, three scenarios were developed. Temperatures were derived applying Eq. 3.1 until 2 Myr, 27 Myr and 31 Myr of simulated orogeny (i.e., 30 Ma, 5 Ma and 1 Ma before today) and applying Eq. 3.3 only thereafter. By this means, it is ensured that all selected particles are exhumed to the surface at the end of the simulation. Thus, we used the same numerical 'sandbox' experiment with three different scenarios of valley incision, with effective incision starting at 30 Ma, 5 Ma and 1 Ma (scenarios Inc_{30}, Inc_5 and Inc_1, respectively). For all three scenarios, synthetic AFT ages are derived and compared both to each other and to the AFT data observed.

4. Reproducing the Central Alps

4.1. Results of reverse numerical 'sandbox' modeling

A double-vergent wedge evolves out of the incoming particles in the numerical 'sandbox' experiment (Fig. 43). Thereby, those unfixed particles, which represent upper crustal material of the European plate, migrate over the fixed backstop (representing the lower crustal indenter of Adriatic origin). The flanks of the double-vergent wedge evolve asymmetrically. Since we compare the results of the numerical 'sandbox' experiment to the structural setting of the Central Alps, we adapt the cardinal directions to the model in calling the direction of subduction 'south' and the opposite direction 'north'. Following this terminology, the evolving wedge can be divided into a northern pro-wedge and a southern retro-wedge. The retro-wedge evolves steeper with a surface slope angle of ~16° due to a frequently activated backthrust (dipping angle ~54°), whereas the northern frontal wedge evolves flatter with ~8° as a result of a periodically forwards progradation of the deformation front. Consequently, after the first culmination (culmination I in Fig. 43A; approximately above the tip of the indenter, ~100 mkm (model-km, i.e. distance along the modeled profile length) has been established, a second culmination further north (culmination II in Fig. 43A) evolves. New forethrusts rise relatively steep with 38° from the 'subducting' bottom wall. These thrusts are reactivated later as out-of-sequence thrusts. The first order reactivated thrusts evolve flatter with around 18°. The second order out-of-sequence thrusts are reactivated with higher dipping angles of ~26° and more. Both groups of out-of-sequence thrusts rearrange the wedge structure in that reactivation leads to a rotation and steepening of formerly flat lying, undisturbed blocks.

4.1.1. Structural interpretation of the numerical 'sandbox' experiment

In the following section we will compare major structural and topographic patterns of the present day Central Alps as observed from the field and from seismic studies to the structures derived from the numerical 'sandbox' experiment (Figs. 43, 44).

(I) Topography: A section of the Central Alps along the NFP20-East profile shows two topographic culminations (elevation data from Shuttle Radar Topography Mission; USGS, 2004), with a smaller one to the north (i.e. the Aar-Gotthard massif) and a slightly bigger one to the south (i.e. the Lepontine Dome). Projecting this profile onto the modeled profile length of the numerical 'sandbox' experiment (including a stretching factor of 1.9), shows that both, wavelength and magnitude agree well between the observed topography and the modeled erosional surface with its two culminations (topographies in Fig. 44). In the following descriptions throughout

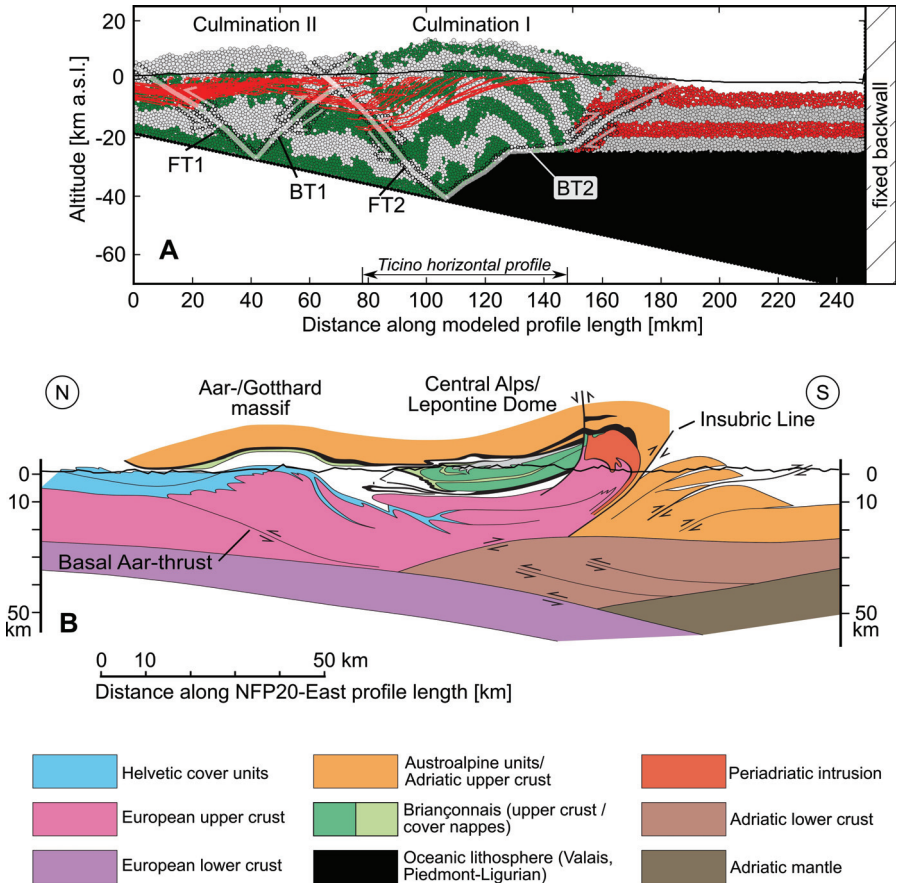

Fig. 43.: Particle situation at the end of the numerical 'sandbox' experiment (A). Green and light gray particles: European upper crust. Red and dark gray particles: Adriatic upper crust. Black body: Adriatic indenter (sunken Adriatic lower crust/mantle). Red lines: Pathways of particles located at 510 m a.s.l. at the end of the simulation. Black line: Calculated erosional topography. Fault zones (semi-transparent white lines) are based on relative particle displacement analyses (FT: Forethrust. BT: Backthrust). B: Profile through the Lepontine Dome and the Central Alps (modified after Schmid et al., 2004b). Black line: Surface topography after Schmid et al. (1996). Please note that the sketch is slightly stretched for reasons of clarity. mkm: model km (i.e. distance along modeled profile length)

this paper, we thus interpret culmination I as being equivalent to the Lepontine Dome, and culmination II as being equivalent to the Aar-Gotthard massif.

(II) The Aar-Gotthard external massif with the basal thrust of the Aar massif: Kinematic modeling based on seismic reflection data suggests that the Aar-Gotthard external massif is exhumed along a major thrust fault below the Aar massif since ~20 Ma (Basal Aar-thrust in Fig. 43B; Schmid et al., 1996, 2004b). Culmination II results from thrusting along a flat south dipping out-of-sequence thrust (FT1) in the numerical 'sandbox' experiment, which shows up early in the course of the simulation (active for the first time at ~30 Ma). We interpret fault FT1 as being equivalent to the Aar basal thrust in the profile of Schmid et al. (1996, 2004b, Fig. 43).

(III) The northern steep belt: Steeply inclined foliations south of the Gotthard massif indicate significant backthrusting of the northern Lepontine Dome. Although not resolved by the

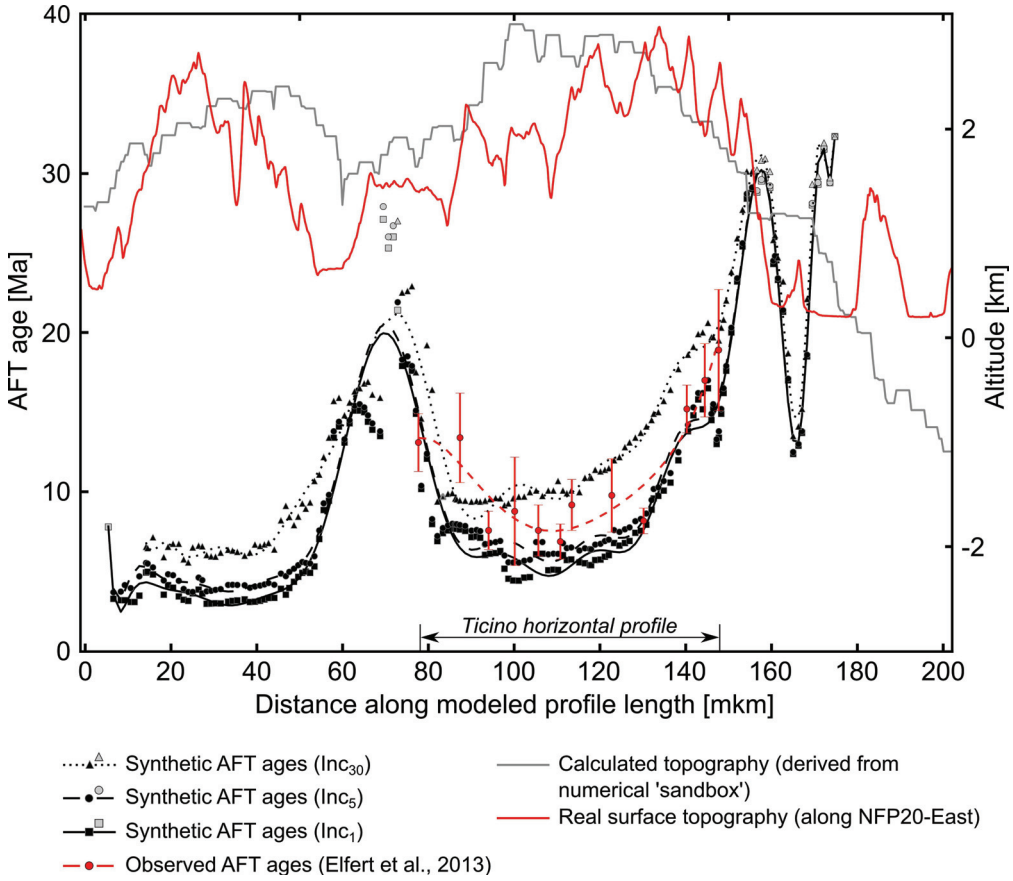

Fig. 44.: Calculated topography from the numerical 'sandbox' experiment and and real topography along NFP20-East (based on data from Shuttle Radar Topography Mission, USGS, 2004) as well as synthetic and observed AFT ages along the profile. Three scenarios were tested with onset of valley incision at 30 Ma (Inc_{30}), 5 Ma (Inc_5) and 1 Ma (Inc_1). Since erosion and temperature were derived after the model run, the resulting thermal histories are occasionally unrealistic. Only time-temperature histories with a complete reset of the AFT system ($>$ 110 °C) are fully trusted. Gray markers: Low-quality time-temperature histories. Lines through the AFT data represent trend polynoms of the corresponding AFT ages. mkm: model km (i.e. distance along modeled profile length)

published seismic reflection profiles, this structure is clearly observed in the field (e.g., Milnes, 1974; Maxelon and Mancktelow, 2005). In the numerical 'sandbox' experiment a steeply north dipping backthrust (BT1) evolves as corresponding thrust to FT1. BT1 crops out at the transition zone between culmination I and culmination II. We interpret the transition zone as corresponding to the northern steep belt. If our simplified numerical 'sandbox' model really reflects the major structures of the Central Alps, than the connection of FT1 and BT1 would suggest that backthrusting along the northern steep belt is related to the activity of the Aar basal thrust.

(IV) Lepontine Dome: The Lepontine Dome evolved over the tip of the Adriatic indenter (Adriatic lower crust in Fig. 43B). Kinematic modeling based on seismic reflection data suggests south dipping faults or unconformities south of the Aar-Gotthard massif (Schmid et al., 1996) reaching deep down below the center of the Lepontine Dome. In the numerical 'sandbox' experiment, a major forethrust (FT2) south of culmination II can be interpreted as a second or-

der out-of-sequence thrust and, in the first place, leads to the uplift of culmination I via basal accretion. The fault system BT1/FT2 prevents culmination I from extending northwards and forces enhanced uplift (i.e. further growth) of this culmination. Position and deep structure of culmination I is interpreted as the Lepontine Dome (Fig. 43). Adapting the structural evolution of culmination I, north-south oriented updoming in the Lepontine Dome can be associated with ongoing convergence of the European and Adriatic plates, and basal accretion.

(V) Insubric Line: The Central Alps are backfolded and backthrusted along the Insubric Line above the root of the Southern Alps. Dividing the European and Adriatic upper crusts, the Insubric Line evolves as north dipping backthrust originating on top of the Adriatic indenter (Fig. 43). The unfixed particles of the numerical 'sandbox' experiment are thrust along the backthrust BT2 and migrate over the fixed backstop (corresponding to the Adriatic indenter). Consequently, we interpret BT2 as being equivalent to the Insubric Line.

Summarizing, we assume to have simulated structures, similar to the most important structures along the NFP20-East profile (Fig. 43).

4.2. Synthetic cooling history derived from the numerical 'sandbox'

Synthetic AFT ages range from 3 Ma to 32.3 Ma (Fig. 44). For all scenarios a maximum age of 32.3 Ma is derived (corresponding to the total model run time). Synthetic AFT ages of all scenarios correlate negatively with the elevation of the erosional surface. While minimum ages are associated with culmination II (Inc_{30}: 5.6 Ma, Inc_5: 3.7 Ma, Inc_1: 3 Ma at 24-28 mkm) and culmination I (Inc_{30}: 9.2 Ma, Inc_5: 5.6 Ma, Inc_1: 4.5 Ma at 98-101 mkm; Fig. 44), AFT ages increase along long-wavelength depressions of the erosional topography. Thus, synthetic AFT ages are U-shapely distributed along each simulated culmination.

The synthetic AFT data are compared to AFT data actually observed along a horizontal profile following the Ticino valley across the Lepontine Dome (Fig. 40; Elfert et al., 2013). The equivalent profile within the numerical 'sandbox' experiment is situated between 78 mkm and 148 mkm and crosses culmination I (Figs. 44, 45). Samples analyzed by AFT thermochronology (Elfert et al., 2013) correspond to particles located at 78, 94, 115, 131, 141, 144 and 148 mkm. These particles are chosen to derive their thermal histories.

Earliest cooling to the temperature range of AFT sensitivity is predicted for the southernmost particle P148 (i.e. the particle located at 148 mkm at the end of the model run. Further particle identifiers are set analogously). Depending on the erosion scenario (discussed in detail in chapter 5), P148 cooled to 110 °C at latest Oligocene/ earliest Miocene (23-22 Ma; Fig. 45). Cooling started successively later towards the center with P115 and P94 reaching 110 °C only at ~11-8 Ma. The northernmost P78, however, already cooled to 110 °C at early to mid Miocene times (16-14 Ma).

The central parts of the profile (P94, P115 and P131) cooled steadily and most rapidly with cooling rates between 9 °C Ma^{-1} and 12 °C Ma^{-1}. Cooling in the north (P78) was generally moderate (6-8 °C Ma^{-1}), but occurred in a succession of small episodic steps. In the south,

cooling from 110 °C continued at low rates (4-7 °C Ma^{-1}), even slowing down in late Miocene times for P141 and P144 (1-3 °C Ma^{-1}).

These findings agree well with inverse thermal history modeling based on the observed AFT and (U-Th-Sm)/He data from the corresponding Ticino horizontal profile, revealing differential Miocene cooling across the Lepontine Dome (Fig. 45; Elfert et al., 2013). Synthetic AFT ages derived from the thermal histories of the numerical 'sandbox' particles between 78 mkm and 148 mkm range between 6 Ma and 20 Ma (Figs. 44, 45) and, thus, also coincide well with the observed AFT ages along the equivalent Lepontine profile (7 to 19 Ma; Elfert et al., 2013). Summarizing, synthetic and observed data are in good agreement concerning age range, shape of age distribution, pattern position and cooling styles along the modeled profile length (Figs. 44, 45).

There are, however, some smaller discrepancies: In detail, time-temperature paths from the numerical 'sandbox' experiment evolve less steady than the inversions from thermal history modeling propose for the corresponding samples. The most prominent divergence can be observed between the modeled (data-based) cooling history of the northernmost sample from the Ticino horizontal profile and the calculated cooling history of P78 (Fig. 45). In contrast to the proposed slow and steady cooling at the northern termination of the profile from inverse thermal history modeling, the corresponding particle of the numerical 'sandbox' experiment cools in short episodic steps.

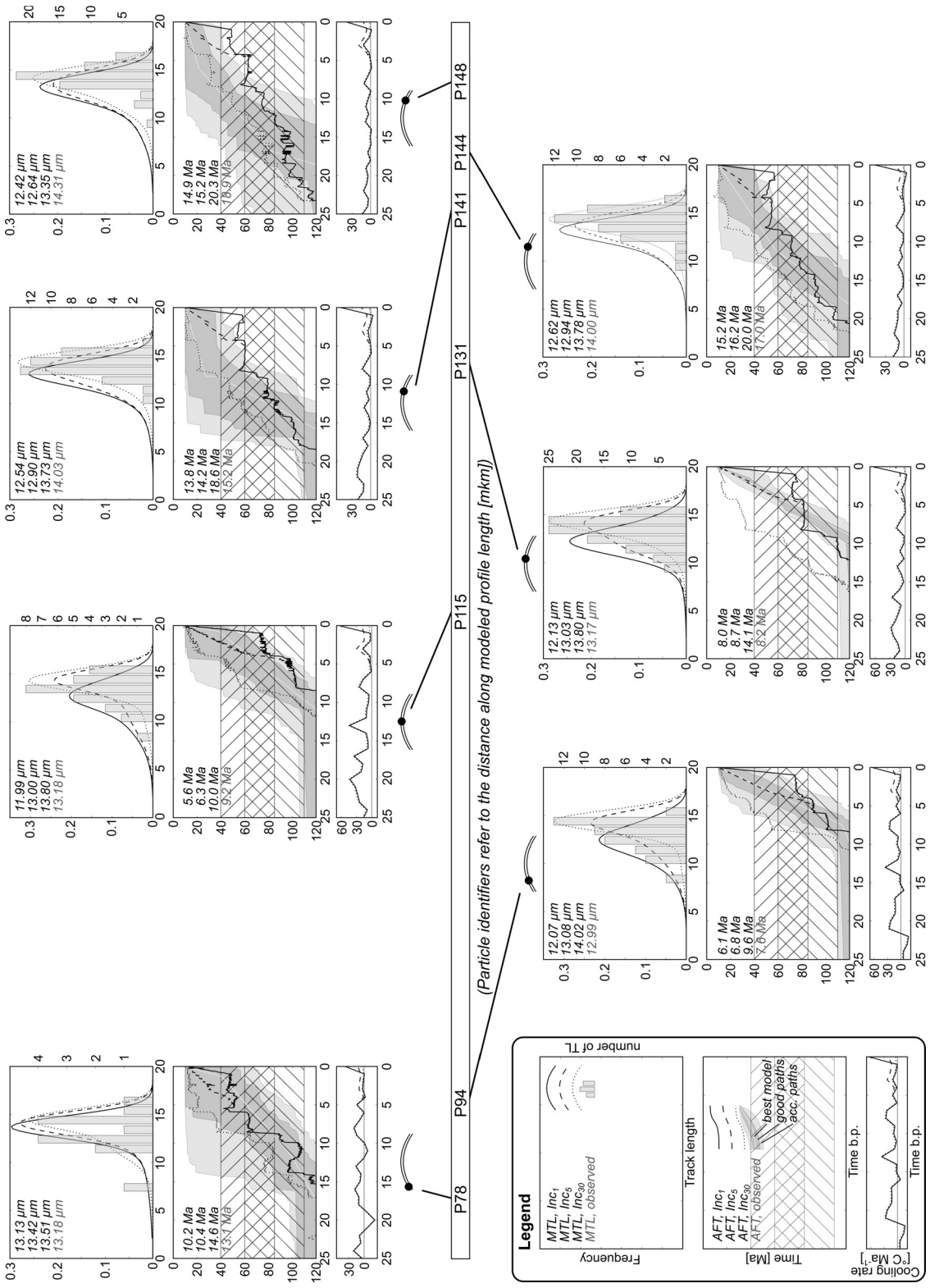

Fig. 45.: Both, synthetic and observed AFT data show differential cooling along the modeled profile length. Thermal history inversions are based on observed AFT and apatite (U-Th-Sm)/He data (Elfert et al., 2013). For each data pair (synthetic and corresponding observed data) track length distributions and mean track lengths (MTL, top sketch), thermal history and AFT ages (mid sketch) and the cooling rate (bottom sketch) are shown (legend sketch in the lower left corner). Solid lines refer to valley incision at 1 Ma (Inc_1), dashed lines to valley incision at 5 Ma (Inc_5), dotted lines to valley incision at 30 Ma (Inc_{30}). mkm: model km (i.e. distance along modeled profile length). Pictograms depict the structural position of the particles along culmination I.

5. Valley incision and related cooling patterns

In the following section, we test the sensitivity of AFT analyses to detect cooling patterns related to valley incision. All numerical 'sandbox' particles, which were selected for thermal history analyses, were exhumed to the same horizontal level at the end of the simulation (510 m a.s.l.). This corresponds to sampling along a horizontal profile formed by a valley bottom. As a first step we compare the synthetic AFT data of the simulated scenarios (i.e., valley incision at 30 Ma, 5 Ma and 1 Ma). Subsequently, we will concentrate on the relation between AFT data and the different structural settings along the profile.

Generally, AFT ages increase with earlier valley incision (Inc_{30} > Inc_5 > Inc_1; ages in section 4.2). Oligocene valley incision (Inc_{30}) results in relatively old AFT ages, in concert with narrow track length distributions and long mean track lengths (MTLs; average MTL and mean standard deviation: 13.71±1.82 μm; Fig. 45). In contrast, Pleistocene valley incision (Inc_1) leads to comparatively young AFT ages.

On average, the MTLs resulting from Inc_1 are shorter compared to Inc_5 and Inc_{30} and show slightly broader track length distributions (12.41±2.06 μm). Inc_5 yields intermediate results compared to Inc_{30} and Inc_1, but broadest track length distributions (average standard deviation: 2.2 μm).

Both, the age trend towards younger ages and the trend towards shorter MTLs with more recent valley incision can be explained by the later exhumation of the valley bottoms to the surface and the associated prolonged residence at higher temperatures. With longer residence below 60 °C (i.e. with earlier valley incision), the amount of only slightly shortened fission tracks increases, resulting in an increased density of fission tracks (i.e. older AFT ages) and longer MTLs. The width of a track length distribution depends on the cooling rate within the PAZ (110-60 °C). Cooling rates of Inc_1 and Inc_5 within the higher temperature range of the PAZ are identical for all particles. Yet most of the particles are still within the PAZ at 5 Ma when valley incision triggers rapid cooling in scenario Inc_5. Although this change results in higher cooling rates compared to Inc_1 (giving reason to expect smaller standard deviations), the associated increase in longer track lengths seems to outrank the impact of the cooling rate and eventually leads to increasing standard deviations. Narrower track length distributions of scenario Inc_{30} can be related to higher cooling rates of Inc_{30} within the PAZ compared to Inc_1 and Inc_5.

Differences between AFT ages resulting from different scenarios (i.e. of the same particle in different scenarios) change with the structural positions. Most pronounced differences are found at the centers of culmination I and II (i.e., at ~46-57 mkm and 98-151 mkm), and at the transition zone between the two culminations (74-82 mkm) where BT1 and FT2 crop out. These

areas are characterized by rapid cooling (as compared to the adjacent regions) and / or tectonic activity. When comparing scenarios Inc_{30} with Inc_5, maximum age differences across the two culminations are 4.7 Myr and 5.7 Myr. Thus, in this case, AFT analyses are able to resolve the difference in timing of valley incision, assuming a typical error range of ~10%. Comparing scenarios Inc_5 with Inc_1 yields a maximum age difference of 1.2 Myr, with an AFT age of 3.6 Ma for Inc_1 and of 4.8 Ma for Inc_5 at the center of culmination II. This age difference may still be resolvable for high-quality samples with about 50 or more dated single grains per analyses (cf. Glotzbach et al., 2008). For 'normal' AFT analyses containing about 20 single dated grains and a typical error of ~10%, however, scenarios Inc_5 and Inc_1 can hardly be distinguished on the basis of their AFT age signatures. Along the depressions adjacent to the culminations, age differences between the tested scenarios decrease to 0.9 Myr (Inc_{30} vs. Inc_5) and 0.1 Myr (Inc_5 vs. Inc_1), and are thus not resolvable by AFT thermochronology.

Summarizing, we show that the onset of valley incision (1) impacts the exhumation histories especially in rapidly cooling and / or tectonically active areas, and (2) may be resolved by AFT analyses in orogenic environments if tested scenarios for valley incision are $\geq$ 4 Myr apart from each other, and if regions of most rapid exhumation and / or tectonic activity are preferentially sampled. In slowly exhuming regions, by contrast, valley incision histories are harder to resolve by AFT analyses.

5.1. Implications for the erosion history of the Central Alps

Assuming that our simplified numerical 'sandbox' model can be transferred to the geological situation of the Central Alps, then the comparison between AFT data observed across the Lepontine with those data derived from the different numerical 'sandbox' model scenarios provides indication for the timing of valley incision in the Alps:

Time-temperature paths and synthetic AFT data derived from Inc_5 are in best agreement with the observed AFT data and inverse thermal history modeling thereof (Figs. 44, 45). Only for P141 and P148 (southern flank of culmination I), time-temperature paths derived from Inc_{30} show slightly better correlation with the corresponding inversions. Most of the observed AFT ages are older than the synthetic AFT ages of Inc_5, but younger than the corresponding AFT ages of Inc_{30}. The age gap between the observed data and those derived from Inc_5, however, varies along the profile. Only the observed AFT age of P131 is younger than the corresponding AFT age from Inc_5 (Figs. 44, 45). The real sample (Ticino-H-23 of Elfert et al., 2013) shows comparatively young AFT and (U-Th-Sm)/He ages, breaking the general trend of the profile, indicating inhomogeneous small-scale deformation (Timar-Geng et al., 2004; Elfert et al., 2013), which cannot be resolved by the numerical 'sandbox' experiment. The MTLs and the shape of the track length distributions of the data observed agree equally well with the MTLs and track length distributions derived from Inc_5 and Inc_{30}. Only for P78, the MTL derived from scenario Inc_1 fits better with the MTL of the data observed as compared to Inc_5 and Inc_{30} (Fig. 45).

Another way of reconciling and comparing the erosion history derived from the numerical 'sandbox' model with that derived from AFT data observed across the Lepontine Dome is by

calculating paleo-overburdens through time. 'Paleo-overburden' refers to the thickness of rocks removed from the presently exposed surface since a given time in the geological past, i.e., to the former crustal depth of the recent surface. Paleo-overburden from the data observed was extracted from thermal history inversions of the AFT data across den Lepontine Dome (Elfert et al., 2013). Paleo-overburdens from the numerical 'sandbox' are simply obtained from the distance between the particle and the erosional surface at each time step for all scenarios, i.e., without assuming a paleo-geothermal gradient.

In Fig. 46, we illustrate how much overburden was removed from the Lepontine Dome and the equivalent section of the numerical 'sandbox' experiment since 10 Ma, 8 Ma, 6 Ma, 4 Ma and 2 Ma according to the AFT data observed and according to the different valley incision scenarios (Inc_{30}, Inc_5 and Inc_1). Except for the 10 Ma time slice (arguing for Inc_{30}), the eroded section of Inc_5 is in remarkable agreement with the erosion history derived from the observed AFT data.

We would not go as far as taking the data from the numerical 'sandbox' experiment as hard proof for valley incision at 5 Ma. However, the good agreement with the AFT data observed at least hints in that direction. It is also in line with the strong increase of sediment supply into the circum-Alpine basins as described by Kuhlemann et al. (2002) (although recently debated, cf. Willenbring and von Blanckenburg, 2010). As reason for enhanced erosion and incision at 5 Ma, a change towards a more erosive climate was discussed by Willett et al. (2006), but an independent proof for this is still lacking. However, together with previously published studies (Kuhlemann et al., 2002; Vernon et al., 2008, 2009; Elfert et al., 2013), our results underline the assumption of a fundamental change of the Alpine erosion regime at the Mio-Pliocene boundary.

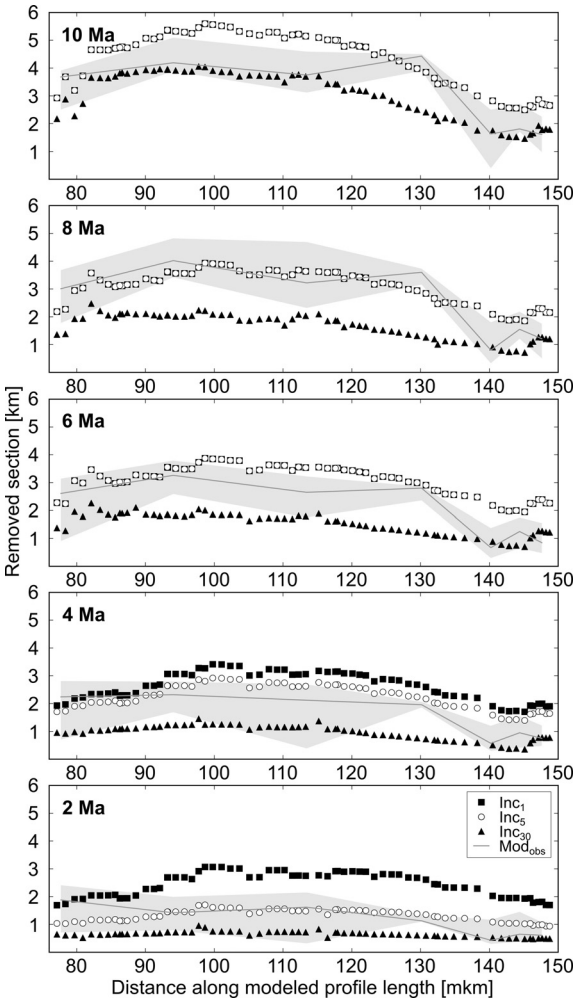

Fig. 46.: Eroded section along the modeled profile length after 10 Ma, 8 Ma, 6 Ma, 4 Ma and 2 Ma (from top to bottom). Gray envelope and line (Modobs) represents the eroded section derived from the observed data by inverse thermal history modeling (Elfert et al., 2013) with the envelope showing the range of possible time-temperature paths in good statistical agreement with the data and the solid line representing the best-fit model. mkm: model km (i.e. distance along modeled profile length).

6. Exhumation revisited – including the lateral component

The temperature of rocks decreases with increasing proximity to the surface, thus exhumation goes along with cooling. Thermochronology utilizes this relation: Thermal history modeling yields time-temperature information which can be translated into an exhumation history by assuming a geothermal gradient.

However, cooling may also result from isotherm relaxation, for example following magmatic intrusions. In this case, cooling would be a static process, so that transferring AFT data into exhumation histories would yield erroneous interpretations.

Also, low-angle normal faulting and thrusting is often associated with significant lateral movements, which does not necessarily result in cooling (e.g., Stüwe and Hintermüller, 2000; ter Voorde et al., 2004). Resulting AFT data would yield low cooling rates, often interpreted as indicating tectonic quiescence, leading to wrong interpretation in terms of the kinematic evolution.

The advantage of our combined approach is that the numerical sandbox allows tracking the structural position of a particle within the 'orogenic' wedge. We can thus directly relate particle pathways including vertical and lateral movements to the resulting (synthetic) AFT data. This allows us to address the following questions:

How does the structural position within an orogenic wedge (i.e., proximity to active faults, singularity, etc.) influence the relation between exhumation (i.e., vertical movement towards the surface) and total displacement (including both, vertical and lateral movements)? When does the exhumation rate (derived from thermochronology) serve as proxy for geodynamic activity?

In the following, rates derived from the 'sandbox' model refer to movements per model time step. Each time step equals 32,000 years of model time, since the total model run time was set as 32 Myr, and one model run comprises 1000 steps. For focusing on larger trends, rates are smoothed by a running average of ten time steps (i.e. equivalent to 0.32 Myr). In a first step, we relate the rate of displacement (i.e. the length of a particle pathway during one model time step) to the corresponding exhumation rate, assuming that a good correlation of both rates indicates that exhumation rates mirror the overall geodynamic activity (Figs. 47, 48). We focus again on the particles along culmination I for directly relating the results to the AFT data observed across the Lepontine Dome. In a second step, we address the underlying reasons why in some parts of the simulated wedge exhumation rates and overall displacement rates are strongly correlated, and in other parts only weakly. As potential steering factors we consider (i) the mean exhumation rate (i.e., is the correlation related to the overall velocity of a process). The mean

exhumation rate reflects the mean velocity of exhumation independent of the exhumation style. (ii) The exhumation style (i.e., continuous vs. episodic exhumation). The exhumation style is independent of the mean exhumation rate and can be described by the standard deviation of the exhumation rates through time: episodic exhumation results in a higher standard deviation, as compared to a steady exhumation resulting in a lower standard deviation. (iii) The displacement style (i.e., the particle direction during movement; Fig. 47). The displacement style is described by the standard deviation of the particle pathway slopes through time. Displacement direction of a particle is related to the distribution of its contact forces. Changing displacement directions, therefore, indicate variations of the forcefield which in turn can be associated with active faulting and/ or thrusting. For assessing the influence of these potential steering factors, we used the coefficient of determination (R2) between exhumation rate and displacement rate, as shown in Fig. 48, and plotted R^2 against (i) mean exhumation rate, (ii) standard deviation of exhumation rate, and (iii) standard deviation of particle pathway slopes (Fig. 49).

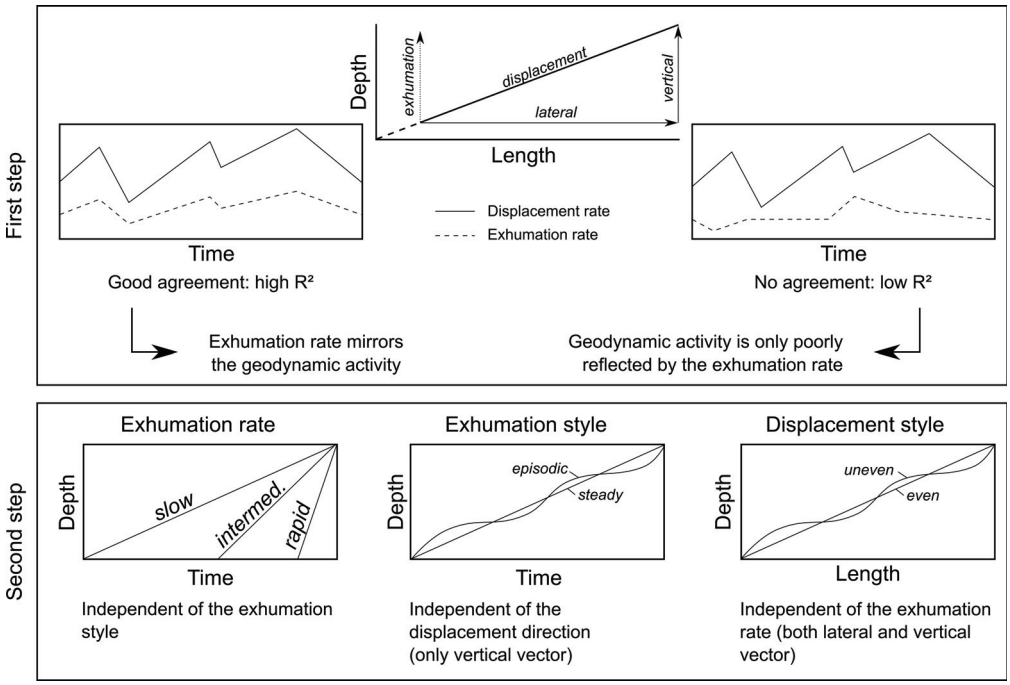

Fig. 47.: The relation between exhumation and displacement (including both, vertical and lateral movement) is analyzed in two steps: In a first step, the statistical agreement (R^2) between exhumation rate and the rate of displacement is derived (Fig. 48). In a second step, the coefficient of determination (R^2) from the first step is related to three possible steering factors (Fig. 49): The mean exhumation rate (reflecting the overall velocity of exhumation), the exhumation style (i.e., continuous vs. episodic exhumation, assessed by the standard deviation of the exhumation rate through time) and the displacement style (i.e., the particle direction during movement assessed by the standard deviation of the particle pathway slopes through time).

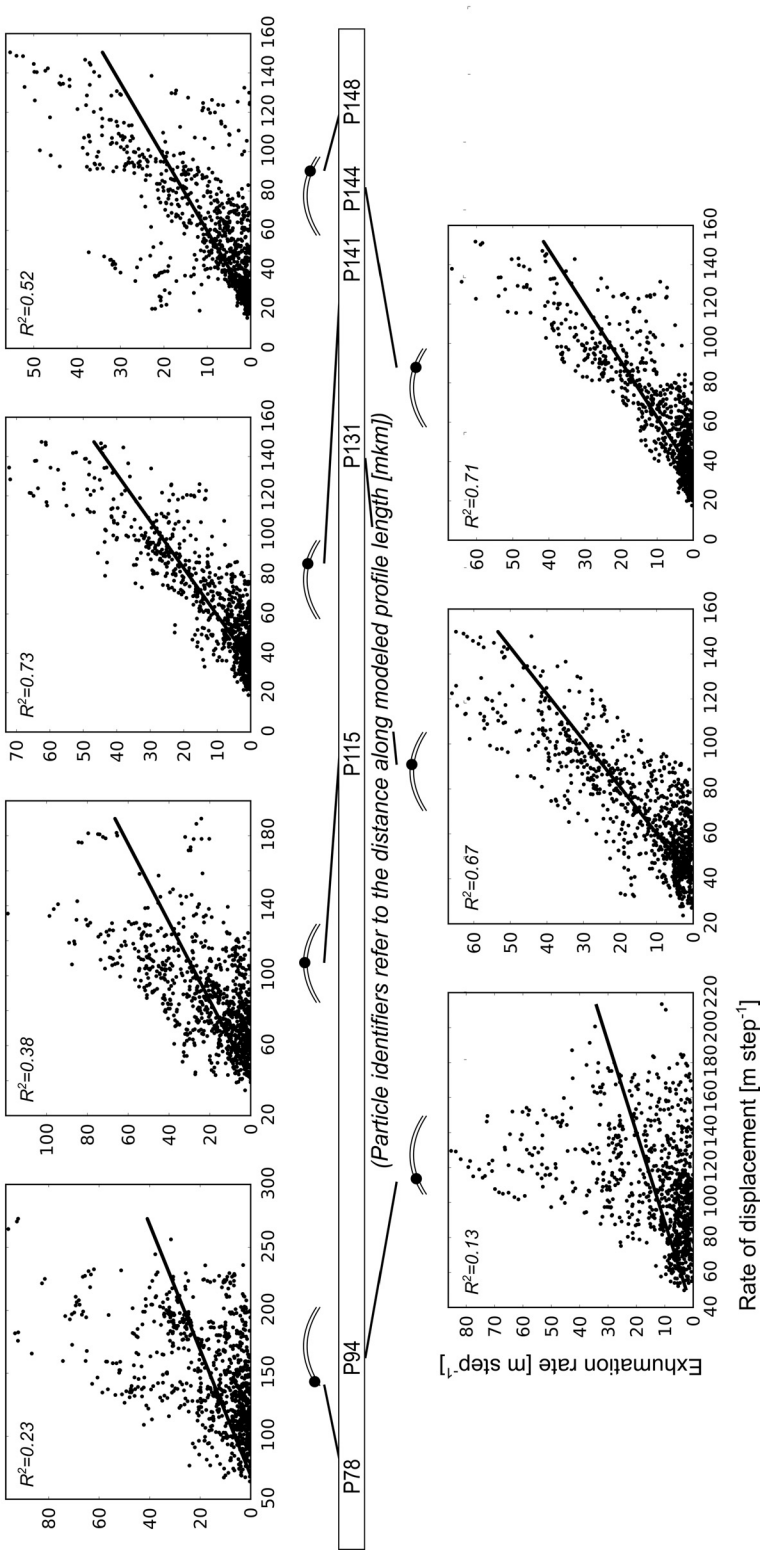

Fig. 48.: Correlation between the rate of displacement (i.e. the length of a particle pathway during one model time step which is equivalent to 32,000 years) and the corresponding exhumation rate of selected particles along the profile (i.e., first step in Fig. 47. See Fig. 45 for thermal histories derived from the pathways of the selected particles from the numerical 'sandbox' experiment). Rates are smoothed by running averages of ten model steps. Pictograms depict the structural position of the particles along culmination I. Coefficient of determination (R^2) was computed with an absolute-valued exhumation since the rate of displacement lacks information about vertical direction.

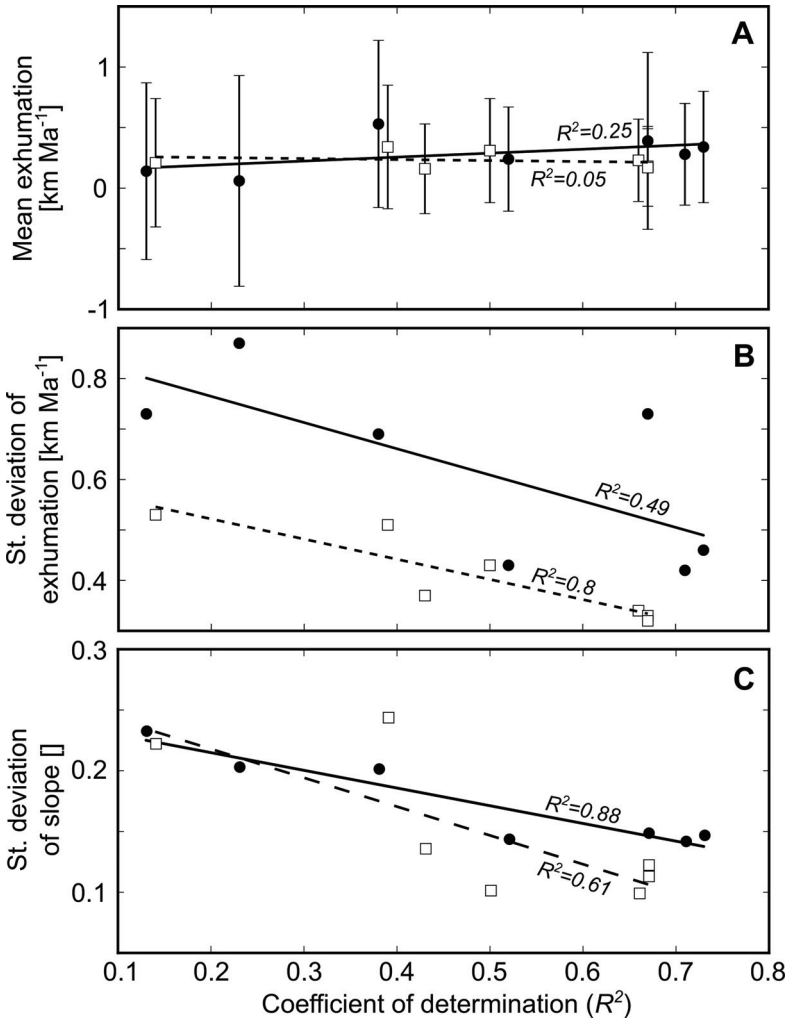

Fig. 49.: Correlation between exhumation rate (i.e. vertical direction) and movement rate (including vertical and lateral directions) of the particles of studied profile (Fig. 48) plotted against the mean exhumation rate (A), the standard deviation of the exhumation rate through time (B) and the standard deviation of particle pathway slope. All rates are smoothed by a running average of ten model time steps (cf. Fig. 48). The standard deviations of both, exhumation rate and slope show a good correlation with R^2 (cf. Fig. 48), suggesting that the exhumation rates mirror the overall geodynamic activity. St. deviation: Standard deviation. Dots and solid lines: Values and first order trend lines derived from the complete model run. Open squares and dashed lines: Values and first order trend lines derived since the particles cooled below 110 °C (i.e. within the temperature sensitivity of the AFT system).

The correlation between the exhumation rate and the rate of displacement (first step) for the selected particles in deed varies along the profile (Fig. 48): Particles along the northern flank of culmination I show basically no correlation (R^2_{P78} = 0.23; R^2_{P94} = 0.13; Fig. 48). The coefficient of determination increases towards the center (R^2_{P115} = 0.38; R^2_{P130} = 0.67) and shows highest values along the southern flank of culmination I (R^2_{P141} = 0.73; R^2_{P144} = 0.71; except for P148, showing weaker correlation: R^2_{P148} = 0.52). Thus, for the central and southern part of culmination I, the exhumation rate provides a good measure for the general geodynamic activity of the orogen. By contrast, in the northern part, the overall particle displacement rates are only poorly reflected by the exhumation rates. While the central and southern part of culmination I is exhumed relatively steadily, exhumation of the northern part is highly episodic. Also, the variability of displacement directions is distinctly lower at the center and along the southern flank of culmination I as compared to the northern flank. Consequently, relatively steady exhumation rates associated with relatively even particle pathways reflect the geodynamic displacement history distinctly better than highly variable exhumation rates associated with strongly varying displacement directions (Fig. 49). Note that the variabilities of exhumation and displacement directions are only spuriously correlated: Both exhumation and displacement directions along the northern flank of culmination I vary distinctly, but not in concert.

In contrast, neither the overall amount of lateral movement (high along both flanks of culmination I) nor the mean exhumation rate (nearly consistent along the profile, Fig. 49) provide information if temporary changes in the exhumation rate can be interpreted in terms of geodynamic activity or not.

6.1. Spatial distribution of lateral displacement and exhumation

To demonstrate the interplay between exhumation, lateral displacement and net movement, we discuss the pathways of three particles being exemplarily for three different structural positions along the modeled profile. Synthetic AFT data discussed in this section is derived from Inc_5.

(I) Particle P78 is located at the hanging wall of FT1 (Fig. 50). Referring to the position at the end of the model run, it is situated at the northern flank of culmination I and is the northernmost particle of the studied profile. The particle pathway is characterized by significant lateral movements and a high number of small-step variation of movement directions. This leads to a slow mean, but highly episodic exhumation (including periods of burial). Forward modeling on the basis of this particle path yields an AFT age of 10.4 Ma, MTL of 13.42 μm with a standard deviation of 2.11 μm.

Fig. 51 exemplarily depicts the relation between the exhumation rate and the rate of displacement at ~14 Ma for P78, illustrating that increasing exhumation rate can go along with a decreasing rate of displacement and vice versa (Fig. 51A). In this case, the particle is transported laterally at high velocity (i.e. with a high rate of displacement), but only little exhumed. The exhumation rate increases shortly before 14 Ma with a short, but pronounced vertical movement impulse, which on the other hand is associated with a decreasing displacement rate (green lines

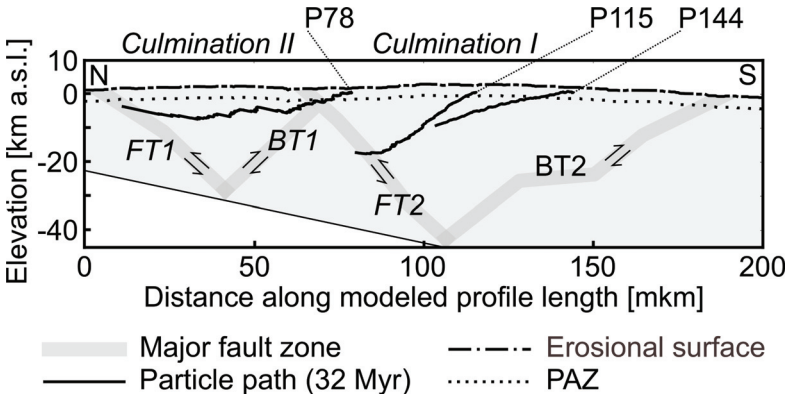

Fig. 50.: Pathways of three exemplary particles (throughout the model run, i.e. equivalent to 32 Myr of orogeny) along culmination I, representing the northern flank and hanging wall of FT2 (P78), the center (P115) and the southern flank (P144). Wedge and tectonic structures are depicted at the end of the model run. P78 and P144 are mostly laterally transported. While P144 moves relatively steadily, the displacement of P78 includes various short periods of nearly vertical uplift. Note that FT2 migrates within the model run time and is not active throughout the entire model run. Therefore, the particle pathway of P78 is not sidetracked by the position of FT2 (i.e. its location at the end of the model run). P115 moves mostly vertically and relatively steadily. FT: Forethrust. BT: Backthrust. PAZ: Partial annealing zone of the AFT system (i.e. the 110 °C isotherm, assuming a geothermal gradient of 30 °C km^{-1}). mkm: model km (i.e. distance along modeled profile length).

in Fig. 51A und B). Afterwards, rock movement accelerates again, related to lateral displacement (red lines in Fig. 51A und B).

Comparing the 'sandbox profile' with the real section through the Lepontine Dome, particle P78 is equivalent to sample Ticino-H-1 of Elfert et al. (2013). Ticino-H-1 is situated at the northern termination of the profile, close to the northern steep belt. Inverse thermal history modeling based on this sample revealed slow and steady Miocene exhumation. The results of the numerical sandbox experiment if transferred to the Central Alps, allow complementing and refining this interpretation. Though exhumation was slow, the rocks south of the northern steep belt moved more rapidly than the fast exhuming central part of the Lepontine Dome, pointing to extensive low-angle to nearly horizontal overthrusting in Miocene times.

(II) Particle P115 is located at the center of culmination I above the tip of the indenter (referring to the position at the end of the model run). The tip of the indenter also represents the singularity of the double-vergent wedge and the point of intersection of the corresponding faults FT2 and BT2 (Fig. 50). P115 moves mostly vertically throughout the model run. Variations of movement directions are less pronounced as compared to P78, leading to rapid and continuous exhumation. Accordingly, a relatively young synthetic AFT age (6.3 Ma) is predicted for P115, along with an MTL of 13 μm and a standard deviation of the track length distribution of 2.5 μm. In contrast to P78, the movement history of P115 is well reflected by the cooling history derived from the numerical 'sandbox' experiment.

(III) Particle P144 is located at the southern flank of culmination I (Fig. 50). P144 is mostly laterally transported, accompanied by nearly steady movement directions (not to be confused

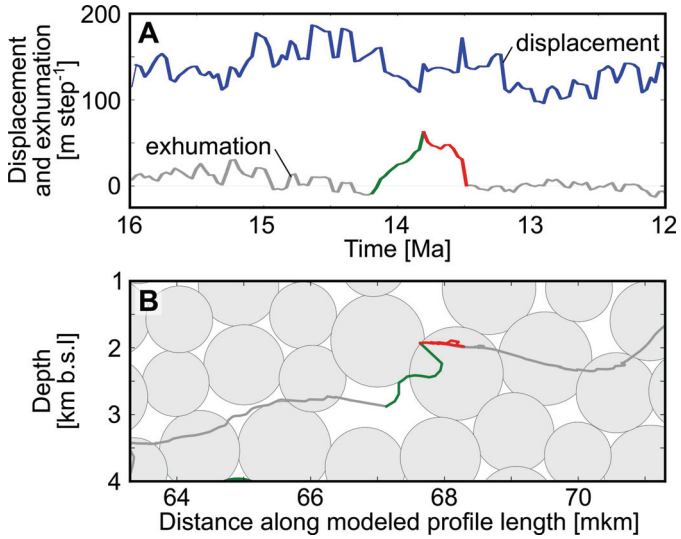

Fig. 51.: Exhumation rate and rate of displacement (A) as well as the particle pathway of P78 from 16 Ma to 12 Ma. Rates of exhumation and displacement refer to one model time step (i.e. 32,000 years). Shown are running averages of ten model time steps. Increasing (green line) and decreasing (red line) exhumation rates are negatively correlated with the corresponding rates of displacement of the particle (A). The particle pathway (B) is colored in the same way, illustrating that the direction of particle movement impacts the exhumation stronger than the length of movement. For reasons of clarity, the gray particle path (B) also shows running averages according to the procedure in Fig. 48. b.s.l.: Below sea level.

with steady velocity). Exhumation along the southern flank is generally slower compared to the culmination center (P115). As a consequence, forward modeling yields an older AFT age as compared to P78 and P115 (16.2 Ma), short MTL (12.94 μm) and a standard deviation of 2.03 μm. The exhumation rate derived from the pathway of P144 is in good agreement with the movement history of the particle.

Summarizing, the general displacement direction of a rock column and the variability of displacement directions are crucially linked to the structural position in the orogenic wedge. Both impact the exhumation style and can thus, at least for the example of the Lepontine Dome, be mirrored by the cooling history: AFT ages and the shape of track length distributions can be related to the lateral component of displacement (i.e. old AFT ages result from slow cooling, which in turn is related to strongly lateral displacement, which can be found along both flanks of an orogenic wedge). MTL can be related to the variability of displacement direction or the exhumation style (i.e. long MTL are correlated with high variability / episodic exhumation, which can be found along the pro-wedge flank of an orogenic wedge).

We conclude that the influence of the lateral component of rock displacement in low-angle thrusting settings can be quantitatively revealed by numerical ‘sandbox’ modeling combined with AFT thermochronology and can thus help interpreting exhumation rates derived from observed AFT data. Particularly, hanging wall velocities of thrust faults are underestimated from solely exhumation rates. On the other hand, exhumation can be directly related to geodynamic activity in steadily exhuming settings with little variability in displacement directions. The ef-

fect of the lateral component and its variability on exhumation can only partly be assessed by thermochronology. Synthetic thermal histories derived from numerical 'sandbox' experiments can be used to gain a fuller understanding.

7. Conclusions

We developed a numerical 'sandbox' experiment aiming to simulate the orogeny of the Central Alps since the Oligocene. Based on particle pathways tracked within the numerical 'sandbox' experiment, we derived three sets of synthetic AFT ages and track-length distributions, and compared them with observed AFT data from the Lepontine Dome of the Central Alps.

Our results allow drawing the following conclusions:

(I) The numerical 'sandbox' experiment successfully reproduces the major structures of the Central Alps as revealed from seismic profiles and structural geology. If the structural findings of the numerical 'sandbox' model can be adapted to the Central Alps, the post-collisional evolution of the Lepontine Dome is strongly linked to the deep fault and thrust zone beneath the northern steep belt and the Aar-/Gotthard massif, triggering updoming of the Lepontine Dome via basal accretion.

(II) Differential Miocene cooling patterns along the modeled numerical 'sandbox' profile are predicted, and this is in good agreement with the results from inverse thermal history modeling based on observed apatite fission track and (U-Th-Sm)/He data from the Lepontine Dome.

(III) Simulating different valley incision scenarios showed that Oligocene and Pliocene valley incision can be distinguished on the basis of AFT thermochronology. In theory, Pliocene vs. Pleistocene valley incision can also be resolved, but only for high-quality samples (1 σ-error $\leq$ 5 %) and for areas of highest exhumation rates and / or tectonic activity. Best match between synthetic AFT data from the numerical sandbox and those actually observed along the Lepontine Dome was obtained for an onset of enhanced valley incision at 5 Ma.

(IV) Tracking particle pathways in the numerical 'sandbox' demonstrated the importance of the lateral component for rock displacement. Particularly velocities of particles derived from hanging walls of thrust faults are underestimated if assessed solely by the exhumation rates. On the other hand, exhumation can be directly related to geodynamic activity in steadily exhuming settings with little variability in displacement directions. The effect of the lateral component and its variability on exhumation can only partly be assessed by thermochronology. Synthetic thermal histories derived from numerical 'sandbox' experiments can be used to gain a more complete understanding.

Acknowledgements

This study is part of the EUROCORES TOPO-EUROPE project from the European Science Foundation and was funded by the German Science Foundation (DfG-Research Center / Cluster of Excellence 'The Ocean in the Earth System' and DfG project SP673/5-1). We would like to thank Lisa-Carmen Eckhart, Sebastian Trüttner and Leonard Rossmann (University of Bremen) for support during data processing.

References

R. Baran, A.M. Friedrich, and F. Schlunegger, 2014. The late Miocene to Holocene erosion pattern of the Alpine foreland basin reflects Eurasian slab unloading beneath the western Alps rather than global climate change. *Lithosphere*, 6(2):124–131.

J. Barbarand, A. Carter, I. Wood, and T. Hurford, 2003. Compositional and structural control of fission-track annealing in apatite. *Chemical Geology*, 198:107–137.

C. Beaumont, P. Fullsack, and J. Hamilton. *Erosional control of active compressional orogens*, pages 1–18. Springer Netherlands, 1992.

A. Berger, I. Mercolli, and M. Engi, 2005. The central Lepontine Alps: Notes accompanying the tectonic and petrographic map sheet Sopra Ceneri (1:100'000). *Schweizerische Mineralogische und Petrographische Mitteilungen*, 85:109–146.

A. Berger, S.M. Schmid, M. Engi, R. Bousquet, and M. Wiederkehr, 2011. Mechanisms of mass and heat transport during Barrovian metamorphism: A discussion based on field evidence from the Central Alps (Switzerland/northern Italy). *Tectonics*, 30:TC 1007.

M. Bernet, M. Zattin, J.I. Garver, M.T. Brandon, and J.A. Vance, 2001. Steady-state exhumation of the European Alps. *Geology*, 29(1):35–38.

M. Bernet, M. Brandon, J. Garver, M.L. Balestieri, B. Ventura, and M. Zattin, 2009. Exhuming the Alps through time: clues from detrital zircon fission-track thermochronology. *Basin Research*, 21:781–798.

G. Bigazzi, 1981. The Problem of the Decay Constant λ_f of ^{238}U. *Nuclear Tracks*, 5(1/2): 35–44.

M. Bonini, 2007. Deformation patterns and structural vergence in brittle-ductile thrust wedges: an additional analogue modelling perspective. *Journal of Structural Geology*, 29(1):141–158.

R. Bousquet, R. Oberhansli, B. Goffe, F. Koller, S.M. Schmid, M. Wiederkehr, R. Schuster, M. Engi, A. Berger, and G. Martinotti, 2008. Metamorphism of metasediments at the scale of an orogen: a key to the Tertiary geodynamic evolution of the Alps. *Geological Society, London, Special Publications*, 298:393–411.

R. Bousquet, S.M. Schmid, G. Zeilinger, R. Oberhänsli, C. Rosenberg, G. Molli, C. Robert, M. Wiederkehr, and Ph. Rossi, 2012. Tectonic framework of the Alps, CCGM/CGMW. *http://www.geodynalps.org*.

M.T. Brandon, M.K. Roden-Tice, and J.I. Garver, 1998. Late Cenozoic exhumation of the Cascadia accretionary wedge in the Olympic Mountains, northwest Washington State. *Geological Society of America Bulletin*, 110(8):985–1009.

A. Brügel, I. Dunkl, W. Frisch, J. Kuhlemann, and K. Balogh, 2000. The record of Periadriatic volcanism in the Eastern Alpine Molasse zone and its palaeogeographic implications. *Terra Nova*, 12:42–47.

D.R. Burbidge and J. Braun, 2002. Numerical models of the evolution of accretionary wedges and fold-and-thrust belts using the distinct-element method. *Geophysical Journal International*, 148(3):542–561.

R.L. Burtner, A. Nigrini, and R.A. Donelick, 1994. Thermochronology of Lower Cretaceous source rocks in the Idaho-Wyoming Thrust Belt. *American Association of Petroleum Geologists Bulletin*, 78:1613–1636.

D.E. Byrne, W.-H. Wang, and D.M. Davis, 1993. Mechanical role of backstops in the growth of forearcs. *Tectonics*, 12(1):123–144.

M. Campani, N. Mancktelow, D. Seward, Y. Rolland, W. Müller, and I. Guerra, 2010. Geochronological evidence for continuous exhumation through the ductile-brittle transition along a crustal-scale low-angle normal fault: Simplon Fault Zone, central Alps. *Tectonics*, 29:TC3002.

W.D. Carlson, R.A. Donelick, and R.A. Ketcham, 1999. Variability of apatite fission-track annealing kinetics: I. Experimental results. *American Mineralogist*, 84:1213–1223.

B. Carrapa, 2009. Tracing exhumation and orogenic wedge dynamics in the European Alps with detrital thermochronology. *Geology*, 37:1127–1130.

C.E. Cederbom, P. Van der Beek, F. Schlunegger, H.D. Sinclair, and O. Oncken, 2011. Rapid extensive erosion of the North Alpine foreland basin at 5-4 Ma. *Basin Research*, 23:528–550.

W.M. Chapple, 1978. Mechanics of thin-skinned fold-and-thrust belts. *Geological Society of America Bulletin*, 89(8):1189–1198.

M. Cloos and R.L. Shreve, 1988. Subduction-channel model of prism accretion, melange formation, sediment subduction, and subduction erosion at convergent plate margins. 1. Background and description. *Pure and Applied Geophysics*, 128(3-4):455–500.

K.D. Crowley, M. Cameron, and R.L. Schaefer, 1991. Experimental studies of annealing of etched fission tracks in fluorapatite. *Geochimica et Cosmochimica Acta*, 55:1449–1465.

P.A. Cundall. *Distinct Element Models of Rock and Soil Structure*, page 129–163. Allen and Unwin, London, 1987.

P.A. Cundall and O.D.L. Strack. BALL - A program to model granular media using the distinct element method, Technical Note. Technical report, Advanced Technology Group. Dames and Moore, London, 1978.

P.A. Cundall and O.D.L. Strack, 1979. A discrete numerical model for granular assemblies. *Géotechnique*, 29(1):47–65.

P.A. Cundall and O.D.L. Strack. *Modeling of microscopic mechanisms in granular material*, page 137–149. Elsevier Science Publishers B.V., Amsterdam, 1983.

D. Davis, J. Suppe, and F.A. Dahlen, 1983. Mechanics of fold-and-thrust belts and accretionary wedges. *Journal of Geophysical Research*, 88(B12):1153–1172.

D.M. Davis and T. Engelder, 1985. The role of salt in fold-and-thrust belts. *Tectonophysics*, 119 (1-4):67–88.

A. Dickin. *Radiogenic Isotope Geology*. Cambridge University Press, 2009. 512 pp.

T. Diehl, S. Husen, E. Kissling, and N. Deichmann, 2009. High-resolution 3-D P-wave model of the Alpine crust. *Geophysical Journal International*, 23:528–550.

M.H. Dodson, 1973. Closure temperature in cooling geochronological and petrological systems. *Contributions to Mineralogy and Petrology*, 40(3):259–274.

R.A. Donelick, 1991. Crystallographic orientation dependence mean etchable fission track length in apatite: An empirical model and experimental observations. *American Mineralogist*, 76:83–91.

R.A. Donelick. A method of fission track analysis utilizing bulk chemical etching of apatite, 1993. U.S. Patent Number 5,267,274.

R.A. Donelick, P.B. O'Sullivan, and R.A. Ketcham, 2005. Apatite Fission-Track Analysis. *Reviews in Mineralogy & Geochemistry*, 179:1133–1147.

I. Dunkl, 2002. Trackkey: a Windows program for calculation and graphical presentation of fission track data. *Computers & Geosciences*, 28:3–12.

T.A. Ehlers and K.A. Farley, 2003. Apatite (U-Th)/He thermochronometry: methods and applications to problems in tectonic and surface processes. *Earth and Planetary Science Letters*, 206:1–14.

S. Elfert, W. Reiter, and C. Spiegel, 2013. Long-lasting tectonic activities of the Lepontine Dome. New evidence from low-temperature thermochronology. *Tectonophysics*, 608:222–236.

S. Elfert, L. Wenk, C. Spiegel, and K. Huhn, in prep. Describing orogenic wedges by a combination of numerical 'sandbox' models and low-temperature thermochronology. II: Applications

to upper crustal processes of the European Central Alps. *In preparation for submission to Journal of Geophysical Research*.

S. Ellis, G. Schreurs, and M. Panien, 2004. Comparisons between analogue and numerical models of thrust wedge development. *Journal of Structural Geology*, 26(9):1659–1675.

M. Engi, C.S. Todd, and D.R. Schmatz, 1995. Tertiary metamorphic conditions in the eastern Lepontine Alps. *Schweizerische mineralogische und petrographische Mitteilungen*, 75(3): 347–369.

M. Engi, R. Bousquet, and A. Berger, 2004. Explanatory Notes to the Map: Metamorphic Structure of the Alps. Central Alps. *Mitteilungen der Österreichischen Mineralogischen Gesellschaft*, 149:157–173.

K.A. Farley, 2000. Helium diffusion from apatite: General behavior as illustrated by Durango fluorapatite. *Journal of Geophysical Research*, 105(B2):2903–2914.

K.A. Farley, 2002. (U-Th)/He dating: Techniques, calibrations, and applications. In P.D. Porcelli, C.J. Ballentine, and R. Wieler, editors, *Noble Gas Geochemistry*, volume 47 of *Reviews in Mineralogy and Geochemistry*, pages 819–843. Mineralogical Society of America, Geochemical Society.

K.A. Farley, R.A. Wolf, and L.T. Silver, 1996. The effects of long alpha-stopping distances on (U-Th)/He ages. *Geochimica et Cosmochimica Acta*, 60(21):4223–4229.

P.G. Fitzgerald and J.W. Gleadow, 1990. New Approaches in Fission Track Geochronology as a Tectonic Tool: Examples from the Transantarctic Mountains. *International Journal of Radiation Applications and Instrumentation. Part D. Nuclear Tracks and Radiation Measurements*, 17(3):351–357.

R.L. Fleischer, P.B. Price, and R.M. Walker, 1965. Ion Explosion Spike Mechanism for Formation of Charged-Particle Tracks in Solids. *Journal of Applied Physics*, 36(11):3645–3652.

R.L. Fleischer, P.B. Price, and R.M. Walker. *Nuclear Tracks in Solids. Principles and Applications.* University of California Press, 1975. 626 pp.

R.M. Flowers, R.A. Ketcham, D.L. Shuster, and K.A. Farley, 2009. Apatite (U–Th)/He thermochronometry using a radiation damage accumulation and annealing model. *Geochimica et Cosmochimica Acta*, 73(8):2347–2365.

M. Frey and R. Ferreiro Mählmann, 1999. Alpine metamorphism of the Central Alps. *Schweizerische Mineralogische und Petrographische Mitteilungen*, 79:135–154.

M. Frey, K. Bucher, and E. Frank, 1980. Alpine metamorphism along the geotraverse Basel-Chiasso : a review. *Eclogae Geologicae Helvetiae*, 73(2):527–546.

W. Frisch, 1979. Tectonic Progradation and Plate Tectonic Evolution of the Alps. *Tectonophysics*, 60:121–139.

W. Frisch, I. Dunkl, and J. Kuhlemann, 2000. Post-collisional orogen-parallel large-scale extension in the Eastern Alps. *Tectonophysics*, 327:239–265.

N. Froitzheim, S.M. Schmid, and M. Frey, 1996. Mesozoic paleogeography and the timing of eclogite-facies metamorphism in the Alps : a working hypothesis. *Eclogae Geologicae Helvetiae*, 89(1):81–110.

R.F. Galbraith and G.M. Laslett, 1993. Statistical models for mixed fission track ages. *Nuclear Tracks and Radiation measurements*, 21:459–470.

K. Gallagher, R. Brown, and C. Johnson, 1998. Fission Track Analysis and its Applications to Geological Problems. *Annual Review of Earth and Planetary Sciences*, 26:519–72.

E. Garzanti and M.G. Malusa, 2008. The Oligocene Alps: Domal unroofing and drainage development during early orogenic growth. *Earth and Planetary Science Letters*, 268:487–500.

C. Gautheron, L. Tassan-Got, J. Barbarand, and M. Pagel, 2009. Effect of alpha-damage annealing on apatite (U-Th)/He thermochronology. *Chemical Geology*, 266:166–179.

C. Gautheron, J. Barbarand, R.A. Ketcham, L. Tassan-Got, P. van der Beek, M. Pagel, R. Pinna-Jamme, F. Couffignal, and M. Fialin, 2013. Chemical influence on α-recoil damage annealing in apatite: Implications for (U-Th)/He dating. *Chemical Geology*, 351:257–267.

A.J.W. Gleadow, 1981. Fission-Track Dating Methods: What are the Real Alternatives? *Nuclear Tracks*, 5(1/2):3–14.

A.J.W. Gleadow. *Fission Track Dating Methods. Principles and Techniques*. School of Earth Sciences. The University of Melbourne, Australia, 3 edition, 2002.

A.J.W. Gleadow and I.R. Duddy, 1981. A natural long-term track annealing experiment for apatite. *Nuclear Tracks*, 5:169–174.

A.J.W. Gleadow and P.G. Fitzgerald, 1987. Uplift history and structure of the Transantarctic Mountains: new evidence from fission track dating of basement apatites in the Dry Valleys area, southern Victoria Land. *Earth and Planetary Science Letters*, 82:1–14.

C. Glotzbach, J. Reinecker, M. Danišík, M.K. Rahn, W. Frisch, and C. Spiegel, 2008. Neogene exhumation history of the Mont Blanc massif, western Alps. *Tectonics*, 27:TC4011.

C. Glotzbach, C. Spiegel, J. Reinecker, M.K. Rahn, and W. Frisch, 2009. What perturbs isotherms? An assessment using fission-track thermochronology and thermal modelling along the Gotthard transect, Central Alps. *Geological Society, London, Special Publications*, 324: 111–124.

C. Glotzbach, J. Reinecker, M. Danišík, M. Rahn, W. Frisch, and C. Spiegel, 2010. Thermal history of the central Gotthard and Aar massifs, European Alps: Evidence for steady state, long-term exhumation. *Journal of Geophysical Research*, 115:F03017.

C. Glotzbach, P.A. Van der Beek, and C. Spiegel, 2011. Episodic exhumation and relief growth in the Mont Blanc massif, Western Alps from numerical modelling of thermochronology data. *Earth and Planetary Science Letters*, 304:417–430.

P.F. Green and I.R. Duddy, 2006. Interpretation of apatite (U–Th)/He ages and fission track ages from cratons. *Earth and Planetary Science Letters*, 244:541–547.

P.F. Green and S.A. Durrani, 1977. Annealing Studies of Tracks in Crystals. *Nuclear Track Detection*, 1(1):33–39.

P.F. Green, I.A. Duddy, A.J.W. Gleadow, and P.R. Tingate, 1985. Fission-Track Annealing in Apatite: Track Length Measurements and the Form of the Arrhenius Plot. *Nuclear Tracks*, 10 (3):323–328.

P.F. Green, I.A. Duddy, A.J.W. Gleadow, P.R. Tingate, and G.M. Laslett, 1986. Thermal Annealing of Fission Tracks in Apatite 1. A Qualitative Description. *Chemical Geology (Isotope Geoscience Section)*, 59:237–253.

P.F. Green, I.A. Duddy, G.M. Laslett, K.A. Hegarty, A.J.W. Gleadow, and J.F. Lovering, 1989. Thermal annealing of fission tracks in apatite. 4. Quantitative modelling techniques and extension to geological timescales. *Chemical Geology (Isotope Geoscience Section)*, 79:155–182.

A.M. Grist and M. Zentilli, 2005. The thermal history of the Nares Strait, Kane Basin, and Smith Sound region in Canada and Greenland: constraints from apatite fission-track and (U-Th-Sm)/He dating. *Canadian Journal of Earth Sciences*, 42(9):1547–1569.

M.A. Gutscher, N. Kukowski, J. Malavieille, and S. Lallemand, 1998. Episodic imbricate thrusting and underthrusting: analog experiments and mechanical analysis applied to the Alaskan accretionary wedge. *Journal of Geophysical Research*, 103(B5):10161–10176.

S. Hardy, C. Duncan, J. Masek, and D. Brown, 1998. Minimum work, fault activity and the growth of critical wedges in fold and thrust belts. *Basin Research*, 10(3):365–373.

W.W. Hay, J.L. Sloan II, and C.N. Wold, 1988. Mass/Age Distribution and Composition of Sediments on the Ocean Floor and the Global Rate of Sediment Subduction. *Journal of Geophysical Research*, 93(B12):14933–14940.

HeFTy user manual, 2009. Version 1.6.7. *Apatite to Zircon, Inc. and Richard A. Ketcham*.

F. Herman, D. Seward, P.G. Valla, A. Carter, B. Kohn, S.D. Willett, and T.A. Ehlers, 2013. Worldwide acceleration of mountain erosion under a cooling climate. *Nature (Letter)*, 504: 423–426.

M.A. House, B.P. Kohn, K.A. Farley, and A. Raza, 2002. Evaluating thermal history models for the Otway Basin, southeastern Australia, using (U-Th)/He and fission-track data from borehole apatites. *Tectonophysics*, 349:277–295.

K. Huhn, I. Kock, and A.J. Kopf, 2006. Comparative numerical and analogue shear box experiments and their implications for the mechanics along the failure plane of landslides. *Norwegian Journal of Geology*, 86:209–220.

M.L. Hunt, 1997. Discrete element simulations for granular material flows : effective thermal conductivity and self-diffusivity. *International Journal of Heat and Mass Transfer*, 40(13): 3059–3068.

J.C. Hunziker, A.J. Hurford, and L. Calmbach, 1997. Alpine cooling and uplift. In O.A. Pfiffner, P. Lehner, P. Heitzmann, S. Mueller, and A. Steck, editors, *Deep Structure of the Swiss Alps: results of NRP 20*, pages 260–264. Birkhauser Verlag, Basel, Switzerland.

A.J. Hurford, 1986. Cooling and uplift patterns in the Lepontine Alps South Central Switzerland and an age of vertical movement on the Insubric fault line. *Contributions to Mineralogy and Petrology*, 92:413–427.

A.J. Hurford, 1990. Standardization of fission track dating calibration: Recommendation by the Fission Track Working Group of the I.U.G.S. Subcommission on Geochronology. *Chemical Geology (Isotope Geoscience Section)*, 80:171–178.

A.J. Hurford and P.F. Green, 1981. A Reappraisal of Neutron Dosimetry and Uranium-238 λ_t Values in Fission-Track Dating. *Earth and Planetary Science Letters*, 59:343–354.

A.J. Hurford and P.F. Green, 1982. A users' guide to fission track dating calibration. *Earth and Planetary Science Letters*, 59:343–354.

A.J. Hurford and P.F. Green, 1983. The Zeta Age Calibration of Fission-Track Dating. *Isotope Geoscience*, 1:285–317.

ITASCA. *PFC 2D 3.1 Manual*. Itasca Consulting Group, Inc., Minneapolis, 3.1 edition, 2004.

ITASCA. PFC2D - ITASCA software. Website, 2014. Available online at `http://www.itascacg.com/software/pfc2d`; visited on April 4th 2014.

E. Janots, M. Engi, D. Rubatto, A. Berger, C. Gregory, and M.K. Rahn, 2009. Metamorphic rates in collisional orogeny from in situ allanite and monazite dating. *Geology*, 37(1):11–14.

L. Jolivet, C. Faccenna, B. Goffé, M. Mattei, F. Rossetti, C. Brunet, F. Storti, R. Funiciello, J.P. Cadet, N. d'Agostino, and T. Parra, 1998. Midcrustal shear zones in postorogenic extension: Example from the northern Tyrrhenian SeaJolive. *Journal of Geophysical Research (Solid Earth)*, 103(B6):12123–12160.

R.A. Ketcham, 2005. Forward and Inverse Modeling of Low-Temperature Thermochronometry Data. *Reviews in Mineralogy & Geochemistry*, 58:275–314.

R.A. Ketcham, R.A. Donelick, and W.D. Carlson, 1999. Variability of apatite fission-track annealing kinetics: III. Extrapolation to geological time scales. *American Mineralogist*, 84: 1235–1255.

R.A. Ketcham, A. Carter, R.A. Donelick, J. Barbarand, and A.J. Hurford, 2007a. Improved modeling of fission-track annealing in apatite. *American Mineralogist*, 92:799–810.

R.A. Ketcham, A. Carter, R.A. Donelick, J. Barbarand, and A.J. Hurford, 2007b. Improved measurement of fission-track annealing in apatite using c-axis projection. *American Mineralogist*, 92:789–798.

R.A. Ketcham, C. Gautheron, and L. Tassan-Got, 2011. Accounting for long alpha-particle stopping distances in (U–Th–Sm)/He geochronology: Refinement of the baseline case. *Geochimica et Cosmochimica Acta*, 75:7779–7791.

P.O. Koons, 1990. The two-sided orogen: Collision and erosion from the sandbox to the Southern Alps, New Zealand. *Geology*, 18:679–682.

J. Kuhlemann, 2007. Paleogeographic and paleotopographic evolution of the Swiss and Eastern Alps since the Oligocene. *Global and Planetary Change*, 58:224–236.

J. Kuhlemann, W. Frisch, I. Dunkl, B. Székely, and C. Spiegel, 2001. Miocene shifts of the drainage divide in the Alps and their foreland basin. *Zeitschrift für Geomorphologie*, 45(2): 239–265.

J. Kuhlemann, W. Frisch, B. Székely, I. Dunkl, and M. Kázmér, 2002. Post-collisional sediment budget history of the Alps: tectonic versus climatic control. *International Journal of Earth Sciences (Geologische Rundschau)*, 91:818–837.

N.H. Kuiper, 1960. Tests concerning random points on a circle. *Proceedings of the Koninklijke Nederlandse Akademie van Wetenschappen, Serie A*, 63:38–47.

M. Kwapinska, G. Saage, and E. Tsotsas, 2006. Mixing of particles in rotary drums: A comparison of discrete element simulations with experimental results and penetration models for thermal processes. *Powder Technology*, 161:69–78.

A. Kühni and O.A. Pfiffner, 2001. Drainage patterns and tectonic forcing: a model study for the Swiss Alps. *Basin Research*, 13:169–197.

E. Kündig, 1936. Tektonischer Überblick über die gesamten Tessiner Alpen. In P. Niggli, H. Preiswerk, O. Grütter, L. Bossard, and E. Kündig, editors, *Geologische Beschreibung der Tessiner Alpen zwischen Maggia- und Bleniotal*, volume 71 of *Beiträge zur Geologischen Karte der Schweiz*, pages 101–132. Schweizerische Geologische Kommission, Bern.

G.M. Laslett, P.F. Green, I.R. Duddy, and A.J.W. Gleadow, 1987. Thermal annealing of fission tracks in apatite. 2. A quantitative analysis. *Chemical Geology (Isotope Geoscience Section)*, 65:1–13.

H.J. Lippolt, M. Leitz, R.S. Wernicke, and B. Hagedorn, 1994. (Uranium+thorium)/helium dating of apatite: experience with samples from different geochemical environments. *Chemical Geology*, 112:179–191.

F. Lisker, B. Ventura, and U.A. Glasmacher, 2009. Apatite thermochronology in modern geology. *Geological Society, London, Special Publications*, 324:1–23.

J. Lohrmann, N. Kukowski, J. Adam, and O. Oncken, 2003. The impact of analogue material properties on the geometry, kinematics, and dynamics of convergent sand wedges. *Journal of Structural Geology*, 25(10):1691–1711.

N.S. Mancktelow, 1985. The Simplon Line : a major displacement zone in the western Lepontine Alps. *Eclogae Geologicae Helvetiae*, 78(1):73–96.

N.S. Mancktelow, 1992. Neogene lateral extension during convergence in the Central Alps: Evidence from interrelated faulting and backfolding around the Simplonpass (Switzerland). *Tectonophysics*, 215:295–317.

G. Mandl. *Mechanics of tectonic faulting*. Elsevier, Amsterdam, 1988. 407 pp.

M. Maxelon and N.S. Mancktelow, 2005. Three-dimensional geometry and tectonostratigraphy of the Pennine zone, Central Alps, Switzerland and Northern Italy. *Earth-Science Reviews*, 71:171–227.

O. Merle, P.R. Cobbold, and S. Schmid, 1989. Tertiary kinematics in the Lepontine dome. *Geological Society, London, Special Publications*, 45:113–134.

C. Meyre, D. Marquer, S.M. Schmid, and L. Ciancaleoni, 1998. Syn-orogenic extension along the Forcola fault: Correlation of Alpine deformations in the Tambo and Adula nappes (Eastern Penninic Alps). *Eclogae Geologicae Helvetiae*, 91:409–420.

I. Michalski and M. Soom, 1990. The Alpine thermo-tectonic evolution of the Aar and Gotthard massifs, Central Switzerland: fission track ages on zircon and apatite and K-Ar mica ages. *Schweizerische Mineralogische und Petrographische Mitteilungen*, 70(3):373–387.

A.G. Milnes, 1974. Structure of the Pennine Zone (Central Alps): A New Working Hypothesis. *Geological Society of America Bulletin*, 85(11):1727–1732.

A.G. Milnes, 1975. On Steep Isogradic Surfaces in the Simplon Area: A Discussion. *Contribution to Mineralogy and Petrology*, 53:65–68.

R.D. Mindlin and H. Deresiewicz, 1953. Elastic Spheres in Contact under Varying Oblique Forces. *Journal of Applied Mechanics-Transactions of the Asme*, 20(3):327–344.

A. Miyakawa, Y. Yamada, and T. Matsuoka, 2010. Effect of increased shear stress along a plate boundary fault on the formation of an out-of-sequence thrust and a break in surface slope within an accretionary wedge, based on numerical simulations. *Tectonophysics*, 484(1-4): 127–138.

P. Molnar, 2004. Late Cenozoic Increase In Accumulation Rates Of Terrestrial Sediment: How Might Climate Change Have Affected Erosion Rates? *Annual Review of Earth and Planetary Sciences*, 32:67–89.

P. Molnar and P. England, 1990. Late Cenozoic uplift of mountain ranges and global climate change: chicken or egg? *Nature*, 346(6279):29–34.

J.C. Moore, 1989. Tectonics and hydrogeology of accretionary prisms: role of the décollement zone. *Journal of Structural Geology*, 11(1-2):95–106.

J.K. Morgan and M.S. Boettcher, 1999. Numerical simulations of granular shear zones using the distinct element method 1. Shear zone kinematics and the micromechanics of localization. *Journal of Geophysical Research*, 104(B2):2703–2719.

G. Mulugeta, 1988. Modelling the geometry of coulomb thrust wedges. *Journal of Structural Geology*, 10(8):847–859.

G. Muttoni, C. Carcano, E. Garzanti, M. Ghielmi, A. Piccin, R. Pini, S. Rogledi, and D. Sciunnach, 2003. Onset of major Pleistocene glaciations in the Alps. *Geology*, 31(11):989–992.

S. Müller, 1989. Deep-reaching geodynamic processes in the Alps. *Geological Society, London, Special Publications*, 45:303–328.

C.W. Naeser. Fission Track Dating. Technical Report 76-190, United States Department of the Interior. Geological Survey, 1976. Open-File Report.

M. Naylor, H.D. Sinclair, S. Willett, and P.A. Cowie, 2005. A discrete element model for orogenesis and accretionary wedge growth. *Journal of Geophysical Research*, 110(B12): B12403.

P. Nievergelt, M. Liniger, N. Froitzheim, and R. Ferreiro Mählmann, 1996. Early to mid Tertiary crustal extension in the Central Alps: The Turba Mylonite Zone (Eastern Switzerland). *Tectonics*, 15(2):329–340.

E. Niggli, 1960. Mineralzonen der alpinen Metamorphose in den Schweizer Alpen. *International Geological Congress XXI Session Norden, Copenhagen, Part B*, pages 132–138.

E. Niggli and C.B. Niggli, 1965. Karten der Verbreitung einiger Mineralien der alpidischen Metamorphose in den Schweizer Alpen (Stilpnomelan, Alkali-Amphibol, Chloritoid, Staurolith, Disthen, Sillimanit). *Eclogae Geologicae Helvetiae*, 58:335–368.

K. S. Persson and D. Sokoutis, 2002. Analogue models of orogenic wedges controlled by erosion. *Tectonophysics*, 356:323–336.

B. Peters, 2002. Measurements and Application of a Discrete Particle Model (DPM) to Simulate Combustion of a Packed Bed of Individual Fuel Particles. *Combustion and Flame*, 131:132–146.

O.A. Pfiffner, W. Frei, P. Finckh, and P. Valasek, 1988. Deep seismic reflection profiling in the Swiss Alps: Explosion seismology results for line NFP 20-East. *Geology*, 16:987–990.

O.A. Pfiffner, E.M. Kaper, A.-M. Mayerat, and P. Heitzmann, 1990. Structure of the basement-cover contact in the Swiss Alps. *Les Mémoires de la Société géologique de France (N.S.)*, 156:247–262.

O.A. Pfiffner, P. Lehner, P. Heitzmann, St. Müller, and A. Steck, editors. *Deep Structure of the Swiss Alps, Results of NFP 20*. Birkhauser Verlag, Basel, 1997. 380 pp.

H. Preiswerk, 1918. Geologische Beschreibung der Lepontinischen Alpen, zweiter Teil – Oberes Tessin- und Maggiagebiet. *Beiträge zur Geologischen Karte der Schweiz*, 26:43–81.

F. Preusser, H.R. Graf, O. Keller, E. Krayss, and C. Schlüchter, 2011. Quaternary glaciation history of northern Switzerland. *Quaternary Science Journal*, 60(2-3):282–305.

P.B. Price and R.M. Walker, 1962a. Electron Microscope Observation of a Radiation-Nucleated Phase Transformation in Mica. *Journal of Applied Physics*, 33(8):2625–2628.

P.B. Price and R.M. Walker, 1962b. Observation of Fossil Particle Tracks in Natural Micas. *Nature*, 196(4856):732–734.

M.K. Rahn, 2005. Apatite fission track ages from the Adula nappe: late-stage exhumation and relief evolution. *Schweizerische Mineralogische und Petrographische Mitteilungen*, 85:233–245.

M.K. Rahn and D. Seward, 2000a. A revised study of the exhumation of the Central Alps: first results from a compilation of more than 500, published and new apatite fission track analyses. *Fission Track 2000, 9th International Conference on Fission Track Dating and Thermochronology, Geological Society of Australia Abstract Series*, 58:275–276.

M.K. Rahn and D. Seward, 2000b. How many track lengths do we need? volume 10/1/20 of *Ontrack, The Newsletter of the International Fission-Track Community*.

L. Ratschbacher, W. Frisch, F. Neubauer, S.M. Schmid, and J. Neugebauer, 1989. Extension in compressional orogenic belts: The eastern Alps. *Geology*, 17:404–407.

J. Reinecker, M. Danišík, C. Schmid, C. Glotzbach, M. Rahn, W. Frisch, and C. Spiegel, 2008. Tectonic control on the late stage exhumation of the Aar Massif (Switzerland): Constraints from apatite fission track and (U-Th)/He data. *Tectonics*, 27:TC6009.

S. Rickelt. *Discrete Element Simulation and Experimental Validation of Conductive and Convective Heat Transfer in Moving Granular Material*. Phd thesis, Ruhr-Universität Bochum, Fakultät für Maschinenbau, 2011.

S. Rickelt, F. Sudbrock, S. Wirtz, and V. Scherer, 2013. Coupled DEM/CFD simulation of heat transfer in a generic grate system agitated by bars. *Powder Technology*, 249:360–372.

E. Rutherford, 1905. Present Problems in Radioactivity. *Popular Science Monthly*, 67. 32 pp.

R. Rütti, M. Maxelon, and N.S. Mancktelow, 2005. Structure and kinematics of the northern Simano Nappe, Central Alps, Switzerland. *Eclogae Geologicae Helvetiae*, 98:63–81.

R. Rütti, D. Marquer, and A.B. Thompson, 2008. Tertiary tectono-metamorphic evolution of the European margin during Alpine collison: example of the Leventina Nappe (Central Alps, Switzerland). *Swiss Journal of Geosciences*, 101:157–171.

S.D. Saltzer and D.D. Pollard, 1992. Distinct element modeling of structures formed in sedimentary overburden by extensional reactivation of basement normal faults. *Tectonics*, 11(1): 165–174.

J.P. Schaer, G.M. Reimer, and G.A. Wagner, 1975. Actual and ancient uplift rate in the Gotthard region, Swiss Alps: a comparison between precise levelling and fission-track apatite age. *Tectonophysics*, 29:293–300.

F. Schlunegger and J. Mosar, 2011. The last erosional stage of the Molasse Basin and the Alps. *International Journal of Earth Sciences*, 100:1147–1162.

F. Schlunegger and S. Willett, 1999. Spatial and temporal variations in exhumation of the central Swiss Alps and implications for exhumation mechanisms. *Geological Society, London, Special Publications*, 154:157–179.

F. Schlunegger, R. Slingerland, and A. Matter, 1998. Crustal thickening and crustal extension as controls on the evolution of the drainage network of the central Swiss Alps between 30 Ma and the present: constraints from the stratigraphy of the North Alpine Foreland Basin and the structural evolution of the Alps. *Basin Research*, 10:197–212.

F. Schlunegger, D. Rieke-Zapp, and K. Ramseyer, 2007. Possible environmental effects on the evolution of the Alps-Molasse Basin system. *Swiss Journal of Geosciences*, 100:383–405.

S.M. Schmid, H.R. Aebli, F. Heller, and A. Zingg, 1989. The role of the Periadriatic Line in the tectonic evolution of the Alps. *Geological Society, London, Special Publications*, 45: 153–171.

S.M. Schmid, O.A. Pfiffner, N. Froitzheim, G. Schönborn, and E. Kissling, 1996. Geophysical-geological transect and tectonic evolution of the Swiss-Italian Alps. *Tectonics*, 15(5):1036–1064.

S.M. Schmid, B. Fügenschuh, E. Kissling, and R. Schuster, 2004a. Tectonic map and overall architecture of the Alpine orogen. *Eclogae Geologicae Helvetiae*, 97:93–117.

S.M. Schmid, B. Fügenschuh, E. Kissling, and R. Schuster, 2004b. TRANSMED transects IV, V and VI: Three lithospheric transects across the Alps and their forelands. In W. Cavazza, F.M. Roure, W. Spakman, G.M. Stampfli, and P.A. Ziegler, editors, *The TRANSMED Atlas: The Mediterranean Region from Crust to Mantle*. Springer Verlag. 141 pp.

J. Selverstone, 2005. Are the Alps collapsing? *Annual Review of Earth and Planetary Sciences*, 33:113–32.

D.L. Shuster, R.M. Flowers, and K.A. Farley, 2006. The influence of natural radiation damage on helium diffusion kinetics in apatite. *Earth and Planetary Science Letters*, 249:148–161.

J.H.W. Smit, J.P. Brun, and D. Sokoutis, 2003. Deformation of brittle-ductile thrust wedges in experiments and nature. *Journal of Geophysical Research*, 108(B10):2480.

M.A. Soom, 1990. Abkühlungs- und Hebungsgeschichte der Externmassive und der penninischen Decken beidseits der Simplon-Rhone-Linie seit dem Oligozan: Spaltspurdatierungen an Apatit/Zirkon und K–Ar-Datierungen an Biotit/Muskowit (Westliche Zentralalpen). *Unpublished PhD thesis, University of Bern*, pages 113–32.

C. Spiegel, J. Kuhlemann, I. Dunkl, W. Frisch, H. von Eynatten, and K. Balogh, 2000. The erosion history of the Central Alps: evidence from zircon fission track data of the foreland basin sediments. *Terra Nova*, 12:163–170.

C. Spiegel, J. Kuhlemann, I. Dunkl, and W. Frisch, 2001. Paleogeography and catchment evolution in a mobile orogenic belt: the Central Alps in Oligo–Miocene times. *Tectonophysics*, 341:33–47.

C. Spiegel, B. Kohn, A. Raza, T. Rainer, and A. Gleadow, 2007. The effect of long-term low-temperature exposure on apatite fission track stability: A natural annealing experiment in the deep ocean. *Geochimica et Cosmochimica Acta*, 71:4512–4537.

C. Spiegel, B. Kohn, D. Belton, Z. Berner, and A. Gleadow, 2009. Apatite (U-Th-Sm)/He thermochronology of rapidly cooled samples: The effect of He implantation. *Earth and Planetary Science Letters*, 285:105–114.

G.M. Stampfli and C. Hochard, 2009. Plate tectonics of the Alpine realm. *Geological Society, London, Special Publications*, 327:89–111.

G.M. Stampfli, G.D. Borel, R. Marchant, and J. Mosar, 2002. Western Alps geological constraints on western Tethyan reconstructions. *Journal of the Virtual Explorer*, 8:77–106.

A. Steck and J. Hunziker, 1994. The Tertiary structural and thermal evolution of the Central Alps – compressional and extensional structures in an orogenic belt. *Tectonophysics*, 238: 229–254.

F. Storti, F. Salvini, and K. McClay, 2000. Synchronous and velocity-partitioned thrusting, and thrust polarity reversal in experimentally produced, doubly-vergent thrust wedges: Implications for natural orogens. *Tectonics*, 19:378–396.

R.J. Strutt, 1905. On the Radio-Active Minerals. *Proceedings of the Royal Society of London. Series A*, 76(508):88–101.

K. Stüwe and M. Hintermüller, 2000. Topography and isotherms revisited: the influence of laterally migrating drainage divides. *Earth and Planetary Science Letters*, 184:287–303.

T. Tagami and P.B. O'Sullivan, 2005. Fundamentals of Fission-Track Thermochronology. *Reviews in Mineralogy & Geochemistry*, 58:19–47.

M. ter Voorde, C.H. de Bruijne, S.A.P.L. Cloetingh, and P.A.M. Andriessen, 2004. Thermal consequences of thrust faulting: simultaneous versus successive fault activation and exhumation. *Earth and Planetary Science Letters*, 223:395–413.

Z. Timar-Geng, D. Grujic, and M.K. Rahn, 2004. Deformation at the Leventina-Simano nappe boundary, Central Alps, Switzerland. *Eclogae Geologicae Helvetiae*, 97:265–278.

C.S. Todd and M. Engi, 1997. Metamorphic field gradients in the Central Alps. *Journal of Metamorphic Geology*, 15(4):513–530.

V. Trommsdorf, 1966. Progressive Metamorphose kieseliger Karbonatgesteine in den Zentralalpen zwischen Bernina und Simplon. *Schweizerische mineralogische und petrographische Mitteilungen*, 46:431–460.

USGS, 2004. Shuttle Radar Topography Mission, 3 Arc Second scene, Unfilled Unfinished 2.0. *Global Land Cover Facility, University of Maryland, College Park*. Maryland, February 2000.

P.G. Valla, D.L. Shuster, and P.A. van der Beek, 2011. Significant increase in relief of the European Alps during mid-Pleistocene glaciations. *Nature Geoscience*, 4:688–692.

P.G. Valla, P.A. van der Beek, D.L. Shuster, J. Braun, F. Herman, L. Tassan-Got, and C. Gautheron, 2012. Late Neogene exhumation and relief development of the Aar and Aiguilles Rouges massifs (Swiss Alps) from low-temperature thermochronology modeling and ^{4}He/^{3}He thermochronometry. *Journal of Geophysical Research*, 117:F01004.

P Van den haute, F. De Corte, R. Jonckheere, and F Bellemans. *The parameters that govern the accuracy of fission-track age determinations: a re-appraisal*, pages 33–46. Kluwer Academic Publishing, Dordrecht, 1998.

W.L. Vargas and J.J. McCarthy, 2002. Conductivity of granular media with stagnant interstitial fluids via thermal particle dynamics simulation. *International Journal of Heat and Mass Transfer*, 45:4847–4856.

P. Vermeesch, 2008. Three new ways to calculate average (U-Th)/He ages. *Chemical Geology*, 249:339–347.

A.J. Vernon, P.A. van der Beek, H.D. Sinclair, and M.K. Rahn, 2008. Increase in late Neogene denudation of the European Alps confirmed by analysis of a fission-track thermochronology database. *Earth and Planetary Science Letters*, 270:316–329.

A.J. Vernon, P.A. Van der Beek, H.D. Sinclair, C. Persano, J. Foeken, and F.M. Stuart, 2009. Variable late Neogene exhumation of the central European Alps: Low-temperature thermochronology from the Aar Massif, Switzerland, and the Lepontine Dome, Italy. *Tectonics*, 28:TC5004.

F. Von Blanckenburg and J.H. Davies, 1995. Slab breakoff: A model for syncollisional magmatism and tectonics in the Alps. *Tectonics*, 14(1):120–131.

H. Von Eynatten, F. Schlunegger, R. Gaupp, and J.R. Wijbrans, 1999. Exhumation of the Central Alps: evidence from 40Ar/39Ar laserprobe dating of detrital white micas from the Swiss Molasse Basin. *Terra Nova*, 11(6):284–289.

G.A. Wagner, 1968. Fission Track Dating of Apatites. *Earth and Planetary Science Letters*, 4: 411–415.

G.A. Wagner. *Correction and Interpretation of Fission Track Ages*, pages 170–177. Springer-Verlag, Berlin, Heidelberg, NY, 1979. 329 pp.

G.A. Wagner and G.M. Reimer, 1972. Fission Track Tectonics: The Tectonic Interpretation of Fission Track Apatite Ages. *Earth And Planetary Science Letters*, 14:263–268.

G.A. Wagner and P. Van den haute. *Fission-Track Dating*. Ferdinand Enke Verlag, Stuttgart, 1992. 285 pp.

G.A. Wagner, G.M. Reimer, and E. Jäger, 1977. Cooling Ages Derived by Apatite Fission-Track, Mica Rb-Sr and K-Ar Dating: the Uplift and Colling History of the Central Alps. *Memorie degli Istituti di Geologia e Mineralogia dell' Università di Padova*, 30:1–27.

L. Wenk and K. Huhn. Mechanics in heterogeneous accretionary wedges - to test implemented rheologies. In H. Zhu, R. Hart, C. Detournay, and Nelson M., editors, *Continuum and Distinct Element Numerical Modeling in Geomechanics*, 3rd International FLAC/DEM Symposium, Hangzhou, China, 2013.

L. Wenk, S. Elfert, C. Spiegel, and K. Huhn, in prep. Describing orogenic wedges by a combination of numerical 'sandbox' models and low-temperature thermochronology I: Linking lower crustal mechanic and kinematic properties with upper crustal processes. *In preparation for submission to Journal of Geophysical Research.*

M. Wiederkehr, R. Bousquet, S.M. Schmid, and A. Berger, 2008. From subduction to collision: thermal overprint of HP/LT meta-sediments in the north-eastern Lepontine Dome (Swiss Alps) and consequences regarding the tectono-metamorphic evolution of the Alpine orogenic wedge. *Swiss Journal of Geosciences*, 101:127–155.

M. Wiederkehr, M. Sudo, R. Bousquet, A. Berger, and S.M. Schmid, 2009. Alpine orogenic evolution from subduction to collisional thermal overprint: The $^{4}0$Ar/$^{3}9$Ar age constraints from the Valaisan Ocean, central Alps. *Tectonics*, 28:TC6009.

J.K. Willenbring and F. von Blanckenburg, 2010. Long-term stability of global erosion rates and weathering during late-Cenozoic cooling. *Nature*, 465(13):211–214.

S. Willett, C. Beaumont, and P. Fullsack, 1993. Mechanical model for the tectonics of doubly-vergent compressional orogens. *Geology*, 21:371 –374.

S.D. Willett, 2010. Late Neogene Erosion of the Alps: A Climate Driver? *Annual Review of Earth and Planetary Sciences*, 38:411–437.

S.D. Willett, F. Schlunegger, and V. Picotti, 2006. Messinian climate change and erosional destruction of the central European Alps. *Geology*, 34(8):613–616.

R.A. Wolf, K.A. Farley, and L.T. Silver, 1996. Helium diffusion and low temperature thermochronometry of apatite. *Geochimica et Cosmochimica Acta*, 60:4231–4240.

R.A. Wolf, K.A. Farley, and D.M. Kass, 1998. Modeling of the temperature sensitivity of the apatite (U–Th)/He thermochronometer. *Chemical Geology*, 148:105–114.

P.K. Zeitler, A.L. Herczig, I. McDougall, and M. Honda, 1987. U-Th-He dating of apatite: a potential thermochronometer. *Geochimica et Cosmochimica Acta*, 51:2865–2868.

A. Sample locations

Sample locations (horizontal profiles). Coordinates refer to the Swiss Grid CH1903.

Sample	Geotectonic unit	x [m]	y [m]	Elevation [m]
Ticino-H1	Leventina	704220	148157	710
Ticino-H4	Leventina	707811	144514	730
Ticino-H6	Leventina	709757	141561	490
Ticino-H9	Leventina	711072	138663	377
Ticino-H11	Leventina	713242	136698	370
Ticino-H18	Leventina	717082	136257	318
Ticino-H13	Leventina	716576	134288	402
Ticino-H22	Leventina	719424	130319	311
Ticino-H23	Leventina	720932	126737	326
Ticino-H27	Simano	721777	121573	300
Ticino-H28	Mergoscia	722695	119680	377
Ticino-H25	Bellinzona	724259	118848	475
Maggia-H-1	Maggia	692794	134861	622
Maggia-H-3	Antigorio	690436	133569	470
Maggia-H-5	Antigorio	690068	131584	481
Maggia-H-6	Antigorio	689637	129095	433
Maggia-H-10	Antigorio	693410	127319	390
Maggia-H-14	Maggia	698390	121690	307
Maggia-H-15	Antigorio	699920	119454	551
Maggia-H-27	Antigorio	701651	116311	288
Maggia-H-25	Monte Rosa	699651	114766	250
Maggia-H-22	Ivrea	699460	110737	246

Sample locations (elevation profiles). Coordinates refer to the Swiss Grid CH1903.

Sample	Geotectonic unit	x [m]	y [m]	Elevation [m]
Ticino-VNo1	Lucomagno	706245	151621	2032
Ticino-VNo2	Lucomagno	706752	151205	1876
Ticino-VNo3	Lucomagno	706453	150123	1596
Ticino-VNo4	Lucomagno	706269	149466	1367
Ticino-VNo5	Lucomagno	704847	150058	1218
Ticino-VNo6	Lucomagno	703887	149619	1000
Ticino-VNo7	Lucomagno	705266	148203	840
Maggia-VNo1	Maggia	690532	137740	2115
Maggia-VNo2	Maggia	690814	137992	1942
Maggia-VNo3	Maggia	691237	138575	1693
Maggia-VNo4	Maggia	691848	138629	1437
Maggia-VNo5	Maggia	692963	138447	1286
Maggia-VNo6	Maggia	693353	137870	1150
Maggia-VNo7	Maggia	693894	138105	940
Ticino-VM1	Cima Lunga	719491	120679	1398
Ticino-VM4	Cima Lunga	721202	120074	820
Ticino-VM8	Cima Lunga	722752	119545	321
Maggia-VS1	Ivrea / SSB	695695	110683	1668
Maggia-VS2	Ivrea / SSB	697025	111073	1416
Maggia-VS3	Ivrea / SSB	697648	111436	1329
Maggia-VS4	Ivrea / SSB	698999	112131	1054
Maggia-VS8	Ivrea / SSB	699821	111351	601

B. AFT Data

Results of AFT analysis (horizontal profiles)[a].

Sample	No. of grains	ρ_s	N_s	ρ_i	N_i	ρ_d	N_d	P(x^2) [%]	Central age [Ma]	$\pm1\sigma$	Dpar [μm]	N_{TL}	MTL [μm]	St.dev	MpTL [μm]	St.dev	U [ppm]
Ticino-H1	21	0.80	58	16.72	1217	16.53	26077	60.4	13.1	1.8	2.26	14	13.18	2.15	14.30	1.33	11.31
Ticino-H4	8	1.07	25	22.36	521	16.81	25196	63.0	13.4	2.8	2.22	4	12.93	2.76	14.11	1.81	15.40
Ticino-H6	20	0.54	40	19.78	1466	16.78	25196	77.8	7.6	1.2	2.14	43	12.99	1.83	14.10	1.26	14.20
Ticino-H9	10	0.23	8	6.70	233	17.53	26314	53.7	10.0	3.6	2.15	3	13.02	2.34	14.11	1.66	4.29
Ticino-H11	9	1.14	23	62.77	1263	24.82	37324	23.3	7.5	1.6	2.38	16	13.22	1.30	14.23	0.92	30.82
Ticino-H18	20	0.67	44	29.88	1971	24.95	37324	26.1	9.2	1.6	2.27	28	13.18	1.67	14.12	1.23	14.95
Ticino-H13	20	0.62	44	36.99	2636	24.87	37324	90.7	6.9	1.1	2.35	1	11.10	-	12.53	-	17.88
Ticino-H22	9	1.28	19	54.57	809	25.00	37324	93.3	9.8	2.3	2.30	18	13.29	1.55	14.26	1.09	22.98
Ticino-H23	20	2.02	133	102.66	6756	25.08	37324	47.7	8.2	0.8	2.26	102	13.17	1.61	14.19	1.17	49.05
Ticino-H27	27	1.54	108	41.65	2924	24.80	36872	86.1	15.2	1.5	2.15	42	14.03	1.22	14.83	0.88	21.60
Ticino-H28	24	0.81	58	19.79	1410	24.88	36872	60.4	17.0	2.3	2.24	40	14.00	1.42	14.80	0.97	9.58
Ticino-H25	20	0.54	26	11.87	571	25.04	37324	99.5	18.9	3.8	2.45	60	14.31	1.31	15.06	0.93	5.93
Maggia-H-1	13	0.65	41	23.81	1509	24.01	36507	2.9	11.7	2.4	2.19	20	14.02	0.95	14.77	0.70	13.75
Maggia-H-3	11	0.46	14	27.45	839	16.86	26077	29.6	4.8	1.4	2.09	-	-	-	-	-	24.10
Maggia-H-5	3	0.43	6	24.79	345	16.80	26077	19.0	5.0	2.2	2.23	1	16.14	-	16.42	-	27.97
Maggia-H-6	11	1.67	67	70.61	2831	16.73	26077	30.5	6.4	1.0	2.15	19	13.73	1.28	14.56	0.94	51.05
Maggia-H-10	5	0.94	5	29.84	158	23.95	36507	27.3	12.6	5.7	2.27	5	13.14	1.08	14.08	0.77	14.89
Maggia-H-14	16	0.66	35	20.13	1066	16.66	26077	72.6	9.1	1.6	2.08	-	-	-	-	-	13.53
Maggia-H-15	21	0.58	54	30.02	2793	23.70	36507	90.1	7.6	1.1	2.24	7	12.68	0.92	13.79	0.73	18.85
Maggia-H-27	19	0.88	40	45.74	2083	23.82	36507	61.5	7.6	1.2	2.47	63	14.18	1.07	14.90	0.78	21.43
Maggia-H-25	26	1.09	70	34.60	2214	16.59	26077	91.8	8.7	1.1	2.11	31	13.83	1.46	14.74	1.00	22.45
Maggia-H-22	24	1.58	258	49.29	8068	23.76	36507	79.6	12.6	0.9	2.79	91	13.75	1.42	14.57	1.04	23.64

[a]No. of grains - number of counted grains. $\rho_s/\rho_i/\rho_n$ - track densities [10^5 tracks cm^{-2}] (spontaneous/induced/on dosimeter). $N_s/N_i/N_d$ - number of counted tracks (spontaneous/induced/on dosimeter). P(x^2) - probability of obtaining the chi-square value (x^2) for n degree of freedom (with n = {No. of grains} - 1). σ - standard error of AFT central age (Galbraith and Laslett, 1993). Dpar - averaged diameter of etch figures from analysed grains. N_{TL} - number of track length measurements. MTL - mean track length. St.dev - standard deviation. MpTL - mean projected track length. U - uranium concentration.

Results of AFT analysis (elevation profiles)[b].

Sample	No. of grains	ρ_s	N_s	ρ_i	N_i	ρ_d	N_d	P(x^2) [%]	Central age [Ma]	$\pm1\sigma$	Dpar [μm]	N_{TL}	MTL [μm]	St.dev	U [ppm]
Ticino-VNo1	20	1.05	43	25.44	1047	21.03	32468	83.9	14.4	2.3	2.14	17	14.56	1.13	13.89
Ticino-VNo3	19	0.51	20	16.99	663	24.27	36872	100.0	12.2	2.8	2.37	27	14.35	1.66	9.15
Ticino-VNo4	18	0.42	18	12.00	518	20.95	32468	73.7	12.1	2.9	2.11	17	14.06	1.31	7.73
Ticino-VNo6	20	0.65	33	20.69	1055	24.43	36872	82.5	12.7	2.3	2.11	39	13.90	1.44	10.05
Ticino-VNo7	21	0.29	14	6.88	332	21.20	32535	44.8	11.5	4.1	2.16	3	14.76	0.89	3.91
Maggia-VNo1	10	0.88	14	37.65	598	23.60	35411	97.0	9.2	2.5	2.18	6	14.60	1.70	17.72
Maggia-VNo2	16	2.03	92	90.78	4120	23.90	36872	70.7	8.9	1.00	2.44	21	14.34	0.71	43.40
Maggia-VNo4	18	0.66	27	28.60	1164	23.57	35411	62.2	9.1	1.8	2.38	20	13.58	1.16	14.21
Maggia-VNo5	20	0.95	50	57.44	3033	24.05	36872	97.7	6.6	1.0	2.43	35	14.45	1.00	26.65
Maggia-VNo7	13	1.10	51	52.06	2418	23.54	35411	12.9	8.3	1.2	2.16	18	13.32	1.42	25.05
Ticino-VM1	9	1.93	50	53.65	1388	21.70	32468	25.2	12.0	2.1	N.N.	-	N.N.	-	29.00
Ticino-VM4	20	0.67	34	15.56	791	21.00	32535	80.5	15.0	2.7	N.N.	-	N.N.	-	10.08
Ticino-VM8	20	1.07	33	33.54	1035	21.66	32601	81.0	11.5	2.1	N.N.	-	N.N.	-	17.71
Maggia-VS1	11	1.71	42	41.86	1026	23.51	35411	98.7	16.0	2.6	N.N.	-	N.N.	-	18.87
Maggia-VS2	20	1.78	57	52.52	1686	21.51	32601	99.7	12.1	1.7	N.N.	-	N.N.	-	28.48
Maggia-VS3	7	1.36	16	28.54	337	21.57	32601	89.2	17.0	4.4	N.N.	-	N.N.	-	15.55
Maggia-VS4	13	1.08	42	32.82	1271	23.48	35411	73.6	12.9	2.1	N.N.	-	N.N.	-	18.51
Maggia-VS8	20	9.30	242	257.78	6708	23.45	35411	33.3	14.1	1.1	N.N.	-	N.N.	-	127.25

[b]No. of grains - number of counted grains. $\rho_s/\rho_i/\rho_n$ - track densities [10^5 tracks cm^{-2}] (spontaneous/induced/on dosimeter). $N_s/N_i/N_d$ - number of counted tracks (spontaneous/induced/on dosimeter). P(x^2) - probability of obtaining the chi-square value (x^2) for n degree of freedom (with n = {No. of grains} - 1). σ - standard error of AFT central age (Galbraith and Laslett, 1993). Dpar - averaged diameter of etch figures from analysed grains. N_{TL} - number of track length measurements. MTL - mean track length. St.dev - standard deviation. U - uranium concentration.

C. AHe Data

Results of AHe analysis (horizontal profiles)[a]. Aliquots, which yielded AHe ages older than the respective AFT age are in italic and were excluded from further interpretation. Bold digits refer to the sample age and the associated error (i.e. the central age and standard deviation in case of more than one successful analysis).

Sample	N_g	Raw age	Error	F_T	Cor. age	Error	C. age	1σ	ø r	Mass	U	Th	Sm	He
		$[Ma]$	$[Ma]$		$[Ma]$	$[Ma]$	$[Ma]$	$[Ma]$	$[\mu m]$	$[\mu g]$	$[ppm]$	$[ppm]$	$[ppm]$	$[ncc]$
Ticino-H1	*3*	*12.96*	*0.80*	*0.76*	*17.13*	*2.02*			*59.55*	*13.85*	*6.43*	*2.46*	*22.40*	*0.16*
	3	2.90	0.18	0.73	3.97	0.47			54.51	10.23	6.41	1.88	14.94	0.03
Ticino-H4	3	6.17	0.38	0.76	8.08	0.95	**5.78**	**1.22**	58.80	13.09	7.01	4.15	25.39	0.08
	3	4.29	0.27	0.76	5.65	0.66			57.78	9.09	7.80	3.93	22.74	0.04
Ticino-H13	3	3.66	0.23	0.76	**4.82**	**0.57**			57.55	11.40	11.43	1.41	17.65	0.06
Ticino-H22	*3*	*17.08*	*1.06*	*0.65*	*26.49*	*3.12*			*40.19*	*4.51*	*1.28*	*1.34*	*1.18*	*0.02*
	3	2.62	0.16	0.66	3.98	0.47			40.29	47.42	25.08	2.11	25.08	0.06
Ticino-H23	3	3.26	0.20	0.73	4.44	0.52	**4.36**	**0.26**	49.97	39.98	20.38	0.84	20.38	0.13
	1	3.41	0.21	0.74	4.60	0.54			51.05	2.16	45.38	2.09	43.27	0.04
	3	*6.76*	*0.42*	*0.73*	*9.26*	*1.09*			*49.60*	*46.27*	*44.77*	*3.93*	*44.77*	*0.33*
	1	*146.14*	*9.06*	*0.67*	*216.50*	*25.48*			*46.40*	*2.14*	*0.20*	*1.38*	*0.12*	*0.02*
	1	*127.07*	*7.88*	*0.66*	*191.20*	*22.50*			*42.30*	*1.80*	*54.34*	*2.50*	*51.82*	*0.02*
	1	*19.47*	*1.21*	*0.73*	*26.53*	*3.12*			*61.45*	*0.95*	*59.52*	*7.60*	*73.13*	*0.14*
	1	*132.16*	*8.19*	*0.74*	*178.25*	*20.97*			*60.70*	*5.16*	*0.03*	*1.04*	*0.03*	*0.02*
Ticino-H28	3	4.18	0.26	0.75	5.59	0.66	**7.4**	**1.99**	55.62	13.38	7.13	1.77	17.81	0.05
	3	7.17	0.44	0.76	9.50	1.12			56.50	0.02	6.46	1.39	13.84	0.10
	3	9.42	0.58	0.67	14.00	1.65			40.03	4.58	3.81	2.46	2.65	0.02
Ticino-H25	3	6.39	0.40	0.66	9.64	1.13	**10.97**	**1.46**	41.13	3.61	12.69	5.24	6.21	0.04
	3	6.91	0.43	0.72	9.57	1.13			53.77	7.30	17.15	5.08	4.96	0.11
	3	*12.87*	*0.80*	*0.69*	*19.84*	*2.33*			*38.47*	*4.53*	*4.88*	*5.03*	*3.76*	*0.04*
	2	*23.69*	*1.47*	*0.71*	*33.54*	*3.95*			*46.40*	*4.13*	*5.39*	*3.52*	*3.30*	*0.07*
	3	*20.73*	*1.28*	*0.71*	*29.04*	*3.42*			*48.54*	*8.97*	*0.96*	*0.62*	*0.76*	*0.03*
	1	*218.98*	*13.58*	*0.77*	*285.63*	*33.61*			*65.40*	*5.72*	*0.12*	*0.88*	*0.04*	*0.05*
	3	2.29	0.14	0.76	2.99	0.35			54.89	15.84	10.57	1.64	3.93	0.05
Maggia-H1	3	3.60	0.22	0.79	4.57	0.54	**3.61**	**0.48**	59.52	16.81	11.77	3.36	4.64	0.09
	2	2.60	0.16	0.82	3.16	0.37			74.22	19.26	6.17	1.08	2.21	0.04
	3	*82.96*	*5.14*	*0.78*	*106.90*	*12.57*			*48.41*	*14.45*	*0.21*	*0.31*	*0.09*	*0.04*
Maggia-H5	*1*	*118.95*	*7.37*	*0.66*	*179.80*	*21.16*			*41.47*	*2.29*	*0.43*	*4.65*	*1.21*	*0.05*
Maggia-H6	4	3.38	0.21	0.76	**4.47**	**0.53**			45.06	14.82	5.85	3.92	0.72	0.04
Maggia-H10	3	3.00	0.19	0.78	**3.87**	**0.46**			52.20	15.17	18.81	9.81	9.81	1.73
	3	4.84	0.30	0.79	6.11	0.72			60.85	21.01	7.48	4.12	1.18	0.10
	6	3.83	0.24	0.71	5.41	0.64			46.35	14.51	3.29	1.79	0.57	0.03
Maggia-H15	3	4.50	0.28	0.68	6.59	0.78	**6.22**	**0.51**	43.46	7.39	11.53	5.93	1.32	0.05
	3	4.04	0.25	0.77	5.22	0.61			60.13	19.27	3.05	1.01	0.71	0.03
	3	5.91	0.37	0.74	7.99	0.94			51.65	7.98	4.13	3.26	1.25	0.03
Maggia-H27	3	3.83	0.24	0.71	**5.36**	**0.63**			52.22	8.23	13.54	2.28	15.53	0.05
	2	*10.58*	*0.66*	*0.76*	*13.86*	*1.63*			*58.68*	*7.96*	*4.75*	*1.05*	*2.24*	*0.05*
	3	*14.90*	*0.92*	*0.73*	*20.36*	*2.40*			*49.55*	*9.80*	*5.76*	*0.71*	*9.93*	*0.11*
	3	*21.91*	*1.36*	*0.78*	*28.00*	*3.29*			*66.32*	*19.57*	*3.10*	*0.41*	*3.15*	*0.17*

[b] N_g - number of grains per aliquot. Error - total analytical error. F_T - weighted factor for α-ejection correction. Cor. age - corrected age. C. age - Central age after (Vermeesch, 2008). 1σ - error of central age. ør - average radius . U/Th/Sm - concentrations of U ($^{235}U + {}^{238}U$)/^{232}Th/^{147}Sm. He - volume [nano-cm^3] of ^4He.

Results of AHe analysis (elevation profiles)[b]. Aliquots, which yielded AHe ages older than the respective AFT age are in italic. Bold digits refer to the sample age and the associated error (i.e. the mean age and standard deviation in case of more than one successful analysis).

Sample	N_g	Raw age	Error	F_T	Cor. age	Error	M. age	1σ	ø r	Mass	U	Th	Sm	He
		$[Ma]$	$[Ma]$		$[Ma]$	$[Ma]$	$[Ma]$	$[Ma]$	$[\mu m]$	$[\mu g]$	$[ppm]$	$[ppm]$	$[ppm]$	$[ncc]$
Ticino-VNo1	3	8.65	0.54	0.73	**11.92**	**1.40**			47.31	7.58	10.29	1.29	17.62	0.09
Ticino-VNo2	3	4.93	0.31	0.65	7.56	0.89	**7.46**	**0.14**	39.39	4.21	18.86	2.29	17.91	0.05
	3	5.44	0.34	0.74	7.36	0.87			51.96	7.32	14.88	1.78	11.71	0.07
	3	*17.44*	*1.08*	*0.71*	*24.63*	*2.90*			*48.99*	*5.12*	*11.38*	*1.70*	*9.61*	*0.13*
Ticino-VNo3	3	6.66	0.41	0.64	**10.40**	**1.22**			38.43	3.56	7.28	5.98	5.62	0.03
	3	*139.49*	*8.65*	*0.71*	*197.42*	*23.23*			*47.11*	*4.73*	*0.20*	*1.21*	*0.72*	*0.04*
	3	*15.49*	*0.96*	*0.69*	*22.55*	*2.65*			*44.49*	*4.52*	*3.40*	*2.45*	*4.96*	*0.03*
Ticino-VNo4	3	6.42	0.40	0.74	**8.63**	**1.02**			57.61	9.26	2.71	1.98	3.83	0.02
	3	*83.99*	*5.21*	*0.62*	*134.52*	*15.83*			*39.16*	*3.00*	*5.03*	*6.18*	*5.57*	*0.20*
Ticino-VNo5	3	*37.98*	*2.35*	*0.67*	*56.95*	*6.70*			*43.72*	*4.65*	*1.45*	*3.24*	*3.74*	*0.05*
	3	*14.55*	*0.90*	*0.75*	*19.39*	*2.28*			*57.16*	*7.80*	*9.72*	*3.52*	*2.72*	*0.15*
Ticino-VNo6	3	4.65	0.29	0.67	**6.95**	**0.82**			44.60	5.47	6.97	3.95	28.99	0.03
	3	*77.32*	*4.79*	*0.72*	*107.11*	*12.60*			*49.12*	*9.32*	*0.11*	*0.64*	*0.39*	*0.02*
Maggia-VNo1	3	3.24	0.20	0.76	**4.28**	**0.50**			53.93	7.80	15.18	6.40	1.21	0.05
	3	*12.96*	*0.80*	*0.67*	*19.47*	*2.29*			*41.00*	*4.59*	*7.59*	*3.19*	*1.09*	*0.06*
Maggia-VNo2	3	4.38	0.27	0.74	**5.90**	**0.69**			55.77	11.94	16.30	9.23	4.41	0.12
	3	*88.98*	*5.52*	*0.69*	*129.38*	*15.22*			*42.09*	*6.59*	*0.40*	*1.16*	*0.04*	*0.05*
	3	*55.14*	*3.42*	*0.76*	*72.52*	*8.53*			*57.12*	*7.21*	*36.26*	*25.06*	*13.19*	*2.04*
Maggia-VNo3	3	3.16	0.20	0.67	**4.68**	**0.55**			42.36	4.14	28.07	7.03	8.35	0.05
	3	*44.50*	*2.76*	*0.74*	*60.02*	*7.06*			*55.26*	*11.62*	*1.35*	*0.48*	*0.28*	*0.09*
	3	*182.59*	*11.32*	*0.74*	*246.99*	*29.06*			*53.05*	*7.10*	*0.25*	*0.96*	*0.07*	*0.08*
Maggia-VNo4	3	*14.37*	*0.89*	*0.74*	*19.36*	*2.28*			*52.23*	*8.73*	*1.73*	*0.72*	*1.43*	*0.03*
Maggia-VNo5	3	*287.78*	*17.84*	*0.71*	*404.72*	*47.62*			*47.67*	*6.92*	*0.33*	*0.79*	*0.58*	*0.13*
Maggia-VNo6	3	6.03	0.37	0.67	8.99	1.06	**6.56**	**2.12**	40.95	3.51	17.02	2.34	6.88	0.05
	3	4.03	0.25	0.71	5.65	0.66			48.44	5.20	27.31	5.84	12.87	0.07
	3	3.86	0.24	0.77	5.05	0.59			58.11	10.75	18.86	0.79	11.87	0.10
	3	*92.08*	*5.71*	*0.68*	*136.36*	*16.04*			*43.47*	*6.27*	*0.39*	*0.93*	*0.19*	*0.04*
Maggia-VNo7	3	*24.10*	*1.49*	*0.63*	*38.02*	*4.47*			*40.04*	*4.07*	*2.42*	*1.44*	*2.68*	*0.03*
	3	*11.00*	*0.68*	*0.69*	*15.89*	*1.87*			*46.14*	*4.54*	*3.21*	*0.99*	*4.67*	*0.02*

[b] N_g - number of grains per aliquot. Error - total analytical error. F_T - weighted factor for α-ejection correction. Cor. age - corrected age. M. age - Mean age. 1σ - standard deviation. ør - average radius . U/Th/Sm - concentrations of U (^{235}U + ^{238}U)/^{232}Th/^{147}Sm. He - volume [nano-cm^3] of ^{4}He.

D. Source code

Both, the source code, presented below and test data are provided on a CD attached to this thesis. All codes are ready to run. To test code, a Python interpreter is required. Furthermore, relative paths to the data folders need to be preserved.

inverse_tT_2D_1_0.py

```
## Inverse time-temperature plotter (2D)
##
## Author: Simon Elfert
##
## Developed for the PhD thesis by Simon Elfert (2009-2014, University of Bremen)
##
## Purpose of this script:
## Plot time-temperature data from inverse thermal history modelling, including
## envelopes for tT-paths statistically in good and acceptable aggreement.
## Furthermore, it contains an export option to provide constraints and envelope
## data for other scripts


# Required libraries
import numpy as np
from pylab import *
import matplotlib.pyplot as plt

# function: data for 2D-Plot for single samples
# dir: directory
# fn: basename for fn1-4 and later figure files (without suffix)
# fn1:  filename for constraints data
# fn2: filename for envelope data
# fn3: filename for best fitting model data
# fn4: filename for weighted mean model data
# shaveflag: True: save, False: show
# exportflag: True: export, False: pass
def inverseHeftyPlot(dir, fn, fn1, fn2, fn3, fn4, shaveflag, exportflag):

    # Loading constraints data
    c = np.loadtxt(fn1, dtype={'names' : ('number', 'MaxTime', 'MinTime', 'MaxTemp', '
        MinTemp'), 'formats' : (int, float, float, float, float)}, skiprows=1)

    # Loading envelope data
    e = np.loadtxt(fn2, dtype={'names' : ('g_time', 'g_high', 'g_low', 'a_time', '
        a_high', 'a_low'), 'formats' : (float, float, float, float, float, float)},
        skiprows=1)

    # Loading best fitting model
    if fn3 == False: b=False
```

```
38      else: b = np.loadtxt(fn3, dtype={'names' : ('time', 'temp'), 'formats' : (float,
            float)}, skiprows=1)
39
40      # Loading weighted mean model data (optional)
41      if fn4==False: wm=False
42      else: wm = np.loadtxt(fn4, dtype={'names' : ('time', 'temp'), 'formats' : (float,
            float)}, skiprows=1)
43
44      # flag processing: 0 and 1: proceed, 2 and greater: do not proceed script (only
            export possible)
45      if shaveflag<2: inverseHeftyPlotter(dir,  fn,  c,  e,  b,  wm,  shaveflag)
46      else: pass
47
48      # flag processing: exporting envelopes and constraints
49      if exportflag: return (e,  b)
50      else: pass
51
52  # function: plot time-temperature data
53  # dir: directory
54  # fn: basename (without suffix)
55  # c: constraints
56  # e: envelopes
57  # b: best fitting model (optional, "False" if not needed)
58  # wm: weighted mean path (optional, "False" if not needed)
59  # shaveflag: flag for saving (True) or showing (False)
60  def inverseHeftyPlotter(dir,  fn,  c,  e,  b,  wm,  shaveflag):
61
62      # Initialise figure and subplot
63      fig = plt.figure()
64      ax=fig.add_subplot(111)
65
66      # plot envelopes
67      ax.fill_between(e['a_time'], e['a_high'], e['a_low'], facecolor='0.5', alpha=0.2)
              # acceptable tT-envelopes
68      ax.fill_between(e['g_time'], e['g_high'], e['g_low'], facecolor='0.3', alpha=0.2)
              # good tT-envelopes
69
70      # plot best model (optional)
71      if b == False: pass
72      else: ax.plot(b['time'],  b['temp'],  'k')
73
74      # plot weighted mean model (optional)
75      if wm == False: pass
76      else: ax.plot(wm['time'],  wm['temp'],  'k')
77
78      # plot constraints
79      for ct in c:
80            ax.add_patch(Rectangle((ct['MinTime'],ct['MinTemp']),ct['MaxTime']-ct['
                MinTime'],ct['MaxTemp']-ct['MinTemp'],   fill=False))
81
82      ax.barh(60,  70,  50,  0,  color="0.8", linewidth=0,  alpha=.3) # plot AFT partial
            annealing zone (60-110 degree celsius = 60+50)
83      ax.barh(40,  70,  45,  0,  color="0.8", linewidth=0,  alpha=.3) # plot AHe partial
            retention zone (40-85 degree celsius = 40+45)
84
85      # set axes dimensions
86      ax.set_xlim((0, 25))
87      ax.set_xlim(ax.get_xlim()[::-1])    # reverse x axis
```

```
88 #     ax.set_ylim((0, 240))    # Maggia horizontal profile (to include constraints
       associated with zircon fission track data)
89     ax.set_ylim((0, 120))    # Ticino horizontal profile
90     ax.set_ylim(ax.get_ylim()[::-1])     # reverse y axis
91
92     # label axes
93     ax.set_ylabel('Temperature␣['+unichr(176)+'C]')
94     ax.set_xlabel('Time␣[Ma]')
95
96     # set figure title
97     ax.text(ax.get_xlim()[0]-1, 12,  fn.split(dir)[1].split('_')[0])  #  Ticino
           horizontal profile
98 #     ax.text(ax.get_xlim()[0]-1, 20,  fn.split(dir)[1].split('_')[0])  # Maggia
       horizontal profile
99
100    # flag processing
101    if shaveflag == 0:  plt.show()  # show plot
102    elif shaveflag == 1:
103         plt.savefig(fn + ".jpg")    # save raster (jpg)
104         plt.savefig(fn + ".pdf")    # save vector (pdf)
105    else: pass
106
107 ################################################
108 ######## Starting point ##############################
109 ################################################
110
111 if __name__ =="__main__":
112
113    # user defined assignments
114    dir = "data/"    # directory # testdata
115    fn = dir + "Ticino-H06__20130118_ucs-inv"    # basename #testdata
116    fn1 = fn+"Cons.txt" # filename for constraints data
117    fn2 = fn+ "Env.txt"  # filename for envelope data
118    fn3 = fn+ "Best.txt" # filename for best fitting model data (optional, "False" if
           not needed)
119    fn4 = False #filename for weighted mean model data (optional, "False" if not needed
           )
120
121    # flags
122    shave =0     # 0: show, 1: save
123    exportflag = False # export constraints and envelope data (True/False)
124
125    # prepare data and proceed according to flag setting
126    inverseHeftyPlot(dir,  fn,  fn1,  fn2,  fn3, fn4,  shave,  exportflag)
127
128    print "done"
```

3D_tT-profile-plots__v1.0.py

```
1 ## 3D-Plotter for time-temperature paths
2 ##
3 ## Author: Simon Elfert
4 ##
5 ## Developed for the PhD thesis by Simon Elfert (2009-2014, University of Bremen)
6 ##
7 ## Purpose of this script:
8 ## Plotting time-temperature histories extracted from HeFTy (Ketcham, 2005) for
```

```
## a batch of samples in 3D. These have to provided externally including constraints,
## envelopes for good (and acceptable) paths and best-fitting models.
## Examplary data from sample Ticino-H (Elfert et al., 2013)


# Allocating necessary libraries
from mpl_toolkits.mplot3d import Axes3D
import mpl_toolkits.mplot3d.art3d as art3d
from mpl_toolkits.mplot3d.art3d import Poly3DCollection
import matplotlib.pyplot as plt
import numpy as np

# Specify file names
dir = "data/"       # directory
profile="Ticino-H"      # basename (first part of filenames)
ids=["01", "06", "18", "23",  "27", "28", "25"]     # sample-IDs  as part of the
    filename
##kms=[0, 8.6, 18.8,  27.6,  32.9, 35.1, 36.8] # (N -> S)
kms = [-36.8,  -28.2,  -18., -9.2,  -3.9,  -1.7,  0 ] # (location of sample along the
    profile; S -> N  in negative values for design reasons, later corrected in
    Inkscape)
date="__20130118"   # as part of the filename
run="_ucs-invEnv"   # file with envelope information
run2="_ucs-invBest" # file with best-fitting model information
pfix=".txt"

cutter=20   # to cut plot at x Ma
ymax=140    # maximum value on y-axis
p3d=True      # 3D plot flag (otherwise creation of 2D plot)

# initialise figure and subplot (the latter according to p3d flag)
fig = plt.figure()
if p3d: ax = fig.add_subplot(111, projection="3d")
else: ax = fig.add_subplot(111)

# loop through samples
for id in range(len(ids)):

      # concatenation of file names
      fn = dir+profile+ids[id]+date+run+pfix
      fn2 = dir+profile+ids[id]+date+run2+pfix

      # loading data (d = envelopes, d1 = best-fitting model)
      d = np.loadtxt(fn, np.dtype({'names':['GoodTime','GoodHi','GoodLo', 'AccTime', '
          AccHi', 'AccLo'], 'formats':[float, float, float, float, float, float]}),
          skiprows=1)
      d2 = np.loadtxt(fn2, np.dtype({'names':['BestTime', 'BestT'], 'formats':[float,
          float]}), skiprows=1)

      # flag processing
      if cutter:
            for j in range(len(d["GoodTime"])):
                  if d["GoodTime"][j]<=20: break
                  else: pass
      else: j=0

      # extracting data
      x=d["GoodTime"][j:]   # x-values = time in Ma
```

```
61      z=np.array([d["GoodLo"][j:],  d["GoodHi"][j:]])  # z-values = temperature (good-
            model envelopes)
62      y=[kms[id] for n in d["GoodTime"][j:]] # y-values = location along the profile
63
64      # creating mesh grid for 3D plane
65      X, Y = np.meshgrid(x, y)
66
67      # creating time-temperature plane according to meshgrid and envelopes
68      Z=np.empty_like(X)
69      for i in range(len(Z)-1): Z[i]=z[0]
70      Z[-1]=z[1]
71
72      # plot time-temperature plane
73      if p3d: ax.plot_surface(X, Y, Z, cstride=2000000,  alpha=0.2)
74      else: pass
75
76      # get bestfit value pair at cutter
77      bestfitT=[]
78      bestfitTime=[]
79      if cutter:
80            for i in range(len(d2["BestTime"])):
81                  if d2["BestTime"][i]<cutter and d2["BestTime"][i-1]>cutter:
82                        tDif=d2["BestTime"][i-1]-d2["BestTime"][i]
83                        tToCut=cutter-d2["BestTime"][i]
84                        pToCut=(100/tDif)*tToCut
85                        TDif=d2["BestT"][i-1]-d2["BestT"][i]
86
87                        # set first value pair after cutter
88                        bestfitTime=[cutter]
89                        bestfitT=[d2["BestT"][i]+(  (pToCut/100)*TDif) ]
90
91                        break
92                  else: pass
93            #endfor
94      else: pass
95
96      # rebuilt time-temperature lists for best-fitting model starting from cutter time
97      for i in range(len(d2["BestTime"])):
98            if cutter:
99                  if d2["BestTime"][i]>cutter: pass
100                 else:
101                       bestfitTime.append(d2["BestTime"][i])
102                       bestfitT.append(d2["BestT"][i])
103                       if d2["BestTime"][i] == 0: break
104           else:
105                 bestfitTime.append(d2["BestTime"][i])
106                 bestfitT.append(d2["BestT"][i])
107                 if d2["BestTime"][i] == 0: break
108     #endfor
109
110     # slightly adjusting y-value (location) for best-fitting model to bring it
            infront of the envelope-plane
111     bfy=[kms[id]-.2  for n in bestfitTime]
112
113     # if 3D plot...
114     if p3d:
115           ax.plot(bestfitTime,bfy, bestfitT,"r",  linewidth=2)      # plot best path
116
```

```
117             # find 110 degree xy and plot helping line...
118             for y in range(len(bestfitT)):
119                   if bestfitT[y]<110:
120                         y_dif=bestfitT[y-1]-bestfitT[y]
121                         dif_toPAZ=(100/y_dif)*(bestfitT[y-1]-110)       # [%] = 0...1
122                         x_dif=bestfitTime[y-1]-bestfitTime[y]
123                         xPAZ=bestfitTime[y-1]-(((bestfitTime[y-1]-bestfitTime[y])/100)*
                                dif_toPAZ)
124                         yPAZ=110
125                         ax.plot([xPAZ, xPAZ], bfy[:2], [yPAZ,  0] ,  "0.2",  linestyle=
                                ":")
126                         ax.plot([xPAZ,  xPAZ],  [bfy[0],  2], [0,  0],  "0.2",
                                linestyle=":")
127                         break
128                   else: pass
129
130             # find 85 degree xy and plot helping line...
131             for y in range(len(bestfitT)):
132                   if bestfitT[y]<85:
133                         y_dif=bestfitT[y-1]-bestfitT[y]
134                         dif_toPRZ=(100/y_dif)*(bestfitT[y-1]-85)       # [%] = 0...1
135                         x_dif=bestfitTime[y-1]-bestfitTime[y]
136                         xPRZ=bestfitTime[y-1]-(((bestfitTime[y-1]-bestfitTime[y])/100)*
                                dif_toPRZ)
137                         yPRZ=85
138
139                         ax.plot([xPRZ, xPRZ], bfy[:2], [yPRZ,  ymax] ,  "0.2",
                                linestyle="--")
140                         ax.plot([xPRZ,  xPRZ],  [bfy[0],  -40], [ymax, ymax],  "0.2",
                                linestyle="--")
141                         break
142                   else: pass
143
144       # if 2D plot
145       else:
146             # plot AFT partial annealing zone and AHe partial retention zone
147             ax.barh(60,  30,  50,  0,  color="red", linewidth=0,  alpha=.01)
148             ax.barh(40,  30,  45,  0,  color="blue", linewidth=0,  alpha=.01)
149
150             # get arithmetic mean temperature of good-model envelopes
151             mGoodT=[(d["GoodHi"][i] + d["GoodLo"][i])/2 for i in range(len(d["GoodTime"
                    ]))]
152
153             # plot arithmetic mean temperature of good-model envelopes
154             ax.plot(d["GoodTime"], mGoodT,  linewidth=2,  label=ids[id])
155             ax.legend(loc="lower␣right")
156 #endfor (sample wise)
157
158 # plot formatting:
159 if cutter: ax.set_xlim((0, cutter))
160
161 # if 3D plot...
162 if p3d:
163       ax.set_xlabel("Time␣[Ma]")
164       ax.set_ylabel("(S)␣␣␣␣␣␣␣␣␣␣␣␣Distance␣along␣profile␣[km]␣␣␣␣␣␣␣␣␣␣␣␣(N)")
165       ax.set_zlabel("Temperature␣["+unichr(176)+"C]")
166       ax.set_zlim((0, ymax))
167 # if 2D plot...
```

```
else:
      ax.set_xlabel("Time [Ma]")
      ax.set_ylabel("Temperature ["+unichr(176)+"C]")

      ax.set_xlim(ax.get_xlim()[::-1])  # reverse x-axis (time)
      ax.set_ylim((0,  ymax))
      ax.set_ylim(ax.get_ylim()[::-1]) # reverse y-axis (temperature)

# show plot
plt.show()

print "done."
```

Partikeltracker3.1.py

```
### ------ Particle-Tracker 3.1 ------
###
### --- by Simon Elfert ---
###
### Developed for the PhD thesis by Simon Elfert (2009-2014, University of Bremen)
###
### Purpose of this script:
### This script translates position of particles from a discrete element model
### (developed for PFC-2D exports) into  time-temperature-paths, which can be
### used for thermal modelling in HeFTy (Ketcham, 2005).
###
### Required data format: ASCII-Text file with *.txt without headline. One file
### for each model save step (enumeration in file name, for example:
### "myrun_001.txt", "myrun_002.txt", ...).
### 1st row: "id x-value1 y-value1 diameter"
### 2nd row: "id x-value2 y-value2 diameter"
### 3rd row: "id x-value3 y-value3 diameter"
### ...
### with id as integer and x-, y- and diameter values as floating point
### numbers [10 km].
###
### Example:
### 64487 1.73916411781e+003 2.46576780551e+002 6.00000000000e+000
### 64488 1.74084848892e+003 2.46175326076e+002 7.00000000000e+000
### 64489 1.74254717133e+003 2.45768084242e+002 5.00000000000e+000
###
### This script may be used for free and be manipulated towards ones needs. If
### it is used without major manipulations please rever in the presentation of
### the results to "Simon Elfert, University of Bremen" and the corresponding
### publications (presently in preparation):
###
### Linda Wenk, Simon Elfert, Cornelia Spiegel and Katrin Huhn (in prep.):
### Linking lower crustal conditions with upper crustal processes of orogenic
### wedges I: combining numerical "sandbox" simulations and apatite fission
### track thermochronology
###
### Simon Elfert, Linda Wenk, Wolfgang Reiter, Katrin Huhn and Cornelia Spiegel
### (in prep.): Linking mechanic and kinematic properties with upper crustal
### processes of orogenic wedges II: an example from the European Central Alps

### Changes to prior versions: more efficient matrix buildup and more straigthforward
### programming. Variables in topomaker.py refering to Wenk et al., in preparation
```

```
43
44
45 # Required scripts
46 import ptTTranslator as p2tT    # path-time-temperature operations
47 import matrixMaker as mM        # create matrix from raw data files
48 import topomaker as tm         # create topography
49 import pathwriter as pwr       # read out particle paths for plotting
50 from tTExporter import *       # export tT-paths
51
52 ##########################################
53 ####    ...to be changed by the user...                    ####
54 ##########################################
55
56 # Name of the current model (with respect to the name of its directory!!!)
57 ##run=['a1', 'a2', 'a3']
58 run = ['a3']
59
60 # Flag to distinguish between geometry scenarios (conceptual study, "geo" is the
       working name for these kind of scenarios)
61 # and the SZ-A-scenario (applied model for the NFP-20 east seismic profile)
62 geo = False # True: geo scenarios, False: SZ-A
63
64 # Path to the directory of the current model's particle pathways
65 d = 'data/'
66 dir = [d+'txt/']
67
68 # Flag for exporting time-temperature paths
69 tTex=True
70
71 # Flag for exporting particle paths
72 pPex=True
73
74 # Flag for cutting the pathways at a certain timestep (lx) - lx=0 means no cutting at
       all
75 ##lx=595
76 ##lx = 1000 # new definition without regarding to literature but only model processing
       (for a-scenarios)
77 ##llx=[1000]
78
79 # Number of time stamps for AFT snapshots
80 #llx=[100, 200, 300, 400, 500, 595] # geo szenarios after 20, 40, 60, 80, 100, 119 km
       shortening
81 #llx=[500]
82 #llx=[1000]  # SZ-A after 119 km shortening
83 llx=[15] # test data
84
85 # Number of save steps within one model run (per scenario)
86 #topo_lx = [595,  595,  595] #geo scenarios
87 #topo_lx=[1000] # SZ-A
88 topo_lx=[15] # test data
89
90 # Factor for calculating the age from timestep
91 # final ftime for geo scenarios (lx=595 == 32 Ma)
92 #ftime = 0.0537815126 # new refinements of convergence rate for (EGT based scenarios (
       deducted from text). 22.3.12)
93
94 # final ftime for SZ-A scenarios (lx=1000 == 32 Ma)
```

```
95 #ftime = 0.032032032 # new definition without regarding to literature but only model
       processing
96 ftime = 2.13333 # testdata
97
98 # boundaries for creating matrix of horizontal profiles...
99 # Maximal present day (or end of simulation) elevation [km a.s.l.] of particle to
       process
100 ##yhigh=30  # all particles
101 yhigh=.51 # SZ-A
102 #yhigh=-9999 # flag for geo scenarios
103
104 # Minimal present day (or end of simulation) altitude [km a.s.l.] of particle to
       process
105 ##ylow=-70  # all particles
106 ylow=.51 # SZ-A
107 #ylow=-9999  # flag for geo scenarios
108
109 # Flag to force the rebuilding of the matrix with respect to the boundaries
110 # specified above (if it does not exist it will be build any way. Lasts about 10
       minutes)
111 #matrixForce=[False,  False,  False]
112 #matrixForce=[True,  True,  True]
113 matrixForce=[False]
114
115 # Prefix of the topography files per timestep (without the number)
116 ##topoPrefix = ['1_211211_', '2_211211_', '3_211211_']
117 #topoPrefix=['3_211211_']
118
119 topoPrefix=['1_231111_']    # test data
120
121 # Flag to force the rebuilding of a topography file (will need some time!)
122 # The topography file will be build if it does not exist even if topoForce=False
123 #topoForce = [False,  False,  False]
124 #topoForce=[True,  True,  True]
125 topoForce=[False]
126
127 # Assumed 'real' maximum elevation of the simulated orogen [km a.s.l.] at simulation
       start (rME_i)
128 maxStart = .5
129
130 # Assumed 'real' maximum elevation of the simulated orogen [km a.s.l.] at simulation
       end (rME_n)
131 maxEnd = 3.
132
133 # Assumed time [Ma] when relief incision starts
134 ##reliefInc = 35 # incision from the start - irrelevant if ylow/yhigh = -9999
135 ##reliefInc =1 # from 1 Ma on
136 ##reliefInc = 5 # Pliocene
137 reliefInc = 30 # Oligocene refering to Garzanti et al. 2008
138
139 # Assumed geothermal gradient [degree C / km]
140 geotherm = 30
141
142 ##########################################
143 ####    ...end of section to be changed by the user!                  ####
144 ##########################################
145
146 # Starting point
```

```
147 if __name__ == "__main__":
148       # for each time stamp (point in time to derive AFT data from)
149       for l in range(len(llx)):
150             # for each scenario in the current user setting
151             for i in range(len(run)):
152                   # getting x values (i.e. array of geological times)
153                   x=p2tT.getX(llx[l], ftime)
154
155                   # Getting the save step when relief incision starts
156                   if geo:
157                         print "No relief incision computed. Sampling on the erosional
                              surface."
158                         reliefTS=999999999 # unless the user runs a billion savesteps,
                              this way no valley incision is calculated
159                   else:
160                         diflist = [abs(xj-reliefInc) for xj in x]     # list of
                              differences between time date and reliefInc
161                         reliefTS = llx[l] - diflist.index(min(diflist))   # save step (
                              SAS) with minimum difference
162                         print "Relief incision from ", str(reliefInc), " Ma (SAS: ",
                              str(reliefTS), ")"
163
164                   # read in topography
165                   topo = tm.makeTopo2(dir[i], topoPrefix[i], geo,  topo_lx[i],
                        topoForce[i], maxStart, maxEnd)
166                   if topoForce[i]==True: topoForce[i]=False # buildup topography only
                        once per scenario
167
168                    # create matrix with respect to boundaries specified on top
169                   matrix = mM.makeMatrix(dir[i], topoPrefix[i], geo,  llx[l], ylow,
                        yhigh, topo[llx[l]-1],  matrixForce[i])
170
171                   # correct matrix
172                   # extract particles which are below the surface at the end of the
                        simulation (only relevant for valley incision scenarios)
173
174                   # for geo scenarios no correction is needed because only subsurface
                        samples are taken into account for the matrix
175                   if geo:
176                         matrix2=matrix
177                   else:
178                         matrix2=[]
179                         for m in matrix:
180                               try:
181                                     if topo[-1][int(round(2*m[-1][1]))]>((ylow+yhigh)
                                          /2): matrix2.append(m) # only if erosional
                                          surface is above hprofile
182                               except:
183                                     # if particle is at km 250, than topo[-1][500]
                                          would be 'index out of range'
184                                     if topo[-1][-1]>((yhigh+ylow)/2): matrix2.append(m)
185
186                   print "Number of particles to be analysed: " + str(len(matrix2))
187
188                   # calculate temperatures
189                   # afterwards the matrix (now called "time-Temperature-Matrix") is
                        extended by a
190                   # valid temperature value for each particle and save step (sas)
```

```
191                     tT_matrix = p2tT.getT(matrix2, topo, llx[l], reliefTS, geotherm)
192
193                     # export time-temperature-paths
194                     if tTex:
195                           logdat=open(d+"log"+str(run[i])+".txt", "a")
196                           # for each particle
197                           for m in tT_matrix:
198                                 # print basic properties of the matrix particles
199                                 logdat.write(str(llx[l])+"\t"+str(run[i])+"\t"+str(m
                                        [-1][0])+"\t"+str(m[-1][1])+"\t"+str(m[-1][2])+"\n")
200                                 export_tTPath(x, m[:,3], dir[i], run[i], llx[l], m[0][0])
201                           logdat.close()
202                           print "For details of script run see: " +d+"log"+str(run[i])+".
                                  txt"
203
204                     # export particle paths
205                     if pPex: pwr.particleExtracter(tT_matrix,  dir[i],  llx[l],  ylow,
                            yhigh)
206
207       print "done."
```

matrixMaker.py

```
1  ## Create matrix (a set of selected particles)
2  ##
3  ## Author: Simon Elfert
4  ##
5  ## Developed for the PhD thesis by Simon Elfert (2009-2014, University of Bremen)
6  ##
7  ## Purpose of this script:
8  ## extract particles from output files by PFC2D saving them as matrix
9
10
11 # Required libraries
12 import os
13 import cPickle
14 import numpy as np
15
16 # define the particle class
17 class Particle:
18     def __init__(self, id, status,  dis):
19         self.id = id
20         self.stat = status      # True = valid particle
21         self.ts = []                # save step (one row)
22         self.enddis = dis       # distance to the surface at the end of simulation
23
24     def getID(self):
25         return self.id
26
27     def getStat(self):
28         return self.stat
29
30     def getEndDis(self):
31         return self.enddis
32
33     def add(self, row):
34         self.ts.append(row)
```

```
35
36      def getTS(self):
37          return self.ts
38
39  # main function
40  def makeMatrix(topodir, topoPrefix, geo,  lx, ylow, yhigh, sastopo,  force):
41          # set matrix filename (binary data)
42          if geo: matrix3fn='matrix3_'+'lx'+str(lx)+'__geo.dat' # geo scenarios
43          else: # sz-a
44                hprofile=((yhigh+ylow)/2)
45                matrix3fn='matrix3_'+'lx'+str(lx)+'__hprofile'+str(hprofile*1000)+'.dat'
46
47          # check for existing matrix3 (3rd generation) file
48          if matrix3fn in os.listdir(topodir) and force == False:
49                print "Reading␣existing␣matrix3␣file..."
50
51                array_final = cPickle.load(open(topodir+matrix3fn, 'rb'))
52
53                print "done"
54          # create matrix3
55          else:
56                if geo: print "Matrix3␣(particles␣at␣the␣computed␣erosional␣surface)␣will␣
                      be␣created..."
57                else: print "Matrix3␣(particles␣intersecting␣␣" + str(hprofile*1000) + "␣m)
                      ␣will␣be␣created..."
58
59                #getting particle-IDs...
60                preF=[]
61
62                # getting filename of the last save step
63                for file in os.listdir(topodir):
64                      if ".txt" in file: preF.append(int(file.strip('.txt').split('_')[-1])
                            )
65                preF.sort()
66
67                # last save step's filename (depending on lx, what is the number of save
                      steps
68                # (can be translated into amount of shortening):
69                f = topodir + topoPrefix + str(preF[lx-1])+".txt"
70
71                # last save step's particles...
72                lastTS = np.loadtxt(f, dtype={'names' : ('id', 'x', 'y', 'dia'), 'formats'
                      : (int, float, float, float)})
73
74                # wildcards for particle IDs within the specified range
75                matrix3=[[] for i in range(lastTS[-1]['id']+1)]
76
77                # for particles in the last sas (lx)
78                for p in lastTS:
79
80                      altitude = (p['y']/10) -70    # for sz-a and Geo-R3 (coordinates are
                            stored in 10 km and the origin of the coordinate system is at y
                            =-70 km)
81
82                      try:
83                            # geo scenarios
84                            if geo:
```

```
85                              # work around for boundary issues at the right side of
                                    the box
86                              if p['x']>3495: myX=499   # (maximum x = 3500... i.e. 250
                                     km in positve x direction and 100 in negative x
                                    direction for refilling of the numerical "sandbox")
87                              else: myX=int(round(2* ((p['x']/10)-100)))    # geo
                                    scenarios with 100 km in negative x direction, power
                                     two because erosional surface comprises two points
                                    per km
88
89                              # work around for boundary issues at the left side of the
                                     box (excluding particles of the refill box)
90                              if myX<0: pass
91                              else:
92
93                                    # Select particle for analysis...
94                                    # if (i) the altitude of the current particle is
                                          equal to of less than the 'quasi' real
                                          elevation at his corresponding x-Value (i.e.
                                          if the centre of the particle is below the
                                          surface)
95                                    # and (ii) the distance to the surface is less than
                                           its radius  (i.e. if the particle intersects
                                          the surface)
96                                    if altitude <= sastopo[myX] and (sastopo [myX]  -
                                          altitude) <= (p['dia'] / 10):
97                                          matrix3[p['id']]=Particle(p['id'], True, (
                                                sastopo[myX]  -  altitude) )  # for Geo
                                                (R3) set particle true and tell distance
                                                 at the end of simulation
98                                    else: matrix3[p['id']]=Particle(p['id'], False,
                                          0.) # set particle False
99                      # sz-a
100                     else:
101                           if abs(hprofile - altitude) <= (p['dia']/10):
102                               # all other (distance at the end of simulation can be
                                      pos or neg! Thus, if pos, then distance will be
                                      added to the altitude, else it will be
                                     subtracted from it.)
103                               matrix3[p['id']]=Particle(p['id'], True,  hprofile-
                                      altitude)
104                           else: matrix3[p['id']]=Particle(p['id'], False,  0.)
105
106             # error exception
107             except:
108                   print "Error matrixMaker - line 82\t" + str(p['x'])
109                   print sastopo[10000]
110
111     k = 0   # counter for standard output controlling
112     # for each timestep...
113     for ts in preF[:lx]:
114           # writing lines of 50 points to see if the script is still working
115           if k<50:
116                 k=k+1
117                 print '.',
118           else:
119                 k=0
120                 print '.'
```

```
121
122                 # loading sas file
123                 tsDat = np.loadtxt(topodir + topoPrefix + str(ts) + '.txt', dtype={'
                        names' : ('id', 'x', 'y', 'dia'), 'formats' : (int, float, float
                        , float)})
124
125                 # for each particle in the current save step...
126                 for p in tsDat:
127                       try:
128                             # only if it is marked as True in its status-flag
129                             if matrix3[p['id']].getStat():
130                                   # values of scaled models need to be divided by 10
                                          ([10 km] -> [km])
131                                   # Altitude of 70 km in the model == 0 km a.s.l. in
                                          reality:: Elevation:=(z/10)-70
132                                   # Appending data to matrix
133                                   # matrix[n][t][0]: ID
134                                   # matrix[n][t][1]: distance from starting point of
                                          the model [km]
135                                   # matrix[n][t][2]: Elevation [km]
136                                   # matrix[n][t][3]: temperature [degree C]
137
138                                   enddis = matrix3[p['id']].getEndDis() # is added up
                                         or to or subtracted from the particle
                                        altitude to end up at the surface or at the
                                        hprofile at the end of simulation
139
140                                   if geo: matrix3[p['id']].add([p['id'], (p['x']/10)
                                        -100, (p['y']/10)-70+enddis, -9999]) # for Geo
                                         (R3)
141                                   else: matrix3[p['id']].add([p['id'], p['x']/10, (p[
                                        'y']/10)-70+enddis, -9999]) # for sz-a
142
143                             else: pass
144                       except: "Error matrixMaker - line 94"
145
146           #save new matrix3 file
147           matrix_final=[]
148           for m in matrix3:
149                 try:
150                       if m.getStat(): matrix_final.append(m.getTS())
151                       else: pass
152                 except: pass
153
154           array_final=np.array(matrix_final)
155
156           try:
157                 pick = cPickle.Pickler(open(topodir+matrix3fn, 'wb'))
158                 pick.fast = True
159                 pick.dump(array_final)
160                 print "\nCreated new matrix3 (" + str(len(matrix_final)) + " entries)
                        and saved as file: " + topodir + matrix3fn
161           except:
162                 cPickle.dump(matrix_final[:(len(array_final)/2)], open(topodir+
                        matrix3fn+'1', 'wb'))
163                 cPickle.dump(matrix_final[(len(array_final)/2):], open(topodir+
                        matrix3fn+'2', 'wb'))
```

```
164                 print "\nCreated␣two␣new␣matrix3␣(" + str(len(matrix_final)) + "␣
                        entries)␣and␣saved␣as␣two␣files:␣" + topodir + matrix3fn + "1/2"
165
166       return array_final
167
168 # Starting point
169 if __name__ == "__main__":
170       import topomaker as tm
171
172       dir = 'data/txt/' # testdata
173       prefix = '1_231111_'  # testdata
174       geo=False
175       lx=15 # testdata
176       ylow=0.51
177       yhigh=.51
178       force=True
179
180       topoForce=True
181       rME_i=.5
182       rME_n=3
183
184       topo=tm.makeTopo2(dir, prefix, geo,  lx, topoForce, rME_i, rME_n)      # create
              erosional topographies
185       matrix = makeMatrix(dir, prefix, geo,  lx, ylow, yhigh, topo,  force)     #
              create matrix
186
187       print matrix[5][:, 2]     # test output
```

topomaker.py

```
1 ## Create topography
2 ##
3 ## Author: Simon Elfert
4 ##
5 ## Developed for of the PhD thesis by Simon Elfert (2009-2014, University of Bremen)
6 ##
7 ## Purpose of this script:
8 ## derive an erosional topography from a numerical "sandbox" experiment
9
10
11 # Required libraries
12 import os
13 import cPickle
14 import numpy as np
15 from scipy import interpolate
16
17 # create a list surface elevations (topography) for each timestep (just the model
18 # data without erosion!)
19 # dir   :   [str] directory
20 # prefix:   [str] prefix of the timestep file names
21 # lx    :   [int] number of timesteps
22 # force :   [bool] force new read in
23 def makeModelTopo(dir, geo,  prefix, lx, force):
24
25       # Filename of model topography (binary data)
26       topofn = prefix+"_lx"+ str(lx) +"_topo1c.dat"
27
```

```
28        # check for existing model topograhy
29        if topofn in os.listdir(dir) and force == False:
30              print "Reading␣existing␣topography␣file..."
31
32              topo = cPickle.load(open(dir+topofn, 'rb'))
33
34        # create model topography
35        else:
36
37              print "Reading␣in␣the␣topography..."
38              preF=[]
39              for file in os.listdir(dir):
40                    # extract save step numbers from file names
41                    if '.txt' in file: preF.append(int(file.strip('.txt').split('_')[-1])
                          )
42              preF.sort() # sort save step numbers
43
44              # sorted list of filenames
45              f = [prefix+str(pF)+".txt" for pF in preF[:lx]]
46
47              # Initiating a list where the topographies of all sas will be stored
48              topo=[]
49
50              # for each filename until lx  (i.e. for each sas)
51              for fn in f:
52
53                    # read in data
54                    dat = np.loadtxt(dir + fn, dtype={'names' : ('id', 'x', 'y', '
                          diameter'), 'formats' : (int, float, float, float)})
55
56                    # exclude empty/bad entries and diameters, and store in the right
                          units (x: [km],  y: [km above sealevel])
57                    d=[]
58
59                    for z in dat:
60                          if  geo:
61                                if z['diameter']>4 and z['x']>=1000 and z['x']<3495: d.
                                      append([z['id'], (z['x']/10)-100, (z['y']/10)-70])
                                      # for Geo (R3)
62                                else: pass
63                          else:
64                                if z['diameter']>4 and z['x']>= 0 and z['x']<2495: d.
                                      append([z['id'], z['x']/10, (z['y']/10)-70])  # for
                                      sz-a
65                                else: pass
66
67                    # further on: d[i] = [id, x in km, y in km a.s.l.]
68
69                    # topo of sas (in km a.s.l.)
70 ####         This has to be modified, when the model space is extended!!!!!!!!!!
71                    topoS = [-50 for i in range(500)] # model space in x-direction = 250
                          km # for sz-a, Geo (R3)
72
73                    logflag=False # for testing purposes
74                    if logflag: log=open("topolog.txt", "w")
75
76                    # each particle
77                    for di in d:
```

```
78                  # if the current topography's y-value at point x is smaller (i.e.
                        deeper)
79                  # than the current data-y value at point x, than set the current
                        topography's
80                  # y-value to current data-y value
81
82                        gc=0  # good counter
83                        ec=0   # error counter
84
85                        # smoothing the surface plusminus 2 km along the profile
86                        for i in range (4):
87                              try:
88                                    if topoS[int(di[1]*2) -  i ] < di[2]:
89                                          topoS[int(di[1]*2) - i] = di[2]
90                                          gc=gc+1
91                                    else: pass
92                              except: ec=ec+1
93                              try:
94                                    if topoS[int(di[1]*2) +  i ] < di[2]:
95                                          topoS[int(di[1]*2) + i] = di[2]
96                                          gc=gc+1
97                                    else: pass
98                              except: ec=ec+1
99
100                       if logflag: log.write(str(di[0])+"\t" + str(gc) + "\t" + str(ec
                              ) + "\t" +  str(di[1]) + "\t"  +str(int(di[1] *2)) +
                                                "\n")
101
102                 if logflag:
103                       log.close()
104                       logflag=False
105
106                 # append the save step's topography to the over-all-topography-list
107                 topo.append(topoS)
108                 print fn # print filename to standard output stream to control status
109
110           #save new topopgraphy file (binary)
111           cPickle.dump(topo, open(dir+topofn, 'wb'))
112
113           print "\nCreated new topography and saved as file: "+ dir + topofn
114
115     return topo
116
117 # Getting the topography for each save step with respect to the starting
118 # and ending elevations WITH erosion.
119 def makeTopo2(dir, prefix, geo,  lx, force, rME_i, rME_n):
120
121     # filename (binary data)
122     topo2fn = prefix+"_lx"+ str(lx) +"_topo2c.dat"
123
124     # check for existing topograhy data
125     if topo2fn in os.listdir(dir) and force == False:
126           print "Reading existing topography (c-generation) file..."
127           topo2 = cPickle.load(open(dir+topo2fn, 'rb'))
128
129     # create erosional topograhy
130     else:
131         # firstly, get model topography
```

```
132             # "topo" is the modelled topography (i.e. withouterosion)
133             topo = makeModelTopo(dir, geo,  prefix, lx, force) #  create or load modelled
                    topograhy
134             maxAll = [max(topo_i) for topo_i in topo]    # get a list with maximum
                    elevation (maxAll[i]=maximum altitude of sas i)
135             mME_i = maxAll[0]                            # maximum elevation of sas 0
136             mME_n = maxAll[-1]                             # maximum elevation of last sas
                    (lx)
137
138             # topography factor: for each timestep the percentage (0-1) of simulated
139             # timestep's max altitude refering to the simulated altitude range between
140             # the first and the last timestep
141             # == internal simulation factor, just simulated data until here...
142             q = [(mME-mME_i)/(mME_n - mME_i) for mME in maxAll]
143
144             print "topoFaktor calculated"
145
146             # erosional max elevation of each sas, now refering to the "real" starting
                    and ending elevations
147             rME = [rME_i+(qs*(rME_n-rME_i)) for qs in q]
148
149             print "maxTopo calculated"
150
151             # initiating the list for the final topographies
152             topo2 = []
153
154             # for each timestep...
155             for s in range(len(topo)):
156
157                 # for each point in x direction on the profile
158                 #       max 'real' Topo *  percentage with respect to simulation
159                 rE_xs = [rME[s] * (mE/max(topo[s])) for mE in topo[s]]      # problem: in
                        depression topo2 above topo1
160
161                 topo2.append(rE_xs)
162             #save new topopgraphy file (binary data)
163             cPickle.dump(topo2, open(dir+topo2fn, 'wb'))
164
165             print "\nCreated new corrected topography and saved as file: "+ dir + topo2fn
166
167         return topo2
168
169 # Starting point
170 if __name__ == "__main__":
171
172         import matplotlib.pyplot as plt
173
174         dir = 'data/txt/'
175         prefix = '1_231111_'
176
177         geoL=False
178         lx=15
179         mTforce=False
180         t2force=False
181         rME_i=.5
182         rME_n=3
183
184         plotflag=True
```

```
185
186       pretopo=makeModelTopo(dir, geoL,  prefix, lx, mTforce)
187       topo=makeTopo2(dir, prefix, geoL,  lx, t2force, rME_i, rME_n)
188
189       if plotflag:
190             fig = plt.figure()
191             ax1 = fig.add_subplot(221)
192             ax2 = fig.add_subplot(222)
193             ax3 = fig.add_subplot(223)
194             ax4 = fig.add_subplot(224)
195
196             x = [xi*.5 for xi in range(len(topo[-1]))]
197
198             y1 = [yi for yi in pretopo[0]]
199             y2 = [yi for yi in topo[0]]
200             y3 = [yi for yi in pretopo[-1]]
201             y4 = [yi for yi in topo[-1]]
202
203             ax1.set_title('pretopo=0')
204             ax1.plot(x,y1)
205
206             ax2.set_title('topo=0')
207             ax2.plot(x,y2)
208
209             ax3.set_title('pretopo=-1')
210             ax3.plot(x,y3)
211
212             ax4.set_title('topo=-1')
213             ax4.plot(x,y4)
214
215             plt.show()
216
217       print "done."
```

ptTTranslator.py

```
1  ## Translator from save step to geological time and depth to temperature
2  ##
3  ## Author: Simon Elfert
4  ##
5  ## Developed for the PhD thesis by Simon Elfert (2009-2014, University of Bremen)
6  ##
7  ## Purpose of this script:
8  ## 1. function: getBoundaries - internal function for preliminary decision making
9  ## 2. function: getX - Provide an array of geological times according to numer of
10 ##    savesteps and ftime
11 ## 3. function: getT - Provide a temperature matrix for a given set of particles
12 ##    (i.e. the matrix), including the recent topography and a geothermal gradient.
13 ##    reliefTS is a counter flag to start effective erosion to assure that all
14 ##    particles are exhumed to the surface at the end of the simulation
15
16 # Required libraries
17 import numpy as np
18
19 # Helping decision making (internal function without link to main program)
20 def getBoundaries(matrix):
21
```

```
22 ##    xids
23     # Getting the x-values for each matrix (to decide wich boundaries to use)
24     xids = [m[0][1] for m in matrix]
25     print "Min␣Anfangs-x:\t", str(min(xids)), "␣(Ball-ID:␣", str(matrix[xids.index(min(
           xids))][0][0]),")"
26     print "Max␣Anfangs-x:\t", str(max(xids)), "␣(Ball-ID:␣", str(matrix[xids.index(max(
           xids))][0][0]),")\n\n---\n\n"
27     print "Proposed␣boundaries:"
28     xids.sort()
29     dif=len(xids)/5
30     print [xids[gr * dif] for gr in range(4)]
31     print "\n---------------------------------\n"
32     yids = [m[0][2] for m in matrix]
33     print "Min␣Anfangs-y:\t", str(min(yids)), "␣(Ball-ID:␣", str(matrix[yids.index(min(
           yids))][0][0]),")"
34     print "Max␣Anfangs-y:\t", str(max(yids)), "␣(Ball-ID:␣", str(matrix[yids.index(max(
           yids))][0][0]),")\n\n---\n\n"
35
36 # lx=number of savesteps
37 # ftime=translator: modelstep to time
38 def getX(lx, ftime):
39     # Defining a numpy array of x-values with x=Ma from start of simulation
40     # (later after reversing the ax it will be Ma before end of simulation i.e. present
           day)
41     pre_x = np.arange(lx)
42     x=pre_x*ftime
43     return x
44
45 # create temperature matrix
46 # matrix=set of particles to derive temperature for
47 # topo=topography array
48 # reliefTS=counter flag for effective erosion
49 # geotherm=geothermal gradient
50 def getT(matrix, topo, lx, reliefTS, geotherm):
51       print "Starting␣to␣calculate␣temperatures..."
52
53       # for each particle pathway...
54       for m in matrix:
55
56             # for each timestep
57             for s in range(len(m)):
58                   try:
59                         # erosional topography at point x at step s
60                         # ...topo[s] = elevation at step s
61                         # ...topo[s][ ... 2 * m[][] ...] = elevation at step s at point
                                x. Power two because the erosional topography is resolved
                                in two points per km.
62                         rE_xs = topo[s][int(round(2*m[s][1]))]     # m=particle-list=[
                               step0, step1, step2, ... step_n], with step0=[id, x, y, t]
63                   except:
64                         # if particle is at km 250, take the corresponding value from
                               topo
65                         rE_xs = topo[s][-1]     # m=particle-list=[step0, step1, step2,
                               ... step_n], with step0=[id, x, y, t]
66
67                   # no effective erosion
68                   if s<reliefTS:
69                       # save temperature
```

```
70                          m[s][3]=((rE_xs - m[s][2])*geotherm)+10
71
72                    # effective erosion
73                    else:
74                          # get final erosional elevation
75                          try:
76                                rE_xn = topo[-1][int(round(2*m[-1][1]))]
77                          except:
78                                rE_xn = topo[-1][-1]    # see above
79
80                          # calculate effective erosion and save temperature subsequently
81                          rG_xs=rE_xs - (  ( float(s+1-reliefTS)/float(lx-reliefTS))  *
                                (rE_xn - m[-1][2] )   )
82                          m[s][3]=((rG_xs - m[s][2])*geotherm)+10
83          return matrix
84
85 # Starting point
86 if __name__ == "__main__":
87
88          # Required scripts
89          import topomaker as tm
90          import matrixMaker as mM
91
92          topodir = 'data/txt/'
93          topoPrefix = '1_231111_'
94          geo=False # scenario
95          lx=15 # test data
96          ftime=2.13333 # test data
97          ylow=0.51 # elevation of horizontal profile
98          yhigh=0.51 # elevation of horizontal profile
99          force=False
100         topoForce=False
101         reliefInc=30  # onset of effective erosion [Ma]
102         geotherm=30 # geothermal gradient [degree celsius per km]
103         rME_i=.5  # assumed initial maximum elevation [km]
104         rME_n=3. # assumed maximum elevation at the end of the simulation [km]
105         tTex=True # export time-temperature paths
106
107 ##############################################
108         topo = tm.makeTopo2(topodir, topoPrefix, geo,  lx, topoForce, rME_i, rME_n)   #
                make (or load) topography
109         matrix = mM.makeMatrix(topodir, topoPrefix, geo,  lx, ylow, yhigh, topo[lx-1],
                force) # make matrix
110
111         # Getting the save step when relief incision starts
112         x=getX(lx, ftime)
113         diflist = [abs(xj-reliefInc) for xj in x]     # list of differences between time
                date and reliefInc
114         reliefTS = lx - diflist.index(min(diflist))    # save step with minimum difference
115
116         getT(matrix, topo, lx, reliefTS, geotherm)     # create temperature matrix
117
118         print "done."
```

pathwriter.py

```
## Writer for particle paths
##
## Author: Simon Elfert
##
## Developed for the PhD thesis by Simon Elfert (2009-2014, University of Bremen)
##
## Purpose of this script:
## Writing paths for selected particles (id... x... y).


# Required script
import os

## Save particle files
def particleExtracter(matrix, dir, llx,  ylow, yhigh):

    # name of the folder for the particle files
    if ylow==-9999: folder = "Partikelpfade_"+str(llx)+"__geo"
    else: folder = "Partikelpfade_"+str(llx)+"__"+str(ylow)+'to'+str(yhigh)


    # test if folder already exists. Otherwise create it
    if folder not in os.listdir(dir):
        os.mkdir(dir+folder)
        print "New folder was created"

        # for each particle
        for m in matrix:
            try:
                file = open(dir+folder+"/"+str(int(m[0][0])),'w')
                # for each timestep
                for row in m: file.write(str(int(row[0]))+'\t'+str(row[1])+'\t'+str(row
                    [2]*(-1))+'\r\n')    # save depth: *(-1)
                file.close()
                print dir+folder+deli+str(int(m[0][0]))+ " was created."
            except: pass # if an empty row in matrix appears (i.e. no values at last ts
                )

    else:
        print "Folder "+folder+" already exist. Please rename or remove the old one!"
```

tTExporter.py

```
## Writer for time-temperature paths
##
## Author: Simon Elfert
##
## Developed for the PhD thesis by Simon Elfert (2009-2014, University of Bremen)
##
## Purpose of this script:
## Writing time-temperature paths for selected particles (Ma, T[degree celsius]).


# Export routine for t-T-paths
#pret=array with geological times (0...n)
```

```
#T=temperature array
#dir=directory
#run, mode, id=for filename creation
def export_tTPath(pret, T, dir, run, mode, id):
      dir=dir.rstrip("/")
      while dir[-1] != "/": dir=dir[:-1]

      # for some miraculous reason, a list has to be created... (does not work with
          array)
      t=[ti for ti in pret]

      wdat=open(dir+str(int(id))+"_"+run+"__lx_"+str(mode)+".txt", "w")

      # temperature is listed forward (first to last timestep), time is currently
      # reversed (last to first timestep).
      # in the export file time has to be reversed, while temperature has to
      # be listed forwardly...
      for i in range(len(t)): wdat.write(str(t[-1-i])+'\t'+str(T[i])+'\n')
      wdat.close()

# Starting point
if __name__ == "__main__":
    t=[0,1,2,3,4,5]
    T=[10,25,40,50,400,500]
    dir="data/txt/"
    run="test"
    id="0001"
    mode=1
    export_tTPath(t, T, dir, run, id, mode)
    print "done."
```

settingplotter_0.91.py

```
## Setting plotter
##
## Author: Simon Elfert
##
## Developed for the PhD thesis by Simon Elfert (2009-2014, University of Bremen)
##
## Purpose of this script:
## Plots particles of a numerical "sandbox" experiment on a defined saving step
### in a cartesian coordinate system


# Required scripts
import numpy as np
import pylab
import matplotlib
from matplotlib.patches import Polygon
import matplotlib.pyplot as plt

import subprocess                 # For issuing commands to the OS.
import os
import sys

# dependency on own script
import topomaker as tm
```

```
25
26 ## Function to plot particles within a given subplot
27 ## axes: x/y axes of current plot
28 ## f: file of current saving step
29 ## cdict: dictionary for particle colouring
30 def my_circle_scatter(axes, f, cdict, **kwargs):
31     count=0 # count plotted particles
32
33     # for particle in file (i.e. one saving step)
34     for p in f:
35         # only take particle if its radius is existent (owed to redundant PFC2D
36         # exports) and it does not belong to the refilling box to the left
37         # (negative x values) of the model
38 #         if p['r']>0 and p['x']>=100: # for geo scenarios
39         if p['r']>0 and p['x']>=-500: # for all others
40
41             # get  particle colouring
42             p_color=cdict[p['id']]
43
44 ##             faultscene (to be uncommented to view only faultscene from Paper
    Contribution 3)
45 #             p_color='w'
46 #             if p['id'] in [4314, 20962, 14035, 6170]: p_color='darkOrange'
47 #             elif p['id'] in [40425, 21144, 30368, 37783]: p_color='g'
48 #             elif p['id'] in [13092, 21901, 3674, 37153, 31193, 10232, 28141]: p_color
    ='darkOrchid'
49 #             else: p_color=cdict[p['id']]
50 ##             end of faultscene
51
52             # plot particle
53 #             circle = pylab.Circle(((p[1]/10)-100,(p[2]/10)-70), facecolor=p_color,
    radius=p[3]/10, **kwargs) # for Geo (R3)
54             circle = pylab.Circle(((p[1]/10),(p[2]/10)-70), facecolor=cdict[p['id']],
                 radius=p[3]/10, **kwargs) # for SZ-A
55             axes.add_patch(circle)
56
57             count += 1  # increase counter
58
59     print "\tPlotting " + str(count) + " particles."
60     return True
61
62 ## Function to initiate and maintain the plotter
63 ## dir: home directory
64 ## tfold: subdirectory of dir with txt-files (one file per saving step)
65 ## figFolder: subdirectory of dir for the herewith created plots
66 ## sztitle: optional: to label plot
67 ## prefix: prefix of txt-files
68 ## geo: flag for geo scenarios (if False: SZ-A)
69 ## lx: current saving step
70 ## llx: max saving step
71 ## force: enforce rebuilding of erosional topography
72 ## maxStart: max elevation of the erosional topography to begin of the simulation
73 ## maxEnd: max elevation of the erosional topography at the end of the simulation
74 ## hp: particle-IDs of the horizontal profile
75 ## pDir: directory (complete path) of particle pathways (one file per particle)
76 ## shave: flag: 0=show (only feasible for single plots), 1=save as pdf (especially for
    creating a series of plots)
```

```
77 def tsplotter(dir, tfold, figFolder, sztitle, prefix, geo,  lx, llx,  force, maxStart,
       maxEnd, hp, pDir, shave):
78
79     # initiating dictionary for coloring
80     cdict={}
81     cdict2={}   # transparent plot (see below)
82
83     # define colourcode
84 #    ccode={0:'k', 1:'0.9', 2:'r', 3:'y', 4:'g', 5:'k', 6:'0.8'}   # Geo scenarios
85 #    ccode={0:'k', 1:'0.9', 2:'r', 3:'y', 4:'.6', 5:'k', 6:'0.8'}   # fault scene
86     ccode={0:'k', 1:'0.9', 2:'k', 3:'r', 4:'g', 5:'0.8', 6:'0.8'} # SZ-A
87
88     # directory of colorcode file
89 #    cdir = 'data//Faerbung_Geo-R3_Sc1Sc2.txt'    # geo scenarios Sc-1, Sc-2
90 #    cdir = 'data/Faerbung_Geo-R3_Sc3.txt'    # geo scenario Sc-3
91     cdir = "data/Faerbung_SZ-A.txt"   # SZA
92
93     # load data
94     dat = np.loadtxt(cdir, dtype={'names' : ('id', 'x', 'y', 'dia', 'c'), 'formats' : (
           int, float, float, float, int)})
95
96     # save colorcode with respect to ID in cdict
97     for p in dat:
98         try: cdict[p['id']]= ccode[p['c']]
99         # exception handling: print particle-ID to standard output
100        except:
101            print '-------------------'
102            print p['id']
103            print p['c']
104            print '-------------------'
105
106 ##    # for semi-transparent figure (lower crustal fragment: choose Sc2 colouring for
       cdir and uncomment the following rows)
107 ##    cdir2 = 'data/Faerbung_Geo-R3_Sc1Sc2.txt'
108 ##    dat2 = np.loadtxt(cdir2, dtype={'names' : ('id', 'x', 'y', 'dia', 'c'), 'formats'
       : (int, float, float, float, int)})
109 ##
110 ##    for p in dat2: cdict2[p['id']]= ccode[p['c']]
111 ##
112 ##    for id in cdict:
113 ##        if cdict[id] == cdict2[id]: pass
114 ##        else:
115 ##            if cdict[id] == '0.9': cdict[id] = '0.5'
116 ##            elif cdict[id] == 'g': cdict[id] = '#003300'
117 ##            else: pass
118 ##  # end semi-transparent figure setting
119
120
121    # getting filenames (of single saving steps)
122    preF=[]
123    for file in os.listdir(dir+tfold):
124        if ".txt" in file: preF.append(int(file.strip('.txt').split('_')[-1]))
125        else: pass
126
127    preF.sort() # sort enumeration
128
129    # loading the erosional topography for current timestep
130    topo = tm.makeTopo2(dir+tfold, prefix, geo, lx, force, maxStart, maxEnd)
```

```
131
132     # getting time in Ma before end of simulation
133     if geo: ftime = 0.0537815126 # for Geo scenarios (lx=595 == 32 Ma)
134     else: ftime = 0.032032032 # for SZ-A scenarios (lx=1000 == 32 Ma)
135
136     pre_time = np.arange(lx)    # [0,1,2,...lx]
137     pre_time2 = pre_time*ftime    # [0,.05, ... lx*.05]
138     time = [pre_time2[-1] - xi for xi in pre_time2] # [lx*.05, ... 0]
139
140
141     # initiate figure
142     fig = plt.figure()
143
144     # for each saving step to plot
145     for i in range(lx):
146         # change comments to create a large series of plots
147 #        if i<594:pass #>0: pass #i<594: pass
148         if llx==lx: llx=llx-1 # prevent index out of memory...
149         if i<llx or i>llx: pass
150         else:
151             # add subplot
152             ax = fig.add_subplot(111)
153
154             # particles of saving step
155             print "Reading␣particles␣of␣timestep␣" + str(i)
156             f = np.loadtxt(dir+tfold+prefix+str(preF[i])+'.txt', dtype={'names' : ('id'
                    , 'x', 'y', 'r'), 'formats' : (int, float, float, float)})
157             print "File␣"+ str(preF[i])
158
159             # erosional topography of saving step
160             t = topo[i]
161
162             # plot particles as circles
163             my_circle_scatter(ax, f, cdict, linewidth=.1, edgecolor='k')
164
165 ##            # saving step of PAZ entry - hotfix for Ticino profile... uncomment for
    faultscene
166 ##            PAZ=[501, 691, 664, 536, 369, 328, 274]
167 ##            pcount=0
168 ##            # end of hotfix
169
170             # particles of horizontal profile
171             for p in hp:
172                 # read particle pathway
173                 ppw = np.loadtxt(pDir+str(p), dtype={'names' : ('id', 'x', 'y'), '
                        formats' : (int, float, float)})
174
175 ##                # TH1-scene, uncomment for TH1-scene
176 ##                start=int(((1000* ftime)-14.2)/ftime)
177 ##                print start
178 ##                mid=int(((1000*ftime) - 13.82)/ftime)
179 ##                print mid
180 ##                end=int(((1000*ftime) - 13.5)/ftime)
181 ##                print end
182 ##                # plot particle pathways in different colours  - only for Ticino-H1
    scene
183 ##                ax.plot(ppw['x'][:start+1], ppw['y'][:start+1]*(-1),'.6', linewidth
    =3)   # normal: linewidth=.5 ; faultscene: linewidth=1.5
```

```
184 ##                ax.plot(ppw['x'][start:mid+1], ppw['y'][start:mid+1]*(-1),'g-',
    linewidth=3)   # normal: linewidth=.5 ; faultscene: linewidth=1.5
185 ##
186 ##                ax.plot(ppw['x'][end:], ppw['y'][end:]*(-1),'.6', linewidth=3)   #
    normal: linewidth=.5 ; faultscene: linewidth=1.5
187 ##                ax.plot(ppw['x'][mid:end+1], ppw['y'][mid:end+1]*(-1),'r-', linewidth
    =3)   # normal: linewidth=.5 ; faultscene: linewidth=1.5
188 ##                # end TH1-scene
189
190
191 ##                # plot particle pathways for faultscene... to be out commented
192 ##                # plot particle pathway until PAZ entry - only for faultscene (
    uncomment for faultscene)
193 ##                ax.plot(ppw['x'][:PAZ[pcount]], ppw['y'][:PAZ[pcount]]*(-1),'r-',
    linewidth=1.5)   # normal: linewidth=.5 ; faultscene: linewidth=1.5
194 ##                # plot particle pathway until current timestep
195 ##                ax.plot(ppw['x'][PAZ[pcount]:i], ppw['y'][PAZ[pcount]:i]*(-1),'b-',
    linewidth=2.5)   # normal: linewidth=.5 ; faultscene: linewidth=1.5
196 ##                pcount += 1   # increase counter
197 ##                # end of faultscene
198
199                 # plot particle pathways for normal plots (to be commented for
                        faultscene!)
200                 ax.plot(ppw['x'][:i], ppw['y'][:i]*(-1),'r-', linewidth=.5)
201             # endfor...
202
203             # Plotting erosional topography
204             # x values for topography (each 500 m one point)
205             x = [xi*.5 for xi in range(len(topo[-1]))]
206             # plot topography
207             ax.plot(x, t, linestyle='-', color = '.4',  linewidth=.2) # faultscene:
                    linewidth = 1.5
208
209             # Plot Adriatic Indenter as black boulder (to be commented for geo Sc3!!!)
210             ax.add_patch(Polygon
                    ([[105.583,-41.4174],[129.891,-25.3745],[250,-26],[250,-72.5]], fc='k'
                    , closed=True))
211
212             # x and y dimensions on the same scale
213             ax.axis('scaled')
214
215             # set x axis dimensions
216
217             # normal
218             ax.set_xlim((0,250))
219 #            ax.set_xlim((-50,180)) #P2-extend
220             ax.set_ylim((-70,25))
221
222 #             # Ticino-H1 scene
223 #             ax.set_xlim((64,72))
224 #             ax.set_ylim((-4,-1))
225
226 #             # faultscene
227 #             ax.set_xlim((70,140))
228 #             ax.set_ylim((-38,12))
229
230             # label plot (uncomment if desired)
231 ##            # add time of timestep
```

```
232 ##             ax.text(20,-50, str(round(time[i],1))+' Ma')
233 ##             ax.text(20,-60, sztitle)
234
235             # label the axes
236             ax.set_ylabel("Altitude␣[km␣a.s.l.]")
237             ax.set_xlabel("Distance␣along␣modeled␣profile␣length␣[km]")
238
239             # leading zeros of current saving step
240             if i < 10: sas = '00'+str(i)            # two leading zeros
241             elif i>=10 and i<100: sas = '0'+str(i)  # one leading zero
242             else: sas = str(i)                      # no leading zero needed
243
244             # flag processing...
245             if shave == 0: plt.show()   # show plot
246             else: plt.savefig(dir+figFolder+sas+'.pdf') # save as pdf
247
248             # clear the figure
249             plt.delaxes()
250
251             print "\tDone"
252
253 # Starting point
254 if __name__ == "__main__":
255
256     # directory of the scenario run (requires a folder named 'txt' with txt and topo
            files)
257     dir = "data/"   # testdata
258     tfold = "txt/"  # subfolder
259     prefix = "1_231111_"    # prefix for txt files
260
261     # plot title and folder for plots (optional)
262     sztitle= ''
263     figFolder = ''
264
265     # flag for showing or saving
266     shave=0     #0: show, else: pdf
267
268     # Max Number of timesteps
269     lx=15 # testdata
270
271     # Flag for geometry scenarios
272     geo=False
273
274     # Flag to force the rebuilding of an erosional topography file (will need some time
            !)
275     # The topography file will be build if it does not exist even if topoForce=False
276     force = False
277
278     # Assumed maximum elevation of the erosional topography [km a.s.l.] to begin of the
            simulation
279     maxStart = .5
280
281     # Assumed maximum elevation of the erosional topography [km a.s.l.] at the end of
            the simulation
282     maxEnd = 3.
283
284 ##    SZ-A3-lx1000
285 #    llx=1000
```

```
286 #     hp=[88005, 90011, 85038, 87297, 87223, 87014, 86338, 86153, 82191, 80452, 80136,
        86332, 80032, 82227, 82050, 80518, 82054, 82397, 80550, 85029, 84226, 82679,
        82225, 82215, 87087, 82416, 84426, 80513, 80320, 82198, 84406, 80407, 82019,
        80542, 80460, 82312, 84215, 80565, 80325, 84224, 80384, 82154, 82450, 84370,
        84050, 82342, 84546, 80119, 80281, 85184, 85220, 86341, 85055, 85162, 85089,
        86000, 85003, 84411, 87041, 85104, 86327, 85250, 86336, 86053, 87144, 86015,
        85225, 74222, 64511, 50078, 51227, 63702, 51163, 50254, 65158, 74168, 70983,
        60673, 61932, 51166, 63612, 62281, 63439, 70162, 73867, 50905, 65029, 70349,
        71008, 50075, 60966, 54057, 50176, 51126, 54490, 50068, 51709, 71643, 63684,
        62554, 70754, 63241, 53145, 64816, 64579, 53548, 71475, 74375, 74773, 50867,
        64724, 62300, 50711, 72247, 60783, 54461, 54491, 71561, 70253, 50278, 65127,
        73119, 50962, 54548, 60553, 63004, 52012, 61096, 53461, 53020, 60657, 52952,
        70797, 70713, 53834, 53748, 54371, 50381, 60684, 53065, 71977, 64149, 52112,
        51475, 72180, 73013, 63325, 74826, 60601, 64484, 63015, 74336, 51899, 73112,
        54252, 52339, 52942, 74544, 761]
287
288 #    #fault-scene particles
289 #     llx=1000
290 #     hp = [4314, 20962, 14035, 6170, 40425, 21144, 30368, 37783, 13092, 21901, 3674,
        37153, 31193, 10232, 28141]
291
292 #     # Particles corresponding to the Ticino horizontal profile
293 #     llx=1000
294 #     hp=[50078,  50905,  53145,  54491,  54548,  52012,  70797]
295
296 #     # Ticino-H1
297 #     llx=1000
298 #     hp=[50078]
299
300 ##      no particle paths
301     llx=15  # testdata
302     hp = []
303
304     # define folder for particle pathways
305     if "GeometrieReihen" in dir: pDir = dir+tfold+'Partikelpfade_'+str(llx)+'__geo/'
306     else: pDir = dir+tfold+'Partikelpfade_'+str(llx)+'__'+str(maxStart)+'to'+str(maxEnd
            )+'/'
307
308     # start main function
309     tsplotter(dir, tfold, figFolder, sztitle, prefix, geo,  lx, llx,  force, maxStart,
            maxEnd, hp, pDir,  shave)
310
311     print "done."
```

Syn-AFT-batch.py

```
1 ## Create evolution plots for synthetic AFT ages
2 ##
3 ## Author: Simon Elfert
4 ##
5 ## Developed for the PhD thesis by Simon Elfert (2009-2014, University of Bremen)
6 ##
7 ## Purpose of this script:
8 ## Plot synthetic AFT ages derived from numerical "sandbox" experiments
9 ## (geo series) along the modelled profile length for different time slots
10 ## (snap shots in time)
11
```

```
12
13 # Required libraries
14 import matplotlib.pyplot as plt
15 import sys
16 import numpy as np
17
18 # required own scripts
19 sys.path.append("../particletracker3.1/")
20 import topomaker as tm
21
22 ## Initial assignments
23 ## Testdata (Sc3 of paper contribution 2)
24 dir = "data/"           # directory     # testdata
25 prefix = 'R3_1_ohneKugel_0,2_'     # basename # testdata: geo-sc3
26 fn = "data/Sc3_llx_20130303.dat"   # AFT data (ages, mean track lengths, evaluations) [
       text file]
27 reihen = [(1,100), (101,199), (200,292), (293, 389), (390, 487),  (488, 587)]   #
       Related to rows in fn associated with time slots (=llx). to read: (a,b) means row
       a+1 to b+1
28
29 geo = True  # flag for geo scenarios (if False: SZ-A; not feasable for this script, but
        necessary information for catching the right erosional topography)
30 lx = 7  # number of saving steps # testdata (geo: 595 )
31 sas = [1, 2, 3, 4, 5,  6]   # saving steps of numerical "sandbox" experiment # testdata
        (geo: 100, 200, 300, 400, 500, 595)
32 force = False # flag to enforce (or not) rebuilding of the erosional topography
33 rME_i = .5  # max elevation of the erosional topography to beginn of the simulation
34 rME_n = 3.  # max elevation of the erosional topography at the end of the simulation
35
36 # Loading array of erosional topographies
37 eSurface = tm.makeTopo2(dir, prefix, geo,  lx, force, rME_i, rME_n)
38
39 # Loading AFT data
40 grad=50 # adjustment of trendline (high grades are necessary to not overinterpret
       boundary conditions)
41 types=np.dtype([('lfd', int), ('lx', int), ('id', int), ('x', float), ('y', float), ('
       AFT', float), ('TL', float), ('StDev', float),  ('Notes', "S20")])
42 data = np.loadtxt(fn, dtype=types, skiprows=1)
43
44 # Initialise AFT lists for time slots (shortening of 20, 40, 60, 80, 100, 119 km)
45 aft20=[]
46 aft40=[]
47 aft60=[]
48 aft80=[]
49 aft100=[]
50 aft119=[]
51
52 # for each time slot
53 for r in range(len(reihen)):
54       # sort corresponding data
55       daten=np.sort(data[reihen[r][0]-1:reihen[r][1]], order="x")
56
57       xvor= daten["x"]   # Extracting x values
58       yvor= daten["AFT"]   # Extracting y values
59
60       notes=daten["Notes"] # Extracting evaluation of tT-paths
61
62       # Initialise necessary lists
```

```
63        x=[]  # model-km (good tT-paths)
64        y=[]  # AFT ages (good tT-paths)
65        x_ok=[] # model-km (also good tT-paths)
66        y_ok=[] # AFT ages (also good tT-paths)
67        x_s=[] # model-km (acceptable tT-paths)
68        y_s=[] # AFT (acceptable tT-paths)
69        x_xs=[] # model-km (bad tT-paths)
70        y_xs=[] # AFT (bad tT-paths)
71
72        # Allocating x/y pairs in respect to their evaluation
73        for n in range(len(notes)):
74              # good tT-paths
75              if notes[n]=="ok":
76                    x_ok.append(xvor[n])
77                    y_ok.append(yvor[n])
78
79                    x.append(xvor[n])
80                    y.append(yvor[n])
81
82              # acceptable tT-paths
83              elif notes[n]=="s":
84                    x_s.append(xvor[n])
85                    y_s.append(yvor[n])
86
87                    x.append(xvor[n])
88                    y.append(yvor[n])
89
90              # bad tT-paths
91              else:
92                    x_xs.append(xvor[n])
93                    y_xs.append(yvor[n])
94
95        # fit trendline to good data
96        t = np.polyfit(x,y,grad)
97        trend=np.polyval(t, x)
98
99        # summarise lists to AFT arrays for time slots
100       if r==0: aft20.append([x,  y,  x_ok,  y_ok,  x_s,  y_s,  x_xs,  y_xs, trend])
101       elif r==1: aft40.append([x,  y,  x_ok,  y_ok,  x_s,  y_s,  x_xs,  y_xs,  trend])
102       elif r==2: aft60.append([x,  y,  x_ok,  y_ok,  x_s,  y_s,  x_xs,  y_xs,  trend])
103       elif r==3: aft80.append([x,  y,  x_ok,  y_ok,  x_s,  y_s,  x_xs,  y_xs,  trend])
104       elif r==4: aft100.append([x,  y,  x_ok,  y_ok,  x_s,  y_s,  x_xs,  y_xs,  trend])
105       elif r==5: aft119.append([x,  y,  x_ok,  y_ok,  x_s,  y_s,  x_xs,  y_xs, trend])
106       else: print "somethings␣missing␣in␣here..."
107
108 ## Plot data
109
110 # Initialise figure and subplots
111 fig = plt.figure()
112 ax1 = fig.add_subplot(611)
113 bx1 = ax1.twinx()
114 ax2 = fig.add_subplot(612)
115 bx2 = ax2.twinx()
116 ax3 = fig.add_subplot(613)
117 bx3 = ax3.twinx()
118 ax4 = fig.add_subplot(614)
119 bx4 = ax4.twinx()
120 ax5 = fig.add_subplot(615)
```

```
121 bx5 = ax5.twinx()
122 ax6 = fig.add_subplot(616)
123 bx6 = ax6.twinx()
124
125 # Prepare data for the erosional topographies
126 x = [xi*.5 for xi in range(len(eSurface[-1]))]  # x values (model-km)
127
128 # erosional topographies extracted from main array of erosional topographies
129 e00 = [yi for yi in eSurface[0]]
130 e20 = [yi for yi in eSurface[sas[0]]]
131 e40 = [yi for yi in eSurface[sas[1]]]
132 e60 = [yi for yi in eSurface[sas[2]]]
133 e80 = [yi for yi in eSurface[sas[3]]]
134 e100 = [yi for yi in eSurface[sas[4]]]
135 e119 = [yi for yi in eSurface[sas[5]]]
136
137 # First subplot
138 ax1.set_title('20␣km␣shortening')
139 ax1.plot(x, e20, "k-")  # eT (erosional topography) after 20 km shortening
140 ax1.plot(x, e00, "k-.") # eT at begin of the simulation
141 bx1.plot(aft20[0][2], aft20[0][3], "ko")   # good AFT data
142 bx1.plot(aft20[0][4], aft20[0][5], color="0.8", marker="o",  linestyle='')  #
       acceptable AFT daten
143 bx1.plot(aft20[0][6], aft20[0][7], "wo")    # bad AFT data
144 bx1.plot(aft20[0][0], aft20[0][8], "k--")   # trendline for good AFT data
145
146 # Second subplot
147 ax2.set_title('40␣km␣shortening')
148 ax2.plot(x, e40, "k-")  # eT (erosional topography) after 40 km shortening
149 ax2.plot(x, e20, "k-.")  # eT (erosional topography) after 20 km shortening
150 bx2.plot(aft40[0][2], aft40[0][3], "ko")  # see first subplot
151 bx2.plot(aft40[0][4], aft40[0][5], color="0.8", marker="o",  linestyle='')    # see
       first subplot
152 bx2.plot(aft40[0][6], aft40[0][7], "wo")  # see first subplot
153 bx2.plot(aft40[0][0], aft40[0][8], "k--")  # see first subplot
154 bx2.plot(aft20[0][0], aft20[0][8], "k:")  # trendline for good AFT data after 20 km
       shortening
155
156 # Third subplot
157 ax3.set_title('60␣km␣shortening')
158 ax3.plot(x, e60, "k-") # eT (erosional topography) after 60 km shortening
159 ax3.plot(x, e40, "k-.") # eT (erosional topography) after 40 km shortening
160 bx3.plot(aft60[0][2], aft60[0][3], "ko")   # see first subplot
161 bx3.plot(aft60[0][4], aft60[0][5], color="0.8", marker="o",  linestyle='')   # see
       first subplot
162 bx3.plot(aft60[0][6], aft60[0][7], "wo") # see first subplot
163 bx3.plot(aft60[0][0], aft60[0][8], "k--") # see first subplot
164 bx3.plot(aft40[0][0], aft40[0][8], "k:") # see second subplot
165
166 # Fourth subplot
167 ax4.set_title('80␣km␣shortening')
168 ax4.plot(x, e80, "k-") # eT (erosional topography) after 80 km shortening
169 ax4.plot(x, e60, "k-.") # eT (erosional topography) after 60 km shortening
170 bx4.plot(aft80[0][2], aft80[0][3], "ko")     # see first subplot
171 bx4.plot(aft80[0][4], aft80[0][5], color="0.8", marker="o",  linestyle='')     # see
       first subplot
172 bx4.plot(aft80[0][6], aft80[0][7], "wo")   # see first subplot
173 bx4.plot(aft80[0][0], aft80[0][8], "k--")   # see first subplot
```

```
174 bx4.plot(aft60[0][0], aft60[0][8], "k:")    # see second subplot
175
176 # Fifth subplot
177 ax5.set_title('100 km shortening')
178 ax5.plot(x, e100, "k-") # eT (erosional topography) after 100 km shortening
179 ax5.plot(x, e80, "k-.") # eT (erosional topography) after 80 km shortening
180 bx5.plot(aft100[0][2], aft100[0][3], "ko")      # see first subplot
181 bx5.plot(aft100[0][4], aft100[0][5], color="0.8", marker="o",  linestyle='')      # see
      first subplot
182 bx5.plot(aft100[0][6], aft100[0][7], "wo")    # see first subplot
183 bx5.plot(aft100[0][0], aft100[0][8], "k--")    # see first subplot
184 bx5.plot(aft80[0][0], aft80[0][8], "k:")    # see second subplot
185
186 # Sixth subplot
187 ax6.set_title('119 km shortening')
188 ax6.plot(x, e119, "k-") # eT (erosional topography) after 119 km shortening
189 ax6.plot(x, e100, "k-.") # eT (erosional topography) after 100 km shortening
190 bx6.plot(aft119[0][2], aft119[0][3], "ko")       # see first subplot
191 bx6.plot(aft119[0][4], aft119[0][5], color="0.8", marker="o",  linestyle='')       #
      see first subplot
192 bx6.plot(aft119[0][6], aft119[0][7], "wo")      # see first subplot
193 bx6.plot(aft119[0][0], aft119[0][8], "k--")      # see first subplot
194 bx6.plot(aft100[0][0], aft100[0][8], "k:")      # see second subplot
195
196 # set axes dimensions
197 ax1.set_xlim((-2, 252))
198 ax2.set_xlim((-2, 252))
199 ax3.set_xlim((-2, 252))
200 ax4.set_xlim((-2, 252))
201 ax5.set_xlim((-2, 252))
202 ax6.set_xlim((-2, 252))
203
204 ax1.set_ylim((-1, 3))
205 ax2.set_ylim((-1, 3))
206 ax3.set_ylim((-1, 3))
207 ax4.set_ylim((-1, 3))
208 ax5.set_ylim((-1, 3))
209 ax6.set_ylim((-1, 3))
210
211 # set scale ticks
212 ax1.locator_params(axis='y',  nbins = 5)
213 bx1.locator_params(axis='y',  nbins = 5)
214 ax2.locator_params(axis='y',  nbins = 5)
215 bx2.locator_params(axis='y',  nbins = 5)
216 ax3.locator_params(axis='y',  nbins = 5)
217 bx3.locator_params(axis='y',  nbins = 5)
218 ax4.locator_params(axis='y',  nbins = 5)
219 bx4.locator_params(axis='y',  nbins = 5)
220 ax5.locator_params(axis='y',  nbins = 5)
221 bx5.locator_params(axis='y',  nbins = 5)
222 ax6.locator_params(axis='y',  nbins = 5)
223 bx6.locator_params(axis='y',  nbins = 5)
224
225 # show plot
226 plt.show()
227
228 print "done."
```

Exhumationplotter_041.py

```
## Exhumation plotter
##
## Author: Simon Elfert
##
## Developed for the PhD thesis by Simon Elfert (2009-2014, University of Bremen)
##
## Purpose of this script:
## plots exhumation rate against relative movement

## version 0.2: only plot running means and synchronize the y-Axis at y=0
## version 0.3 --- experimental!!! trys to figure out the effect of negative
##      vertical offset (ie burial). Furthermore handling absolute values of
##      exhumation  and no longer neg. and pos. values
## version 0.35 ... cleaned up version
## version 0.41 ... plotting exhumation rate and relative movement against time (ax)
     and directly against each other (bx)

# required libraries
# include libraries for statistics and numerical operations
from scipy import stats
import numpy as np

# include libraries for plotting
from pylab import *
import matplotlib.pyplot as plt

# import cPickle for reading binary data (for erosional topography)
import cPickle

# function: plot exhumation vs. relative movement
# tTSandbox: time-temperature data derived from numerical "sandbox" experiment
# xySandbox: particle position data from numerical "sandbox" experiment
# PAZ: list of saving steps corresponding to the first entry of a particle into the AFT
      partial annealing zone
# topo: array of erosional topographies
# fign: figure filename
# savefigure: flag for saving (True) or showing (False) plot
def exhumationplotter(tTSandbox,  xySandbox,  PAZ,  topo,   fign,  savefigure):

      # Initialise figure and subplot
      fig = figure ()
      ax = fig.add_subplot(111)
      ax.axhline(y=0,  color='0.9') # horizontal line at zero

      ########################################
      # exhumation rates (*1: Inc_01, *2: Inc_05, *3: Inc_30)
      ttx1,  tty1,  ttx2,  tty2,  ttx3,  tty3 = tTSandbox   # unpack tuple

      # derive exhumation rates
      e1 = [ ((tty1[i]-tty1[i+1]) /30) * 1000  for i in range(len(ttx1) -1)]    #
          Inc_01
      e2 = [ ((tty2[i]-tty2[i+1]) /30) * 1000  for i in range(len(ttx2) -1)]    #
          Inc_05
      e3 = [ ((tty3[i]-tty3[i+1]) /30) * 1000  for i in range(len(ttx3) -1)]    #
          Inc_30

```

```
52      # derive running mean (moving average) of exhumation rates
53      rme1 = [np.mean(e1[i:i+10]) for i in range(len(e1) - 9)]      # Inc_01
54      rme2 = [np.mean(e2[i:i+10]) for i in range(len(e2) - 9)]   # Inc_05
55      rme3 = [np.mean(e3[i:i+10]) for i in range(len(e3) - 9)]   # Inc_30
56
57      # absolute values for inc05
58      absrme2 = [abs(e) for e in rme2]
59
60      # running means of exhumation rates until PAZ-entry
61      ax.plot(ttx3[10:PAZ+1],  absrme2[:PAZ-9],  'k:',  linewidth=.5)    # to be
            commented for TH1-scene...
62      ax.plot(ttx1[10:PAZ+1],  rme1[:PAZ-9],  'r-',  linewidth=1)          # to be
            commented for TH1-scene...
63      ax.plot(ttx2[10:PAZ+1],  rme2[:PAZ-9],  'r--',  linewidth=1)        # to be
            commented for TH1-scene..
64      ax.plot(ttx3[10:PAZ+1],  rme3[:PAZ-9],  'r:',  linewidth=1)          # to be
            commented for TH1-scene...
65
66      # running means of exhumation rates since PAZ-entry
67      ax.plot(ttx3[PAZ:],  absrme2[PAZ-10:],  'k:',  linewidth=.5)          # to be
            commented for TH1-scene...
68      ax.plot(ttx1[PAZ:],  rme1[PAZ-10:],  'r-',  linewidth=2)               # to be
            commented for TH1-scene...
69      ax.plot(ttx2[PAZ:],  rme2[PAZ-10:],  'r--',  linewidth=2)              # to be
            commented for TH1-scene...
70      ax.plot(ttx3[PAZ:],  rme3[PAZ-10:],  'r:',  linewidth=2)               # to be
            commented for TH1-scene...
71
72  ##      # TH1-Scene, comment out if needed and comment rows above as mentioned
73  ##      ftime= 0.032032032
74  ##      start=int(((1000* ftime)-14.2)/ftime)
75  ##      print start
76  ##      mid=int(((1000*ftime) - 13.82)/ftime)
77  ##      print mid
78  ##      end=int(((1000*ftime) - 13.5)/ftime)
79  ##      print end,  "\n\n"
80  ##      try: ax.plot(ttx3[10:start+1],  rme3[:start-9],  '.6',  linewidth=1.5)
81  ##      except: print "bei 1"
82  ##      try: ax.plot(ttx3[start:mid+1],  rme3[start-10:mid-9],  'g',  linewidth=1.5)
83  ##      except: print "bei 2"
84  ##      try: ax.plot(ttx3[end:],  rme3[end-10:],  '.6',  linewidth=1.5)
85  ##      except: print "bei 3"
86  ##      try: ax.plot(ttx3[mid:end+1],  rme3[mid-10:end-9],  'r',  linewidth=1.5)
87  ##      except: print "bei 4"
88  ##      # end TH1-Scene
89
90      ##############################################
91      # plotting erosional topography (for case studies near to the surface)
92
93      if topo:
94          # selceted erosional topography at 77.5 mkm from
95          selTopo = [sasT[155] for sasT in topo]
96          ax.plot(ttx3,  selTopo,  "k:")
97
98      ##############################################
99      # relative movement
100
101     xx,  yy = xySandbox   # unpack tuple of x/y positions
```

```
102         # lengths of movement within one saving step
103         mov = [   np.sqrt(   ((yy[i+1] - yy[i] ))**2  +  (xx[i+1] - xx[i] )**2      ) *
                1000       for i in range(len(xx) -1)]     # in [m]
104         # vertical direction of movement within on saving step
105         vert = [    yy[1+1] - yy[i]   for i in range(len(xx)-1)]   # positive if particle
                is uplifted,  negative if particle is buried (values in [km])
106
107         # running mean (moving average) of relative movement and vertical offsets
108         rmMov = [np.mean(mov[i:i+10]) for i in range(len(mov) - 9)]
109         rmVert = [np.mean(vert[i:i+10]) for i in range(len(vert) - 9)]
110
111         # plot relative movement
112         ax.plot(ttx1[10:PAZ+1],  rmMov[:PAZ-10+1],  'b-',  linewidth=1)     # until PAZ
                entry
113         ax.plot(ttx1[PAZ:],  rmMov[PAZ-10:],  'b-',  linewidth=2)                    #
                from PAZ entry on
114
115
116         bfig = figure()
117         bx = bfig.add_subplot(111)
118
119         bx.plot(rmMov[62:], absrme2[62:],  "k.",  markersize=10)
120         slope, intercept, r_value, p_value, std_err = stats.linregress(rmMov[62:],
                absrme2[62:])
121         print 'R2 first step correlation:\t',  r_value**2
122         line = [slope* i + intercept for i in rmMov[62:]]
123
124         bx.plot(rmMov[62:],line,'k-', linewidth=5)
125         bx.set_ylim((0, max(absrme2[62:])+1))
126         bx.tick_params(axis="both",  labelsize="25",  pad=15)
127         for axis in ['top','bottom','left','right']:
128             bx.spines[axis].set_linewidth(2)
129
130         ###############################################
131         # set axes dimensions
132
133         # set x-limit to 30 Ma
134         ax.set_xlim(ax.get_xlim()[0], 30)
135 #        ax.set_xlim(12.,  16)     # TH1-Scene
136         ax.set_xlim(ax.get_xlim()[::-1])    # reverse x-axis
137
138         ax.set_ylim(min(rme3[62:])-20, max(rmMov[62:])+20)
139 #        ax.set_ylim(-25, 200) # H1-Scene
140
141         # flag processing: save or show figure
142         if savefigure:
143               plt.savefig(fign + ".eps",  format="eps")    # save  vector (eps)
144               plt.savefig(fign + ".png")  # save raster (png)
145         else: plt.show()  # show plot
146
147         ################################################
148         # statistics
149
150         # analyse percentage of negative vertical movement
151         negAll = [y for y in rmVert if y<0]                              # all negative
                vertical offsets
152         posAll = [y for y in rmVert if y>=0]                              # all positive
                vertical offsets
```

```
153       negPAZ = [y for y in rmVert[PAZ-10:] if y<0]            # all negative vertical
              offsets since PAZ
154       posPAZ = [y for y in rmVert[PAZ-10:] if y>=0]            # all positive vertical
              offsets since PAZ
155       pNegAll = abs(sum(negAll))/sum(posAll)                                  # percentage
              of negative to vertical offsets
156       pNegPAZ = abs(sum(negPAZ))/sum(posPAZ[PAZ-10:])         # percentage of negative
              to vertical offsets since PAZ
157
158       s,a,r_all,p,e= stats.linregress(absrme2[62:], rmMov[62:]) # sas 62 = 30 Ma... to
              except faulty values regarding to boundary conditions at the begin of the
              model run
159       s,a,r_PAZ,p,e= stats.linregress(absrme2[PAZ-10:], rmMov[PAZ-10:])
160
161       print np.mean(rme3),  "\t", # mean of running mean (Inc_30)
162       print np.std(rme3),  "\t",  # standard deviation of running mean (Inc_30)
163       print np.mean(rme3[PAZ-10:]),  "\t",  # mean of running mean (Inc_30) from PAZ
              entry on
164       print np.std(rme3[PAZ-10:]),  "\t", # standard deviation of running mean from PAZ
               entry (Inc_30) on
165       print r_all**2, "\t",  # R^2 between exhumation (Inc30) and relative movement
166       print r_PAZ**2  # R^2 between exhumation (Inc30) and relative movement since PAZ
167
168 # function: Loading time-temperature data
169 # f3: filename for tT-data
170 def openTTDat(f3):
171       tTp = np.loadtxt(f3,  dtype={'names' : ('time', 'temp'), 'formats' : (float,
              float)})
172       x=tTp['time']
173       y=tTp['temp']
174
175       return x,  y
176
177 # function: Loading position data
178 # fnxy: filename for xy-position information
179 def openXYDat(fnxy):
180       XYp = np.loadtxt(fnxy,  dtype={'names' : ('id','x', 'y'), 'formats' : (int,
              float, float)})
181       x=XYp['x']
182       y=XYp['y']
183
184       return x,  y
185
186 ######################################################
187 ######## Starting point ##################################
188 ######################################################
189
190 if __name__ == "__main__":
191
192       dir = "data/sza3-NA-lx1000_"  # directory of time-temperature data    # testdata
193       topodir = False    # directory of topography data    # for case studies near the
              erosional surface
194       xydir = "data/xytestdata/"  # directory of x/y position data    # testdata
195
196       # particles corresponding to real samples...
197       p = [50078,  50905,  53145,  54491,  54548,  52012,  70797]   # particle IDs
198       PAZ=[501, 691, 664, 536, 369, 328, 274] # saving step of PAZ-entry of particles
199
```

```
200       id =  0 # current particle
201
202       # if erosional topography shall be plotted (path to file necessary!)
203       topoflag=False
204
205       # Saving flag
206       savefigure=False  # False for showing, True for saving
207
208 ###################################################
209
210       # erosional topography...
211       if topoflag:
212           print "loading_topography..."
213           topo = cPickle.load(open(topodir+"3_211211__lx1000_topo2c.dat", 'rb'))
214           print "done"
215       else: topo=False
216
217 ###################################################
218
219       # tT-paths
220       ttx1,  tty1 = openTTDat(dir+"inc01/"+str(p[id])+"_a3__lx_1000.txt")
221       ttx2,  tty2 = openTTDat(dir+"inc05/"+str(p[id])+"_a3__lx_1000.txt")
222       ttx3,  tty3 = openTTDat(dir+"inc30/"+str(p[id])+"_a3__lx_1000.txt")
223       tTSandbox = (ttx1,  tty1,  ttx2,  tty2,  ttx3,  tty3)                          #
              tuple packing
224
225 ###################################################
226
227       # xy-paths
228       xx,  yy = openXYDat(xydir +str(p[id]))  # independent from incision!
229       xySandbox = (xx,  yy)
                                                                                        # tuple
              packing
230
231 ###################################################
232
233       # Figure name
234       fign= "data/"+str(p[id])
235
236       # call main function
237       exhumationplotter(tTSandbox,  xySandbox,  PAZ[id],  topo,  fign,  savefigure)
238
239       print "done."
```

AFT-TL-CR_plotter_0.12b.py

```
1 ## Summaryplotter for observed and synthetic AFT data
2 ##
3 ## Author: Simon Elfert
4 ##
5 ## Developed for the PhD thesis by Simon Elfert (2009-2014, University of Bremen)
6 ##
7 ## Purpose of this script:
8 ## Plots track length distributions, tT-paths and cooling rates for three scenarios
9 ## (incision 1, 5 and 30 Ma) for one sample in three subplots
10 ## Option: Test script with one sample, view plot(s) (feasible only in test
11 ## environment), save plot(s)
```

```
12 ## Version 0.12b - plot observed data to selected particles
13
14 # required libraries
15 import numpy as np
16 from pylab import *
17 import matplotlib.pyplot as plt
18
19 # required own script
20 import inverse_tT_2D_1_0 as itT2D
21
22 # function: plot track length distributions, tT-paths and cooling rates
23 # x1/y1/m1: TL distribution and mean track length of scenario Inc_01 (effective erosion
       since 1 Ma)
24 # x2/y2/m2: TL distribution and mean track length of scenario Inc_05 (effective erosion
       since 5 Ma)
25 # x3/y3/m3: TL distribution and mean track length of scenario Inc_30 (effective erosion
       since 30 Ma)
26
27 # ttx1/tty1/AFT1: time-temperature path for scenario Inc_01 and corresponding AFT age
28 # ttx2/tty1/AFT2: time-temperature path for scenario Inc_05 and corresponding AFT age
29 # ttx3/tty1/AFT3: time-temperature path for scenario Inc_30 and corresponding AFT age
30
31 # obsdata: constraints and envelopes of good and acceptable statistical aggreement with
       the observed data from inverse thermal history modelling
32 # aft: Central AFT age (determined from field data)
33 # otlx/otly: TL distribution (determined from field data)
34 # omtl: Mean track length of best fitting model from inverse thermal history modelling
      of field data
35 # fign: figure name
36 # savefigure: flag for saving plot (if False: show)
37 def tlplotter(x1,  y1,  m1,  x2,  y2,  m2,  x3, y3,  m3, ttx1,  tty1,  AFT1,  ttx2,
      tty2,  AFT2,  ttx3,  tty3,  AFT3, obsdata, aft,  otlx,  otly,  omtl,  fign,
      savefigure):
38
39       # Initialise figure
40       fig = figure (figsize=(7, 12))
41
42 ##       # First subplot: TL-Distributions
43       ax = fig.add_subplot(311)
44
45       ax.plot(otlx,  otly,  "0.8",  linewidth=2)     # modelled from observed  data
46
47       ax.plot(x1, y1,  "k-")     # inc01
48       ax.plot(x2, y2,  "k--")    # inc05
49       ax.plot(x3, y3,  "k:")     # inc30
50
51       # arange postition of subplot
52       ax.set_position([0.15, 0.6, 0.8, 0.35])
53
54       # set scale ticks
55       major_locator = plt.MultipleLocator(.05)
56       major_formatter = plt.FormatStrFormatter('%5.2f')
57       ax.yaxis.set_major_locator(major_locator)
58       ax.yaxis.set_major_formatter(major_formatter)
59
60       plt.xticks(fontsize=24)
61       plt.yticks(fontsize=24)
62
```

```
63        # set legend text (Mean track lengths)
64        ax.text(ax.get_xlim()[0]+1,ax.get_ylim()[1]-.14, "i01:␣"+str(m1)+"\ni05:␣"+str(m2
              )+"\ni30:␣"+str(m3) + "\nobs:␣"+str(omtl),  fontsize=24,  bbox=dict(
              facecolor='white'))
65
66 ##       # Second subplot: tT-paths
67        ax2 = fig.add_subplot(312)
68
69        # plot AFT partial annealing zone and AHe partial retention zone differently
              hatched
70        ax2.axhspan(60, 110,  fill=False, edgecolor= ".7",  hatch = '/')
71        ax2.axhspan(40, 85,  fill=False,  edgecolor='.7',  hatch='\\')
72
73        # plot envelopes of observed (modelled) acceptable and good paths
74        e,  b = obsdata # unpack list (e: envelopes)
75        ax2.fill_between(e['a_time'], e['a_high'], e['a_low'], facecolor='0.5', alpha
              =0.2)    # envelope of acceptable tT-paths
76        ax2.fill_between(e['g_time'], e['g_high'], e['g_low'], facecolor='0.3', alpha
              =0.2)    # envelope of good tT-paths
77
78        # plot best model of observed data
79        ax2.plot(b['time'],  b['temp'],  '.9',  linewidth=2)
80
81        # plot tT-paths derived from numerical "sandbox" modelling
82        ax2.plot(ttx1,  tty1,  "k-")  # Inc_01
83        ax2.plot(ttx2,  tty2,  "k--") # Inc_05
84        ax2.plot(ttx3,  tty3,  "k:")  # Inc_30
85
86        # set axes dimensions and reverse axes
87        ax2.set_xlim(ax2.get_xlim()[0], 25)
88        ax2.set_xlim(ax2.get_xlim()[::-1])
89        ax2.set_ylim((0, 120))
90        ax2.set_ylim(ax2.get_ylim()[::-1])
91
92        # arange postition of subplot
93        ax2.set_position([0.15, 0.2, 0.8, 0.35])
94
95        # set scale ticks
96        major_locator2 = plt.MultipleLocator(20)
97        major_formatter2 = plt.FormatStrFormatter('%3i')
98        ax2.yaxis.set_major_locator(major_locator2)
99        ax2.yaxis.set_major_formatter(major_formatter2)
100
101       plt.xticks(fontsize=24)
102       plt.yticks(fontsize=24)
103
104       # set legend text (AFT ages)
105       ax2.text(24,46, "i01:␣"+str(AFT1)+"\ni05:␣"+str(AFT2)+"\ni30:␣"+str(AFT3)+"\nobs:
              ␣"+str(aft),  fontsize=24,  bbox=dict(facecolor='white'))
106
107 ##       # Third subplot: cooling rate
108       ax3=fig.add_subplot(313)
109
110       # arange postition of subplot
111       ax3.set_position([0.15, 0.05, 0.8, 0.1])
112
113       # prepare x values (31 Ma... 0 Ma)
114       cx=[31-i for i in range(32)]
```

```
115
116 #       # calculating cooling rate for xy1 (Inc_01)
117       precy1=[tty1[0]]  # mean temperature per Ma
118       i=0   # counter
119       ysum=[]   # temporary  summed temperature for calculation of average
120
121       # for each time-temperature pair
122       for j in range(len(tty1)):
123             # only consider data until current Myr-slot (data starts at 32 Ma. cx
                  starts with 31,
124             # therefore in the first loop only data from 32 Ma to 31 Ma is considered)
125             if ttx1[j]>=cx[i]: ysum.append(tty1[j])
126             else:
127                 # if no more x/y pairs are in the current Myr-slot, than derive average
                        cooling and
128                 # start new Myr-slot
129                 try:
130                     precy1.append(np.mean(ysum))
131                     ysum=[tty1[j]]
132                 except:
133                     precy1.append(0)
134                     ysum=[tty1[j]]
135                 i+= 1   # increase counter
136       # endfor
137
138       precy1.append(10) # end with temperature 10 degree C
139
140       # prepare cooling rate for plotting
141       cy1 = [ precy1[i]-precy1[i+1]            for i in range(len(precy1)-1)] # cooling
               rate [Degree C Ma-1]
142
143
144 #       # calculating cooling rate for xy2 (Inc_05). See last section  for introduction
145       precy2=[tty2[0]]
146       i=0
147       ysum=[]
148
149       for j in range(len(tty2)):
150             if ttx2[j]>=cx[i]: ysum.append(tty2[j])
151             else:
152                   try:
153                         precy2.append(np.mean(ysum))
154                         ysum=[tty2[j]]
155                   except:
156                         precy2.append(0)
157                         ysum=[tty2[j]]
158                   i=i+1
159       precy2.append(10)
160       cy2 = [ precy2[i]-precy2[i+1]            for i in range(len(precy2)-1)]
161
162 #       # calculating cooling rate for xy3 (Inc_30). See last section for introduction
163       precy3=[tty3[0]]
164       i=0
165       ysum=[]
166
167       for j in range(len(tty3)):
168             if ttx3[j]>=cx[i]: ysum.append(tty3[j])
169             else:
```

```
170                 try:
171                       precy3.append(np.mean(ysum))
172                       ysum=[tty3[j]]
173                 except:
174                       precy3.append(0)
175                       ysum=[tty3[j]]
176                 i=i+1
177       precy3.append(10)
178       cy3 = [ precy3[i]-precy3[i+1]            for i in range(len(precy3)-1)]
179
180       # plot cooling rates
181       ax3.plot(cx, cy1,  'k-')  # Inc_01
182       ax3.plot(cx, cy2,  'k--') # Inc_05
183       ax3.plot(cx, cy3,  'k:')  # Inc_30
184
185       # set x axis dimension
186       ax3.set_xlim((25, 0))
187       ax3.axhspan(0, 0) # horizontal line at zero (degree C)
188
189       # get y-limits
190       yl=[]
191       yl.append(min(cy1[-26:]))
192       yl.append(min(cy2[-26:]))
193       yl.append(min(cy3[-26:]))
194       yl.append(max(cy1[-26:]))
195       yl.append(max(cy2[-26:]))
196       yl.append(max(cy3[-26:]))
197
198       # set y axis dimensions related to the value range (as tight as possible)
199       if min(yl) > -10: ylmin=-11
200       elif min(yl) < -30 and min(yl)>-50: ylmin=-55
201       else: ylmin = min(yl)-5
202       if max(yl) < 10: ylmax=11
203       elif max(yl) > 30 and max(yl)<50: ylmax=55
204       else: ylmax = max(yl)+5
205
206       ax3.set_ylim((ylmin, ylmax))
207
208       # set scale ticks
209       ax3.locator_params(axis='y',  nbins = 3)
210
211       if ylmax-ylmin<40:
212             major_locator3 = plt.MultipleLocator(10)
213             major_formatter3 = plt.FormatStrFormatter('%3i')
214             ax3.yaxis.set_major_locator(major_locator3)
215             ax3.yaxis.set_major_formatter(major_formatter3)
216       elif ylmax-ylmin<60:
217             major_locator3 = plt.MultipleLocator(20)
218             major_formatter3 = plt.FormatStrFormatter('%3i')
219             ax3.yaxis.set_major_locator(major_locator3)
220             ax3.yaxis.set_major_formatter(major_formatter3)
221       elif ylmax-ylmin<100:
222             major_locator3 = plt.MultipleLocator(30)
223             major_formatter3 = plt.FormatStrFormatter('%3i')
224             ax3.yaxis.set_major_locator(major_locator3)
225             ax3.yaxis.set_major_formatter(major_formatter3)
226       else:
227             major_locator3 = plt.MultipleLocator(50)
```

```
228             major_formatter3 = plt.FormatStrFormatter('%3i')
229             ax3.yaxis.set_major_locator(major_locator3)
230             ax3.yaxis.set_major_formatter(major_formatter3)
231
232       # format scale ticks
233       plt.xticks(fontsize=24)
234       plt.yticks(fontsize=24)
235
236       # flag processing: save (both eps and png) or show figure
237       if savefigure:
238             print fign
239             plt.savefig(fign + ".eps",  format="eps")
240             plt.savefig(fign + ".png")
241       else: plt.show()
242
243
244 # function: Reading track length data from file
245 # fn2: filename for track length data
246 def openTLDat(fn2):
247       f2=open(fn2+".txt",  'r') # open
248       tldata=f2.readlines()            # read out
249       f2.close()                              # close
250
251       # Initialise lists for TL data
252       x=[]
253       y=[]
254
255       # for TL frequency pair in data (first row: header)
256       for l in tldata[1:]:
257             x.append(float(l.split('\t')[2]))
258             y.append(float(l.split('\t')[3]))
259
260       return x, y
261
262 # function: Reading time-temperature data from file (derived from numerical "sandbox"
      experiment)
263 # fn2: filename for track length data
264 def openTTDat(f3):
265       # load data to array
266       tTp = np.loadtxt(f3,  dtype={'names' : ('time', 'temp'), 'formats' : (float,
            float)})
267       x=tTp['time']
268       y=tTp['temp']
269
270       return x,  y
271
272 ################################################
273 ####### Starting point ##############################
274 ################################################
275
276 if __name__ == "__main__":
277
278       # working directory
279       dir = "data/" # testdata
280
281       lx=1000   # number of saving steps in the numerical "sandbox" experiment -
            related to shortening
282
```

```
283       fn1 = dir+"sz-a3-NA-llx"+str(lx)+".txt"   # filename for synthetic AFT data (
              position, ages, mean track lengths and evaluation of tT-paths)
284       incs=["inc01", "inc05", "inc30"]  # scenarios: effective erosion since 1 Ma, 5 Ma
               and 30 Ma, respectively
285
286       # loading synthetic AFT data
287       f1=np.loadtxt(fn1, dtype={'names' : ('lx', 'inc', 'id', 'x', 'y',  'AFT',  'TL',
               'StDev','note'), 'formats' : (int, 'S20', int,  float,  float,  float,
              float, float,  'S20')}, skiprows=1)
288
289       # particles corresponding to real samples from paper contribution 1 (Elfert et al
              ., 2013)
290       ps = [50078,  50905,  53145,  54491,  54548,  52012,  70797]
291       # real samples
292       ths = ["Ticino-H01",  "Ticino-H06",  "Ticino-H18",  "Ticino-H23",  "Ticino-H27",
               "Ticino-H28",  "Ticino-H25"]    # IDs
293       afts = [13.1,  7.6,  9.2,  8.2,  15.2,  17.,  18.9] # AFT, central ages (
              determined from field data)
294       mtls = [13.15,  13.49,  13.48,  13.48,  13.91,  13.89,  14.13] # mean TL (non c-
              axis projected) from best fitting model != real measurement!!!
295
296       test=True # Plotting single pairs of synthetic and observed data
297       curPair =  1  # current pair of particle/sample
298       testp=ps[curPair] # get current particle
299
300       savefigure=False  # False for showing, True for saving
301
302       # Loading observed data...
303       obsdir = "data/"  # testdata
304       ofn = obsdir + ths[curPair] + "__20130118_ucs-inv"    # basename testdata
305       ofn1 = ofn+"Cons.txt"    # filename for constraints data (for inverse thermal
              history modelling)
306       ofn2 = ofn+ "Env.txt"     # filename for envelope data (good and acceptable paths
               from inverse thermal history modelling)
307       ofn3 = ofn+ "Best.txt"    # filename for bestfitting model (from inverse thermal
              history modelling)
308       tlfn = obsdir + ths[curPair]+ "__TL_rD02_20130718.txt"  # filename for measured
              TL data (frequencies)
309
310       obsshave =2       # flag... 0: show, 1: save, 2: nothing
311       exportflag = True  # exportflag for observed data (to be submitted to
              communicating script)
312
313 ##############################################
314 ##  end of user defined section  ##########################
315 ##############################################
316
317       t=True    # hotfix for test handling
318       # each particle, exported from numerical "sandbox" experiment
319       for p in f1:
320             if p['id']==testp: t=True
321             else:
322                   if test: t=False
323                   else: t=True
324
325             # test if the particle has data for all incs. To do so, fix it to the first
                    and count the occurences of the current particle-id (has to equal the
                    no. of incs)
```

```
326             if t and p['inc']==incs[0] and (array(f1['id'])==p['id']).sum()==len(incs):
327                   # first part of directory  path of the TL-data (without inc-
                          specification)    # testdata
328                   dir2 = "data/TL-NA-lx"+str(lx)+"_"
329                   # first part of directory of the tT-data (without inc-specification)
                           # testdata
330                   dir3 = "data/sza3-NA-lx"+str(lx)+"_"
331
332                   # Loading TL-Distributions
333                   x1, y1=openTLDat(dir2+incs[0]+"/"+ str(p['id'])+"_tl"+str(lx)+"_"+
                          incs[0] )               # inc = 1 Ma
334                   x2, y2=openTLDat(dir2+incs[1]+"/"+ str(p['id'])+"_tl"+str(lx)+"_"+
                          incs[1] )               # inc = 5 Ma
335                   x3, y3=openTLDat(dir2+incs[2]+"/"+ str(p['id'])+"_tl"+str(lx)+"_"+
                          incs[2] )               # inc = 30 Ma
336
337                   # Loading tT-paths
338                   ttx1,  tty1 = openTTDat(dir3+incs[0]+"/"+str(p['id'])+"_a3__lx_"+str(
                          lx)+".txt")              # inc = 1 Ma
339                   ttx2,  tty2 = openTTDat(dir3+incs[1]+"/"+str(p['id'])+"_a3__lx_"+str(
                          lx)+".txt")              # inc = 5 Ma
340                   ttx3,  tty3 = openTTDat(dir3+incs[2]+"/"+str(p['id'])+"_a3__lx_"+str(
                          lx)+".txt")            # inc = 30 Ma
341
342                   # extract average values
343                   m1 = p['TL']  # Mean TL (Inc_01)
344                   AFT1=p['AFT'] # Mean AFT age (Inc_01)
345
346                   # search all particles for the next occurence of the particle and
                          extract the specific MTL and AFT ages for the other inc-
                          scenarios
347                   for pi in f1:
348                         if pi['id']==p['id'] and pi['inc']==incs[1]:
349                               m2=pi['TL']      # Mean TL (Inc_05)
350                               AFT2=pi['AFT'] # Mean AFT age (Inc_05)
351                         elif pi['id']==p['id'] and pi['inc']==incs[2]:
352                               m3=pi['TL']     # Mean TL (Inc_30)
353                               AFT3=pi['AFT']     # Mean AFT age (Inc_30)
354                         else: pass
355
356                   # Figure name (code model-km, particle ID and lx into filename)
357                   fign= "data/"+str(round(p['x'], 2))+"__"+ str(p['id'])+"_lx"+str(lx)
358
359                   # Loading observed tT-data utilizing the communicating script
360                   obsdata = itT2D.inverseHeftyPlot(obsdir,  ofn,  ofn1,  ofn2,  ofn3,
                          False,  obsshave,  exportflag)
361
362                   # Loading observed TL-data
363                   file = open(tlfn,  'r')
364                   rawdata = file.readlines()
365                   file.close()
366
367                   # Initialise lists for TL data
368                   otlx = []
369                   otly = []
370
371                   # extract TL data (first row: header)
372                   for d in rawdata[1:]:
```

```
373                     row = d.split('\t')    # data is tab separated
374                     otlx.append(float(row[2]))
375                     otly.append(float(row[3]))
376
377                 # start main function
378                 tlplotter(x1,  y1,  m1,  x2,  y2,  m2,  x3, y3,  m3,
379                           ttx1,  tty1,  AFT1,  ttx2,  tty2,  AFT2,  ttx3,  tty3,
                              AFT3, obsdata, afts[curPair],  otlx,  otly, mtls[
                              curPair],
380                           fign,  savefigure)
381
382     print "done."
```

E. Curriculum vitae

PERSONAL DATA

Name:	Simon Elfert
Contact:	Erlenstr. 101, 28199 Bremen
	T 0421–2089080
	M 0175–6362695
	simon.elfert@web.de
Date of birth:	12.11.1981
Place of birth:	Osterholz-Scharmbeck
Family status:	married
Citizenship:	German

WORK EXPERIENCE

11/2012 – 04/2013	research associate/ consultant, DHI-WASY, Syke
10/2012 – 03/2013	lecturer at the University of Bremen (Geographic Information Systems)
01/09 until today	PhD student at the University of Bremen
01/09 – 03/12	research associate at the University of Bremen
04/07 – 07/08 and 11/04 – 12/06	student assistant at the University of Oldenburg (hydrology working group)

EDUCATION

10/01 – 03/09	Study of Landscape Ecology at the Carl von Ossietzky University of Oldenburg Graduation: Diploma in Landsape Ecology
07/07	Learning ArcGis Desktop (for ArcGis 9.0 – 9.1, ESRI Training und Education, online class)
03/05	First place at the "Wasserpreis des OOWV" for the development of an internet based information plattform on the subject of potable water protection (www.uni-oldenburg.de/hydrologie/einbit)
01/05	c/c++ class
09/88 – 04/01	Freie Evangelische Bekenntnisschule Bremen Graduation: A level

PEER REVIEWED PUBLICATIONS

2013 Elfert S., Reiter W., Spiegel C. (2013): Long-lasting tectonic activities of the Lepontine Dome. New evidence from low-temperature thermochronology. Tectonophysics, 608, 222-236

2013 Reiter W., Elfert S., Glotzbach C., Bernet M., Spiegel C. (2013): Relations between denudation, glaciation, and sediment deposition: implications from the Plio-Pleistocene Central Alps. Basin Research, 25, 1-16

2011 Bormann H., Pinter N., Elfert S. (2011): Hydrological signatures of flood trends on German rivers: Flood frequencies, flood heights and specific stages, Journal of Hydrology, 404, 50-66

2010 Bormann H., Elfert S. (2010): Application of WaSiM-ETH model to Northern German lowland catchments: model performance in relation to catchment characteristics and sensitivity to land use change, Advances in Geosciences, 27, 1-10

2010 Elfert S., Bormann H. (2010): Simulated impact of past and possible future land use changes on the hydrological response of the Northern German lowland ‚Hunte' catchment. Journal of Hydrology, 383, 245-255

IN PREPARATION FOR PEER REVIEWED PUBLICATION

2014* Wenk L., Elfert S., Spiegel C., Huhn K. (*in preparation): Describing orogenic wedges by a combination of numerical 'sandbox' models and low-temperature thermochronology I: Linking lower crustal geometries and mechanic properties with upper crustal processes. In preparation for submission to Journal of Geophysical Research

2014* Elfert S., Wenk L., Spiegel C., Huhn K. (*in preparation): Describing orogenic wedges by a combination of numerical 'sandbox' models and low-temperature thermochronology. II: Applications to upper crustal processes of the European Central Alps. In preparation for submission to Journal of Geophysical Research

Talk

2011 Elfert S., Reiter W., Spiegel C. (2011): Timing and evolution of Neogene updoming of the Lepontine Dome. Constraints through new fission track and (U-Th-Sm)/He data on apatites. 10th Alpine Workshop, CorseAlp 2011, St. Florent/France

Abstracts

2014 Elfert W., Wenk L., Huhn K., Spiegel C. (2014): Describing orogenic wedges by a combination of numerical sandbox models and low-temperature thermochronology - Implications for the exhumation of the Central Alps. Poster presentation, Thermo2014, 14th International Conference on Thermochronology, Chamonix/France

2011 Elfert S., Reiter W., Spiegel C. (2011): Timing and evolution of Neogene updoming of the Lepontine Dome. Constraints through new fission track and (U-Th-Sm)/He data on apatites. Oral presentation, 10th Alpine Workshop, CorseAlp 2011, St. Florent/France

2011 Reiter W., Elfert S., Spiegel C. (2011): Plio-Pleistocene changes in drainage evolution and implications for the denudation history of the Central European Alps. Oral presentation, 10th Alpine Workshop, CorseAlp 2011, St. Florent/France

2011 Elfert S., Reiter W., Spiegel C. (2011): Doming and unroofing of the Lepontine Dome (Central European Alps). New insights from Low-Temperature thermochronology. Poster presentation, General Assembly of the European Geosciences Union 2011, Vienna/Austria

2011 Reiter W., Elfert S., Spiegel C. (2011): Plio-Pleistocene denudation history of the Central European Alps revealed through detrital thermochronology. Poster presentation, General Assembly of the European Geosciences Union 2011, Vienna/Austria

2010 Elfert S., Reiter W., Spiegel C. (2010): Interrelations between the exhumation history and the drainage evolution of the European Alps during the Neogene. Poster presentation, Thermo2010, 12th International Conference on Thermochronology, Glasgow/UK

2010 Reiter W., Elfert S., Spiegel C. (2010): Reconstructing circum-Alpine drainage evolution since the Pliocene using detrital thermochronology. Poster presentation, Thermo2010, 12th International Conference on Thermochronology, Glasgow/UK

2009 Elfert, S., Reiter, W., Dörr, N., Spiegel, C. (2009): Sources of Pliocene erosion of the Alps - The Lepontine Dome as a potential source area. Poster presentation, 9th Alpine Workshop, Cogne/Italy

2009 Reiter W., Elfert S., Spiegel C. (2009): Pliocene erosion and drainage evolution of the Alps: Constraints from Neogene sedimentary deposits. Poster presentation, 9th Alpine Workshop, Cogne/Italy

2009 Bormann H., Elfert S. (2009): Impact of past and possible future land use changes on the hydrological behaviour of the Northern German lowland 'Hunte' river. Poster presentation, General Assembly of the European Geosciences Union 2011, Vienna/Austria

2009 Klassen K., Elfert S., Bormann H. (2009): Einfluss von Pflegemaßnahmen auf den Bodenwasser- und Nährstoffhaushalt einer Heidelandschaft. In: Fohrer N., Schmalz B., Hörmann G., Bieger K. (Hrsg.): Hydrologische Systeme im Wandel. Beiträge zum Tag der Hydrologie 2009. Forum für Hydrologie und Wasserbewirtschaftung 26.09, Poster-CD